Probing the structure and dynamics of gas-phase molecules with coincidence momentum imaging

by

Anbu Selvam Venkatachalam

B.E., College of Engineering, Guindy, Anna University, Chennai, India, 2005

M.S., University of Vermont, 2013

M.Sc., Indian Institute of Technology Hyderabad, India, 2017

AN ABSTRACT OF A DISSERTATION

submitted in partial fulfillment of the
requirements for the degree

DOCTOR OF PHILOSOPHY

Department of Physics
College of Arts and Sciences

KANSAS STATE UNIVERSITY
Manhattan, Kansas

2026

Abstract

Understanding how molecular structure evolves following interaction with light is essential for explaining chemical reactivity and for developing strategies to control molecular transformations. Coincidence momentum imaging of charged fragments (ions and electrons), in particular Coulomb explosion imaging (CEI), provides a direct route to this information for gas-phase molecules by mapping nuclear geometry and dynamics onto fragment-ion momenta. This thesis covers four closely related research projects that span time-resolved and static CEI, high-dimensional multi-ion coincidence combined with machine learning, and ion–electron coincidence spectroscopy.

First, ultrafast structural dynamics in diiodomethane (CH_2I_2) are explored using an ultraviolet (UV) pump–infrared (IR) probe CEI scheme. Momentum-resolved ion coincidence data reveal several competing dissociation pathways, including direct C–I bond fission, three-body breakup channels, and molecular iodine formation. Delay-dependent kinetic energy and angular observables provide evidence for a short-lived iso-CH_2I_2-like configuration that forms and decays on a sub-100 fs timescale. These measurements demonstrate how time-resolved CEI can isolate weak, transient configurations in the presence of other dominant reaction channels.

Second, static CEI is used to establish three-dimensional momentum fingerprints of molecules relevant to ring-opening photochemistry. Strong-field Coulomb explosion of molecules such as isoxazole, 3-chloro-1-propanol, and epichlorohydrin yields multi-ion Newton maps that encode out-of-plane motion and angular correlations. Distinct momentum patterns associated with planar ring, open-chain, and ring–chain structures are identified and qualitatively reproduced by classical Coulomb explosion simulations. These results show that robust structural discrimination for medium-sized molecules is achievable with tabletop laser systems and motivate efforts toward complete coincidence detection for these molecules.

Third, high-dimensional CEI with complete six-ion coincidence is combined with machine learning to extract structural information from complex momentum data. Dimensionality-reduction

methods and density-based clustering separate *cis*- and *trans*-1,2-dichloroethylene (DCE) isomers directly from experimental mixtures, while supervised models trained on simulated data sets extend the analysis to additional geometries such as 1,1-DCE and transient twisted configurations. Eight-fold coincidence data for isoxazole illustrate how complete channels sharpen angular momentum and energy distributions. Together, these studies demonstrate that multi-coincidence CEI combined with machine learning can automatically identify subtle structural differences and minor channels from high-dimensional data.

Finally, ion–electron coincidence measurements on core-ionized methyl iodide (CH_3I) at a synchrotron beamline are used to connect inner-shell electronic decay to specific ionic fragmentation outcomes. Channel-resolved Auger–Meitner electron spectra, obtained by correlating electrons with well-defined ion channels, reveal systematic changes in band positions and widths as a function of final charge state and hydrogen loss. Comparison of two-body and three-body kinetic energy releases isolates contributions from channels involving neutral iodine fragments and highlights the sensitivity of the low energy electron spectrum to details of the fragmentation pathway. These measurements provide benchmark data for state resolved Auger decay and complement the laser-based CEI studies by adding an explicit electronic-structure perspective.

Overall, this thesis advances coincidence momentum imaging as a structural and dynamical probe for polyatomic molecules. Time-resolved and static CEI establish momentum space fingerprints of transient and equilibrium geometries, high dimensional multi-coincidence measurements combined with machine learning enable event-level molecular structure differentiation, and ion–electron coincidence spectroscopy links core-level decay to fragmentation patterns. Together, these approaches lay the groundwork for future efforts to image and control molecular dynamics on their natural femtosecond timescales.

Probing the structure and dynamics of gas-phase molecules with coincidence momentum imaging

by

Anbu Selvam Venkatachalam

B.E., College of Engineering, Guindy, Anna University, Chennai, India, 2005

M.S., University of Vermont, 2013

M.Sc., Indian Institute of Technology Hyderabad, India, 2017

A DISSERTATION

submitted in partial fulfillment of the
requirements for the degree

DOCTOR OF PHILOSOPHY

Department of Physics
College of Arts and Sciences

KANSAS STATE UNIVERSITY
Manhattan, Kansas

2026

Approved by:

Major Professor
Prof. Daniel Rolles

Copyright

Abstract

Understanding how molecular structure evolves following interaction with light is essential for explaining chemical reactivity and for developing strategies to control molecular transformations. Coincidence momentum imaging of charged fragments (ions and electrons), in particular Coulomb explosion imaging (CEI), provides a direct route to this information for gas-phase molecules by mapping nuclear geometry and dynamics onto fragment-ion momenta. This thesis covers four closely related research projects that span time-resolved and static CEI, high-dimensional multi-ion coincidence combined with machine learning, and ion–electron coincidence spectroscopy.

First, ultrafast structural dynamics in diiodomethane (CH_2I_2) are explored using an ultraviolet (UV) pump–infrared (IR) probe CEI scheme. Momentum-resolved ion coincidence data reveal several competing dissociation pathways, including direct C–I bond fission, three-body breakup channels, and molecular iodine formation. Delay-dependent kinetic energy and angular observables provide evidence for a short-lived iso-CH_2I_2-like configuration that forms and decays on a sub-100 fs timescale. These measurements demonstrate how time-resolved CEI can isolate weak, transient configurations in the presence of other dominant reaction channels.

Second, static CEI is used to establish three-dimensional momentum fingerprints of molecules relevant to ring-opening photochemistry. Strong-field Coulomb explosion of molecules such as isoxazole, 3-chloro-1-propanol, and epichlorohydrin yields multi-ion Newton maps that encode out-of-plane motion and angular correlations. Distinct momentum patterns associated with planar ring, open-chain, and ring–chain structures are identified and qualitatively reproduced by classical Coulomb explosion simulations. These results show that robust structural discrimination for medium-sized molecules is achievable with tabletop laser systems and motivate efforts toward complete coincidence detection for these molecules.

Third, high-dimensional CEI with complete six-ion coincidence is combined with machine learning to extract structural information from complex momentum data. Dimensionality-reduction

methods and density-based clustering separate *cis*- and *trans*-1,2-dichloroethylene (DCE) isomers directly from experimental mixtures, while supervised models trained on simulated data sets extend the analysis to additional geometries such as 1,1-DCE and transient twisted configurations. Eight-fold coincidence data for isoxazole illustrate how complete channels sharpen angular momentum and energy distributions. Together, these studies demonstrate that multi-coincidence CEI combined with machine learning can automatically identify subtle structural differences and minor channels from high-dimensional data.

Finally, ion–electron coincidence measurements on core-ionized methyl iodide (CH_3I) at a synchrotron beamline are used to connect inner-shell electronic decay to specific ionic fragmentation outcomes. Channel-resolved Auger–Meitner electron spectra, obtained by correlating electrons with well-defined ion channels, reveal systematic changes in band positions and widths as a function of final charge state and hydrogen loss. Comparison of two-body and three-body kinetic energy releases isolates contributions from channels involving neutral iodine fragments and highlights the sensitivity of the low energy electron spectrum to details of the fragmentation pathway. These measurements provide benchmark data for state resolved Auger decay and complement the laser-based CEI studies by adding an explicit electronic-structure perspective.

Overall, this thesis advances coincidence momentum imaging as a structural and dynamical probe for polyatomic molecules. Time-resolved and static CEI establish momentum space fingerprints of transient and equilibrium geometries, high dimensional multi-coincidence measurements combined with machine learning enable event-level molecular structure differentiation, and ion–electron coincidence spectroscopy links core-level decay to fragmentation patterns. Together, these approaches lay the groundwork for future efforts to image and control molecular dynamics on their natural femtosecond timescales.

Table of Contents

List of Figures

List of Tables

Acknowledgments

A PhD is a long, uneven road, and I didn't walk it alone. What's here is the result of steady help, patient guidance, and good company from many people. I'm grateful for all of it.

I thank my doctoral committee—Cosmin Blaga, Loren Greenman, Christine Aikens, Artem Rudenko, and Daniel Rolles—for their time, questions, and clear feedback throughout.

My home base has been our group with Daniel Rolles and Artem Rudenko. I'm grateful for the scientific home they built—resources, opportunities, and the kind of environment where it's easy to think freely, try ideas with help, and get things done. I want to thank Daniel for shaping how I approach science and problem solving, and for pushing me to stay patient, optimistic, and clear under stress. His scientific knowledge, energy, and enthusiasm kept me motivated, and his encouragement made a real difference when I needed it. I'm also very grateful to Artem for his consistent, critical insight on my work. His comments, suggestions, and questions raised the quality and rigor of what I did. I'm thankful too for their broad collaborations that allowed me to take part in experiments at national and international facilities. Those experiences broadened my understanding and helped me develop the research instincts I brought back to the lab.

Beyond faculty and my committee, I'm very grateful to the people who took the time to show me how to actually do things. Early on, Kanaka Raju Pandiri (Raju) and Jan Tross walked me through lasers, optics, and running experiments—the practical details that matter every day. That foundation shaped how I worked in the lab, how I tried to help others, and how I approached new problems.

Day to day, the work happened shoulder to shoulder with friends and colleagues. Huynh Lam was an integral part of almost all the work I did here—experiments, analysis, and code. I'm grateful for his steady help and clear thinking, and working with him raised the level of my work. Thank you Seyyed Javad Robatjazi and Shashank Pathak for commissioning KAMP, and Surjendu Bhattacharyya for getting the KAMP chamber running in the FLAME room and for teaching me the analysis that became routine for me. I'm just as grateful for the friendship with Huynh

and Surjendu, and the steady back-and-forth on any topic that grew alongside the work. I'm grateful as well to former and current group members for jumping in on projects, sharing know-how, and keeping things moving. To everyone in the group, thank you for the quick checks, hallway conversations, and small fixes that keep experiments and everyday work moving. They made the long hours in the lab and on experiments cheerful and manageable rather than just long.

I'm thankful for the skill and patience of the critical personnel who keep the JRML lab running, supporting whatever the lab needed—from design, build, and repair work to hardware and electronics, computers and software, lasers, and safety.

Outside the lab, I also learned a lot from time spent with collaborators at SLAC (TMO, UED, X-ray), EuXFEL, FERMI, LBNL, the University of Connecticut, Brown University, and the University of Nebraska–Lincoln. Those experiences shaped how I design experiments, analyze data, and think about what we do.

I'm grateful to friends—in and out of the department—who turned Manhattan into home and kept life balanced alongside the work. The connections we built at K-State continue beyond the department on any topic under the sun, from science help to random questions to simply catching up. I'm grateful I can always reach out, and that you do the same.

To my family, Thiba Nagaraja and Vettri Selvam make the good days better and the hard days lighter. Their love and everyday presence are a steady source of joy. My parents and brother have backed me throughout, and their care and encouragement gave me the confidence to pursue this path. I'm grateful for the example they set and the lessons they taught me. That constant support made this possible.

I'm grateful to Kansas State University, the James R. Macdonald Laboratory, and the Physics Department, and to the various funding agencies, for the space and opportunities to do this work. I'm thankful for their support.

Publications

Publications with leading or co-leading contribution

1. Exploiting correlations in multi-coincidence Coulomb explosion patterns for differentiating molecular structures using machine learning. **Anbu Selvam Venkatachalam**, Loren Greenman, Joshua Stallbaumer, Artem Rudenko, Daniel Rolles, and Huynh Van Sa Lam *Nature Communications*, 16, 11366 (2025)

2. Imaging transient molecular configurations in UV-excited diiodomethane. **Anbu Selvam Venkatachalam**, Huynh Van Sa Lam, Surjendu Bhattacharyya, Balram Kaderiya, Enliang Wang, Yijue Ding, Loren Greenman, Artem Rudenko, and Daniel Rolles *The Journal of Chemical Physics*, 163, 164308 (2025)

3. Simultaneous imaging of vibrational, rotational, and electronic wave-packet dynamics in a triatomic molecule. Huynh Van Sa Lam, Van-Hung Hoang, **Anbu Selvam Venkatachalam**, Surjendu Bhattacharyya, Keyu Chen, Sina Jacob, Sanduni Kudagama, Tu Thanh Nguyen, Daniel Rolles, Uwe Thumm, Artem Rudenko, and Vinod Kumarappan *Physical Review A*, 111(6), L061101 (2025)

4. Differentiating three-dimensional molecular structures using laser-induced Coulomb explosion imaging. Huynh Van Sa Lam, **Anbu Selvam Venkatachalam**, Surjendu Bhattacharyya, Keyu Chen, Kurtis Borne, Enliang Wang, Rebecca Boll, Till Jahnke, Vinod Kumarappan, Artem Rudenko, and Daniel Rolles *Physical Review Letters*, 132(12), 123201 (2024)

5. Coulomb explosion imaging: a robust method for distinguishing molecular structures and tracking structural changes in photochemical reactions. Huynh Van Sa Lam, **Anbu Selvam Venkatachalam**, Surjendu Bhattacharyya, Enliang Wang, Kurtis Borne, Keyu Chen, Artem Rudenko, and Daniel Rolles *Ultrafast Nonlinear Imaging and Spectroscopy XI*, Proceedings of SPIE, 12681, 42–47 (2023)

Collaborative publications based on beamtimes

JRML experiments

1. Delayed Dissociation and Transient Isomerization during the Ultrafast Photodissociation of the Tribromomethane Cation. Surjendu Bhattacharyya, Enliang Wang, Kurtis Borne, Keyu Chen, **Anbu Selvam Venkatachalam**, Huynh Van Sa Lam, Farzaneh Ziaee, Shashank Pathak, Anton Khmelnitskiy, Kevin D. Carnes, Charles W. Fehrenbach, Itzik Ben-Itzhak, Artem Rudenko, and Daniel Rolles *The Journal of Physical Chemistry Letters*, 15(49), 12188–12196 (2024)

2. Time-resolved Coulomb explosion imaging unveils ultrafast ring opening of furan. Enliang Wang, Surjendu Bhattacharyya, Keyu Chen, Kurtis Borne, Farzaneh Ziaee, Shashank Pathak, Huynh Van Sa Lam, **Anbu Selvam Venkatachalam**, Xiangjun Chen, Rebecca Boll, Till Jahnke, Artem Rudenko, and Daniel Rolles *arXiv preprint*, arXiv:2311.05099 (2023)

3. Strong-field-induced Coulomb explosion imaging of tribromomethane. Surjendu Bhattacharyya, Kurtis Borne, Farzaneh Ziaee, Shashank Pathak, Enliang Wang, **Anbu Selvam Venkatachalam**, Xiang Li, Nathan Marshall, Kevin D. Carnes, Charles W. Fehrenbach, Travis Severt, Itzik Ben-Itzhak, Artem Rudenko, and Daniel Rolles *The Journal of Physical Chemistry Letters*, 13(25), 5845–5853 (2022)

4. Two- and three-body fragmentation of multiply charged tribromomethane by ultrafast laser pulses. Surjendu Bhattacharyya, Kurtis Borne, Farzaneh Ziaee, Shashank Pathak, Enliang Wang, **Anbu Selvam Venkatachalam**, Nathan Marshall, Kevin D. Carnes, Charles W. Fehrenbach, Travis Severt, Itzik Ben-Itzhak, Artem Rudenko, and Daniel Rolles *Physical Chemistry Chemical Physics*, 24(45), 27631–27644 (2022)

5. Angle-dependent strong-field ionization and fragmentation of carbon dioxide measured using rotational wave packets. Huynh Van Sa Lam, Suresh Yarlagadda, **Anbu Selvam Venkatachalam**, Tomthin Nganba Wangjam, Rajesh K. Kushawaha, Chuan Cheng, Peter Svihra, Andrei Nomerotski, Thomas Weinacht, Daniel Rolles, and Vinod Kumarappan *Physical Review A*, 102(4), 043119 (2020)

External facilities (XFELs, synchrotrons, and other large-scale experiments)

1. Visualizing the three-dimensional arrangement of hydrogen atoms in organic molecules by Coulomb explosion imaging. Alice E. Green, Keyu Chen, Surjendu Bhattacharyya, Felix Allum, Sergey Usenko, Michael N. R. Ashfold, Thomas M. Baumann, Kurtis D. Borne, Mark Brouard, Michael Burt, Martin Centurion, Carlo Callegari, Tommaso Calvi, Ruaridh J. G. Forbes, Christopher S. Hansen, David M. P. Holland, Rebecca A. Ingle, Huynh V. S. Lam, Sri Bhavya Muvva, Joao P. F. Nunes, Arnaud Rouzée, Artem Rudenko, Richard J. Squibb, Florian Trinter, **Anbu Selvam Venkatachalam**, Peter M. Weber, Adam Kirrander, Rebecca Boll, and Daniel Rolles *Journal of the American Chemical Society*, 147(41), 37133–37143 (2025)

2. Direct observation of ultrafast symmetry reduction during internal conversion of 2-thiouracil using Coulomb explosion imaging. Till Jahnke, Sebastian Mai, Surjendu Bhattacharyya, Keyu Chen, Rebecca Boll, Maria Elena Castellani, Simon Dold, Ulrike Frühling, Alice E. Green, Markus Ilchen, Rebecca Ingle, Gregor Kastirke, Huynh Van Sa Lam, Fabiano Lever, Dennis Mayer, Tommaso Mazza, Terence Mullins, Yevheniy Ovcharenko, Björn Senfftleben, Florian Trinter, Atia-Tul-Noor, Sergey Usenko, **Anbu Selvam Venkatachalam**, Artem Rudenko, Daniel Rolles, Michael Meyer, Heide Ibrahim, and Markus Gühr *Nature Communications*, 16(1), 2074 (2025)

3. Imaging a light-induced molecular elimination reaction with an X-ray free-electron laser. Xiang Li, Rebecca Boll, Patricia Vindel-Zandbergen, Jesús González-Vázquez, Daniel E. Rivas, Surjendu Bhattacharyya, Kurtis Borne, Keyu Chen, Alberto De Fanis, Benjamin Erk, Ruaridh J. G. Forbes, Tommaso Mazza, Michael Meyer, Jochen Mikosch, Huynh Van Sa Lam, Joseph W. McManus, Terence Mullins, Yevheniy Ovcharenko, Oksana Plekan, Kevin C. Prince, Primož Rebernik, Florian Trinter, **Anbu Selvam Venkatachalam**, Arnaud Rouzée, Artem Rudenko, and Daniel Rolles *Nature Communications*, 16(1), 7006 (2025)

4. Monitoring the evolution of relative product populations at early times during a photochemical reaction. Joao Pedro Figueira Nunes, Lea Maria Ibele, Shashank Pathak, Andrew R.

Attar, Surjendu Bhattacharyya, Rebecca Boll, Kurtis Borne, Martin Centurion, Benjamin Erk, Ming-Fu Lin, Ruaridh J. G. Forbes, Nathan Goff, Christopher S. Hansen, Matthias Hoffmann, David M. P. Holland, Rebecca A. Ingle, Duan Luo, Sri Bhavya Muvva, Alexander H. Reid, Arnaud Rouzée, Artem Rudenko, Sajib Kumar Saha, Xiaozhe Shen, **Anbu Selvam Venkatachalam**, Xijie Wang, Matt R. Ware, Stephen P. Weathersby, Kyle Wilkin, Thomas J. A. Wolf, Yanwei Xiong, Jie Yang, Michael N. R. Ashfold, Daniel Rolles, and Basile F. E. Curchod *Journal of the American Chemical Society*, 146(6), 4134–4143 (2024)

5. Ultrafast electronic relaxation pathways of the molecular photoswitch quadricyclane. Kurtis D. Borne, Joseph C. Cooper, Michael N. R. Ashfold, Julien Bachmann, Surjendu Bhattacharyya, Rebecca Boll, Matteo Bonanomi, Michael Bosch, Carlo Callegari, Martin Centurion, Marcello Coreno, Basile F. E. Curchod, Miltcho D. Danailov, Alexander Demidovich, Michele Di Fraia, Benjamin Erk, Davide Faccialà, Raimund Feifel, Ruaridh J. G. Forbes, Christopher S. Hansen, David M. P. Holland, Rebecca A. Ingle, Roland Lindh, Lingyu Ma, Henry McGhee, Sri Bhavya Muvva, Joao P. F. Nunes, Asami Odate, Shashank Pathak, Oksana Plekan, Kevin C. Prince, Primož Rebernik, Arnaud Rouzée, Artem Rudenko, Alberto Simoncig, Richard J. Squibb, **Anbu Selvam Venkatachalam**, Caterina Vozzi, Peter M. Weber, Adam Kirrander, and Daniel Rolles *Nature Chemistry*, 16(4), 499–505 (2024)

6. Valence shell electronically excited states of norbornadiene and quadricyclane. Joseph C. Cooper, David M. P. Holland, Rebecca A. Ingle, Matteo Bonanomi, Davide Faccialà, Nelson De Oliveira, Abdul R. Abid, Julien Bachmann, Surjendu Bhattacharyya, Kurtis Borne, Michael Bosch, Martin Centurion, Keyu Chen, Ruaridh J. G. Forbes, Huynh V. S. Lam, Asami Odate, Artem Rudenko, **Anbu Selvam Venkatachalam**, Caterina Vozzi, Enliang Wang, Peter M. Weber, Michael N. R. Ashfold, Adam Kirrander, and Daniel Rolles *The Journal of Chemical Physics*, 160(6), 064305 (2024)

7. Exploring the ultrafast and isomer-dependent photodissociation of iodothiophenes via site-selective ionization. Weronika O. Razmus, Felix Allum, James Harries, Yoshiaki Kumagai, Kiyonobu Nagaya, Surjendu Bhattacharyya, Mathew Britton, Mark Brouard, Philip H. Bucksbaum, Kieran Cheung, Stuart W. Crane, Mizuho Fushitani, Ian Gabalski, Tatsuo Gejo,

Aaron Ghrist, David Heathcote, Yasumasa Hikosaka, Akiyoshi Hishikawa, Paul Hockett, Ellen Jones, Edwin Kukk, Hiroshi Iwayama, Huynh V. S. Lam, Joseph W. McManus, Dennis Milesevic, Jochen Mikosch, Shinichirou Minemoto, Akinobu Niozu, Andrew J. Orr-Ewing, Shigeki Owada, Daniel Rolles, Artem Rudenko, Dave Townsend, Kiyoshi Ueda, James Unwin, Claire Vallance, **Anbu Selvam Venkatachalam**, Shin-ichi Wada, Tiffany Walmsley, Emily M. Warne, Joanne L. Woodhouse, Michael Burt, Michael N. R. Ashfold, Russell S. Minns, and Ruaridh Forbes *Physical Chemistry Chemical Physics*, 26(16), 12725–12737 (2024)

8. Hydrogen migration in inner-shell ionized halogenated cyclic hydrocarbons. Abdul Rahman Abid, Surjendu Bhattacharyya, **Anbu Selvam Venkatachalam**, Shashank Pathak, Keyu Chen, Huynh Van Sa Lam, Kurtis Borne, Debadarshini Mishra, René C. Bilodeau, Ileana Dumitriu, Nora Berrah, Minna Patanen, and Daniel Rolles *Scientific Reports*, 13, 2107 (2023)

Chapter 1

Introduction

The interaction between light and matter is a common and essential aspect of many fundamental processes in nature[1;2]. Light drives photosynthesis in plants and bacteria, enabling solar energy conversion and oxygen production[3–5], initiates the primary steps of vision through ultrafast isomerization of retinal in rhodopsin[6–9], and triggers the synthesis of vitamin D in human skin[10;11]. Ultraviolet light can also damage DNA and biological tissue, requiring efficient photoprotection and repair mechanisms[12–14]. In the atmosphere, photochemistry controls the fate of many trace gases and contributes to ozone formation and depletion[15]. In all of these examples, at the molecular level light-induced processes are governed by coupled electronic and nuclear motion on ultrafast timescales. Electronic excitations typically evolve on attosecond to few-femtosecond scales. Vibrational motion occurs on tens to hundreds of femtoseconds, while rotational dynamics often span picoseconds and beyond. Capturing such motion in real time requires experimental techniques that can both initiate and probe molecular dynamics with femtosecond time resolution and high structural sensitivity.

Time-resolved pump–probe spectroscopy provides a general framework for following photoinduced dynamics. In a typical experiment, an ultrafast pump pulse prepares an excited electronic or vibrational state, and a delayed probe pulse interrogates the evolving system. Experimental developments have combined ultrafast excitation with a variety of structural and spectroscopic probes, including time-resolved photoelectron spectroscopy[16], ultrafast electron diffraction[17;18], and x-ray scattering. These techniques have revealed rich details of nuclear motion in isolated molecules, con-

densed phases, and biological systems. Despite this progress, directly imaging isolated gas-phase molecules remains challenging. Diffraction-based methods work best when a large number of identically prepared molecules contribute coherently to the signal[17;19;20]. Moreover, many transient intermediates are short-lived and present only in small fractions of the ensemble. Alternative approaches that can provide structural information from single-molecule events are, therefore, highly valuable. Coulomb explosion imaging (CEI) is one such approach and is the central experimental tool used in this thesis.

1.1 Coulomb Explosion Imaging as a Structural Probe

Coulomb explosion imaging probes molecular structure by rapidly removing several electrons from a molecule, the highly charged molecule explodes, causing the ionic nuclei to repel each other and fragment. If the ionization step is fast compared to nuclear motion, the momenta of the resulting ions carry information about the geometry at the instant of ionization[21–23]. By measuring these momenta in coincidence, one can infer the complex structural features of the molecular system in momentum space. CEI can be driven by strong-field laser pulses or intense x-ray pulses, making it compatible with tabletop laser systems and large-scale light sources[23–28].

CEI experiments on small molecules demonstrated that fragment momenta can be used to reconstruct three-dimensional structures and follow vibrational wave-packet motion[21;22;29;30]. In time-resolved implementations, this approach has been used to study bond breaking, roaming dynamics, and passage through conical intersections in a variety of systems[19;31;32]. CEI is also well suited for probing the structure of more complex polyatomic molecules. Coulomb explosion experiments have been used to distinguish molecular structures based on their fragment momenta[28;33–35], and to determine the absolute stereochemistry of chiral molecules[36;37].

The advent of x-ray free-electron lasers (XFELs) has opened a complementary regime of CEI, where intense, ultrashort x-ray pulses remove many core and valence electrons from heavy atoms within a molecule. Under these conditions, large organic molecules can be driven to high charge states and fully fragmented into atomic ions[38]. Momentum-resolved detection of these ions provides direct access to the instantaneous geometry of complex molecules, including all hydrogens, and can

reveal ultrafast charge redistribution and bond rearrangements during the interaction with the x-ray pulse[38–40]. Such experiments highlight the potential of CEI as a structural probe for increasingly large and complex systems.

In summary, CEI complements more traditional time-resolved methods by providing a direct link between fragment momenta and molecular structure in the gas phase. Because CEI is sensitive to the full three-dimensional correlation between fragments, it can distinguish different reaction pathways, transient intermediates, and structural isomers that might be difficult to separate using ensemble-averaged observables alone.

1.2 Structural Sensitivity, Data-Driven Analysis, and Coincidence Spectroscopy

Molecules with the same chemical formula can exist in multiple isomeric forms that differ in connectivity or three-dimensional arrangement of atoms. Even subtle changes in geometry, such as cis versus trans configurations or differences in stereochemistry, can lead to large changes in chemical reactivity and biological function[41;42]. In pharmaceutical and biological contexts, different isomers can have very different activity because they may interact differently with chiral biological targets (enzymes and receptors). For example, the two enantiomers of thalidomide are associated with distinct biological effects, illustrating that one isomer can be therapeutically beneficial while another can be harmful[41]. Being able to distinguish and, when possible, quantify different isomeric and conformational populations is therefore an important goal in molecular science. CEI provides a natural route to isomer differentiation, because different three-dimensional structures generally lead to different fragment momentum correlations after Coulomb explosion. Experiments have shown that structural isomers and enantiomers can produce distinct multi-ion momentum patterns that allow their identification and, in some cases, determination of absolute configuration; for example, CEI has been used to image the absolute configuration of a chiral epoxide[36], to directly determine absolute molecular stereochemistry in the gas phase[37], and to distinguish geometric (cis/trans) and conformational isomers from their multi-ion momentum correlations[33;34;43]. These results suggest that CEI can serve as a structural fingerprinting tool for gas-phase molecules, even without

molecular alignment.

As the number of fragments and channels increases, however, the resulting data become high-dimensional and exhibit complex correlations. Reliable separation of overlapping channels, identification of rare pathways, and differentiation of similar structures benefit from automated and data-driven analysis[44;45]. Dimensionality reduction and clustering methods developed in the machine learning community, such as principal component analysis (PCA), t-distributed stochastic neighbor embedding (t-SNE) and uniform manifold approximation and projection (UMAP), provide powerful tools for visualizing and grouping high-dimensional data[46–48]. In this thesis, coincidence momentum imaging is combined with such data-driven analysis to extract structural information from complex CEI measurements. This allows us to take full advantage of the structural sensitivity of CEI.

Coincidence techniques that combine fragment-ion detection with electron spectroscopy provide a complementary type of structural and electronic sensitivity. In inner-shell photoionization, conventional x-ray photoelectron and Auger-Meitner[49] electron spectra often suffer from severe spectral congestion because many intermediate and final states contribute within a narrow energy range[50–55]. By measuring electrons in coincidence with specific ion pairs, it becomes possible to disentangle overlapping contributions and assign decay pathways to well-defined electronic and nuclear final states[56]. The work presented in this thesis explores Coulomb explosion imaging as a structural probe for gas-phase polyatomic molecules. Across the different projects, the central questions are how fragment momentum information can be used to track ultrafast structural dynamics, to distinguish between different molecular geometries, and to connect electronic decay with specific fragmentation outcomes.

1.3 Organization of the Thesis

The thesis is organized as follows. Chapter 2 describes the experimental setups, data acquisition, and analysis methods used throughout the work. This includes an overview of the femtosecond laser systems, ultraviolet sources, and vacuum chambers, as well as the ion and ion–electron momentum imaging spectrometers and the basic procedures for event reconstruction and calibration[57–59].

Chapter 3 presents the time-resolved Coulomb explosion imaging study of diiodomethane (CH_2I_2) using a UV pump and strong-field IR probe. It introduces the relevant photodissociation pathways of CH_2I_2, describes the pump–probe CEI measurements, and analyzes how the fragment momentum distributions evolve with pump–probe delay. Particular attention is given to signatures of transient isomer formation and to the two-body and three-body breakup channels. Next Chap. 4 examines static laser-induced CEI of molecules designed to mimic closed-ring and open-chain structures related to typical photoproducts. Here, the goal is to establish how three-dimensional fragment momentum distributions reflect underlying molecular geometry and to demonstrate that laser-induced CEI can distinguish between these structures in a robust way[60]. Following this, Chap. 5 turns to isomer differentiation using coincidence momentum imaging combined with data-driven analysis. Using dichloroethylene as example, this chapter introduces the machine-learning tools employed to cluster and classify multi-ion momentum patterns[46–48]. The chapter demonstrates how these tools can separate cis and trans isomers and identify additional structural classes in a largely automated way, and discusses how such approaches may be generalized to more complex molecules[28;34;35]. Chapter 6 presents the ion–electron coincidence study of CH_3I at the Advanced Light Source. Introducing inner-shell photoionization and Auger-Meitner decay in CH_3I, the chapter describes the experimental configuration used to detect electrons and ions in coincidence. It then reports channel-resolved electron spectra associated with different ionic fragmentation channels and interprets these spectra in terms of electronic decay pathways and final charge states of the molecular cation[50;52;54–56].

The thesis concludes with a summary of the main findings and an outlook on future directions. Possible extensions include applying CEI and data-driven analysis to larger and more flexible molecules, combining CEI with other time-resolved probes, and exploiting advances in light sources to achieve higher temporal and structural resolution. Together, the studies presented here highlight the strengths of coincidence momentum imaging as a tool for visualizing and understanding light-induced molecular transformations in the gas phase.

Chapter 2

Experimental Methods and Analysis

In this chapter, we describe the experimental methods used in this work to study photo-induced dynamics and fragmentation of isolated gas-phase molecules. The measurements use two different types of light sources: intense, femtosecond near-infrared pulses from a tabletop ultrafast laser and soft X-ray pulses from a synchrotron radiation storage ring source. Fragment ions (and, when applicable, electrons) are recorded in coincidence on an event-by-event basis, enabling reconstruction of full three-dimensional momenta and a kinematic view of molecular structure and dynamics. We first outline the light sources and the optical layout, then describe the spectrometer, the time- and position-sensitive detectors, and the vacuum systems. Finally, we summarize the data-acquisition and analysis workflow used to process ion–ion and ion–electron coincidence events and retrieve three-dimensional momenta.

2.1 Laser Sources and Optical Layout

2.1.1 Ultrafast Intense Laser System

The majority of the work presented in this dissertation uses an ultrafast laser—the **F**emtosecond **LA**ser for **M**ulticolor **E**xperiments (FLAME)—in the James R. Macdonald Laboratory to excite and/or probe (ionize and fragment) molecules. The laser is based on the chirped-pulse amplification (CPA) technique, developed by G. Mourou and D. Strickland[61;62] and awarded the 2018 Nobel Prize in Physics, which enables amplification of broadband femtosecond pulses to mJ levels. In CPA,

femtosecond oscillator pulses are stretched to picoseconds, amplified, and then recompressed to a femtosecond pulse duration. FLAME is a Ti:sapphire system that produces ∼5 mJ, linearly polarized pulses at 3 kHz repetition rate with a central wavelength near 810 nm (see Fig. 2.1). The output beam of the Ti:sapphire system is split into two beam with equal pulse energy, one of which can be used to drive an optical parametric amplifier (OPA) to produce continuously tunable femtosecond laser pulses from the deep ultraviolet (DUV) to the mid infrared (MIR), as described in Section 2.1.2. The other beam is typically used for strong-field ionization at the fundamental 810-nm wavelength. With a compressed pulse duration of ∼25 fs, this beam is focused in the experimental chamber to reach peak intensities on the order of $\sim 10^{15}$ W/cm^2. FLAME is a commercial Coherent Legend Elite DUO USX system comprising a mode-locked oscillator (Vitara) pumped by a 532-nm CW laser (Verdi), a two-stage amplifier pumped by 527-nm pulsed lasers (Revolution), and two independent grating compressors. A schematic layout is shown in Fig. 2.1, and the physical layout and control hardware are shown in Fig. 2.2. The key elements for generation, amplification, and compression are summarized below.

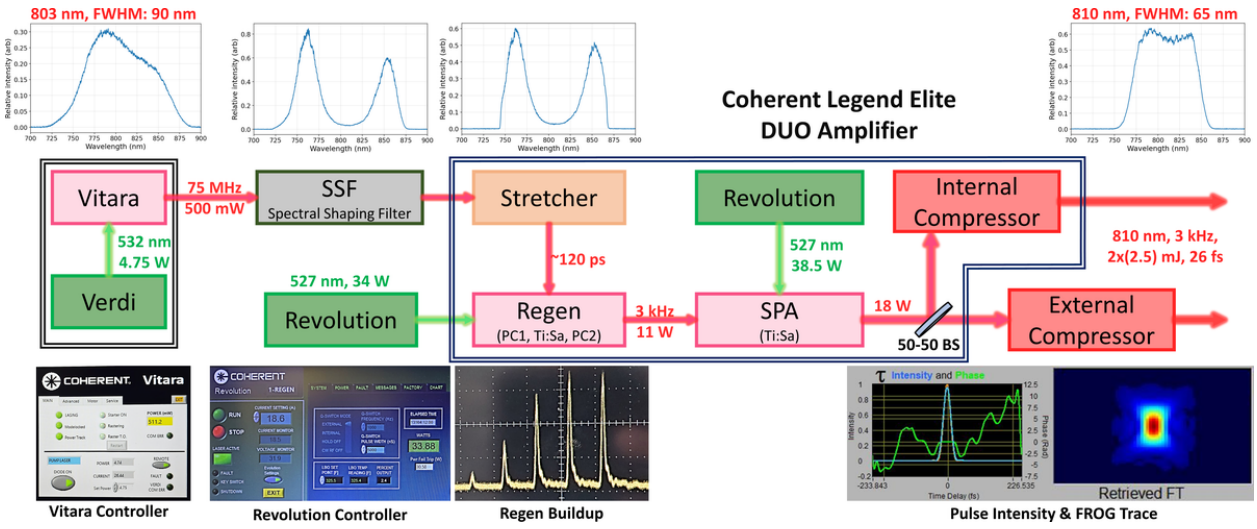

Figure 2.1: Block diagram of the FLAME laser system along with some typical measurements for each component. Broadband pulses from the Vitara oscillator are spectrally conditioned with a Spectral Shaping Filter (SSF) and temporally stretched. The chirped seed is amplified in a regenerative (Regen) amplifier and then in a single-pass amplifier (SPA), both pumped by green Revolution lasers. The amplified beam is split and compressed in two independent grating-based compressors. Typical spectra measured at different stages are shown in the top row. The bottom row shows representative LabVIEW control interfaces for the oscillator and pump lasers, the gain build-up in the regen cavity, and a compressed-pulse SHG-FROG trace.

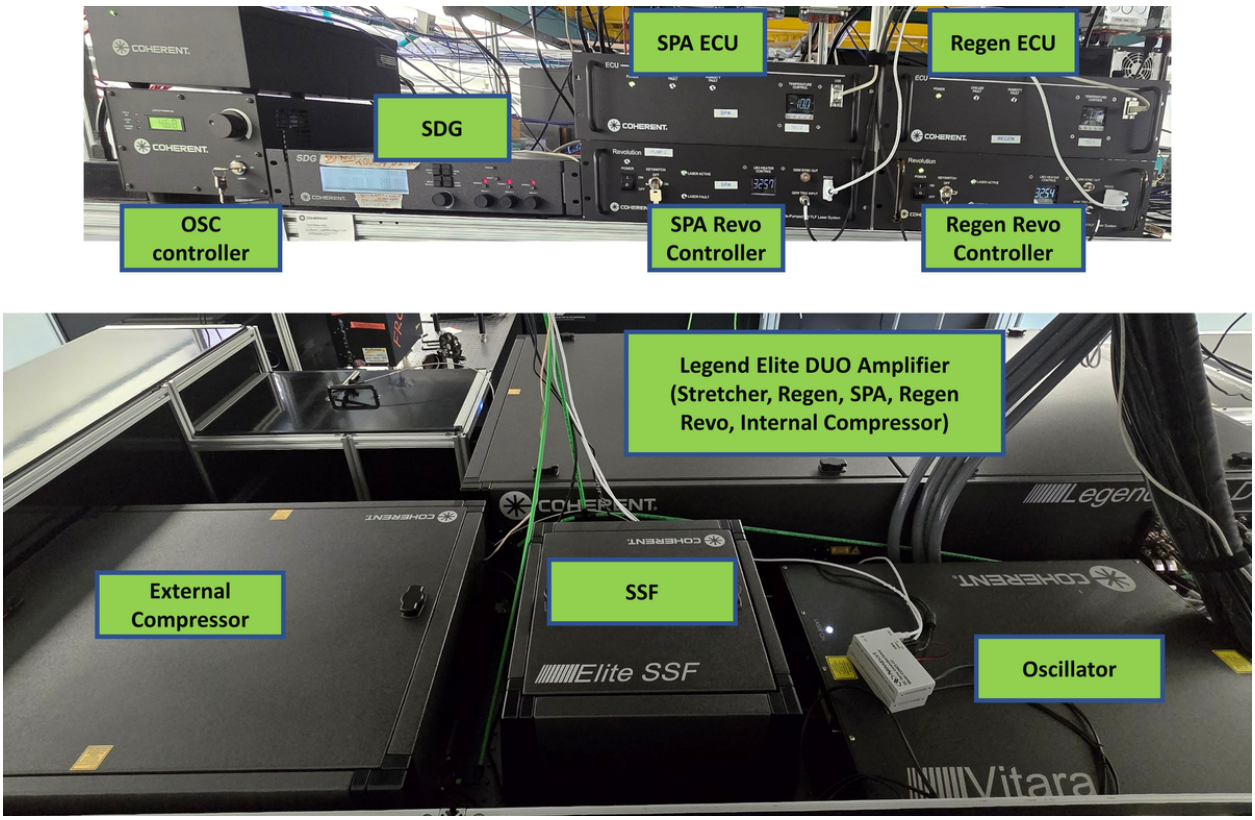

Figure 2.2: Physical layout and control hardware of the FLAME system. Major components include the Vitara oscillator with a CW pump laser (Verdi), the Legend Elite DUO amplifier, pump lasers (Revolution), enclosed Ti:sapphire regenerative (Regen) and single-pass amplifier (SPA) stages with environmental control units (ECU), internal and external grating compressors, beam-delivery optics, and synchronization and delay generator (SDG). See text for a brief description of each of these units. Controllers used for oscillator and pump-laser control are also shown.

Oscillator and Seed

A Coherent Vitara oscillator is pumped by a 532 nm CW laser, and upon mode-locking produces a broadband femtosecond pulse train at 75 MHz repetition rate with ∼500 mW average power. The seed beam produced by the oscillator is spectrally conditioned to suppress the center of the spectrum using a specially coated Spectral Shaping Filter (SSF). Spectra before and after multiple passes through the SSF are shown in Fig. 2.1. A grating stretcher imparts positive chirp, stretching the pulses to ∼120 ps for chirped-pulse amplification.

Seed Selection and Amplification

The stretched pulse train is s-polarized and injected into the regenerative (regen) amplifier stage. The regen cavity uses polarization-sensitive optics to select and amplify a single pulse every 333 μs, thereby establishing the 3 kHz repetition rate. Only the p-polarized (horizontal) pulse circulates in the cavity and passes through all elements. The cavity includes two Pockels cells, a half-wave plate, a Brewster-cut Ti:sapphire crystal inside a temperature- and humidity-controlled enclosure with Brewster windows, and thin-film polarizers. The first Pockels cell, located upstream of the cavity, selects one stretched oscillator pulse per repetition cycle by switching its polarization from s-pol to p-pol. The switched seed is focused by the cavity mirrors, overlaps with the green pump in the Ti:sapphire crystal, is amplified on each round trip, and is extracted by the second Pockels cell after 15 round trips. With a round-trip period of $\sim$10 ns, the observed amplitude build-up and extraction are illustrated by the oscilloscope trace in Fig. 2.1. The typical average power after the regen is $\sim$10–11 W at 3 kHz. The regen-amplified seed then drives a single-pass amplifier (SPA) pumped by an independent Revolution laser and reaches $\sim$18 W average power after two stages of amplification. Temperature and humidity of the two enclosed crystal chambers are maintained by independent environmental control units (ECUs). The ECUs circulate dry air through the crystal enclosures and hold the temperatures at -12°C (Regen) and -10°C (SPA). The repetition rate, Pockels cells, and green pumps are synchronized by gated delay signals from the synchronization/delay generator (SDG), shown schematically in Fig. 2.2.

Grating Compressors

The output beam from the Legend amplifier is expanded and split 50:50 by a broadband near-infrared (NIR) beam splitter. One branch is sent to the **internal compressor** and used primarily as the pump/driver for the tunable optical parametric amplifier (OPA). The second arm is sent to an independent **external compressor** and used as the NIR beam for experiments (Fig. 2.1). Typical compressed NIR pulses at the experiment are $\sim$26 fs with $\sim$2.5 mJ per pulse at 3 kHz. The pulses are characterized spatially and temporally: with a 10–11 mm beam diameter ($1/e^2$), the pulse duration measured by SHG-FROG[63–66] is $\sim$26 fs. Representative spectra at the oscillator, after

SSF, after the stretcher, and after amplification are shown in Fig. 2.1 (top row), and SHG-FROG traces used to retrieve the NIR pulse duration are shown in the bottom row.

2.1.2 Tunable OPA (TOPAS-Prime with NirUVis DUV)

Tunable radiation from the visible to deep-UV is generated using a Light Conversion TOPAS-Prime OPA with the NirUVis frequency-mixing unit (DUV extension). The ∼25 fs pulse from the FLAME laser serves as the OPA pump. White-light continuum is first produced by focusing a small fraction of the NIR into a Ti:sapphire crystal and is then parametrically amplified by the 800 nm pump to yield the **signal** (1160–1600 nm, V-pol.) and **idler** (1600–2600 nm, H-pol.). Subsequent frequency conversion in the NirUVis provides second-harmonic generation and sum-/difference-frequency mixing to reach the VIS/UV/DUV. Output beam routing is handled by motorized crystal stages and a four-position output selector. Typical UV pulse durations out of the OPA are ∼70–80 fs with a beam diameter of ∼2–3 mm. Cross-correlation measurements and spectra for the specific UV wavelengths used in the experiments are provided in the respective Chap. 3.

2.1.3 Synchrotron Soft X-ray Source (ALS, Beamline 10.0.1)

Soft X-ray measurements were carried out at the Advanced Light Source (ALS) at Lawrence Berkeley National Laboratory[67]. The ALS is a third-generation storage-ring synchrotron operating at 1.9 GeV electron beam energy and high beam current, delivering tunable, high-brightness radiation to over 40 specialized beamlines (Fig. 2.3). Our experiments used Beamline 10.0.1, a soft X-ray line with a monochromator covering a photon energy range of ∼17–340 eV and supporting high-resolution photoemission and gas-phase studies[68;69]. The experiments presented in this thesis were performed when the synchrotron operated in multibunch mode (RF = 500 MHz; 2 ns bucket spacing; ∼276–320 bunches filled)[70]. To accommodate the 2 ns spacing in multibunch mode, we triggered the data acquisition on the electron time-of-flight signal, enabling unambiguous association of ions and electrons with each event[35]. A roll-up endstation equipped for coincident ion–electron momentum imaging, described in more detail in Section 2.2.2, was installed at the 10.0.1 endstation for these measurements.

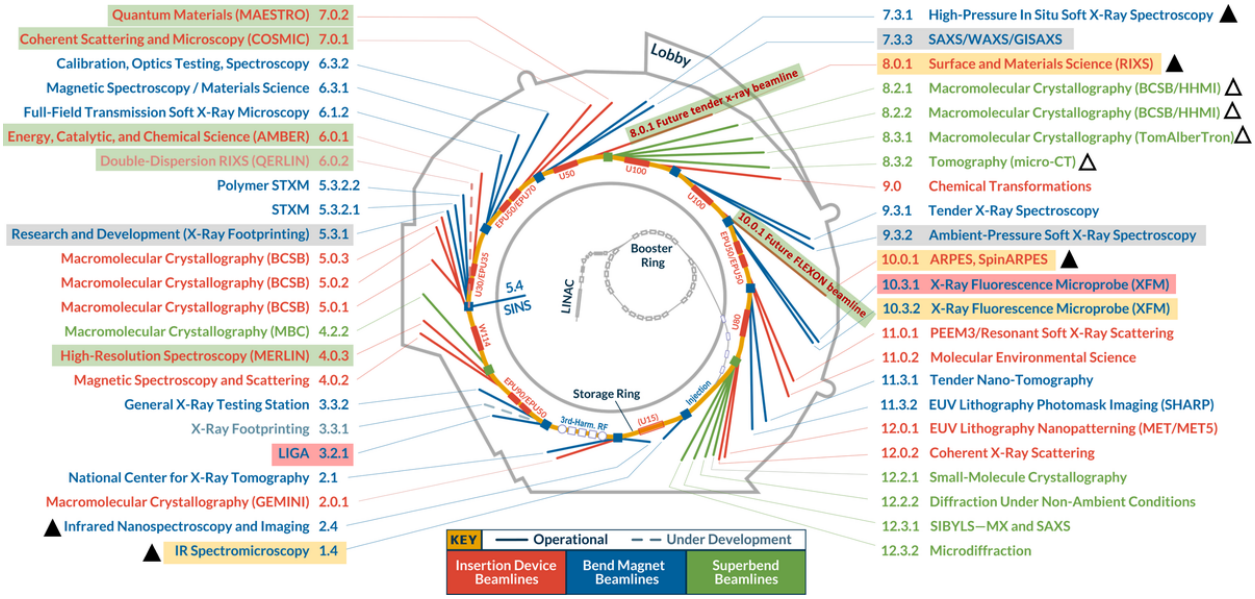

Figure 2.3: Schematic of the Advanced Light Source storage ring and beamlines. The present work was performed at Beamline 10.0.1, a soft X-ray beamline supplying high-resolution, monochromatized photons for gas-phase experiments.

2.2 Velocity Map Imaging Setup for Ion and Electron Detection

2.2.1 Kansas Atomic and Molecular Physics Apparatus (KAMP)

The KAMP (Kansas Atomic and Molecular Physics) chamber, shown schematically in Figure 2.4, is a custom-designed, double-sided velocity map imaging (VMI) spectrometer optimized for coincidence measurements of ions and electrons. The apparatus, built by Seyyed Javad Robatjazi[71] and Shashank Pathak[72] has undergone subsequent modifications, including removal of the effusive jet and XUV spectrometer, and implementation of broadband back-focusing mirror for table-top NIR and UV laser beams. This section provides a brief overview of the apparatus, covering vacuum, molecular beam delivery, the VMI spectrometer, detectors, and optical focusing.

Vacuum Arrangement and Cold Molecular Beam Delivery

The KAMP system comprises multiple differentially pumped sections to maintain ultra-high vacuum in the main interaction chamber. A cold molecular beam source introduces gas-phase targets via a two-stage supersonic expansion chamber. The first stage is pumped by a 1000 L/s turbomolecular pump, reaching 10^{-3}–10^{-4} Torr during operation. The second stage is pumped by a

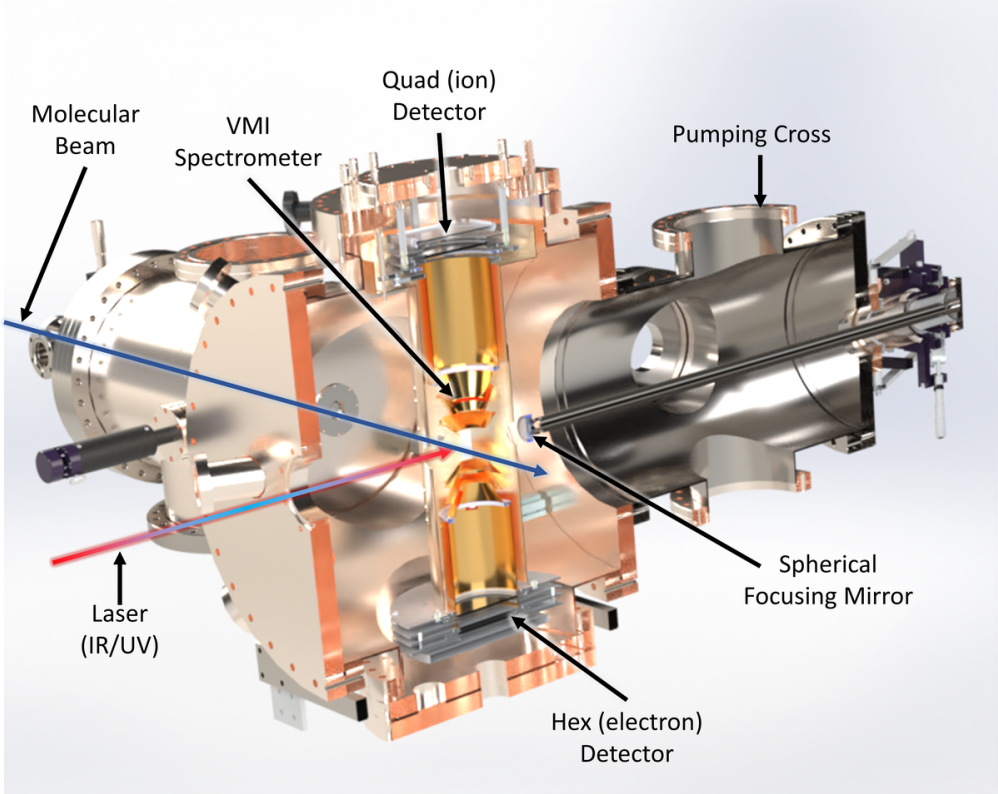

Figure 2.4: Schematic of the KAMP chamber, showing major components including the molecular beam source, VMI spectrometer electrodes, ion (quad) and electron (hex) detectors, spherical focusing mirror, and the pumping cross. The NIR/UV laser enters from the front port and is focused by a spherical mirror into the interaction region, where it intersects the molecular beam at the spectrometer center.

700 L/s pump, with pressures typically around 10^{-6}–10^{-7} Torr when the molecular beam is on. A two-stage molecular beam catcher on the opposite side of the main chamber efficiently removes the gas load and prevents backflow. Each stage is differentially pumped, achieving base pressures as low as 10^{-11} Torr. During operation, the catcher maintains pressures around 10^{-9} Torr. The interaction region is housed in a large cylindrical main chamber, which connects to a pumping cross equipped with three turbomolecular pumps (two 700 L/s and one 1000 L/s). These pumps bring the main chamber to pressures in the mid-10^{-11} Torr range, essential for high order multi-coincidence detection of ions (see Figure 2.4).

Gas targets are introduced via supersonic expansion through a 30 µm nozzle mounted on an XYZ manipulator. The high pressure of the target gas before the nozzle (typically between a few mTorr up to a few bar) causes the gas to expand and cool, generating a molecular beam with reduced

translational and internal energy. This collimated beam is skimmed with a 500 µm skimmer and further collimated through a 1 mm aperture to create a narrow, cold beam (the jet temperature was not directly measured in this work; a representative value of ∼45 K has been reported for a comparable cold-jet target in our laboratory[73]) that intersects the laser focus at the center of the spectrometer (see Figure 2.4).

Velocity-Map Imaging Spectrometer and Detectors

Building on earlier ion-imaging work, Eppink and Parker demonstrated velocity-map imaging (VMI), in which an electrostatic lens stack focuses charged particles (ions or electrons) with equal velocity to the same point on the detector, irrespective of the creation position of the fragments within the interaction region[57;58]. The basic VMI lens comprises three electrodes: a repeller, an extractor, and a ground (screen) plate. The electric field in a VMI spectrometer is nonuniform, and by adjusting the three electrode voltages, the field—and hence the equipotential surfaces—is shaped to produce an electrostatic-lensing effect on charged-particle trajectories. For appropriate voltage settings, ions (or electrons) with the same transverse velocity (parallel to the detector plane) are focused to the same point on the detector plane.

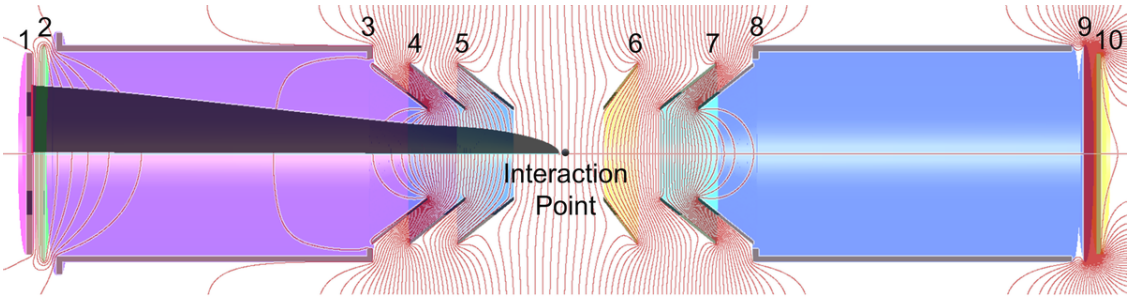

1	Ion MCP	-2165 V	6	Electron extractor	275 V
2	Ion mesh	-2200 V	7	Electron focus	1139 V
3	Ion drift tube	-2000 V	8	Electron drift tube	2000 V
4	Ion focus	-864 V	9	Electron mesh	2000 V
5	Ion extractor	-320 V	10	Electron MCP	70 V

Figure 2.5: KAMP double-sided VMI electrode geometry and typical operating voltages used in this work (ion-only operation). Equipotential contours (red) and simulated ion trajectories (up to 30 eV) originating from the interaction point are overlaid. Electrode numbering corresponds to the inset table.

In a double-sided VMI spectrometer, each side (moving outward from the interaction region) comprises an extractor, a dedicated focusing electrode, and a field-free drift tube that projects either ions or electrons onto their detector[74]. Because the extraction field is shared across the source region, the ion-side extractor simultaneously acts as the electron-side repeller (and vice versa). The focusing electrode on each side—located between the extractor and the drift region—is used to compensate field curvature and to refocus particles created at different positions in the interaction volume[74;75]. The coupled ion/electron optics and open, shared-field geometry make simultaneous optimum focusing nontrivial. Figure 2.5 shows the electrode layout and the representative equipotential lines for the KAMP VMI.

The KAMP double-sided VMI employs six gold-plated conical electrodes, enabling simultaneous extraction and focusing of ions and electrons. The interaction region is centered between the ion and electron extraction electrodes, with 12.5-cm drift tubes on both sides. The design, adapted from similar spectrometers in the CAMP[76;77] and LAMP[78] endstations at the LCLS and FLASH free-electron lasers, enables high-resolution momentum mapping over a large solid angle (e.g., at typical electrode biases up to ±4 kV, electrons up to ∼65 eV can be imaged in full 4π)[71;72], though simultaneous optimal focusing of ions and electrons is inherently challenging in the shared-field geometry. Typical operational voltage settings used for this work are shown in Fig. 2.5. Charged particles are detected using microchannel plates (MCPs) coupled to delay-line anodes. Ions are detected on the funnel-type MCP with a quad delay-line anode; electrons on hex side. Funnel MCPs feature a higher open-area ratio and a funneled channel-inlet geometry, thereby reducing backscattering, improving gain uniformity, and increasing effective detection efficiency[79–81]. The quad and hex DLDs measure the x-y positions of incoming particles based on timing differences between signal pairs. A quad DLD uses two wire layers for x and y coordinates, while a hex DLD includes a third layer to mitigate dead time and support multihit detection. The MCPs operate in a chevron stack configuration to amplify the electron cascade, typically producing gains up to 10^6.

2.2.2 ALS Velocity Map Imaging (VMI) Spectrometer

Soft X-ray photoionization measurements were performed with the ALS double-sided VMI endstation. As in the KAMP spectrometer, the ion extractor simultaneously serves as the electron re-

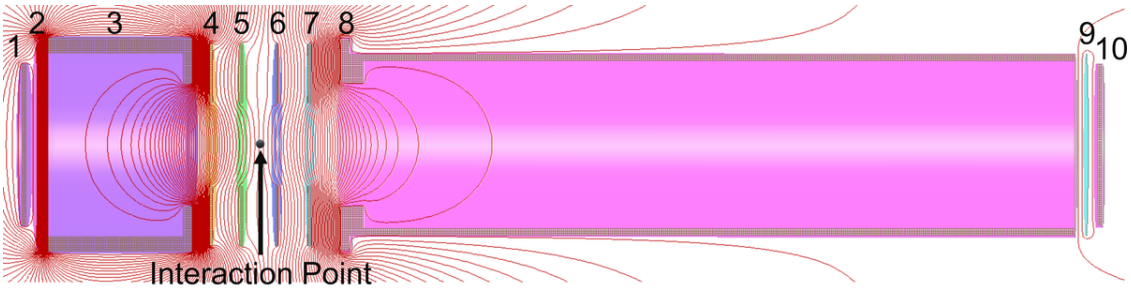

1	Electron MCP	500 V	6	Ion extractor	-100 V
2	Electron mesh	550 V	7	Ion focus	-700 V
3	Electron drift tube	3100 V	8	Ion drift tube	-2500 V
4	Electron focus	600 V	9	Ion mesh	-2750 V
5	Electron extractor	100 V	10	Ion MCP	-2650 V

Figure 2.6: ALS VMI electrode layout, representative equipotential lines, and typical operating voltages used in this work. The electron side employs a shortened drift section to accept electrons up to ∼300 eV, while the ion side is configured for fragments up to ∼25 eV per charge[59].

peller and vice-versa. Each side has a focusing electrode and a drift region. The ALS VMI employs flat-plate electrodes, and the electron side drift tube is intentionally shortened to accommodate high-energy electrons[59;72]. The spectrometer is optimized for coincident ion–electron detection in the soft X-ray regime, to capture photoelectrons and Auger-Meitner electrons up to ∼300 eV while simultaneously detecting fragment ions up to ∼25 eV per charge[59]. Typical operating voltages and equipotential contours used in this work are shown in Fig. 2.6.

The endstation couples the ALS beam through the front flange onto a continuous, skimmed molecular beam intersecting the spectrometer axis. The interaction chamber is differentially pumped and routinely reaches base pressures in the 10^{-9} mbar range during operation[59]. Microchannel plates (MCPs) with multihit delay-line anodes record time and position for both electrons and ions. In standard ALS multibunch mode (2 ns bunch spacing), data acquisition is triggered on the first detected electron[59]. Additional implementation details and performance benchmarks are provided in Ref.[59;72].

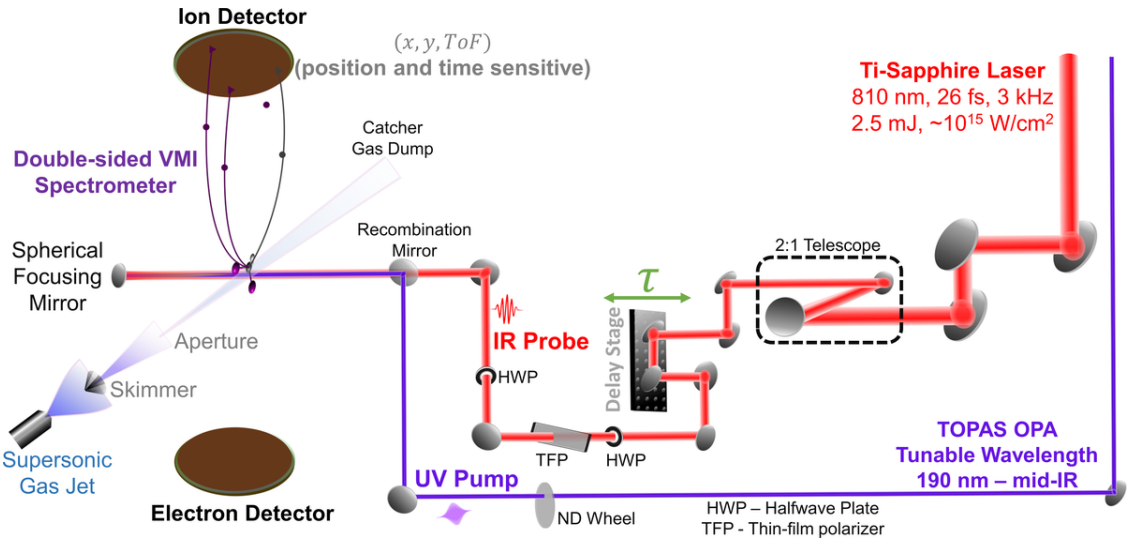

Figure 2.7: Schematic of the Coulomb explosion imaging (CEI) setup. The near-infrared (NIR) probe and tunable ultraviolet (UV) pump from the OPA are recombined collinearly and back-focused onto a cold molecular gas jet at the center of a double-sided velocity-map imaging (VMI) spectrometer inside the KAMP chamber. Both ions and electrons produced by the laser–molecule interaction are detected with time- and position-sensitive detectors. Ions are detected on a funnel-type microchannel plate (MCP) with a quad-anode readout, and electrons on an MCP with a hex-anode readout. Measured time-of-flight and impact positions on the detectors yield high-resolution momentum images of the fragmentation dynamics.

2.3 KAMP Pump-Probe Optical Layout

The optical layout integrates the NIR probe and a tunable OPA beam (typically in the UV), routed collinearly and back-focused onto a supersonic molecular beam with a spherical mirror. For clarity, Fig. 2.7 shows the spectrometer, gas jet, and focusing optics, while the vacuum chamber is not shown.

The laser (NIR or UV) is focused at the interaction region by a spherical mirror mounted on the rear of the chamber, on a XYZ manipulator. The back-focusing mirror, with focal length ∼7.5 cm, produces a tight focus at the spectrometer center where the beam intersects the molecular jet (see Fig. 2.4). The beam enters via a 2 mm CaF_2 window on the front port and is directed to the focus by the mirror. NIR pulse energy is controlled with a half-wave plate and thin-film polarizer, whereas the UV power is set with a neutral-density wheel. With ∼60 mW average NIR power at 3 kHz, the back-focused geometry yields peak intensities on the order of 10^{15} W/cm^2 at the interaction region, suitable for strong-field ionization under ultrahigh-vacuum conditions. The pump–probe delay is

set by a motorized delay stage in the NIR arm, which controls the NIR arrival time relative to the UV pump, as indicated in Fig. 2.7.

2.4 KAMP Data Acquisition and Analysis

2.4.1 KAMP DAQ Hardware

A schematic of the KAMP data-acquisition (DAQ) and timing electronics is shown in Fig. 2.8. During normal operation, the detectors (MCP and delay-line anodes) are biased with high DC voltages from iseg NIM high voltage modules, distributed via voltage dividers and decouplers. The transient pulses from the MCP and delay-line anodes are decoupled from the DC-bias by an RC decoupling network in the HV decouplers and fed to a low-noise fast amplifier (Ortec FTA820A). Amplified pulses are discriminated by Ortec 935 constant-fraction discriminators (CFD), which produce fixed-width pulses with timing that is largely insensitive to pulse amplitude, thereby minimizing time walk. The 3 kHz master trigger is derived from a delayed output of the FLAME synchronizer/delay generator (SDG). This trigger serves as a common timing reference for the VME crate and, via an adjustable delay box, defines the acquisition window, typically $\sim$40 μs in our measurements.

The trigger, delayed trigger, and CFD outputs from the position and time channels (x, y, t) are digitized by a CAEN V1290N 16-channel multihit time-to-digital converter (TDC) with 25 ps LSB time bin and 52 µs full-scale range. The TDC timestamps every hit on each channel independently within the active gate, providing arrival times for the x, y, and time-of-flight signals. A CAEN V785N 16-channel peak-finding analog-to-digital converter (ADC) digitizes slow analog monitors (e.g., UV/NIR photodiodes), and a CAEN V560N scaler records event rates. TDC, ADC, and scaler data are buffered in the VME crate and transferred to the DAQ computer via a PCI-to-VME optical link. A separate controller computer drives the motorized delay stage for pump–probe measurements and reports the step number and stage status to the DAQ computer so that each acquisition block is tagged with the corresponding pump–probe delay step and acquisition occurs only when the stage is stationary. Data from the optical link and the delay step number are written to disk as event files by the DAQ readout software. Online streams and offline files are then sorted and visualized with SpecTcl[82;83]. SpecTcl is a Tcl/Tk-driven event-sorting and

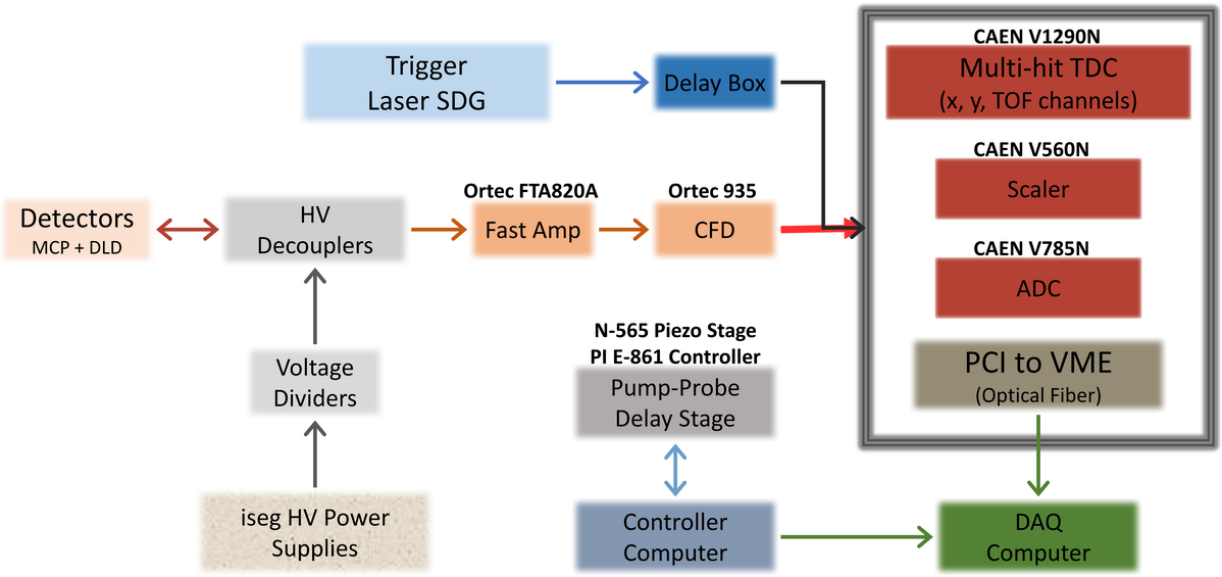

Figure 2.8: Block diagram of the KAMP data-acquisition (DAQ) and timing electronics. High voltages for the VMI electrodes and detector stacks are supplied by iseg multichannel HV units and routed through voltage dividers to the MCP and anode assemblies. HV decouplers deliver the required DC biases while RC networks extract the fast pulses from the MCP and delay-line anodes. The pulses are amplified and sent to a constant-fraction discriminator (CFD), which produces timing signals that are free of amplitude-dependent time walk. The master trigger is provided by the FLAME SDG–a delayed copy defines the acquisition gate. Event-by-event timestamps for each of the detector signals (MCP and anodes) are recorded by a CAEN V1290N multihit TDC (x, y, TOF channels). A CAEN V785N peak-finding ADC logs auxiliary analog signals such as photodiode power, and a CAEN V560N scaler records count rates. All VME modules are read out through a PCI-to-VME optical bridge to the DAQ computer.

spectrum-generation framework built on an object-oriented C++ analysis layer. In SpecTcl, a custom event processor function decodes the multihit TDC time data from the raw event words, and applies the calibrations that convert TDC time bins into TOF and detector (X, Y) coordinates. The resulting parameters are visualized (from online stream or offline event files) using user-defined spectra, including time-of-flight (TOF) distributions, 2D detector images and (X, Y)–TOF maps, anode time-sum checks for signal validation, and multi-ion coincidence histograms such as PIPICO and TRIPICO.

2.4.2 Event Building and Momentum Reconstruction

Figure 2.9 summarizes the end-to-end pipeline from SpecTcl event files to calibrated fragment momenta, and visualizing other experiment specific observables. After hardware readout and online

sorting in SpecTcl, events from the offline event files are exported as a compact binary stream. Each event contains the analog monitor (ADC1), the pump–probe delay step, number of hits, and position and time-of-flight (x, y, t) for all detected ions and electrons. The binary is parsed in a Python workflow to produce two tables: (i) a per-event hit table with columns x, y, and t for up to 16 ions (ion-only mode), and (ii) the second table containing the delay and ADC values.

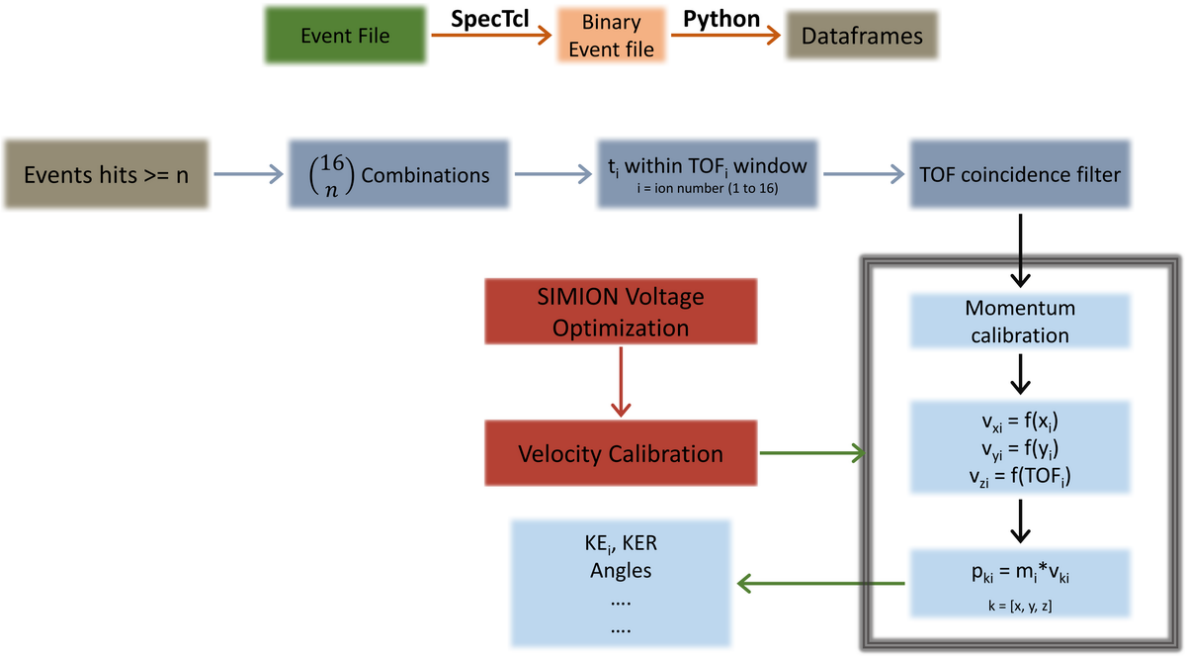

Figure 2.9: KAMP analysis workflow. Event files are exported from SpecTcl to a binary format and read in Python to build dataframes. For events with at least n ion hits, all $\binom{16}{n}$ combinations are formed, gated in the fragment TOF windows, and filtered by TOF-coincidence. SIMION voltages are optimized to match the experimental TOF mass–charge slope, then velocity calibrations $v_x(x)$, $v_y(y)$, and $v_z(\mathrm{TOF})$ are derived from simulated trajectories. Fragment momenta are reconstructed to generate KER, angular, and yield observables used throughout this thesis.

We first select events consistent with the desired number of fragments detected. For an n-ion channel, we require events with $\geq n$ ion hits and enumerate all $\binom{16}{n}$ hit combinations within each event. For each item from the combination, the arrival time t_i of every ion is filtered by a broad TOF window TOF_i assigned to that fragment, which removes combinations that include empty slots or ions from out-of-channel species. Ion TOF coincidence maps (PIPICO, TRIPICO or higher coincidence maps) are then used to gate kinematically allowed combinations and suppress random/false coincidences.

Because the VMI extraction field is intentionally nonuniform, analytic inversion from (x, y, TOF)

to initial momentum is not available. Instead, we model the exact VMI geometry and the operating voltages in SIMION[84] and derive empirical calibration functions that map detector observables to the initial velocity components[74;75]. This approach follows established practice for double-sided VMI spectrometers[59;72].

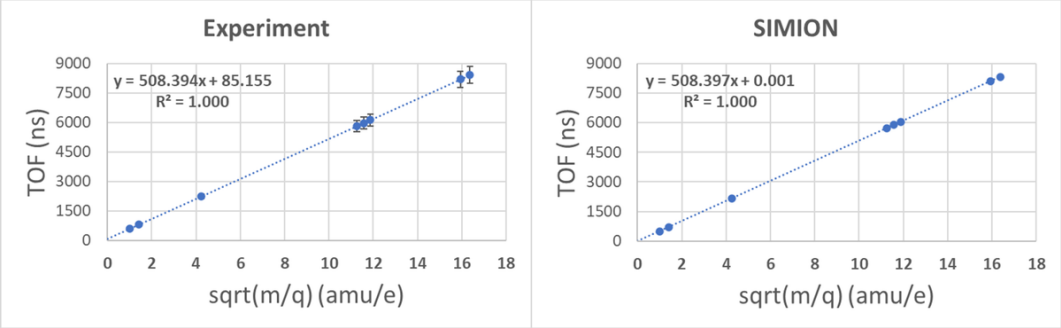

Figure 2.10: Experimental and SIMION time-of-flight calibration. Linear TOF vs. $\sqrt{m/q}$ slopes are matched by adjusting the drift-tube voltage in simulation. Agreement of slopes validates the effective extraction field used for trajectory calculations.

Before extracting calibration functions, the simulated voltages are tuned (primarily the drift-tube value) so that the simulated TOF vs. $\sqrt{m/q}$ slope for reference fragments matches the experimental slope, as shown in Fig. 2.10. This step aligns the effective extraction field in simulation with the experiment to first order[59].

With the voltages mapped, ions are launched from the interaction region with a grid of transverse and longitudinal kinetic energies that span the experimental range, similar to the ion trajectories shown in black in Fig. 2.5. The motions of charged particles in the x, y and z directions can be assumed to be decoupled from each other. In this case, the simulations can be performed using SIMION independently in each initial-velocity direction. For each species, simulated detector positions and time-of-flight are fitted with second-order polynomials to obtain $v_x = f_x(x)$, $v_y = f_y(y)$, and $v_z = f_t(t)$[74;75]. Cylindrical symmetry implies equivalent mappings in x and y barring any small alignment corrections. An exemplary fit function for v_x and v_z from x position on the detector and the time-of-flight from SIMION simulation is given in Fig. 2.11.

For each gated hit combination in an event, the calibrated relations yield v_x, v_y, and v_z, which are converted to momentum via $\mathbf{p} = m\,\mathbf{v}$. The resulting per-event ion momenta form the basis for all downstream observables, including kinetic-energy release (KER), pairwise and many-body

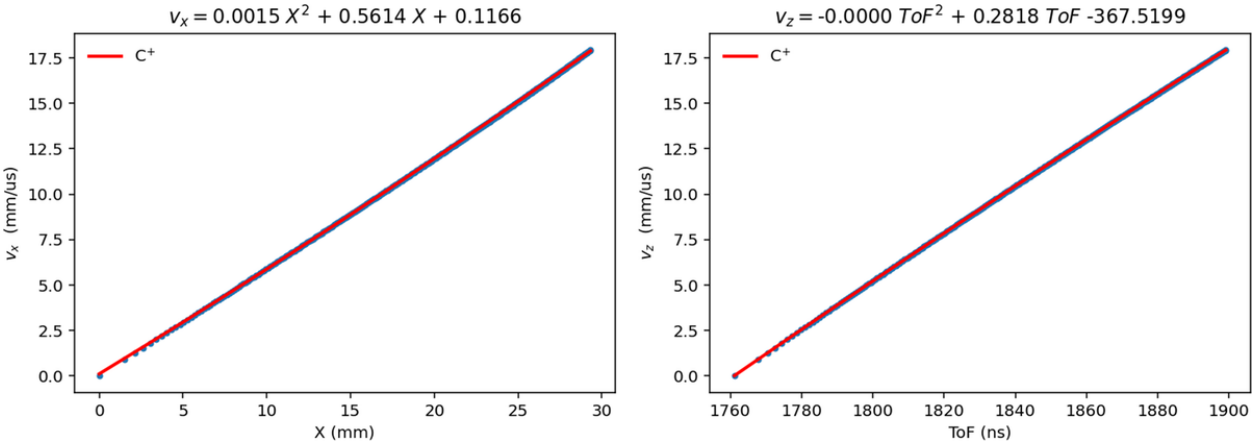

Figure 2.11: SIMION-based velocity calibration for a representative fragment (C^+ shown). Left: transverse calibration v_x vs. x with quadratic fit. Right: longitudinal calibration v_z vs. TOF with a quadratic fit about TOF_c. These mappings are obtained with the electrode geometry and voltages that reproduce the experimental TOF slope.

angular correlations, correlation analyses, and delay-resolved distributions.

2.5 Electron Imaging, Abel Inversion, and Energy Calibration

The electron spectrometer is operated in velocity–map imaging (VMI) mode, where the transverse velocity distribution of the emitted electrons is projected onto a position-sensitive detector. For the analysis of the two-dimensional detector images, we apply Abel inversion techniques[85] under the assumption of cylindrical symmetry around the spectrometer axis. The electron images are centered and circularized with the centering tools provided by the PyAbel Python package, using both convolution and center-of-mass methods as cross checks[85].

The Abel inversion is performed with the BASEX method implemented in PyAbel[85;86]. The resulting distribution is then angularly integrated to obtain a one-dimensional radial intensity profile $I(r)$, which corresponds to the electron kinetic energy distribution. This procedure is similar to that described for the coincidence velocity-map imaging spectrometer used in earlier work at the ALS[59]. Representative examples of the circularized images, inverted images, and the corresponding radial distributions are shown in Fig. 2.12. To convert detector radius to electron kinetic energy, we recorded calibration data using neon gas and soft X-ray photons between 55 and 145 eV. At each photon energy, photoelectron images were measured for the well-known Ne $2p$ and $2s$ photolines.

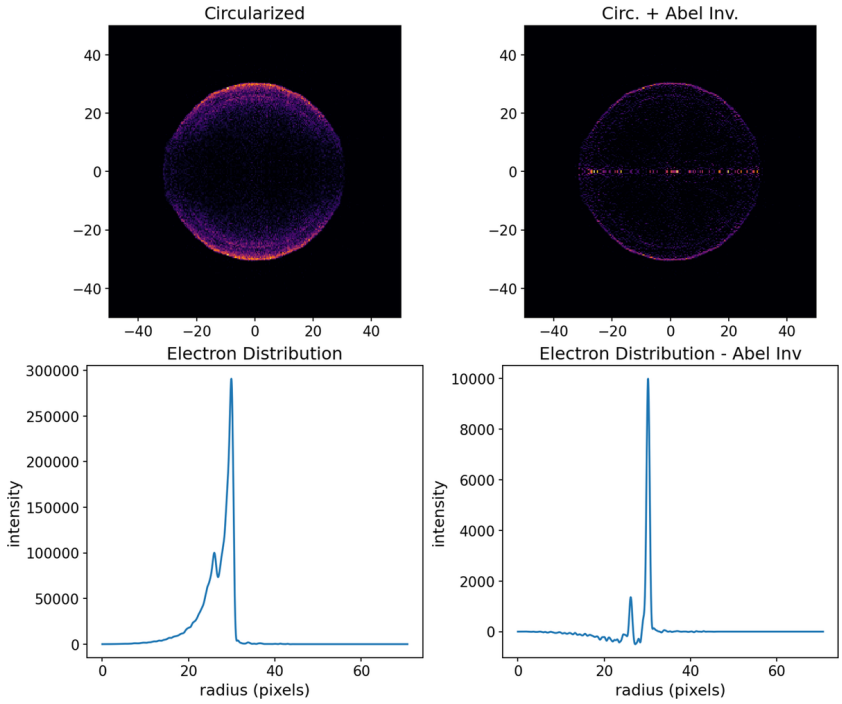

Figure 2.12: Electron image processing and Abel inversion used for the energy calibration with neon using 115 eV synchrotron X-ray photons. The upper panels show a representative circularized electron image (left) and the corresponding Abel inverted image (right). The lower panels show the radial electron intensity distributions obtained before (left) and after (right) Abel inversion.

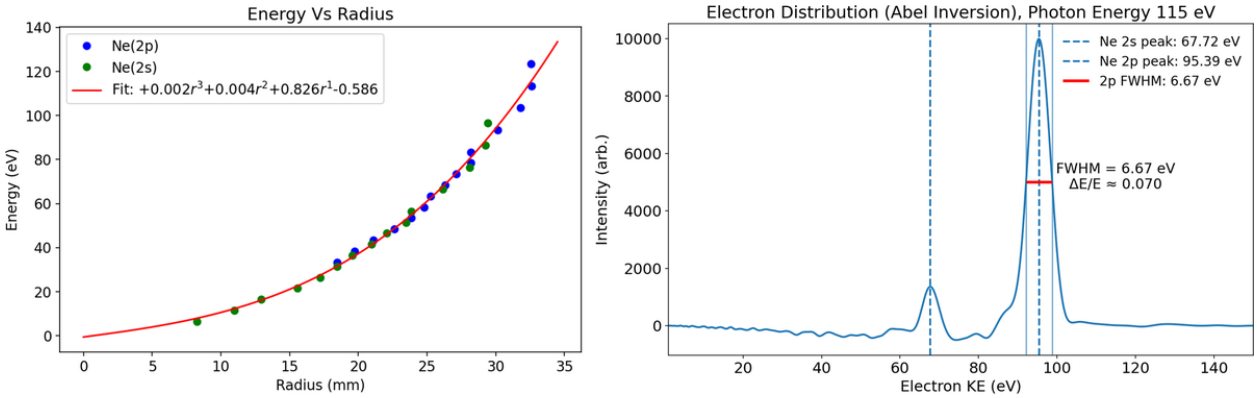

Figure 2.13: Left: Electron kinetic energy calibration using neon $2p$ and $2s$ photolines measured with synchrotron X-ray photons scanned from 55–105 eV in 5 eV steps and from 115–145 eV in 10 eV steps. The symbols show the known kinetic energies of the Ne $2p$ (blue) and $2s$ (green) photoelectrons plotted versus the corresponding detector radius extracted from the Abel inverted images. The red curve is a third-order polynomial fit used to convert detector radius to electron kinetic energy. Right: Representative Abel-inverted radial spectrum converted to kinetic energy at $h\nu = 115$ eV showing the Ne $2s$ and $2p$ peaks (dashed vertical lines) and the $2p$ full width at half maximum (FWHM) corresponding to $\Delta E/E \approx 0.070$.

After circularization and Abel inversion, the peak positions in the radial distributions were extracted by fitting Gaussian profiles. The known kinetic energies of the Ne $2p$ and $2s$ electrons were plotted as a function of the corresponding detector radii, and a third-order polynomial was fit to this energy–radius relation (see Fig. 2.13) A representative Abel-inverted spectrum at $h\nu = 115$ eV is shown in the right panel of Fig. 2.13. The Ne $2p$ peak at $E \approx 95.39$ eV has $\Delta E_{\mathrm{FWHM}} \approx 6.67$ eV, corresponding to an energy resolution of $\Delta E/E \approx 0.070$ under the calibration conditions.

2.6 Classical Coulomb Explosion (CE) Simulation

Coulomb explosion (CE) simulations are used to interpret coincidence momentum images by propagating nuclei as classical point charges on a purely repulsive potential. In the high charge state limit relevant to this work, Coulomb repulsion dominates over bonding and other interactions, because the nuclei experience strong pairwise repulsive forces from multiple localized positive charges on a femtosecond timescale. So a simple classical model reproduces momentum–angle correlations robustly, even though fragment kinetic energies (KEs) are often overestimated[60;87;88].

Initial Geometries and Ensemble Preparation

Ground-state equilibrium neutral geometries are first optimized using a quantum chemistry package and used as the reference for sampling initial nuclear configurations. Two ensemble–generation strategies are employed in this thesis:

- **Wigner sampling of vibrational ground state.** Ground–state normal modes are computed, and initial conditions are drawn from Wigner[89] phase–space distributions via Newton-X[90;91], and the resulting geometries and momenta seed the Coulomb explosion propagation.
- **Gaussian geometry randomization with initial KE.** Each atomic position is displaced by a three–dimensional Gaussian (typical standard deviation ~ 0.25 Å), and a small total KE (e.g., 500 meV) is randomly partitioned among atoms. This practical choice reproduces the experimentally observed width of the momentum distributions by capturing broadening from nuclear motion during ionization, laser–imparted KE, and a spread over ionic states[60;88].

For statistics, we typically sample ∼10,000 geometries per molecule. For the dynamics simulation in pump–probe cases in this thesis, the neutral molecule is propagated along the reaction coordinate, and the instantaneous positions and velocities at a given delay then define the initial conditions for CE simulation.

Forces and Equations of Motion

In the simulation, we assume the following: (i) point charges at nuclear positions, (ii) a purely Coulombic repulsive potential, (iii) instantaneous, vertical ionization at $t = 0$, with each atom i assigned a final charge $q_{i,\mathrm{f}}$ and zero or modest initial velocity, and (iv) complete breakup into the ions detected for the chosen channel.

Each nucleus i is treated as a classical point charge of mass m_i and charge $q_{i,f}$, located at $\mathbf{r}_i(t)$. At t=0, we begin the propagation from the sampled $\mathbf{r}_{i,0}$ and $\mathbf{v}_{i,0}$.

The equations of motion are

$$m_i\,\ddot{\mathbf{r}}_i(t) = \mathbf{F}_i\big(\mathbf{r}_j(t), t\big) = \sum_{j\neq i} \mathbf{F}_{ij}(t) \tag{2.1}$$

$$\mathbf{F}_{ij}(t) = \frac{1}{4\pi\varepsilon_0}\,\frac{q_i(t)\,q_j(t)}{\big\|\mathbf{r}_i(t) - \mathbf{r}_j(t)\big\|^3}\,\big(\mathbf{r}_i(t) - \mathbf{r}_j(t)\big) \tag{2.2}$$

Numerical Propagation

We propagate the classical nuclei by solving the coupled first–order system for positions and velocities. For each fragment i, we evolve

$$\dot{\mathbf{r}}_i(t) = \mathbf{v}_i(t) \tag{2.3}$$

$$m_i\,\dot{\mathbf{v}}_i(t) = \sum_{j\neq i} \mathbf{F}_{ij}(t) \tag{2.4}$$

with $\mathbf{F}_{ij}$ given by Eq. (2.2), and initial conditions $\mathbf{r}_i(0) = \mathbf{r}_{i,0}$ taken from the sampled geometry and $\dot{\mathbf{r}}_i(0) = \mathbf{v}_{i,0}$ (either zero, Wigner–sampled, or drawn from the small added–KE distribution noted above).

Fragment position and velocity are stacked into a state vector $\mathbf{y}(t) = \big(\mathbf{r}_1, \ldots, \mathbf{r}_N, \mathbf{v}_1, \ldots, \mathbf{v}_N\big)$. Eqs. (2.3)–(2.4) define $\dot{\mathbf{y}} = \mathbf{f}(\mathbf{y})$. The coupled ODEs are propagated using an explicit Runge–Kutta

scheme (RK45) until velocities reach asymptotic values, typically tens of ps. All simulations in this thesis were implemented in Python using `NumPy`[92] vectorized force evaluations over all pairs (i, j) for efficiency, and `solve_ivp()`[93] for time propagation. We employ fine steps during the early, high–acceleration phase (few fs step size) and progressively larger steps thereafter, integrating until the velocities converge to asymptotic values (typically tens of ps). Numerical diagnostics include conservation of total momentum and monitoring of the instantaneous Coulomb potential plus kinetic energy. For each trajectory, the asymptotic velocities $\mathbf{v}_i(\infty)$ give the final momenta $\mathbf{p}_i = m_i \mathbf{v}_i(\infty)$ and kinetic energies $K_i = \frac{1}{2} m_i \|\mathbf{v}_i(\infty)\|^2$ for each fragment. The total kinetic–energy release (KER) and angle correlations are computed from the set $\{K_i, \mathbf{p}_i\}$.

Summary

In summary, this chapter established the experimental and computational tools used throughout the thesis. We described the coincidence VMI spectrometer and DAQ workflow used to reconstruct three-dimensional fragment momenta from multihit timing and position data. We also introduced the classical Coulomb-explosion simulation framework that maps assumed charge configurations and initial geometries onto the measured observables, such as fragment momenta, KER, and angular correlations. With these tools in place, the next chapter applies time-resolved CEI in a UV-pump/NIR-probe scheme, using delay-dependent KER and momentum-correlation observables to extract ultrafast structural dynamics and to search for transient structural signatures.

Chapter 3

Imaging Transient Molecular Configurations in UV–Excited CH_2I_2 by Time–Resolved Coulomb Explosion Imaging

Femtosecond structural dynamics of diiodomethane (CH_2I_2) triggered by ultraviolet (UV) photoabsorption at 290 nm and 330 nm are studied in this chapter using time-resolved coincident Coulomb explosion imaging driven by a near-infrared probe pulse. We map the dominant single-photon process—the cleavage of the carbon–iodine bond producing a rotationally excited CH_2I radical—and identify additional contributions from the three-body ($CH_2 + I + I$) dissociation and molecular iodine formation channels, which are primarily induced by multiphoton absorption. We demonstrate the presence of a weak reaction pathway involving short-lived transient species resembling iso-CH_2I_2-like geometries with a slightly shorter I–I separation than in the ground-state CH_2I_2 molecule. These transient configurations, isolated through specific momentum-correlation conditions among three ionic fragments, form within approximately 100 fs after the initial photoexcitation and decay within the next 100 fs.

This chapter is adapted from our work titled "Imaging transient molecular configurations in UV-

excited diiodomethane" published in The Journal of Chemical Physics[88].

3.1 Motivation and Overview

UV-induced photodissociation reactions of halogenated alkanes are significant sources of reactive halogens, which have a considerable impact on environmental and atmospheric chemistry. Iodine, one of the halogens, plays diverse roles in chemistry, serving as a fundamental element in human health and bio-chemistry, a useful catalyst in organic synthesis[94], and a major contributor to the destruction of ozone molecules[95]. Due to its strong absorption of sunlight in a broad range of UV wavelengths, diiodomethane (CH_2I_2), a polyhalogenated alkane, is a major source of highly reactive iodine molecules influencing tropospheric chemistry and the marine boundary layer[96].

Numerous studies have been published on the UV-induced photochemistry of CH_2I_2, which have reported the primary cleavage of one of the C–I bonds and the formation of CH_2I and $I(^2P_{3/2})$ or $I^*(^2P_{1/2})$ photoproducts[97–99]. Using ions generated by a (2+1) resonance enhanced multiphoton ionization process, Xu *et al.*[100] measured the translational kinetic energy distributions of both $I(^2P_{3/2})$ and $I^*(^2P_{1/2})$ fragments in the wavelength range of 277–305 nm and concluded that the CH_2I co-fragment is produced with significant internal excitation, with approximately 80% of the total available energy being partitioned into the internal energy of the CH_2I fragment.

Reid *et al.*[101;102] later drew attention to the importance of isomerization of halogenated alkanes into iso-haloalkanes upon UV absorption as a major pathway leading to the production of molecular halogens. The photoisomerization of CH_2I_2 to iso-CH_2I_2 has been reported to be an extremely efficient process upon UV absorption in the solution phase and in cages[20;103;104]. Since it has been suggested that the dominant isomerization mechanisms in these studies are driven by the interaction with solvent molecules or cage, it is helpful to examine the process in isolated gas-phase molecules, free from such interactions. Borin *et al.*[105] reported observing photoisomerization of CH_2I_2 in the gas phase upon 330 nm UV excitation by probing it with femtosecond transient absorption. The delayed rise in the transient absorption of CH_2I_2 at 380 and 612 nm, approximately 35–90 fs after UV excitation, was attributed to the creation of a short-lived iso-CH_2I_2. A recent ultrafast electron diffraction (UED) study, where Liu *et al.*[17] directly mapped the C–I cleavage upon 266 nm

excitation, quantified the resulting increase of the C–I and I–I separations, and observed signatures of the rotation of the CH_2I radical after the C–I bond cleavage, but did not mention any observation of iso-CH_2I_2 formation.

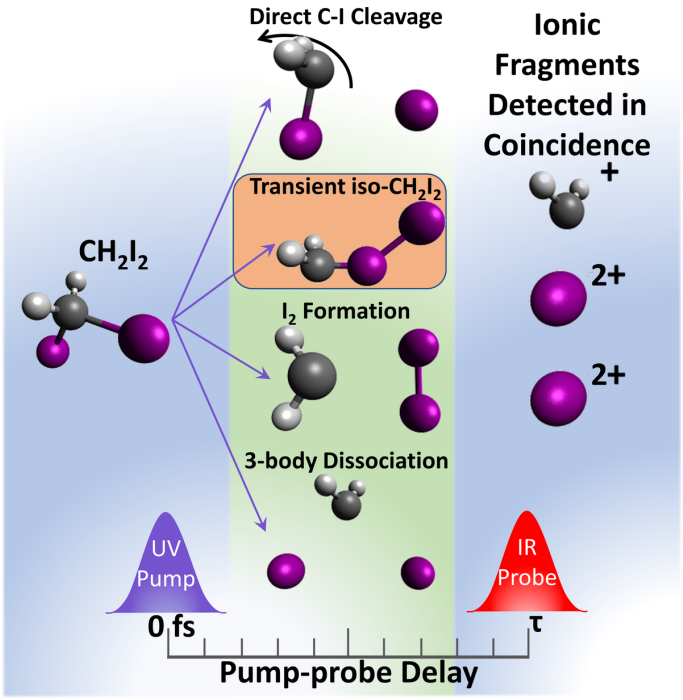

Figure 3.1: Sketch depicting the pump–probe process and the different reaction pathways after photoexcitation of CH_2I_2 (left) by the ultraviolet (UV) pump pulse. The products and possible intermediates (middle) are ionized to a fivefold final charge state by the intense near–infrared (NIR) probe pulse, and the ionic fragments are detected in coincidence.

Here, we employ Coulomb Explosion Imaging (CEI), a powerful method for determining the geometric structure of gas-phase molecules, to investigate the structural dynamics of CH_2I_2 upon UV photoabsorption. CEI has been shown to be a useful tool in identifying molecular isomers[35] and conformers[34] of polyhalogenated alkanes and other organic molecules[60], and even imaging the complete structure of halogenated alkanes[87;106] and ring molecules[38;43;60]. When used as a time-resolved method in a pump-probe scheme, laser-induced CEI can measure wave-packet dynamics, visualize vibrational motion, and image photodissociation with high temporal resolution[22;30;107–113]. In particular, CEI provides multidimensional data crucial for identifying any transient structural changes in the molecule upon UV excitation, often with the help of simple classical modeling and computations.

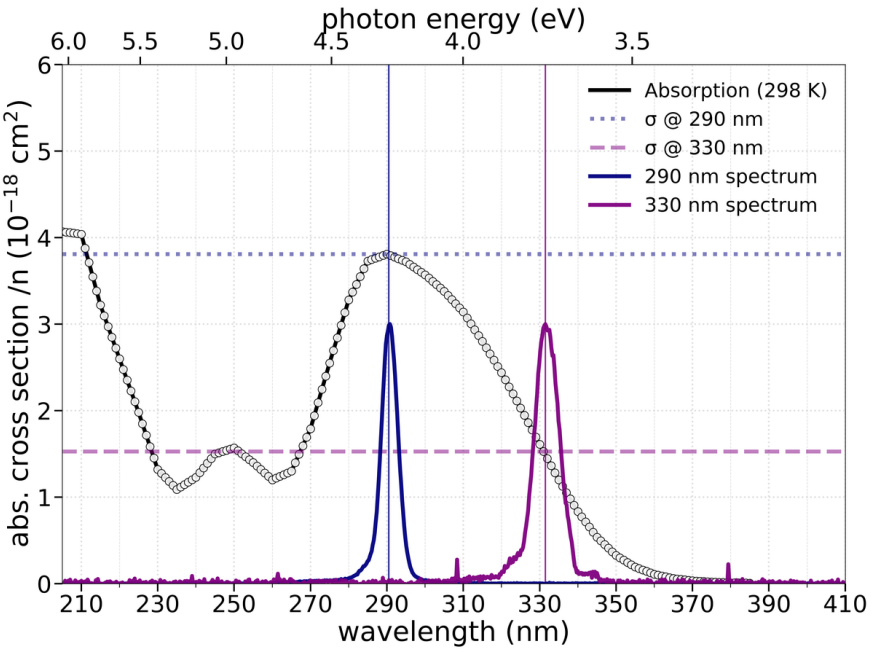

Figure 3.2: Room–temperature absorption cross section of CH_2I_2 (black circles)[100], with the measured UV pump spectra centered at 290 nm (blue) and 330 nm (magenta) overlaid. Horizontal dotted lines mark the approximate cross sections at the two pump wavelengths.

In this chapter, we study the ultrafast structural dynamics of diiodomethane upon UV excitation, specifically at 290 nm and 330 nm, using ionization and Coulomb explosion by an intense strong-field near-infrared (NIR) probe pulse. Excitation at both 290 nm (4.28 eV) and 330 nm (3.76 eV) can access several excited states that adiabatically lead to CH_2I+$I(^2P_{3/2})$ dissociation. Excitation at 290 nm can also access states leading to CH_2I+$I^*(^2P_{1/2})$ dissociation[114]. A schematic of the pump–probe experiment and the different reaction pathways after UV photoexcitation is shown in Fig. 3.1, and Fig. 3.2 shows the room–temperature UV absorption cross section with the measured pump spectra overlaid. As seen in Fig. 3.2, the 290 nm pump spectrum overlaps the peak of the CH_2I_2 absorption band, whereas the 330 nm spectrum samples a region of smaller cross section. Accordingly, we expect higher overall signal and broader state access at 290 nm and reduced yields at 330 nm which we use primarily to enable comparison with the transient–absorption work by Borin *et al.*[105]. The primary objective is to explore possible signatures of the intramolecular photoisomerization process in CH_2I_2, guided by the findings reported by Borin *et al.*[105]. We analyze the delay-dependent angular correlations between the momenta of the ions, the total kinetic energy release (KER), and the kinetic energies (KE) of individual ionic fragments to differentiate

the possible photoisomerization channel from the direct two-body breakup channel that leads to $CH_2I + I$ (or I^*) products. We also identify the three-body ($CH_2 + I + I$) dissociation and the I_2 formation channels, which primarily occur after the absorption of multiple UV photons.

3.2 Methods

3.2.1 Experimental

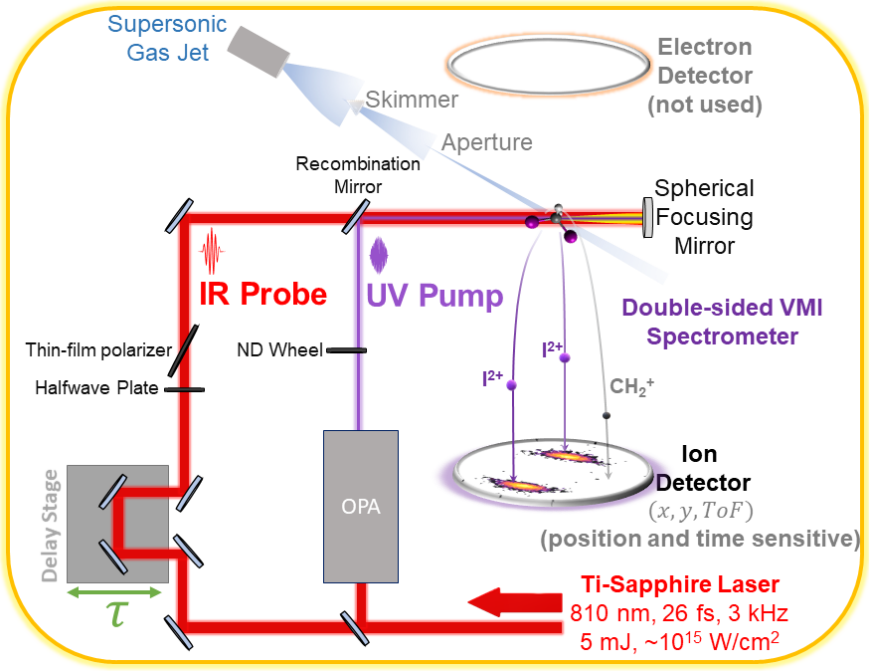

Figure 3.3: Schematic of the pump–probe setup and the coincident ion momentum imaging system. The diagram depicts the propagation of the ultraviolet (UV) pump and near–infrared (NIR) probe pulses into the experimental chamber. Both pulses are collinearly directed and focused onto a cold supersonic molecular jet containing diiodomethane. The setup is integrated with a double–sided velocity map imaging (VMI) spectrometer, operated in multi–ion coincidence mode. Ions are detected in coincidence using a time–and position–sensitive detector comprising a microchannel plate (MCP) and a delay line anode assembly. It should be noted that in this particular experiment, the electron detector is not utilized.

General CEI/VMI details and data processing are covered in Chapter 2; we summarize only experiment–specific parameters here for completeness. Figure 3.3 illustrates the experimental setup for the UV-pump and NIR-probe CEI experiment. The 3 kHz Ti:sapphire system delivered near-Fourier-transform-limited NIR probe pulses (26 fs FWHM, 810 nm), and the OPA provided ∼70-80 fs UV pumps at 290 and 330 nm, with pulse energy up to 15 μJ. The UV and NIR beams were

recombined and sent collinearly through a 1-mm calcium fluoride (CaF_2) window into the vacuum chamber, then focused by a 75 mm spherical mirror with UV-enhanced aluminum coating, into a cold supersonic CH_2I_2 jet. Diiodomethane, which is liquid at room temperature, is introduced into the vacuum chamber as a supersonic molecular beam expanded through a 30-μm nozzle using helium at 3 psig as carrier gas, which is collimated by a skimmer with a 500-μm diameter opening. The differential pumping stages in the molecular beam, separated from the interaction chamber by a 700-μm aperture, and a beam dump comprising of two differential pumping stages ensure that the base vacuum in the interaction chamber stays around 10^{-10} mbar when the molecular beam is operating. We scanned the pump–probe delay with 15 fs steps up to 800 fs and 100 fs steps thereafter, reconstructed fragment momenta from time–and position–sensitive detection, and used multi–ion coincidence to select specific fragmentation channels.

3.2.2 Coulomb Explosion Simulation

To guide the search for a possible isomer and identify the different reaction channels, we performed classical Coulomb explosion simulations for the molecular geometries corresponding to the CH_2I_2 equilibrium geometry, the iso-CH_2I_2, and the C–I bond cleavage pathway including rotation of the CH_2I intermediate. The simulations, explained in detail in Methods Sec. 2.6, are based on solving Newton's equations of motion for three point charges located at the positions of the carbon and iodine atoms. To match the experimental observables, the CH_2 fragment was kept intact. It is treated as a point particle in the simulations. The ionization and fragmentation process induced by the probe pulse was assumed to be instantaneous (i.e., for $CH_2^+ + I^{2+} + I^{2+}$ channel, instantaneously breaking both C–I bonds and resulting in a charge q=1 on the carbon atom and q=2 on each of the two iodine atoms), and the repulsion between the three fragments was treated as purely Coulombic.

The optimized structures of the molecule in the equilibrium geometry of the neutral electronic ground state and the isomer geometry were taken from Borin *et al.*[105]. For each case, an ensemble of 5000 geometries was generated by randomly varying the initial atomic positions within a radius of 0.1 Å around the equilibrium geometries and the initial velocities by up to $2\text{x}10^{-4}$ a.u., respectively. These parameters were chosen empirically in order to approximately match the width

of the fragment kinetic energy and momentum distributions observed in the experiment. In the simulation for the dissociation channel, a rotational period of ∼300 fs (obtained experimentally for the two-body dissociation into CH_2I + I following UV absorption and C–I cleavage, was used for the CH_2I intermediate, and the translational KEs used for the ion pairs were obtained from the experimental asymptotic KER for the respective channels.

3.3 Probe–only Characterization and Channel Selection

The intense NIR probe pulse ionizes both, the unpumped and the photoexcited molecules, resulting in multiple channels with different final charge states and different ionic fragments. In this section, we present spectra obtained with the strong-field NIR probe pulse alone (UV blocked) to establish the probe-only contributions. Figure 3.4 shows the ion time-of-flight (ToF) spectrum, with peaks corresponding to different ionic fragments produced by the strong-field NIR pulse. Figure 3.5 shows the detector hit position along the molecular beam axis. The various islands correspond to the different ions produced after ionization by the probe pulse, and rings indicating larger fragment momenta from Coulomb explosion with a coincident ionic partner. The observed offset (slanted dashed black line) reflects the velocity of the molecular jet and helps distinguish target ions from background. The peaks corresponding to the different ions are indicated with red vertical lines and labeled based on their respective mass-to-charge ratios.

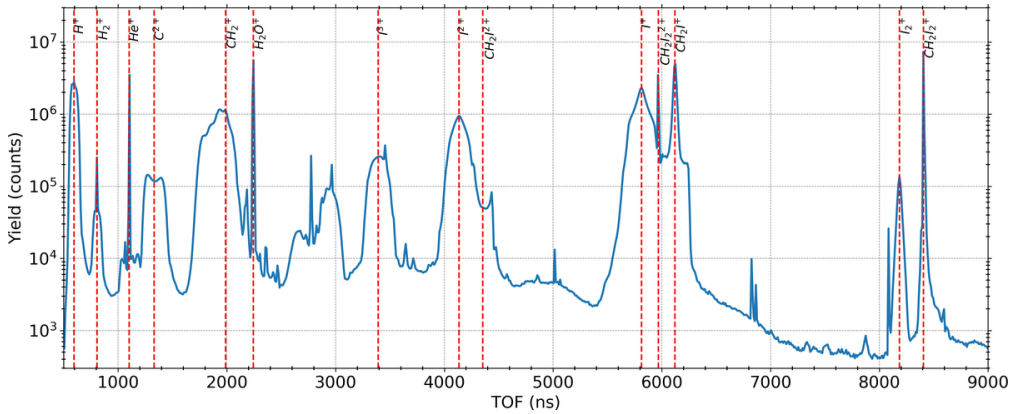

Figure 3.4: Ion time–of–flight (TOF) spectrum generated by strong–field ionization of CH_2I_2 molecule with the NIR pulse only, i.e., without UV pulse. The red vertical lines indicate the calculated ToF for the indicated ions with zero kinetic energy. Peaks are labeled based on their respective mass–to–charge ratios.

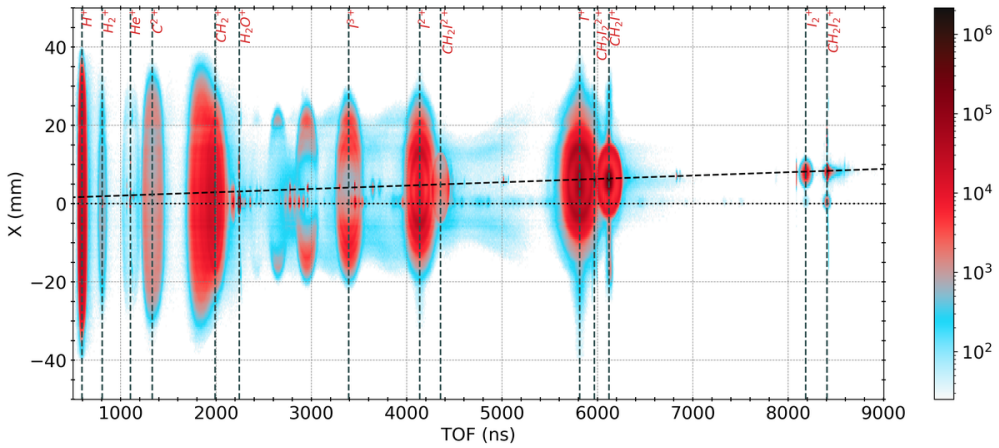

Figure 3.5: Ion time–of–flight (TOF) spectrum as above but including the detector hit position along the X (molecular beam) direction. The color bar indicates the counts per bin on a log color scale. The offset in X, indicated by the diagonal dashed line, is due to the velocity of the molecular beam, which helps separate ions generated by the ionization of molecules in the beam from those from residual gas.

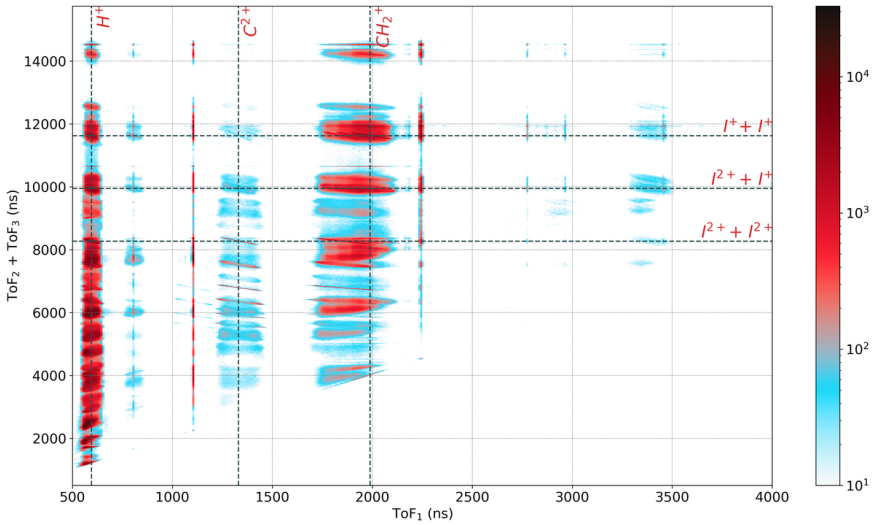

Figure 3.6: Photoion–photoion–photoion coincidence (TRIPICO) yield generated by strong–field ionization of CH_2I_2 molecule with the NIR pulse only. The different coincidence islands correspond to distinct fragmentation channels accessible under probe–only conditions. The color scale represents the counts per bin in log scale. This highlights the various coincident breakup pathways available and provides the basis for identifying the specific probe channel for UV–induced dynamics.

Figure 3.6 displays the three-ion coincidence (TRIPICO) spectrum under probe-only conditions. This highlights the various accessible coincidence channels generated by the NIR pulse and shows the different fragmentation pathways that can be probed by the strong field. Fragmentation channels that are complete can be distinguished from other channels by the sharp lines—the char-

acteristic signature of momentum conservation. Selecting a narrow region around these lines yields events belonging to those momentum-conserved channels. This minimizes the contamination from false coincidences and background ions.

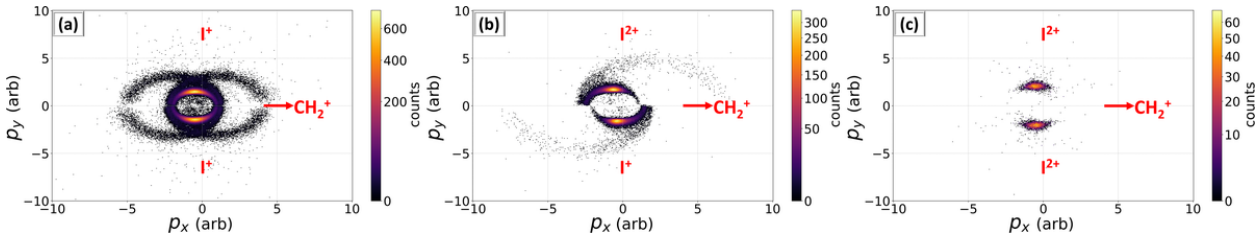

Figure 3.7: Newton plots of the (a) $CH_2^+ + I^+ + I^+$, (b) $CH_2^+ + I^{2+} + I^+$, and (c) $CH_2^+ + I^{2+} + I^{2+}$ coincidence channels for ionization by the NIR pulse alone. The momenta are normalized to the magnitude of the CH_2^+ fragment, and the reference frame is chosen such that the CH_2^+ momentum is aligned along the x–axis, with the xy plane defined by the first detected iodine ion in each channel. The circular features in [(a) and (b)] are clear indications of sequential breakup.

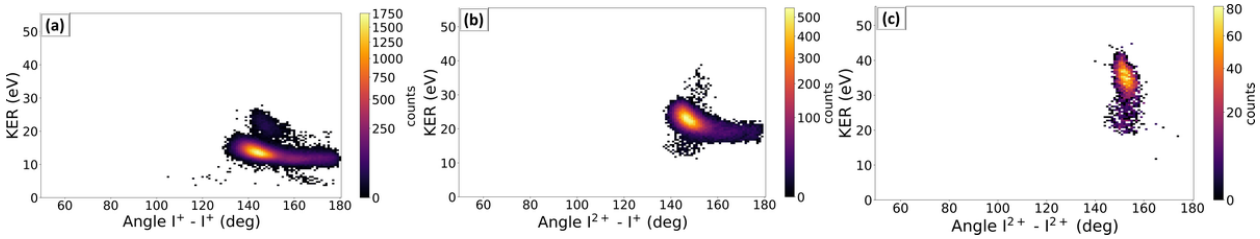

Figure 3.8: Ion yield as a function of KER and angle between the momentum vectors of the two iodine ions for (a) $CH_2^+ + I^+ + I^+$, (b) $CH_2^+ + I^{2+} + I^+$ and (c) $CH_2^+ + I^{2+} + I^{2+}$ coincidence channels, again for ionization by the NIR pulse alone. The first two channels exhibit strong sequential breakup contributions, consistent with rotational excitation of the intermediate fragments. In contrast, the $CH_2^+ + I^{2+} + I^{2+}$ channel shows minimal sequential character, making it the most suitable fragmentation channel for probing pump–induced dynamics.

Figures 3.7 and 3.8 show the Newton plots and the KER versus I–I momentum angle distributions, respectively, for the three dominant three-body fragmentation channels involving emission of two iodine fragments, with total final charge states of three, four and five: $CH_2^+ + I^+ + I^+$, $CH_2^+ + I^{2+} + I^+$ and $CH_2^+ + I^{2+} + I^{2+}$. The first two exhibit strong contributions from sequential breakup, evident from the circular features (Figs. 3.7(a) and (b)) associated with formation and rotation of an intermediate CH_2I fragment. In contrast, the $CH_2^+ + I^{2+} + I^{2+}$ channel in Fig. 3.7(c) displays a purely concerted breakup without significant contribution from sequential breakup. This is also evident in Fig. 3.8, where the (a) three- and (b) four-fold channels show a tail from the main lobe extending to large angles. This behavior is consistent with sequential fragmentation, where rotation

of the intermediate fragment broadens the I–I momentum angle toward larger values. By contrast, the five-fold channel ($CH_2^+ + I^{2+} + I^{2+}$) shows minimal contributions from sequential breakup, with yield confined to a narrow range of I–I momentum angles centered near 150°. Sequential fragmentation introduces rotational excitation of the intermediate fragments, which obscures the signatures of pump-induced dynamics and complicates the identification of weaker competing pathways. We therefore select the $CH_2^+ + I^{2+} + I^{2+}$ channel as the most suitable probe of the UV-induced dynamics, with the probe-only analysis establishing the baseline for interpreting the UV-pump/IR-probe results.

3.4 UV–pump/NIR–probe Dynamics at 290 nm

While the main objective in this chapter is to investigate the transient photoisomerization of diiodomethane (CH_2I_2) after UV photoabsorption, the majority of the photoexcited molecules undergo direct dissociation following C–I bond cleavage, and the first task is therefore to identify the signatures of these competing reaction pathways. We begin with the 290 nm dataset, which has higher UV absorption cross section for CH_2I_2[73] compared to 330 nm. This wavelength provides the highest signal–to–noise in our measurements, allowing us to establish the analysis pipeline and benchmarks for transient–geometry identification. In what follows, we track the evolution of the $CH_2^+ + I^{2+} + I^{2+}$ channel as a function of pump–probe delay and use the associated angle–resolved and fragment–resolved observables to separate any contributions from iso–CH_2I_2–like signatures from other channels.

Figure 3.9 introduces the KER–delay map—ion yield as function of the KER and the pump-probe delay. Three distinct features are visible in Fig. 3.9(a): (i) a horizontal band in the KER range between 30 and 40 eV, which corresponds to the Coulomb explosion of bound (i.e. non-dissociating) molecules that may or may not have absorbed a UV photon and that were five-fold ionized by the probe pulse; (ii) a curved feature whose KER decreases with increasing pump-probe delay and which emerges from the horizontal band near time-zero, reaching a KER of approximately 15–18 eV at a delay of 2 ps and 9–14 eV at a delay of 13.5 ps (see Fig. 3.9(b)); and (iii) another curved feature whose KER decreases even faster than that of feature (ii), reaching a KER of

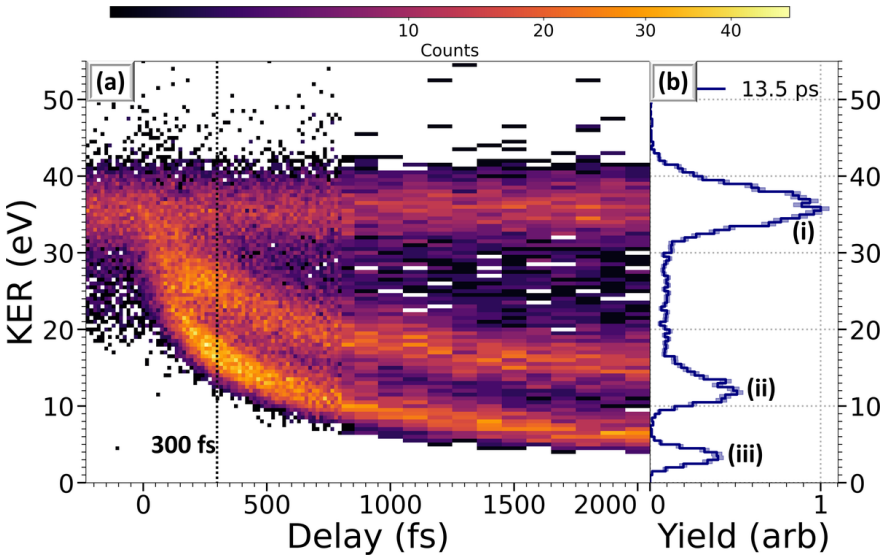

Figure 3.9: (a) $CH_2^+ + I^{2+} + I^{2+}$ ion coincidence yield as function of pump–probe delay and KER. Positive delays correspond to the NIR probe pulse arriving after the UV pump pulse. A step size of 15 fs and 100 fs was used for delays up to and beyond 800 fs, respectively. (b) KER spectra of the same coincidence channel recorded at a fixed delay of 13.5 ps. The data shown here were recorded at a pump wavelength of 290 nm. The equivalent plots for this and all the following figures with the data recorded at 330 nm are shown in Sec. 3.5. The vertical dashed line at 300 fs in panel (a) indicates the experimentally obtained rotational period of the CH_2I fragment.

approximately 8–10 eV at a delay of 2 ps and 1–5 eV at a delay of 13.5 ps, at which point the KER no longer changes with delay. Features (ii) and (iii) originate from the molecules that dissociated upon UV photoabsorption, with feature (ii) corresponding to two-body dissociations into CH_2I and I or CH_2 and I_2, while feature (iii) corresponds to direct three-body dissociation by the UV pulse into CH_2, I and I. While these assignments can be made with good confidence based on the asymptotic KERs of both channels, further insights and confirmation are obtained when inspecting the angular correlation between the momentum vectors of the ionic fragments [73].

Figure 3.10 summarizes how new structures emerge upon UV excitation. At negative delay [Fig. 3.10(a)], the probe-only distribution forms a compact island, as seen in Fig. 3.8(c). As the delay becomes positive (UV-early/IR-late) [Fig. 3.10(b)], events with similar KER spread to larger angles, and by 60–150 fs [Fig. 3.10(c)] a pronounced large-angle population appears together with a growing low-KER band. With increasing delay [Fig. 3.10(d)], these low-KER features separate into discrete blobs that mirror the two decaying bands in the delay–KER map [Fig. 3.9(a)]. By 1.5–2.0 ps [Fig. 3.10(e)], the lower-KER contributions associated with dissociation and I_2 formation are clearly

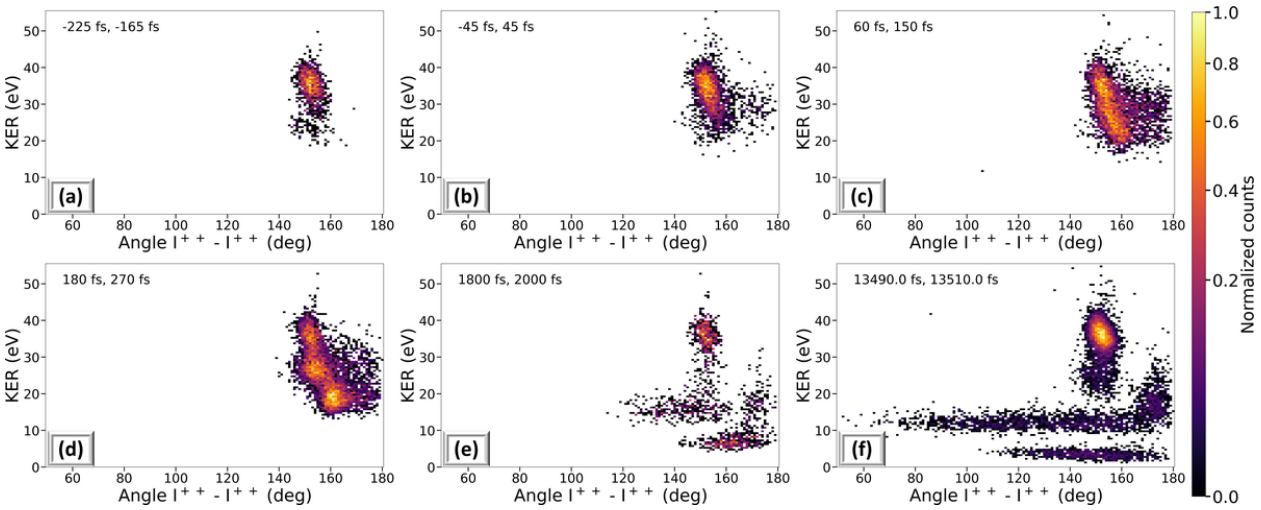

Figure 3.10: Delay–sliced snapshots of the $CH_2^+ + I^{2+} + I^{2+}$ yield as a function of total KER and the I^{2+}–I^{2+} momentum angle at representative pump–probe delay windows. (a) Probe-only baseline (negative delay) shows a single localized island. (b) At short positive delays, a shoulder at similar KER extends toward larger angles. (c) By 60–150 fs, this large-angle contribution strengthens and a low-KER band appears, resembling an extension of the probe-only population. (d) With further delay, distinct blobs emerge that correspond to the two decaying branches seen in the delay–KER map (Fig. 3.9). (e) At long delays (1.5–2.0 ps), the lower-KER distributions associated with two- and three-body dissociation and I_2 formation separate clearly, while the high-KER shoulder has disappeared. (f) In the asymptotic delay slice, the features are well separated into the characteristic regions associated with bound-molecule Coulomb explosion, two- and three-body dissociation, and I_2 formation.

resolved from the high-KER island. In the asymptotic-delay slice [Fig. 3.10(f)], the regions are well isolated, paving the way for the long-delay analysis.

Figure 3.11(a) shows the coincidence ion yield at the asymptotic delay of 13.5 ps as a function of the KER and the angle between the momentum vectors of the two iodine dications. The most intense feature at a KER of 30–40 eV (with a smaller side-peak between 20–30 eV) and relatively well defined (I^{2+}, I^{2+}) angle centered around 150° (marked by the black ellipse in Fig. 3.11(a)) stems from the Coulomb explosion of bound molecules in or near their equilibrium geometry, as confirmed by the data taken without the UV pulse present shown in Fig. 3.8. At a KER of approximately 15 eV (red ellipse), an angularly broad feature spanning 60–180 degrees in the (I^{2+}, I^{2+}) angle can be attributed to C–I cleavage and dissociation into CH_2I + I induced by a single-UV-photon absorption. The broad spread in angle results from high rotational excitation of the CH_2I fragment due to the torque imparted from the C–I bond cleavage, as also observed in other

dihalomethanes[115–120].

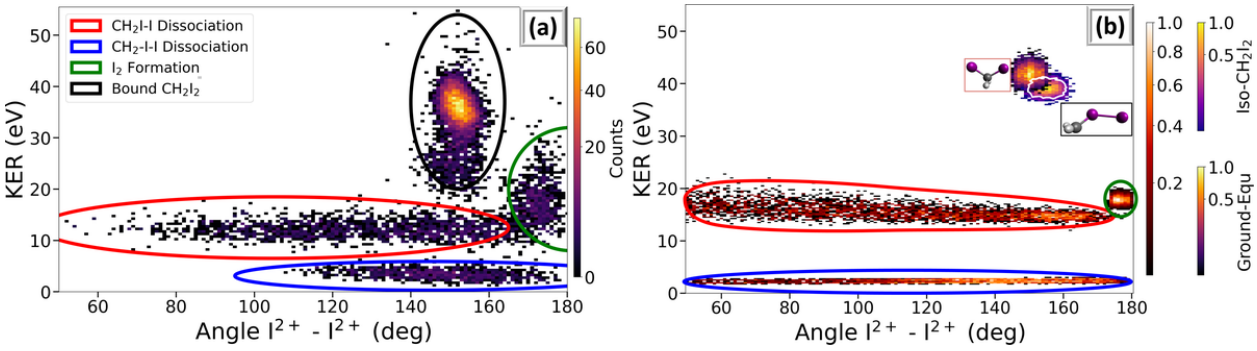

Figure 3.11: (a) $CH_2^+ + I^{2+} + I^{2+}$ ion coincidence yield as a function of KER and angle between the momentum vectors of the two iodine dications for a fixed pump–probe delay of 13.5 ps. Four clearly separated components can be distinguished: a high–KE peak and a lower–KE spot both located at large I_2^+–I_2^+ opening angles, corresponding to two different contributions with similar I–I momentum–space angles. The former is associated with a shorter I–I distance in the Coulomb explosion, while the latter corresponds to an increased I–I separation. In addition, a low–KE spot at small I_2^+–I_2^+ angles is attributed to three–body breakup, and a broad band at larger KER values points to Coulomb explosion of bound molecules. (b) Simulation results for the neutral equilibrium geometry, iso–CH_2I_2 equilibrium geometry, and several dissociation channels.

Two additional features, each of them with approximately half the number of events as in the red ellipse discussed above, are prominent in Fig. 3.11. First, a rather localized spot peaked at a KER slightly below 20 eV and an (I^{2+}, I^{2+}) angle close to 180° (green ellipse) can be uniquely attributed to I_2 formation after UV excitation (i.e., dissociation into $CH_2 + I_2$) since both the KER and the back-to-back emission of the two iodine ions are consistent with a Coulomb explosion of I_2. Second, a clearly separated contribution at low KER (blue ellipse) is attributed to the UV-induced three-body dissociation into $CH_2 + I + I$. Both of these features result mainly from multi-photon excitation by the UV pulse. This assignment is based on (i) the energy required to trigger three-body dissociation (4.8 - 5 eV[114;121]), (ii) earlier experimental work that reported rather low quantum yield of I_2 elimination upon single-photon excitation[121], and (iii) on the observed dependence on the UV power. The log–log analysis, as shown in Fig. 3.24, reveals that the C–I dissociation yield scales linearly with pump intensity (slope ≈ 1), consistent with a one-photon absorption process. In contrast, the molecular I_2 formation and the $CH_2 + I + I$ three-body fragmentation scale nonlinearly (slope ≈ 2), showing two-photon character.

The results of the classical Coulomb explosion simulations for the neutral ground-state geometry

and the iso-CH_2I_2 equilibrium geometry are shown in Fig. 3.11(b), along with the simulation results for the CH_2I + I, CH_2 + I_2 and CH_2 + I + I dissociation channels at 13.5 ps pump-probe delay. Apart from overestimating the measured KER, most likely due to the assumption of a purely Coulombic potential, the simulated results qualitatively match the experimental observations for all channels, validating the use of these simulations in identifying the observables corresponding to the possible formation of the isomer.

Although the simulations show a subtle difference in the KER of the equilibrium geometry and the isomer, this distinction can be expected to be much less pronounced in the experiment, where a significant spread in the KER is observed even when no UV pulse is present. However, the simulations also predict that the Coulomb explosion of the isomer will lead to some ion yield at larger angles between the (I^{2+}, I^{2+}) momenta than those realized by the Coulomb explosion of the equilibrium geometry. In the experiment, essentially no events are observed with (I^{2+}, I^{2+}) angles larger than 160° when no UV pulse is present as seen in Fig. 3.8(c), but a transient signal with high KER is observed in this region for pump probe delays between 0 and 250 fs, Fig. 3.10. By selecting only those events in the experimental data where the (I^{2+}, I^{2+}) angle is larger than 160°, we can thus almost completely suppress the contribution from molecules in the equilibrium geometry.

However, from the experimental data, it is evident that the three dissociation pathways—(i) CH_2I-I two-body dissociation with CH_2I rotation, (ii) CH_2-I–I three-body dissociation and (iii) molecular I_2 formation—could also contribute to the region with the (I^{2+}, I^{2+}) angle larger than 160° (at least at large delays), as seen in Fig. 3.11(a). Contributions from these pathways need to be filtered out to identify possible signatures of isomerization to CH_2I–I. The simulations in Fig. 3.12 show that after the Coulomb explosion, the sum of the KEs of the two I^{2+} fragments is larger for the iso-CH_2I_2 molecules than that of the CH_2I_2 molecules that undergo direct dissociation into CH_2I and I through C–I cleavage. Furthermore, in the cases of three-body dissociation or molecular iodine formation, the KE of the methyl ion decreases rapidly with pump-probe delay as the CH_2 fragment quickly moves away from the two iodine atoms or the I_2 molecule. Therefore, the sum of the KEs of the two I^{2+} fragments and the KE of the CH_2 fragment can serve as additional parameters to discriminate the different channels.

Since it is very likely that any isomer-like geometries, were they to be formed as predicted by

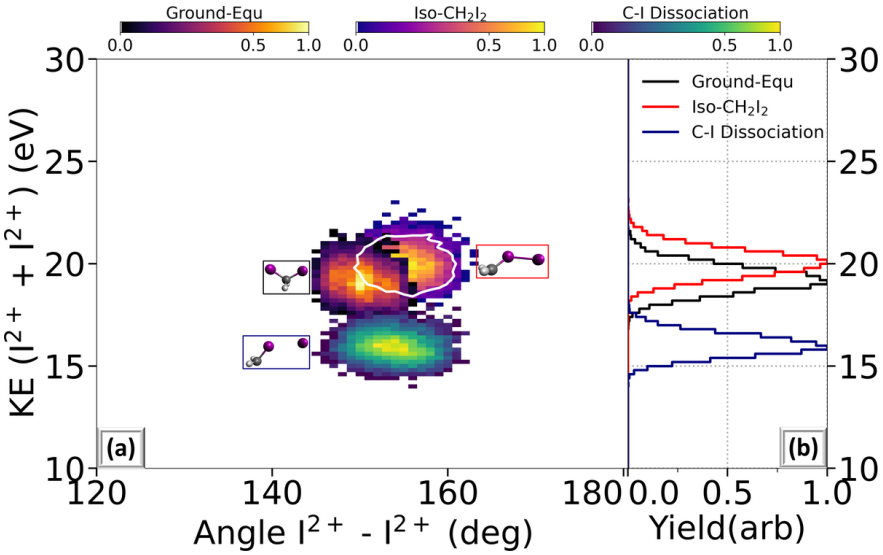

Figure 3.12: Coulomb explosion simulations of CH_2I_2 for the following molecular geometries: the ground–state equilibrium geometry, the iso–geometry, and three states along the C–I dissociation pathway. Panel (a) shows the dependence of the I_2^+ KE sum on the I_2^+–I_2^+ angle, while panel (b) presents the corresponding one–dimensional distributions. The color bars report the normalized counts per bin in each case using a power-norm color scale. These simulations suggest that large I_2^+–I_2^+ angles are more likely for the iso–geometry than for the equilibrium geometry, whereas contributions from C–I dissociation cover a broader range of KE sums and angles.

Borin *et al.*[105], would be visited quickly due to the large amount of internal energy deposited into the molecule by the UV photon, we will concentrate our search on the smaller delays below 1 ps, where the isomer-geometry should appear as an additional contribution in the region corresponding to the bound molecules. However, we have also searched for larger pump-probe delays, but have not found any statistically significant indications of isomer-like geometries at larger delays.

In Fig. 3.13, the KE distribution of the methyl cation (CH_2^+) is shown as a function of the pump-probe delay up to 800 fs and only for those events where the (I^{2+}, I^{2+}) angle is larger than 160°. Based on the reasoning outlined in the previous paragraph, we can conclude that the events with quickly decreasing KE, below the blue line in Fig. 3.13, correspond to either CH_2-I–I three-body dissociation or molecular iodine formation. The events above the blue line at 13 eV mainly correspond to dissociation of CH_2I_2 into CH_2I and I (with subsequent rotation of the CH_2I fragment) as well as any possible formation of iso-CH_2I_2, with only spurious contributions from the three-body dissociation and molecular iodine formation pathways at small delays below 200 fs. The choice of 13 eV as the boundary is motivated by the experimental data, where a distinct separation

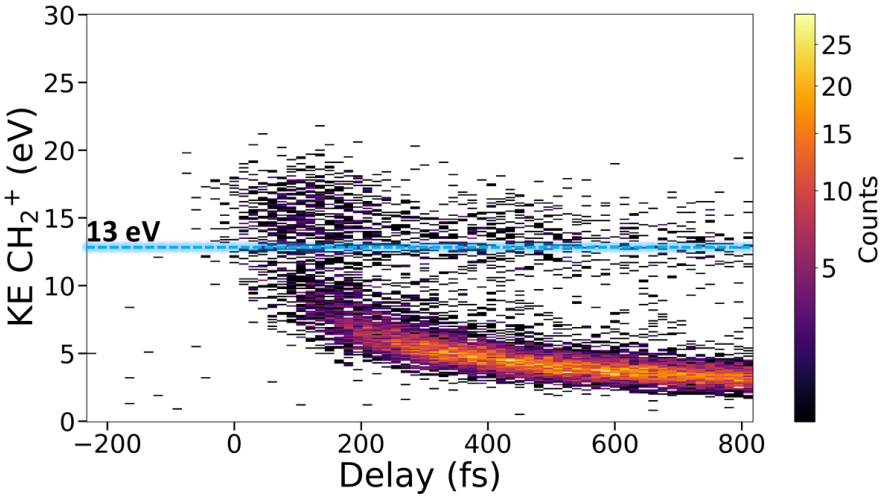

Figure 3.13: Kinetic energy of the CH_2^+ fragment as a function of the pump–probe delay with only those coincidence events shown where the angle between the two I^{2+} momentum vectors is greater than 160°. The region below the blue line, at 13 eV kinetic energy of methyl cation, corresponds to the events from CH_2–I–I three–body dissociation and molecular I_2 formation pathways (see the text). The region of interest, above 13 eV, is where any events from photoisomerization following UV excitation would appear, along with the contribution from two–body dissociation producing I (or I^*) and rotationally excited CH_2I.

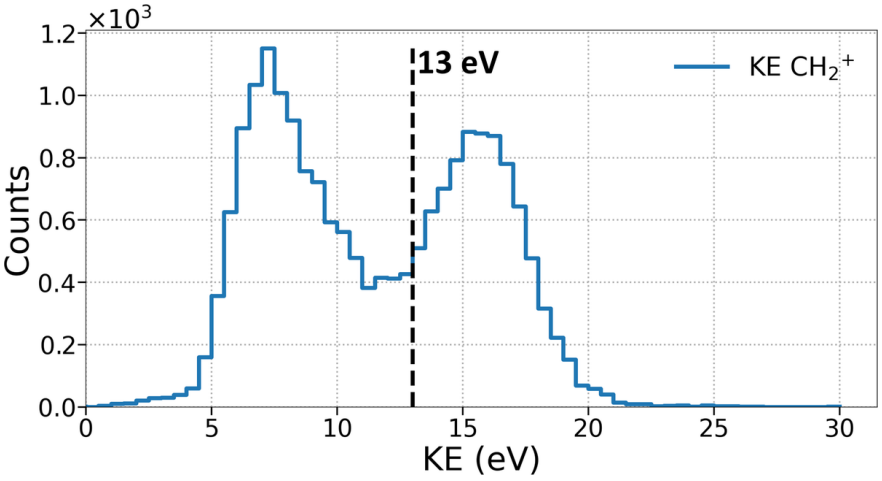

Figure 3.14: Delay–integrated (<300 fs) kinetic energy distribution of the CH_2^+ fragment from the $CH_2^+ + I^{2+} + I^{2+}$ coincidence channel, gated on I^{2+}–I^{2+} momentum angles larger than 160°. The distribution shows a dip that separates the decaying low–KE band from the higher–KE island observed in the 100–200 fs region (see Fig. 3.13). The dashed line at 13 eV corresponds to the upper edge of this dip and is used as the threshold to distinguish between these two contributions.

is observed between the decaying low-KE band and the high-KE island in the 100–200 fs region as seen in the delay–integrated yield of the CH_2^+ as a function of kinetic energy shown in Fig. 3.14. Although the constant 13 eV horizontal line in Fig. 3.13, intersects other features at later delays,

our analysis focuses only on the early-delay (<300 fs) region, so those intersections do not affect the conclusions.

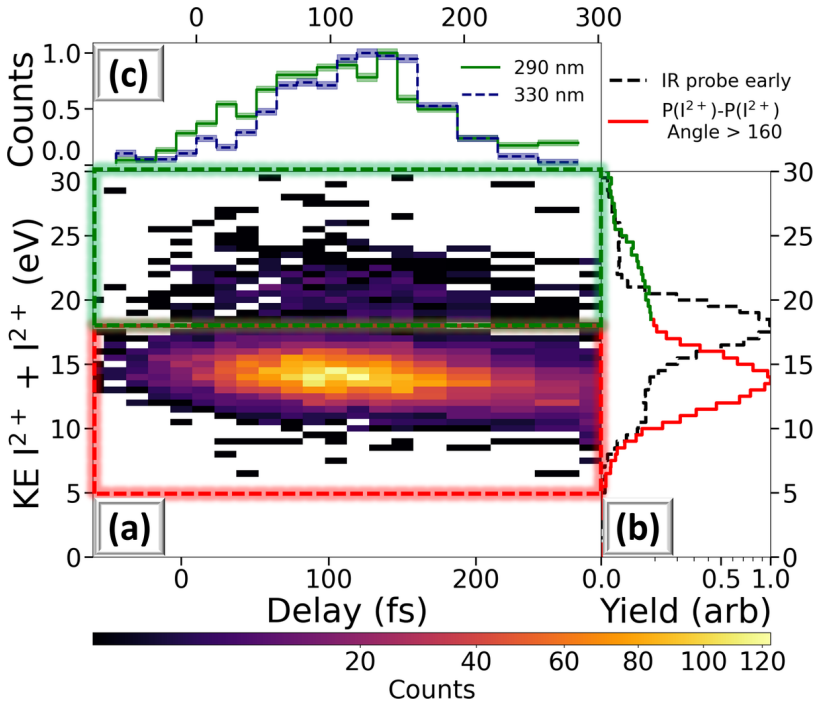

Figure 3.15: (a) Coincidence ion yield as a function of pump–probe delay and KE sum of the two I^{2+} fragments, for only those events where the angle between the two I^{2+} momentum vectors is greater than 160° and the KE of the CH_2^+ fragment is greater than 13 eV (above the blue line in Fig. 3.13). The two regions of interest are described in the text. (b) Projection of the coincident ion yield in panel (a) on the KE axis, with unpumped reference shown as a black dotted line. (c) Projection of the coincident ion yield in the green ROI on the pump–probe delay axis (green), compared to 330 nm (blue).

Next, we select only those events with kinetic energy of CH_2^+ ionic fragment above 13 eV from Fig. 3.13 and plot the sum of the KEs of the two iodine fragments as a function of pump-probe delay in Fig. 3.15(a). The plot reveals two contributions: an intense feature with a KE sum between 10 and 17 eV (marked by the red rectangle), and a much weaker feature at a higher KE sum, marked by the green rectangle, which contains approximately 7% of the events in the intense feature. The projection in panel (b) reveals that these two contributions are shifted toward lower (solid line, red section) and higher energies (solid line, green section), respectively, compared to the KE sum of the unpumped molecules (black dotted line). The integrated yield inside the green region of interest as a function of the pump-probe delay is shown as green line in Fig. 3.15(c). Based on the simulations shown in Fig. 3.12(b), we assign the events with the higher KE sum to molecular

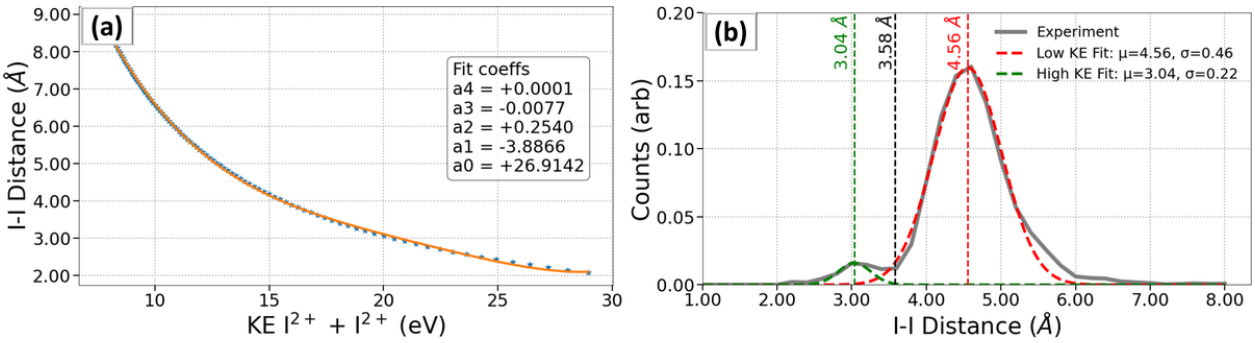

Figure 3.16: (a) Calibration curve obtained from Coulomb explosion simulations with varied I–I separations, showing the correlation between the kinetic energy sum of the two I^{2+} ions and the underlying I–I distance. (b) Estimated I–I distance distributions derived from the experimental data in Fig. 3.15 using the calibration in panel (a). A Gaussian fit to the peak with high KE sum yields a shortened I–I distance of ˜3.04 Å, while the Gaussian fit to the peak with low KE sum yields an extended I–I distance of ˜4.56 Å. The dashed line denotes the I–I distance in the neutral ground equilibrium CH_2I_2 geometry.

geometries resembling the iso-CH_2I_2 structure predicted by Borin *et al.*[105], which have a slightly smaller I–I distance than geometries resulting from the dissociation of CH_2I_2.

To quantify the change in the I–I distance, we calibrate the relationship between the KE sum of the two I^{2+} ions and the I–I distance using Coulomb explosion simulations with varied I–I distances. The I–I distances and the KE sums of the two I^{2+} fragments obtained from the simulation are fitted with a polynomial, as shown in Fig. 3.16(a). Applying this calibration to the experimental data yields an estimated I–I distances of ∼3.0 Å for the events with high KE sum and ∼4.6 Å for the events with low KE sum [Fig. 3.16(b)], compared to ∼3.58 Å in the ground equilibrium geometry. Fig. 3.15(c) shows that the occurrence of these iso-CH_2I_2-like structures peaks at a delay of approximately 120 fs and quickly decays again on a similar time scale. Analysis of the pump-probe data recorded at a pump wavelength of 330 nm, following the exact same steps as described above (see Sec. 3.5 later in the chapter), yields the blue dashed line in Fig. 3.15(c), which shows the same behavior as the data at 290 nm except for possibly a subtle shift towards slightly longer delays, which is at the borderline of statistical significance for the present data set.

To further demonstrate the time dependence of the iso-CH_2I_2-like contribution, Fig. 3.17 presents selected snapshots of the delay-dependent $CH_2^+ + I^{2+} + I^{2+}$ coincidence yield as a function of the total KER and the angle between the momenta of the two I^{2+} ions. The events associated with the two rectangular regions in Fig. 3.15 are overlaid as green and red scatter points to emphasize

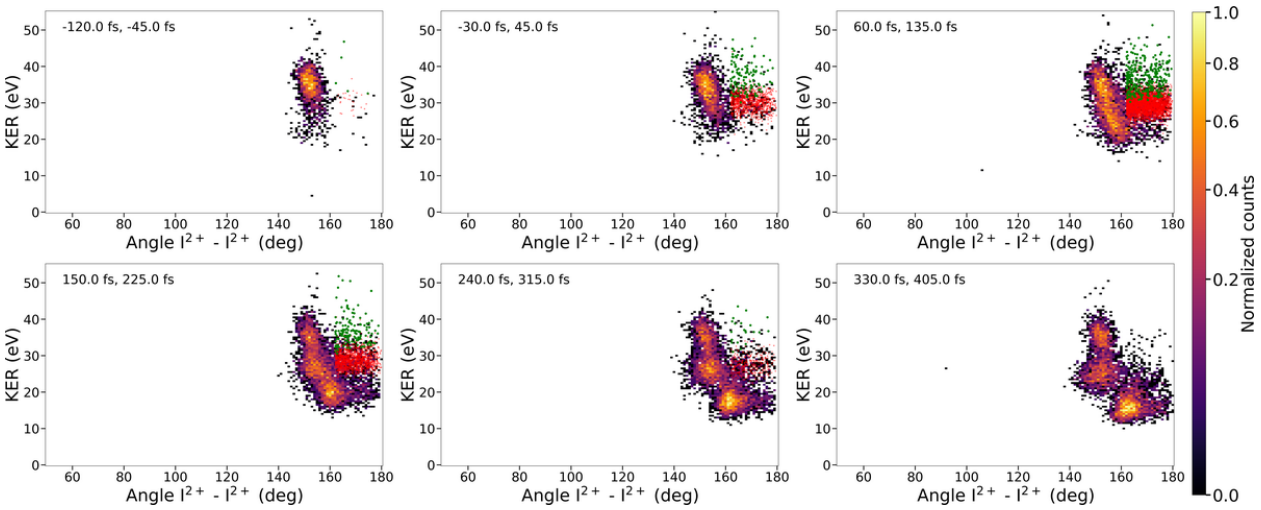

Figure 3.17: Delay–sliced snapshots of the coincident ion yield as a function of the total KER and the angle between the two I^{2+} ion momenta for the events shown in Fig. 3.15(a). The iso–like (green) and the dissociation–like (red) regions of interest (ROIs) are overlaid.

the iso-CH_2I_2-like contributions. The figure shows that this transient feature is confined to a narrow temporal window and disappears at later delays, consistent with the dynamics discussed in Fig. 3.15.

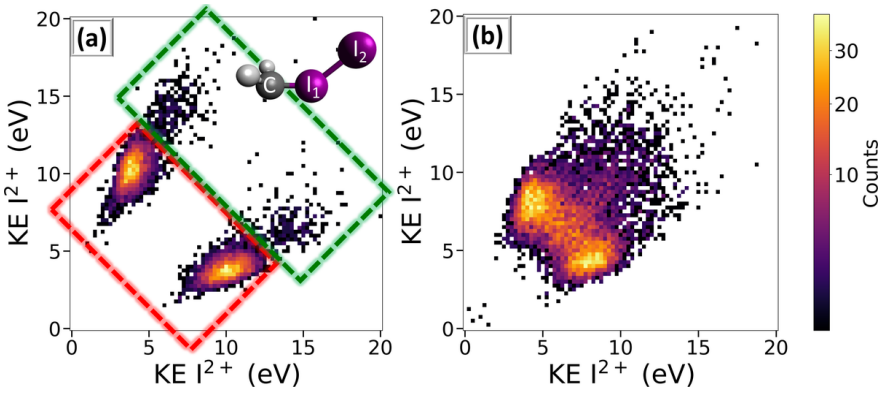

Figure 3.18: Energy sharing between the two I^{2+} fragments, integrated over the pump-probe delays shown in Fig. 3.15, for only those events where the angle between the two I^{2+} momentum vectors is greater than 160° and (a) the KE of the CH_2^+ fragment is greater than 13 eV (above the blue line in Fig. 3.13); or (b) the KE of the CH_2^+ fragment is less than 13 eV (below the blue line in Fig. 3.13). The red and green rectangles in panel (a) correspond to events originating from the respective rectangular regions in Fig. 3.15.

Additional information on the geometry of the transient species can be obtained by considering the energy sharing between the two detected I^{2+} fragments, as shown in Fig. 3.18. Symmetric geometries, such as the original CH_2I_2 geometry, or any molecules excited to symmetric vibrational

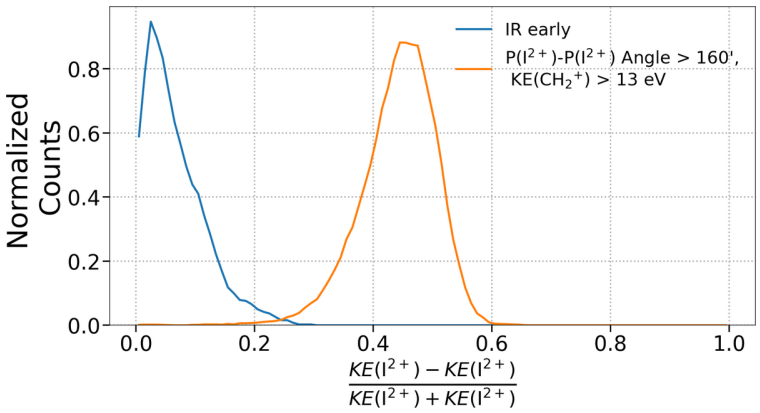

Figure 3.19: Energy-sharing ratio between the two I^{2+} fragments, defined as the normalized difference between the kinetic energies of the two I^{2+} ions. For symmetric energy sharing, this ratio is expected to peak near zero, while asymmetric energy sharing produces broader distributions shifted away from zero. The blue curve corresponds to the IR-early events, where the distribution peaks near zero, indicating symmetric energy sharing consistent with the symmetric ground equilibrium geometry. The orange curve corresponds to the events shown in Fig. 3.18(a), where the distribution is shifted and broadened around a peak near 0.5, revealing asymmetric energy sharing characteristic of these geometries. This comparison supports the interpretation of Fig. 3.18 that the iso-CH_2I_2-like contribution is associated with asymmetric fragmentation dynamics.

modes, would lead to equal energy sharing, whereas strongly asymmetric geometries such as the predicted iso-CH_2I_2 species, would lead to a pronounced asymmetry in the energy sharing. The gated events that survive both filters—large I^{2+}–I^{2+} momentum angle and high CH_2^+ energy—exhibit distinctly asymmetric energy sharing between the two I^{2+} ions, as shown in Fig. 3.18(a). This is further illustrated in Fig. 3.19, where the energy-sharing ratio between the two I^{2+} fragments is shown. While IR-early events peak sharply near zero, indicating symmetric sharing, the gated events of Fig. 3.18(a) yield a broadened distribution centered near 0.5, confirming their asymmetric character and supporting the assignment to iso-CH_2I_2-like geometries. In contrast, Fig. 3.18(b) shows that symmetric geometries dominate when the CH_2^+ energy is low, corroborating our assignment of these events to the I_2 formation channel.

To complement the two–dimensional energy–sharing maps in Fig. 3.18 and the one–dimensional ratio in Fig. 3.19, we present Dalitz plots, which compactly encode the three–body energy partitioning for the $CH_2^+ + I^{2+} + I^{2+}$ channel (Fig. 3.20). Panel 3.20(a) shows simulations for the three representative geometries used in Fig. 3.12: the ground–state equilibrium structure, an iso–CH_2I_2 equilibrium geometry, and a C–I dissociation geometry constrained to the iso angle. In the Dalitz

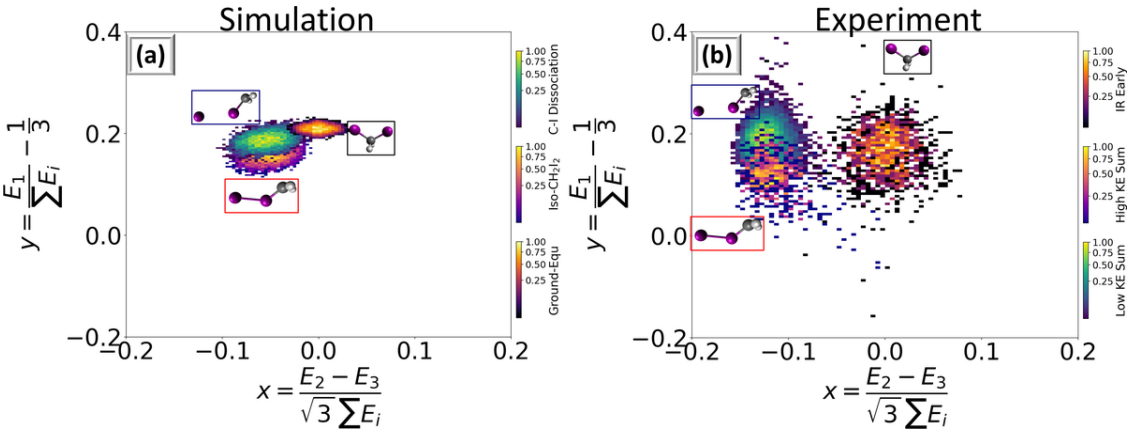

Figure 3.20: Dalitz plots for the $CH_2^+ + I^{2+} + I^{2+}$ channel from simulation (a) and experiment (b). The color bars represent the bin counts (normalized to the max count) using power-norm color scale. The simulation shows contributions from the three sets of geometries used in Fig. 3.12. Panel (b) shows the experimental Dalitz plots corresponding to IR-early events, and the two gated regions marked by the red and green boxes in Fig. 3.15. The insets show ball-and-stick models of the corresponding molecular geometries.

representation, symmetric geometries such as the ground–state equilibrium CH_2I_2 cluster near the horizontal center, reflecting equal momentum sharing between the two I^{2+} fragments. By contrast, the simulated iso–CH_2I_2 and C–I dissociation geometries populate off–center islands, indicating asymmetric iodine configurations. Comparison of the two off–center clusters further shows that the CH_2^+ fragment carries a smaller fractional energy in the iso geometry than along the C–I dissociation path, consistent with a shorter I–I distance in the iso–CH_2I_2 configuration. Panel 3.20(b) displays the experimental Dalitz plots for similar selections: the NIR–early events, which reflect Coulomb explosion of the unperturbed ground–state geometry, and the two gated regions marked by the red and green boxes in Fig. 3.15. As discussed above, these gates separate high–and low–KE sums of the I^{2+} ions for events with large I–I momentum angles and high CH_2^+ kinetic energy, corresponding to iso–like and C–I dissociation–like contributions, respectively. For the high– and low–KE sum events, the iodine fragments are sorted by kinetic energy to enable direct comparison with the simulations. The experimental clusters fall at positions that qualitatively match the simulated islands, reinforcing the assignment of the gated populations to iso–CH_2I_2–like and dissociation–like geometries and highlighting the asymmetric energy sharing characteristic for the events with high CH_2^+ kinetic energy in Fig. 3.15(a).

3.5 330 nm UV-excitation Dynamics

Having established the geometry–sensitive signatures at 290 nm, we now repeat the analysis at 330 nm to compare with the transient–absorption study of Borin *et al.*[105] and assess similarities and differences in the transient–structure observables identified at 290 nm. Although 330 nm wavelength lies at a smaller absorption cross section than 290 nm (see Fig. 3.2), the overall phenomenology closely mirrors the 290 nm results: the same set of long–delay (10 ps) components is present, and the iso–CH_2I_2–like selection appears in the same early–time window. Where the datasets differ is primarily in relative yields and clarity of certain delay–sliced structures, as detailed below.

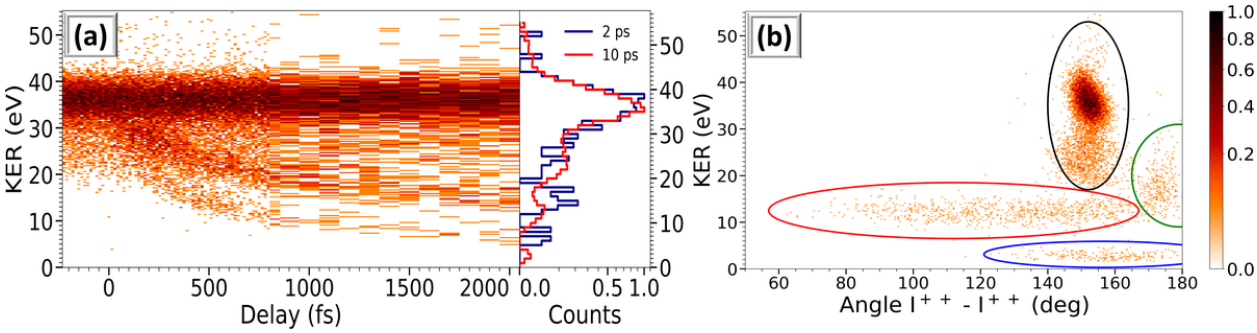

Figure 3.21: (a) Coincidence yield of the $CH_2^+ + I^{2+} + I^{2+}$ channel as a function of pump–probe delay and total KER at 330 nm. Right panel: KER spectra at delays of 2 ps (blue) and 10 ps (red). (b) $CH_2^+ + I^{2+} + I^{2+}$ ion yield as a function of the KER and angle between the momentum vectors of the iodine ions at an asymptotic delay (10 ps). The color bar gives the intensity in counts per bin, plotted using power-norm scale. The colored ovals mark the same contributions as described at 290 nm.

The delay–KER map at 330 nm [Fig. 3.21(a)] displays the same three distinct contributions observed at 290 nm (Fig. 3.9): a horizontal band attributable to Coulomb explosion of bound molecules, a two–body band whose KER decreases with delay, and a more rapidly decreasing three–body contribution, although this band is noticeably weaker here than at 290 nm. The coincidence ion yield as a function of the total KER and the I^{2+}–I^{2+} momentum angle at an asymptotic delay of 10 ps [Fig. 3.21(b)] shows the same set of regions identified at 290 nm (Fig. 3.11). Relative to 290 nm, the three–body and I_2 formation components are reduced in yield, consistent with the smaller absorption cross section at 330 nm (Fig. 3.2) and with fewer pathways accessing higher lying states that favor multiphoton channels.

Following the 290 nm workflow, we select large I^{2+}–I^{2+} momentum angles ($> 160°$) and apply

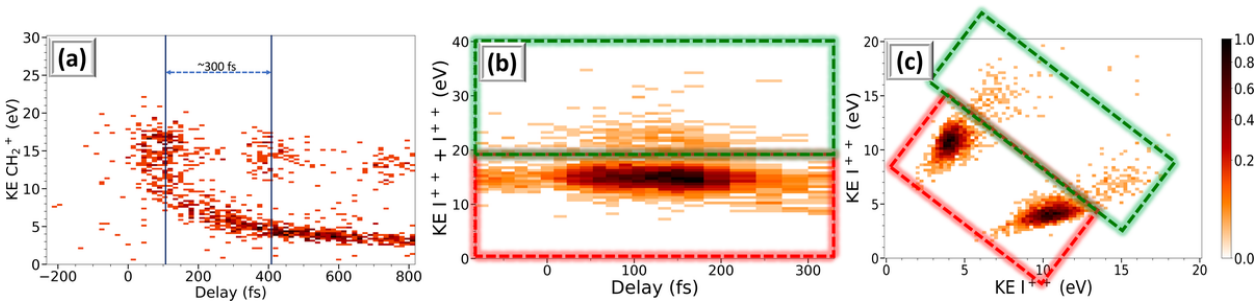

Figure 3.22: (a) Yield of the $CH_2^+ + I^{2+} + I^{2+}$ coincidence channel plotted as a function of pump–probe delay and the kinetic energy of the CH_2^+ fragment, shown only for those events where the angle between the iodine ion momentum vectors is greater than 160° as in Fig. 3.13. The vertical lines indicate a time interval of ˜300 fs, corresponding to the rotational period of the neutral CH_2I radical formed after UV excitation and C–I bond cleavage. (b) Ion yield as a function of the kinetic energy sum of the two I^{2+} ions and the pump-probe delay, for events with the I–I momentum angle greater than 160° and kinetic energy of CH_2^+ greater than 13 eV, similar to Fig. 3.15. (c) Coincidence ion yield of the $CH_2^+ + I^{2+} + I^{2+}$ channel as a function of the kinetic energy sharing between the two iodine ions, analogous to Fig. 3.18. The color bar indicates the normalized counts per bin on a power scale

the same CH_2^+ kinetic-energy threshold chosen from the delayed, angle-gated kinetic energy spectrum (Fig. 3.14). The CH_2^+ KE versus delay at 330 nm [Fig. 3.22(a)] shows well-separated rotational islands without the diffuse band seen at 290 nm (Fig. 3.13). This cleaner pattern is consistent with a simpler dissociation manifold at 330 nm, where fewer competing pathways predominantly lead to two-body dissociation into CH_2I + I, producing a rotationally excited CH_2I fragment. Under the same large-angle gate, the islands occur at delays when the CH_2I fragment has rotated so that the projected I–I axis is near linear, consistent with the large I–I momentum angle.

Following the analysis steps from 290 nm and selecting events where the kinetic energy of the CH_2^+ ion is greater than 13 eV, the yield as a function of the I^{2+}–I^{2+} KE sum and pump-probe delay [Fig. 3.22(b)] exhibits the same features emphasized at 290 nm (Fig. 3.15). The high-KE sum yield peaks near the same 100–150 fs timescale as at 290 nm, within our temporal resolution, and decays thereafter. As in the 290 nm case, we interpret the high–KE sum region—events inside the green rectangles in Fig. 3.22 panels (b) and (c)—as the signature of transient iso–CH_2I_2–like geometries, while the low–KE sum contribution tracks dissociation–like events that share large momentum angles but arise from longer I–I separations. The weaker overall intensity of the high–KE sum shoulder at 330 nm falls in line with the smaller absorption cross section at this wavelength.

Overall, the 330 nm dataset reinforces the conclusions drawn from the 290 nm analysis. First, the same long–delay components are present at both wavelengths and occupy the same regions in KER–angle space. Second, the large I–I momentum angle, high–KE(CH_2^+) selection isolates a weaker population with higher I^{2+}–I^{2+} kinetic energy sum and asymmetric iodine energy sharing, consistent with transient iso–CH_2I_2–like geometries. Differences between the wavelengths are primarily attributable to lower overall yield—especially for the three–body and I_2 formation channels—at 330 nm and to cleaner rotations seen in KE(CH_2^+) versus delay plots. These differences likely reflect the smaller absorption cross section at 330 nm and the access at 290 nm to higher–lying electronic states that open multiple dissociative pathways leading to CH_2I + I or I^* fragments.

3.6 UV Power Dependence

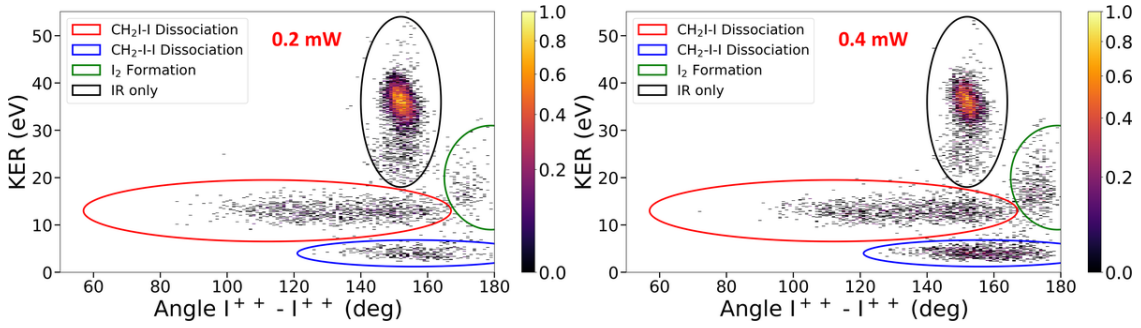

Figure 3.23: CH_2^+ + I^{2+} + I^{2+} ion yield as a function of KER and angle between the momenta of the iodine ions for two different powers of the 290 nm UV pulse. The color scale represents the normalized counts per bin (power scale)

This section presents the UV power dependence of fragment yields extracted from different regions of the KER versus I–I angle distributions at asymptotic pump–probe delays. To quantify photon orders for the main fragmentation pathways, we evaluate coincidence yields as a function of the average UV power. Figure 3.23 shows KER versus I–I momentum angle maps at two exemplary 290 nm pump powers, illustrating the representative gated regions used for the power scaling analysis. The narrow I–I momentum angle region (black ellipse) corresponds to Coulomb explosion of bound molecules, the two–body band region (in red) at intermediate KER corresponds to C–I dissociation, and the large I–I angle features in green isolates the I_2 formation channel and the blue low KER band corresponds to three-body C–I–I breakup. These regions are defined

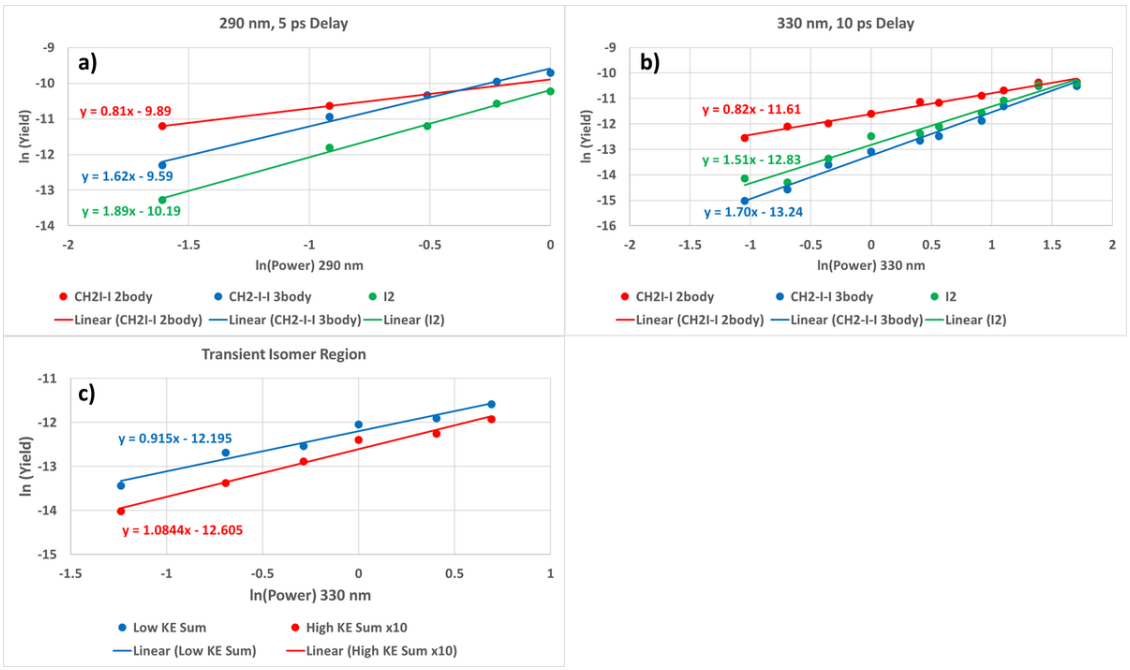

Figure 3.24: Coincidence ion yields of different channels as a function of power of the 290 nm (a) and the 330 nm (b and c) UV pulses. The linear fits in the double logarithmic plot of yield vs average UV power give a rough estimate of the order of the UV–excitation process: a slope of approximately 1 corresponds to a single–photon process, a slope of approximately two to a double–photon process.

consistently with the selections used earlier in the 290 nm and 330 nm analyses (cf. Figs. 3.11 and 3.21), and the yields are integrated at long pump–probe delays where the components are well separated.

Figure 3.24 summarizes the power dependence in double–logarithmic form. Panels 3.24(a) and 3.24(b) show the slopes extracted for the same KER–angle regions at 290 nm and 330 nm, respectively, using the asymptotic–delay gates described above. For both excitation wavelengths (290 nm and 330 nm), the log–log fits to the integrated yields show that the C–I dissociation channel scales with a slope of approximately one, consistent with a one-photon absorption process. By contrast, the molecular I_2 formation and the three–body C–I–I fragmentation channels display slopes closer to two, indicating that these channels are predominantly populated through two–photon absorption. Panel 3.24(c) reports the power scaling for the yields of the low-KE sum and high-KE sum regions, with gates defined analogously to the 290 nm and 330 nm kinetic energy sum maps (Figs. 3.15 and 3.22). Both the high and low KE sum regions exhibit slopes near one,

consistent with single–photon excitation underlying the transient iso-CH_2I_2-like selection (high KE sum) and the dissociation–like selection at large angles (low KE sum). Taken together, the KER–angle snapshots at two UV powers and the log–log scaling of integrated yields establish a clear distinction between single– and two–photon processes and further validate the channel assignments made in the analysis.

3.7 Summary and Outlook

In this chapter, we applied time–resolved three–body Coulomb explosion imaging (CEI) to study UV–induced photochemical dynamics of gas–phase CH_2I_2 at 290 nm and 330 nm. Beyond the dominant two–body dissociation into CH_2I + I following C–I bond cleavage, we identified weaker channels corresponding to I_2 formation and three–body breakup (CH_2 + I + I), which are consistent with multiphoton excitation under our conditions. Most notably, the analysis of delay–dependent KER–angle patterns and iodine energy–sharing distributions reveals a short–lived population with iso–CH_2I_2–like geometries that forms within ∼100 fs after photoexcitation and decays within the next ∼100 fs. Within experimental uncertainties, the relative yield as well as the formation and decay times of these iso–like configurations are similar at 290 nm and 330 nm, suggesting a weak dependence on the excitation wavelength. At the same time, power–law scalings of gated yields support a single–photon origin for the dissociation–like and iso–like selections, whereas I_2 formation and three–body breakup exhibit two–photon character, providing an internal consistency check on the channel assignments.

It is important to emphasize the scope and limitations of these conclusions. The mapping from nuclear configuration space to fragment momentum space in CEI is not unique[122], and therefore different geometries can, in principle, generate similar momentum–space signatures. Consequently, the present data cannot definitively establish whether the observed process should be labeled "isomerization," nor can CEI alone identify the instantaneous electronic state when the molecule adopts iso–like geometries. With the geometric constraints imposed jointly by the KER–angle distributions, iodine energy sharing, and their delay evolution, we consider iso–CH_2I_2–like geometries to be the most likely explanation for the observed signatures, consistent with earlier work[105]. Since

the strong–field ionization probability depends on both electronic state and geometry and thereby prevents a reliable branching–ratio determination, it appears that the observed iso–CH_2I_2-like population is only a small fraction of the photoexcited ensemble. These considerations help rationalize why complementary ultrafast structural probes with limited signal–to–noise or temporal resolution may not readily resolve such fleeting configurations, as in prior gas–phase UED work[17]. Whether or not the process observed should be termed "isomerization" cannot be decided from the experimental data alone, and also depends on the exact definition of "isomerization" one chooses to use. Given the short time that the molecules spend in the isomer-like geometry, which is less than the timescale of the rotation of the CH_2I fragment that is produced by direct C–I bond cleavage, the process might be better described as a *transient passage through isomer-like geometries* rather than an actual trapping in the potential well of the isomer, and a definitive classification will require careful theoretical modeling.

In summary, the CH_2I_2 UV–pump/NIR–probe CEI measurements reveal an ultrafast passage through iso–CH_2I_2–like geometries whose timing and qualitative features are consistent across 290 nm and 330 nm excitation. While CEI alone cannot unambiguously classify the process as "isomerization," the combined geometric constraints from our observables support the iso–CH_2I_2–like interpretation and delineate clear experimental targets for future theory–experiment comparisons.

Chapter 4

Single-Pulse Coulomb Explosion Imaging of Ring and Chain Structures

In this chapter, we present the results of a static, single-pulse CEI study that differentiates ring, open-chain, and ring-chain molecular structures of several halogenated hydrocarbon molecules consisting of 9 atoms using a tabletop near-infrared (NIR) strong-field probe and coincidence ion momentum imaging.

This chapter adapts and extends material from our article published in Physical Review Letters, titled "Differentiating Three-Dimensional Molecular Structures Using Laser-Induced Coulomb Explosion Imaging"[60].

4.1 Overview and Motivation

Coulomb explosion imaging (CEI) with x-ray free-electron lasers (XFELs) is a powerful method for obtaining detailed structural information on gas-phase planar ring molecules[38]. Compared with diffraction methods, CEI provides excellent temporal resolution and strong sensitivity to light atoms while directly encoding three-dimensional geometry in fragment-momentum correlations[21]. However, the low count rate of multiparticle coincidence measurements has led most time-resolved CEI studies to focus on two- and three-body fragmentation[19;23;25–27;123–126]. As a result, while CEI has been highly successful in imaging small molecules[24;29;107;127–130], only limited structural infor-

mation has been obtained for larger systems. Building on advances in high-repetition-rate sources, multi-hit detectors[79], and new data analysis methods, Boll *et al.* showed that partial coincidence measurements can recover structural information for planar-ring molecules with approximately ten atoms[38].

Here we establish static, molecule-specific three-dimensional momentum fingerprints using tabletop, strong-field CEI for both planar and nonplanar systems. Prior demonstrations of complete structural imaging with tabletop sources were limited to small systems, notably five-atom targets with detection of all fragments in coincidence[37;87]. In this chapter, we present a general approach to using strong-field CEI to probe the three-dimensional molecular structure of photochemical products, creating a baseline for subsequent time-resolved studies. As illustrated in Fig. 4.1, a prototypical ring-opening reaction can produce vibrationally hot ring-closed molecules as well as several ring-opened products. Ring-opened products are typically open-chain and ring-chain structures, with the latter containing a smaller, highly strained ring. For example, upon absorbing a 266 nm photon, the heterocycle thiophenone can form open-chain (ketene) or ring-chain (episulfide) photoproducts or return to the ring-closed geometry[16]. Similar photoproducts are predicted for furan[131;132] and oxazole[133;134]. Distinguishing these products in a time-resolved measurement remains challenging. We perform static CEI measurements on three photoproduct analogues—isoxazole (planar ring), 3-chloro-1-propanol (open chain), and epichlorohydrin (ring-chain) —- to provide well-defined structural benchmarks for later dynamics studies.

4.2 Isoxazole: Closed-ring Planar System

We first examine the closed-ring planar example of isoxazole. The molecule consists of a 5-member ring with three carbon atoms, one nitrogen, and one oxygen atom, with one hydrogen attached to each carbon atom. In the ideal case, a strong-field laser pulse ionizes all atoms so that the subsequent Coulomb explosion encodes the molecular geometry in the fragment momenta. A representative complete breakup of isoxazole is

$$C_3H_3NO \rightarrow C^{(i+)} + C^{(j+)} + C^{(k+)} + H^+ + H^+ + H^+ + N^{(p+)} + O^{(q+)}, \tag{4.1}$$

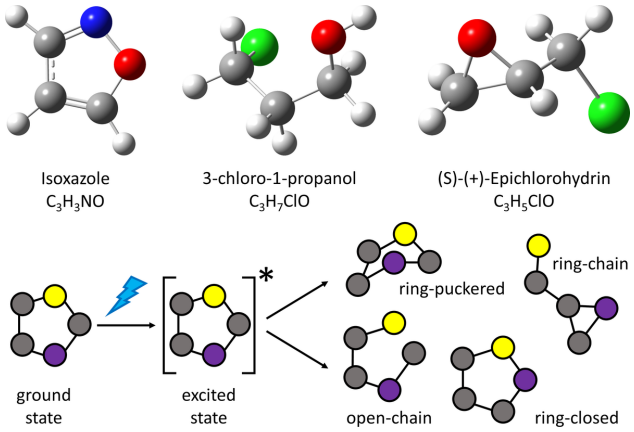

Figure 4.1: **Top row:** ball-and-stick models of the three molecules studied in this work: isoxazole, 3-chloro-1-propanol, and epichlorohydrin. **Bottom row:** schematic of a light-induced ring-opening reaction (modeled after the UV-induced ring opening of oxazole [32,33]). Isoxazole, 3-chloro-1-propanol, and epichlorohydrin mimic the structures of the ring-closed, open-chain, and ring-chain products, respectively.

where the superscripts denote the final charge states of the atomic ions. We show that by detecting only a subset of the atomic ions—specifically a four-fold coincidence channel—the structural fingerprint of the molecule can be inferred. For isoxazole, we select events where both N^+ and O^+ are detected, along with at least one H^+ and one C^+.

Figure 4.2 shows the Newton plots constructed from the four-fold (H^+, C^+, N^+, O^+) coincidence channel. The molecular frame is rotated such that the O^+ momentum defines $+x$ and the N^+ momentum lies in the upper xy plane, and the C^+ and H^+ momenta are plotted in this frame. Although only one C^+ and one H^+ are required per event, distinct localized maxima for the three carbons and the three hydrogens appear in the xy projection, matching the neutral equilibrium geometry. When more than one carbon or hydrogen ion is detected, multiple 4-fold events are created by taking all combinations of (H^+, C^+, N^+, O^+) from the detected ions. For visualization, the C^+ and H^+ counts are multiplied by three because only one of the three carbons (or protons) is plotted per N^+–O^+ pair. The third and fifth columns in Fig. 4.2 show classical Coulomb-explosion simulations using the neutral equilibrium geometry. The neutral geometry (Table 4.1) is optimized at the B3LYP/aug-cc-pVDZ level using Gaussian[135], and the ensemble of initial geometries is generated via thermal Wigner sampling using NewtonX[90;91].

The C^+, N^+, and O^+ time-of-flight (TOF) regions partially overlap. Specifically, C^+ ions flying

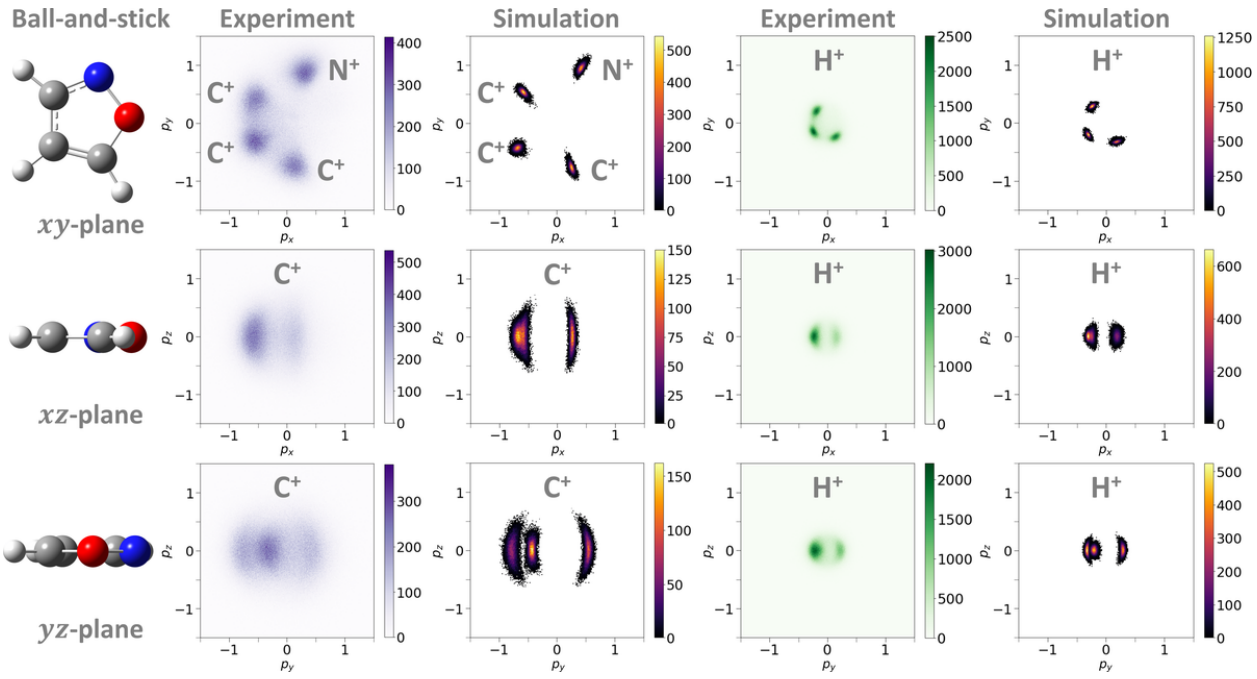

Figure 4.2: Measured and simulated CEI patterns of isoxazole. The first column shows the ball-and-stick model views of isoxazole in three principal planes. The plots in the second and fourth columns are projections of the measured fragment-ion momenta (Newton plots) from the (H^+, C^+, N^+, O^+) 4-fold coincidence channel onto these three principal planes. The first, second, and third rows are the xy plane, xz plane, and yz plane, respectively. For each event, the coordinate frame is rotated such that the O^+ momentum points along the x axis ($p_{O,y} = p_{O,z} = 0$) and the N^+ momentum lies in the upper xy plane ($p_{N,y} \geq 0$; $p_{N,z} = 0$). The momenta of C^+ and H^+ are plotted in this coordinate frame. No background was subtracted. The color bars represent the number of counts per bin on linear scales. All momenta are normalized to the O^+ momentum ($|p_O| = 1$, not shown). Newton plots of H^+ and C^+ show localized spots corresponding to the three carbons and three hydrogens of isoxazole. For laser shots where more than one carbon or hydrogen ion was detected, multiple 4-fold coincidence events were created by making all possible combinations of the detected (H^+, C^+, N^+, O^+) fragments. For data visualization, the C^+ counts are multiplied by three since only one of the three carbon ions is plotted for each nitrogen and oxygen ion that is plotted. The third and fifth columns show the results of classical Coulomb explosion simulations for the neutral molecule in its equilibrium geometry.

away from the detector (longer TOF) overlap with N^+ ions flying toward the detector (shorter TOF), and there is additional overlap between N^+ and O^+ in a similar fashion. Because the channel is kinematically incomplete, strict momentum gating cannot be applied to fully suppress false coincidences and background. Therefore, species selection uses a combination of TOF and position-versus-TOF windows. We apply a "half-moon" cut that keeps only the right halves of the N^+ and O^+ TOF peaks to avoid overlap with carbon and with each other, and we use position–TOF gates to remove diffuse background, as shown in Fig. 4.3.

Table 4.1: Equilibrium geometry of isoxazole optimized at the B3LYP/aug-cc-pVDZ level.

isoxazole				
Index	Atom	x	y	z
1	C	-3.38504	1.85456	0.00000
2	C	-1.99880	1.62072	0.00000
3	C	-1.89721	0.25412	0.00000
4	H	-1.19389	2.33914	0.00000
5	N	-4.08579	0.71797	0.00000
6	H	-3.91694	2.79554	0.00000
7	O	-3.13814	-0.29474	0.00000
8	H	-1.07633	-0.44730	0.00000

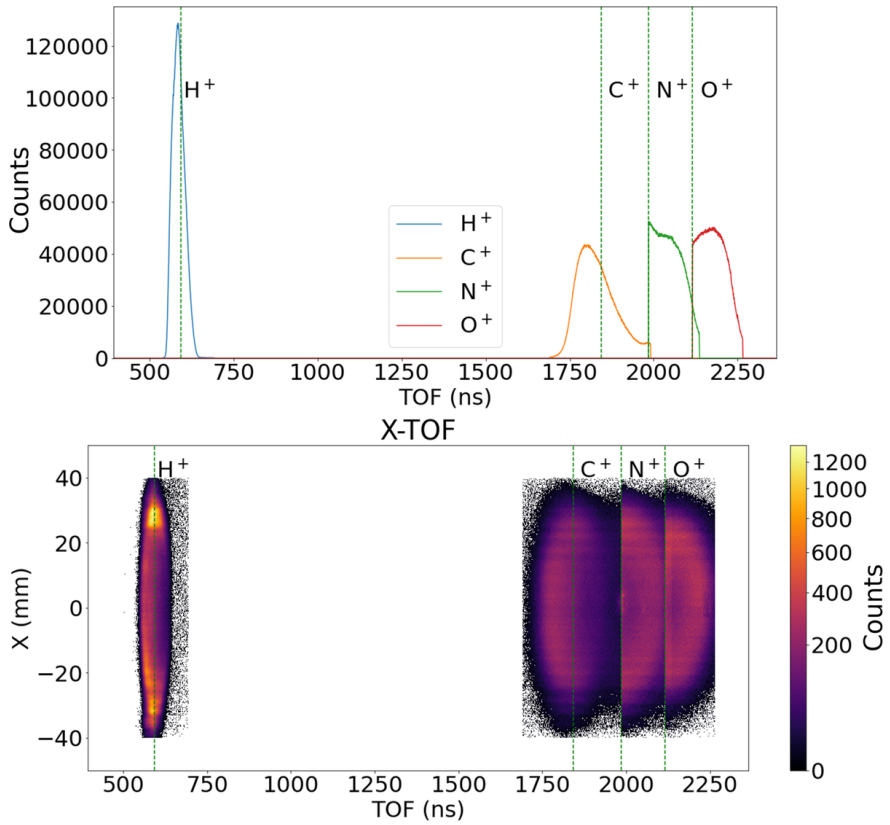

Figure 4.3: Time-of-flight spectra and position-versus-time-of-flight distributions for isoxazole four-fold events. The selection windows for H^+, C^+, N^+, and O^+ are indicated, including the half-moon cuts on the N^+ and O^+ peaks used to avoid overlap with carbon fragments and with each other.

Figure 4.4 shows the two-dimensional TOF-coincidence map for the four-body channel and representative Newton plots with and without the N^+/O^+ half-moon gates. The coincidence map is plotted as the TOF of the first fragment (H^+) versus the sum of the TOFs of the other three fragments. Because only the right halves of the N^+ and O^+ peaks are selected, filtered events

lie predominantly above the black cross due to the larger TOF sum in the vertical-axis. In the lower panels, the momentum image with gating is much cleaner, showing clear structures, whereas limited structural information is visible without gating.

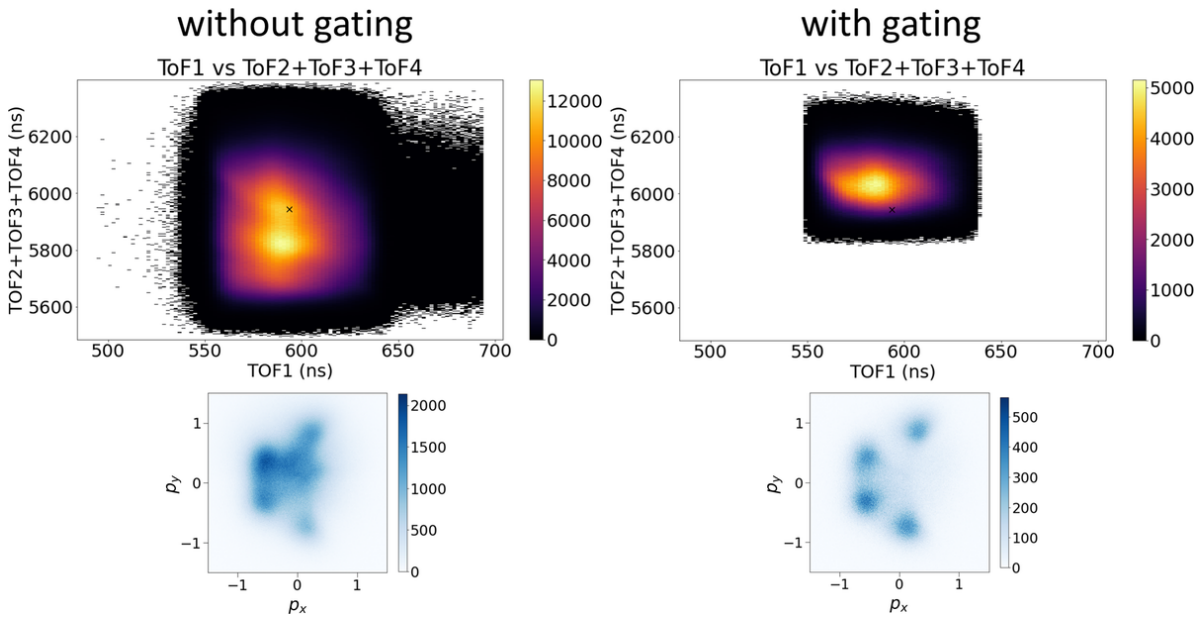

Figure 4.4: Left panels: TOF-coincidence map and Newton plots for isoxazole without half-moon gating on N^+ and O^+. Right panels: the same with half-moon gates applied, demonstrating improved channel purity and clearer momentum features. The color bars correspond to counts per bin on a linear scale.

4.2.1 Correlated Out-of-plane Fragment Motion

For planar molecules, the projection onto the molecular plane (e.g., the xy plane for isoxazole in Fig. 4.2) is often sufficient to visualize the overall layout. However, our experimental and theoretical analysis of the other two planes (xz and yz) reveals a broad out-of-plane component that reflects the distribution of geometries in the initial neutral ensemble mapped by the explosion. The middle carbon, C(2) in Fig. 4.5, exhibits a smaller out-of-plane momentum spread than the other two carbons in the yz projection, as shown in bottom row of Fig. 4.2. This arises from the choice of reference ions used to define the reference frame and from atom-specific correlated motion in the normal modes. Because the frame is defined event-by-event, such effects depend on the chosen reference and are straightforward to examine in simulations.

In panel (a) of Fig. 4.5, the molecular plane is defined by the planar equilibrium geometry, and

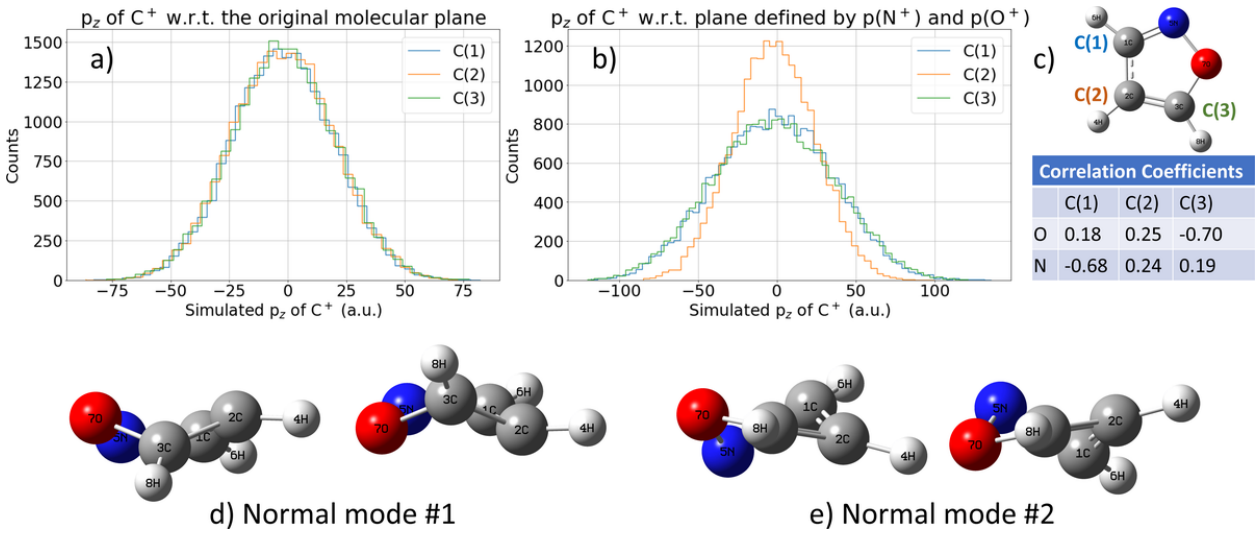

Figure 4.5: Correlation analysis for isoxazole out-of-plane components. Panels (a) and (b) show the out-of-plane momentum distributions for the three carbons in the original molecular frame and in the chosen reference frame defined by O^+ and N^+, respectively. The middle carbon appears narrower in p_z due to correlated motion with the O^+ and N^+ reference ions. Panels (c)–(e) show the correlation coefficients of the carbons with the reference ions and the two normal modes that exhibit strong out-of-plane motion.

each atom is allowed to move in-plane and out-of-plane according to the normal modes. For each geometry in this ensemble of vibrating molecules, we simulate the Coulomb explosion and plot the p_z components of the carbon-ion momenta with respect to the original molecular plane. In this representation, all three carbons exhibit similar out-of-plane spreads.

In panel (b), we repeat the analysis but define the molecular plane event-by-event using the momenta of O^+ and N^+, consistent with the experimental results in Fig. 4.2. In this case, the out-of-plane momentum distribution of the middle carbon C(2) remains narrow, whereas the distributions of C(1) and C(3) are broader relative to panel (a). This reflects that, in relevant normal modes, the motion of C(2) is correlated with the motion of nitrogen and oxygen, so $p_z(\mathrm{C(2)})$ is more likely to lie close to the plane defined by $p(N^+)$ and $p(O^+)$.

To quantify these correlations, we compute the correlation coefficients between $p_z(C^+)$ and $p_z(N^+)$ and between $p_z(C^+)$ and $p_z(O^+)$, shown in panel (c) of Fig. 4.5. C(2) shows small positive correlations, indicating that its p_z tends to vary in the same direction as $p_z(N^+)$ and $p_z(O^+)$. C(1) and C(3) show strong negative correlations with $p_z(N^+)$ or $p_z(O^+)$, indicating that their p_z tends to vary in the opposite direction. Thus, when $p(N^+)$ and $p(O^+)$ are chosen to define the event

frame, the out-of-plane momenta for C(1) and C(3) broaden relative to C(2).

A qualitative inspection of the normal modes shows two modes with strong out-of-plane motion of N and O, as illustrated in panels (d) and (e) of Fig. 4.5. In the first mode, the middle carbon, C(2), moves in the same direction as N and O, which yields similar variations in their p_z components. In the second mode, C(2) moves with N but opposite to O, partially canceling the correlation. This frame-dependent narrowing of C(2) is a direct signature of correlated normal-mode motion and highlights why full three-dimensional analysis and explicit frame definitions matter even for planar systems. These observations indicate that even single-pulse IR data (i.e., without a pump–probe scheme) contain information about correlated motion between atoms in the molecule, consistent with recent x-ray-induced CEI studies on 2-iodopyridine[136].

4.3 Experiment–simulation: Agreement and Discrepancies (Isoxazole)

We now assess how a classical Coulomb–explosion model reproduces the measured momentum fingerprints for isoxazole. Here we restrict ourselves to qualitative features relevant for structure inference, while the detailed explanation of the simulation workflow and parameters are documented in the Methods chapter Sec. 2.6. In brief, the model assumes instantaneous ionization of the neutral molecule to atomic ions, followed by point-charge repulsion, with initial geometries sampled from a thermal Wigner distribution of the ground equilibrium. As in prior CEI studies, we find that the model reproduces *angular* correlations that encode geometry, whereas the absolute momenta and kinetic energies are systematically larger in simulation than in experiment[21;24;107;127].

Table 4.2: Comparison of peak momentum and kinetic energy for the 4-body channel in experiment and simulation shown in Fig. 4.6. Ratios are simulation-to-experiment values.

Ion	**Momentum (a.u.)**			**Kinetic Energy (eV)**		
	Sim.	Exp.	Ratio	Sim.	Exp.	Ratio
H^+	146	108	1.35	79	42	1.88
C^+	317	275	1.15	31	21	1.48
N^+	396	345	1.15	42	29	1.45
O^+	384	329	1.17	34	24	1.42

Figure 4.6 shows the ion momentum and kinetic energy spectra for the four detected species.

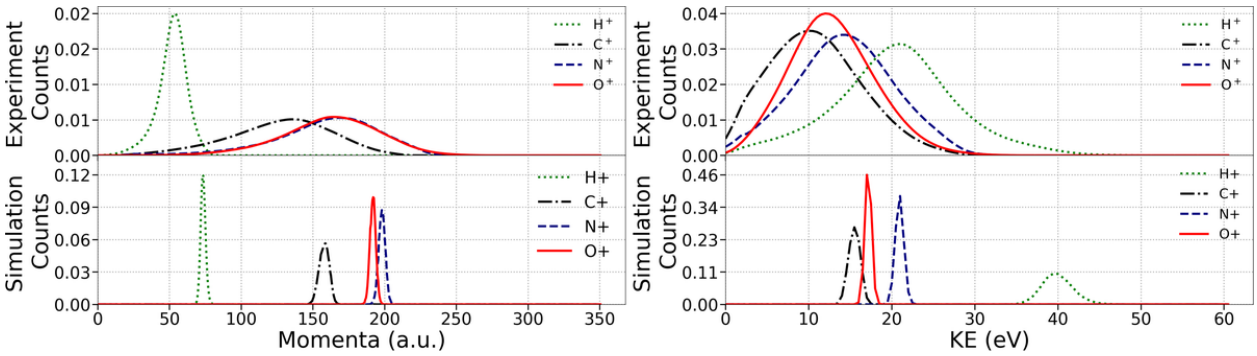

Figure 4.6: Isoxazole momentum and kinetic energy distributions for the four–fold channel (H^+, C^+, N^+, O^+). Top row: experiment. Bottom row: classical CE simulations using the neutral equilibrium geometry and thermal Wigner sampling. Left: atomic ion momentum magnitudes. Right: kinetic energy spectra. The simulations reproduce the relative ordering of the fragment momenta but overestimate absolute values, especially for H^+.

The experimental spectrum exhibits broad, partially overlapping momenta distributions for carbon, nitrogen, and oxygen, while the proton distribution shows a long low-energy tail. The simulation yields higher absolute values for the fragment momenta and larger kinetic energies, most prominently for H^+. This behavior is consistent with earlier studies and is commonly attributed to limitations of the point-charge model with a purely Coulombic potential, including instantaneous charging and the absence of bond-softening or other non-Coulombic forces during the initial phase of the explosion[24;29;128]. The peak values of the distributions for simulation and experiment are tabulated in Table 4.2. The simulated momenta are larger by about 35% for H^+ and by 15% for the heavier ions (C^+, N^+, O^+). Similarly, the simulated kinetic energies are larger than the experimental values by approximately 90% for protons and 45% for the heavier fragments. A complementary channel-to-channel comparison—contrasting the 4-fold with the 5-fold and with the complete 8-fold channels—is presented in Sec. 4.6. Because structural information in CEI is carried most robustly by angle between momenta pairs, we next compare angular correlations.

Figure 4.7 shows proton and carbon angular distributions in the reference frame used throughout this chapter, with $\hat{x}$ along $p(O^+)$ and $p(N^+)$ lies in the upper xy plane. The two-dimensional maps (top and middle rows) reveal well-localized bands in azimuthal angle and $\cos(\theta)$ and show qualitative agreement between experiment and simulation.

One–dimensional azimuthal projections (bottom row) highlight that peak positions and separations are reproduced. While the experimental distributions have well separated peaks, the distribu-

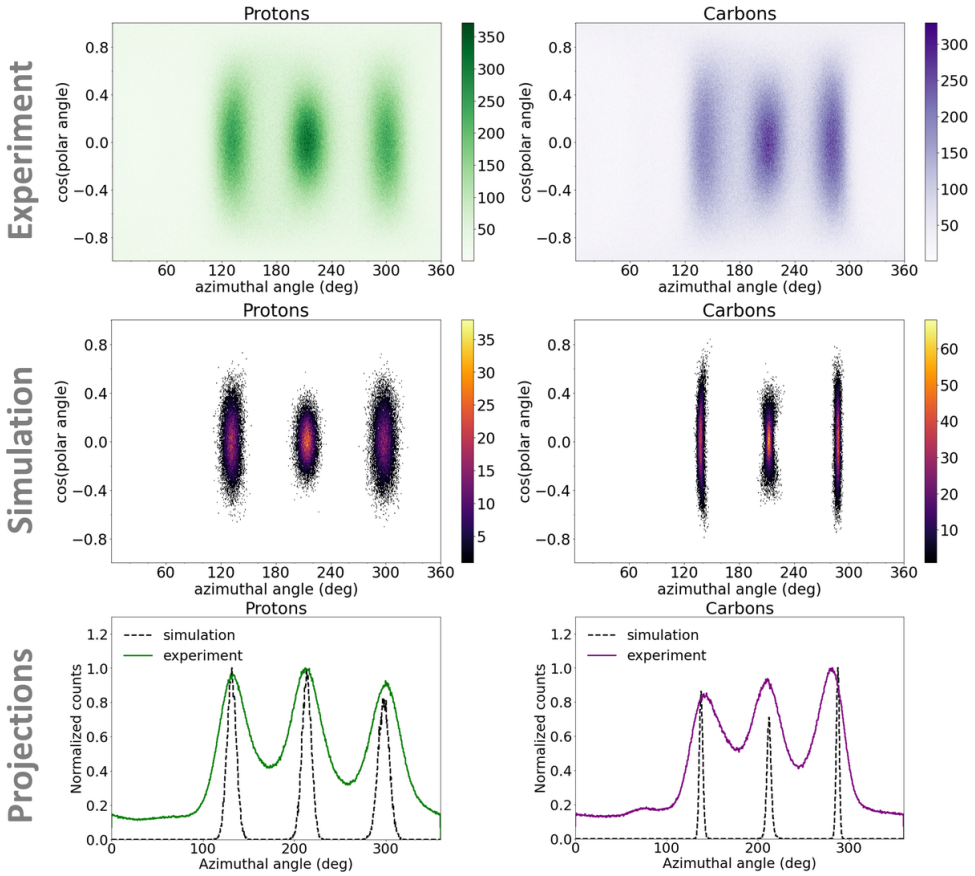

Figure 4.7: Angular correlations for isoxazole in the O^+–N^+ recoil frame. The color bars indicate the counts per bin on a linear color scale. Top: experimental distributions of azimuthal angle and cos(polar angle) for H^+ (left) and C^+ (right). Middle: corresponding classical–simulation maps. Bottom: one–dimensional azimuthal projections comparing experiment (solid) and simulation (dashed). The positions of the angular maxima agree well, establishing that the model correctly encodes the heavy–atom topology even when absolute momenta differ.

tions are broader and overlap significantly. The simulated peaks are narrower, which we attribute to the low initial temperature (low kinetic energies) assumed for the thermal-Wigner ensemble. This underscores another limitation of the model. The agreement in peak angles underpins the use of the classical model as a geometric guide and justifies relying on angular fingerprints for structure discrimination, while treating absolute kinetic energies with some caution. The robustness of angular correlations explains why the four–fold channel already provides a clear ring fingerprint in Fig. 4.2. In the next section, we turn to the nonplanar targets, where the same analysis framework yields distinct two–dimensional fingerprints for the open–chain and ring–chain topologies.

4.4 Nonplanar Molecules: Open-chain and Ring-chain Systems

We now analyze two nonplanar molecular analogues that mimic ring-opened photoproducts: 3-chloro-1-propanol (open-chain) and epichlorohydrin (ring-chain). The TOF and position-TOF spectra for the two molecules are shown in Fig. 4.8. These chlorine-containing molecules provide clean TOF separation of C^+, O^+, and Cl^+ and therefore do not require the half-moon gating used for isoxazole in Fig. 4.3. This simplifies fragment selection for the coincidence channels.

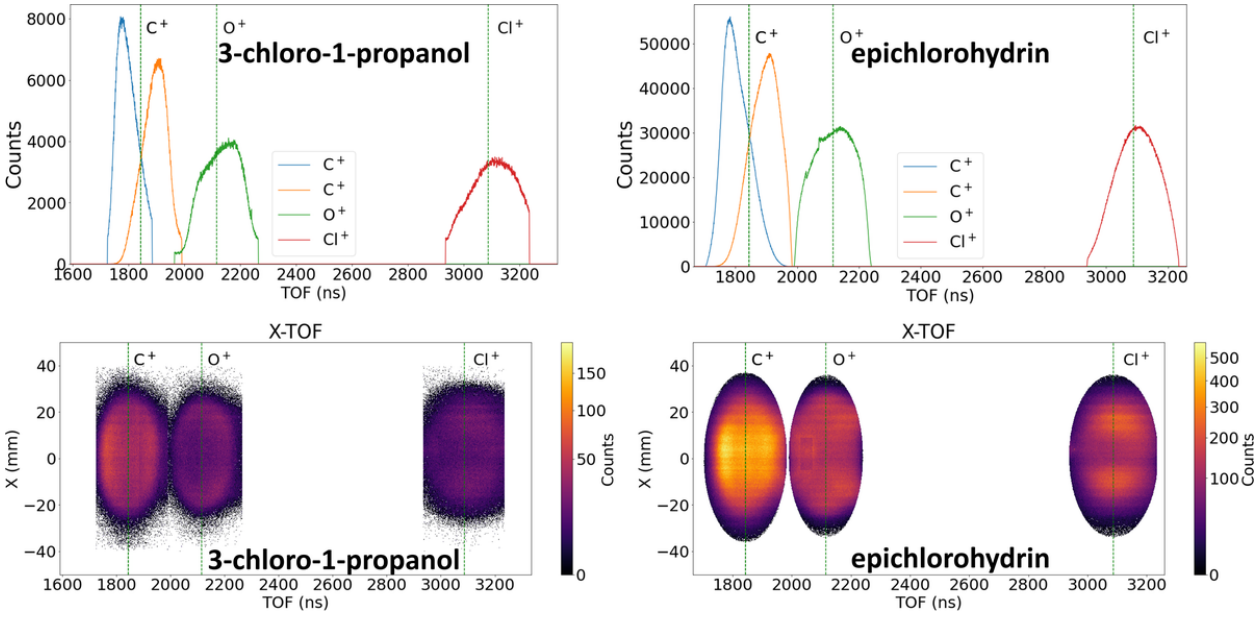

Figure 4.8: Time-of-flight and position–TOF spectra with channel-selection windows for 3-chloro-1-propanol (left panels) and epichlorohydrin (right panels). Fragment ions do not overlap in time-of-flight, so half-moon cuts are not used.

The experimental momentum images in Fig. 4.9 are obtained from the (C^+, C^+, O^+, Cl^+) 4-fold coincidence channel. As in the isoxazole case, we compare experimental projections with classical CE simulations. The optimized neutral geometries are given in table 4.3. The frame of reference for 3-chloro-1-propanol is set by the momentum vectors of Cl^+ and O^+ (x- and xy-reference ions, respectively); the C^+ ions are plotted in this frame. For epichlorohydrin, the momentum of Cl^+ is along the x-axis, and the xy-plane is defined by the first detected C^+ ion since the O^+ momentum is often nearly back-to-back with the Cl^+ momentum. Because the three carbons are not distinguished experimentally, the xy-reference C^+ can be any of the three carbon sites in epichlorohydrin. Therefore, we sum all three simulation patterns obtained by fixing Cl^+ along the

Table 4.3: Equilibrium geometries optimized at the B3LYP/aug-cc-pVDZ level.

(a) Equilibrium geometry of 3-chloro-1-propanol.

3-chloro-1-propanol				
Index	Atom	x	y	z
1	Cl	1.81375	-0.44317	-0.11624
2	O	-2.09120	-0.56939	0.57725
3	C	-0.54867	1.01743	-0.32061
4	C	0.58777	0.69071	0.63709
5	C	-1.46011	-0.15824	-0.64254
6	H	-1.15328	1.80802	0.15313
7	H	-0.14451	1.42965	-1.25576
8	H	-2.21666	0.15805	-1.37985
9	H	-0.87530	-0.98471	-1.07563
10	H	1.15158	1.58739	0.91084
11	H	0.22564	0.18531	1.53653
12	H	-2.56556	-1.39408	0.42512

(b) Equilibrium geometry of epichlorohydrin.

epichlorohydrin				
Index	Atom	x	y	z
1	Cl	1.90603	0.22967	-0.03337
2	O	-2.06694	-0.52063	0.00520
3	C	-0.77103	-0.10592	-0.46384
4	C	-1.66573	0.85322	0.19592
5	C	0.38643	-0.73097	0.26711
6	H	-0.67399	-0.06702	-1.55264
7	H	-1.47679	1.13817	1.23410
8	H	-2.21539	1.57929	-0.40708
9	H	0.58739	-1.74602	-0.09132
10	H	0.21379	-0.74172	1.34755

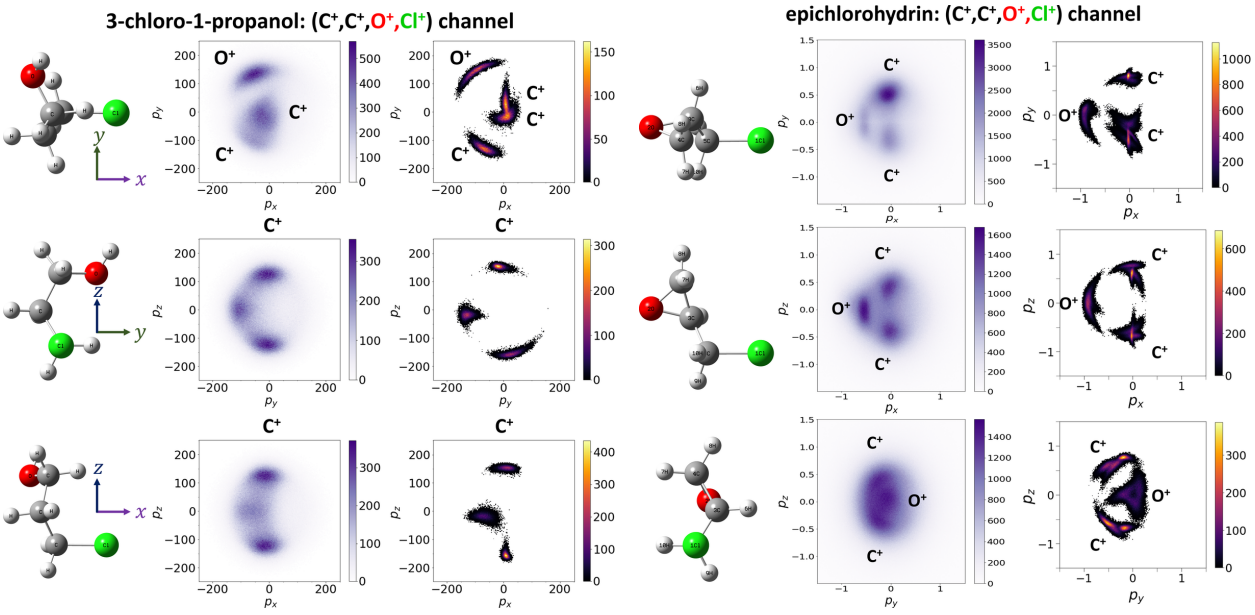

Figure 4.9: Two-dimensional momentum projections and classical-simulation overlays for the non-planar targets: (left) 3-chloro-1-propanol and (right) epichlorohydrin. For 3-chloro-1-propanol, C^+ projections are shown with Cl^+ along x and O^+ defining the xy plane. In the zy projection, one carbon is hidden behind the chlorine. The curvatures in carbon features in the real space are also evident in the momentum space, both in the experiment and simulations. For epichlorohydrin, C^+ projections are plotted in a frame with Cl^+ along x and the first-detected C^+ defining the xy plane. Localized carbon maxima evident in the experimental momentum images (middle column) are reproduced qualitatively by the classical CE simulations (right blocks). The color bars indicate the counts per bin on a linear scale.

x-axis and in turn, choosing each carbon to define the xy plane.

Figure 4.9 shows that even for nonplanar molecules with low symmetry, the ion-momentum distributions remain localized and well separated, providing a clear correspondence between the real-space equilibrium molecular geometry and the momentum-space CEI patterns. In 3-chloro-1-propanol, the distinct backbone curvatures exhibited by the three carbons in the $yz-$ and $xz-$planes in real space are mirrored by the arc-like C^+ features in momentum space. Classical simulations reproduce the angular separations and the overall curvature. Epichlorohydrin exhibits a ring–chain fingerprint that is distinct from both the ring and the open-chain cases. In the chosen frame, well-localized C^+ maxima and a compact O^+ island are observed across the different 2D projections. These localized patterns are reproduced qualitatively in the simulations, and their separations provide a robust discriminator from the open-chain topology, which shows broader arcs and a connecting band. The curvature and band structure of the carbon features provide immediate visual cues to separate open-chain from ring–chain geometries in the two-dimensional projections.

4.4.1 Temperature Broadening and Conformer Specificity in 3-chloro-1-propanol

The experimental momentum distributions for 3-chloro-1-propanol, as in Fig. 4.9, exhibit diffuse stripes connecting the C^+ momenta. This behavior is reproduced in the simulations by increasing the temperature of the initial ensemble by a few hundred meV (3000 K), shown in Fig. 4.10. Raising the effective temperature produces diffuse stripes connecting the C^+ momenta, similar to the experimental patterns. We attribute this as a broadened initial vibrational ensemble of molecular geometries. This observation suggests that these stripes could be attributed to vibrational excitation that happens during the strong-field ionization process (e.g., via Raman excitation), spanning different geometries induced by different vibrational modes.

Open-chain and ring-chain structures have single bonds that are able to rotate, leading to the existence of multiple conformers with low-energy barriers[137–141]. The conformer naming follows Refs.[137–139]. Figure 4.11 shows that individual conformers with similar energies but different geometries generate distinct, conformer-specific momentum patterns. The relative positions of the C^+ arcs and their curvature differ among the conformers.

Overall, a three-dimensional analysis that considers projections on all three principal planes

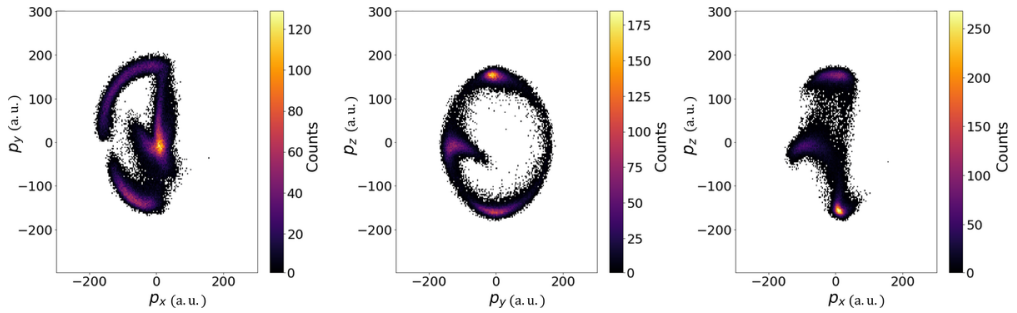

Figure 4.10: Effect of a hotter (3000 K) initial ensemble on 3-chloro-1-propanol Coulomb explosion simulations. Projections shown for the same channel (C^+, C^+, O^+, Cl^+) as in the experiment. Raising the effective vibrational temperature broadens the distributions.

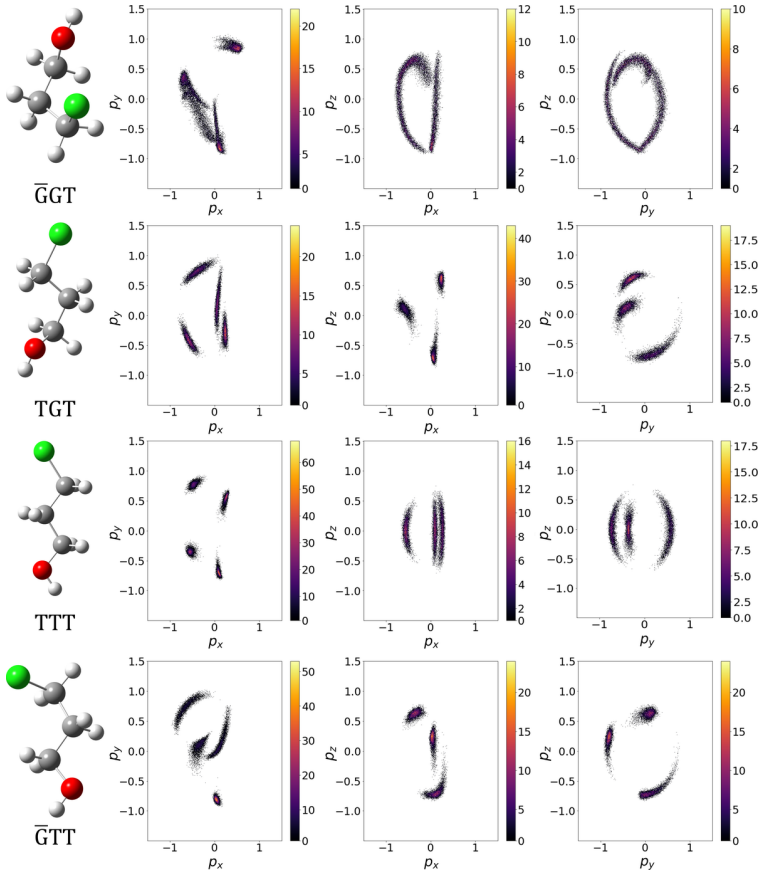

Figure 4.11: 3-chloro-1-propanol conformer sensitivity. Simulated momentum images for several low-energy conformers show distinct patterns when plotted with Cl^+ momentum along the x axis and the momentum of O^+ ion oriented to lie in the xy plane. The color bars indicate the counts per bin on a linear scale.

is essential for nonplanar molecules, where any single projection provides only partial information about the structure. To this end, in the next chapter we place all three systems on equal footing by reconstructing three-dimensional scatter plots.

4.5 Three-dimensional Momentum Representation

We now compare the three targets by plotting their three-dimensional (3D) fragment-momentum distributions in the reference frames defined above. Figure 4.12 presents 3D scatter plots for isoxazole, 3-chloro-1-propanol, and epichlorohydrin in panels (a)–(c), corresponding to the (C^+, C^+, N^+, O^+), (C^+, C^+, O^+, Cl^+), and (C^+, C^+, O^+, Cl^+) 4-fold coincidence channels, respectively. The C^+, N^+, and O^+ ions are shown in purple, blue and red, respectively, to distinguish them from the grayscale projections.

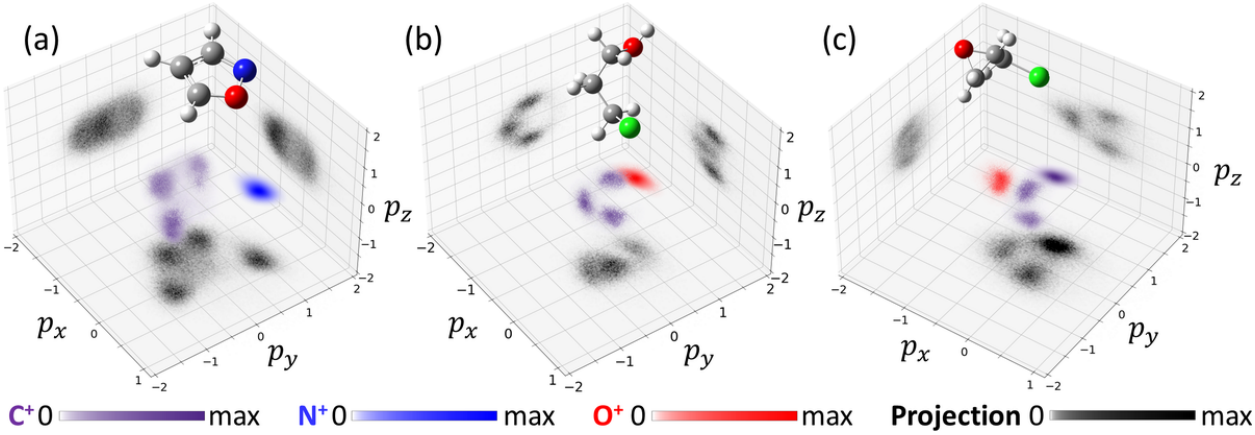

Figure 4.12: 3D scatter plots showing the normalized measured momenta of individual ions from (a) isoxazole, (b) 3-chloro-1-propanol, and (c) epichlorohydrin from the (a) (C^+, C^+, N^+, O^+), (b) (C^+, C^+, O^+, Cl^+), and (c) (C^+, C^+, O^+, Cl^+) 4-fold coincidence channels. C^+, N^+ and O^+ ions in 3D scatter plots are shown in purple, blue and red, respectively, to distinguish them from projections shown in gray scale. The position of each data point is determined by its normalized momentum, while its color corresponds to the density. In (a), the recoil frame is rotated such that the momentum of O^+ (so-called x-reference ion) is set as the unit vector along the x axis, and the momentum of N^+ (referred to as xy-reference ion) is in the upper xy plane. The momenta of other ions are plotted in this coordinate frame. The x- and xy-reference ions are Cl^+ and O^+ in (b), and Cl^+ and the first-detected C^+ in (c). The x-reference ion is not plotted in any panel. We also do not plot the xy-reference ion in the p_z–p_x and p_z–p_y projections since they are simply intense lines along $p_z = 0$.

Each species exhibits a distinct 3D momentum fingerprint. Together with the three principal-plane projections, the 3D scatter plot resolves ambiguities by displaying features that overlap in one projection but separate cleanly in another, and it makes the out-of-plane structure apparent. In Fig. 4.12, panel (a) appears as a thin, near-planar cluster, panel (b) shows curved carbon bands, and panel (c) forms a compact structure with a distinct carbon and oxygen lobes. These qualitative differences are visible at a glance in three dimensions and are consistent with the detailed

two-dimensional analyses given in the preceding sections. This result is noteworthy because the open-chain and ring-chain targets are less rigid than planar ring molecules.

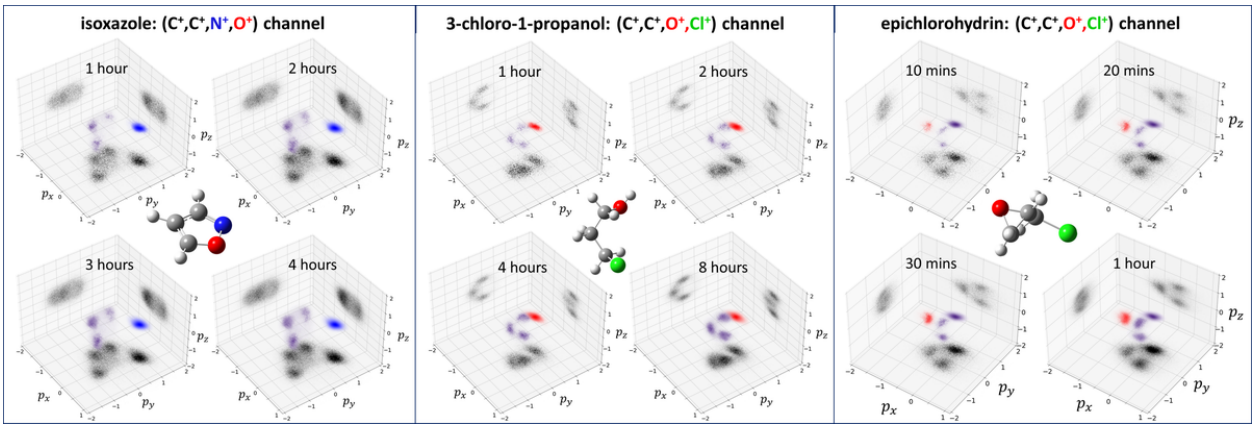

Figure 4.13: Acquisition-time build-up of the 3D momentum signatures for the same channels as in Fig. 4.12. Panels show representative reconstructions after progressively longer integrations for each molecule. Characteristic features emerge rapidly and then sharpen with statistics, indicating that the structural discrimination relies on angular localization rather than on high-count kinetic-energy detail.

To document practicality and quantify data requirements, we examine how these patterns build with acquisition time at a 3 kHz repetition rate. Figure 4.13 provides representative event rates and data accumulation for the three targets. Characteristic 3D features emerge rapidly and then sharpen with statistics within one to a few hours. With a 3 kHz laser, clear 3D structures can be obtained within tens of minutes for epichlorohydrin (ion count rate ∼6.5 kHz), on the order of an hour for isoxazole (∼5 kHz), and within a few hours for 3-chloro-1-propanol (∼1.9 kHz), the latter limited by the sample's lower vapor pressure. Commercially available intense femtosecond lasers with higher repetition rates (e.g, 100 kHz) can significantly reduce the required acquisition time, opening the possibility of obtaining these structures as a function of pump-probe delay on practical timescales.

4.6 Higher Coincidence and Complete Coincidence Channels

We now examine how channel completeness affects the inferred structure for isoxazole by comparing a kinematically incomplete coincidence (4-fold) with higher-coincidence channels (5-fold and the complete 8-fold channel). The goals are twofold: first, to test whether incomplete channels re-

cover the same structural information and second, to highlight qualitative advantages of complete detection that motivate the next chapter.

4.6.1 Four-body vs Five-body Coincidence in Isoxazole

Figure 4.14 contrasts Newton plots and TOF-coincidence maps for the $(C^+, C^+, C^+, N^+, O^+)$ 5-fold channel (top) and the (C^+, C^+, N^+, O^+) 4-fold channel (bottom). While the TOF coincidence maps (right column) show a sharper feature in the 5-fold channel and an order of magnitude fewer in statistics than the 4-fold channel, the Newton plots for both channels are similar: the nitrogen and three carbon hotspots appear in the $p_x p_y$ projection in the reference frame fixed by O^+ and N^+ momenta. These observations indicate that the additional C^+ detected in the 5-fold events does not alter the geometry and that the 4-fold channel has sufficient information encoded to infer the molecular structure.

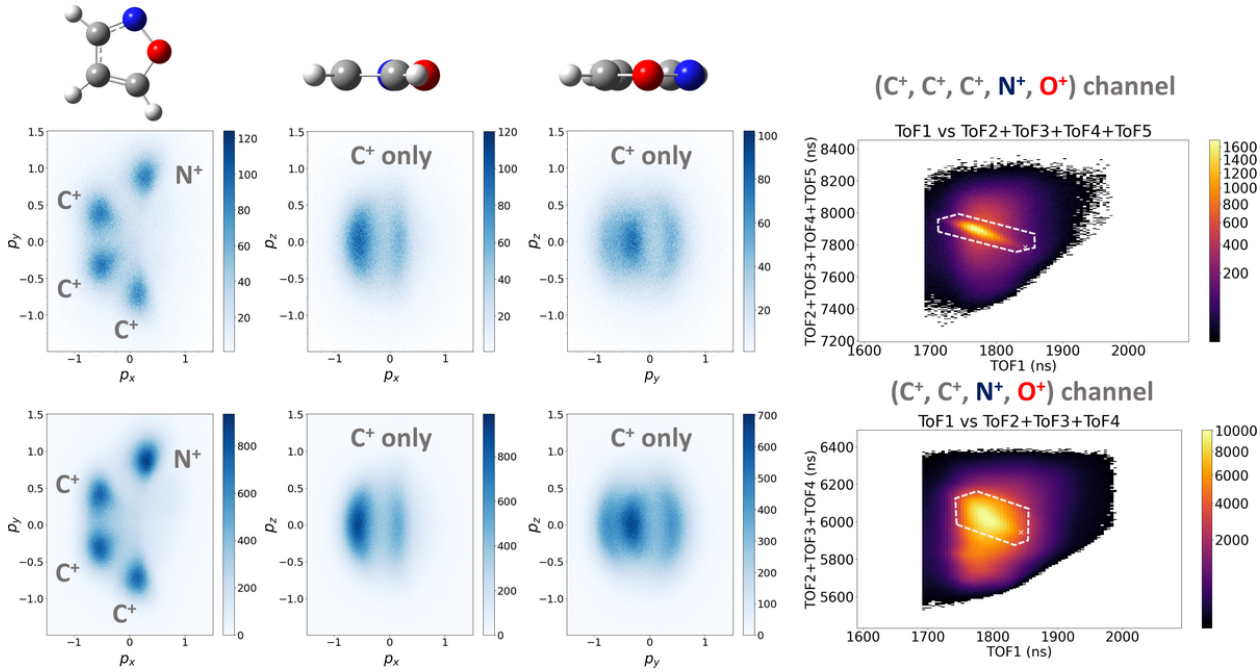

Figure 4.14: Isoxazole channel comparison. Top row: $(C^+, C^+, C^+, N^+, O^+)$ 5-fold channel. Bottom row: (C^+, C^+, N^+, O^+) 4-fold channel. Newton plots show similar spatial fingerprints, indicating a common underlying final state. The color bars correspond to counts per bin on a linear scale. Right columns: Ion TOF coincidence maps for the 5-fold and 4-fold channels with the selected region in white. The color bars show the counts per bin on power-norm scale.

A comparison of kinetic energy spectra and azimuthal-angle distributions is given in Fig. 4.15.

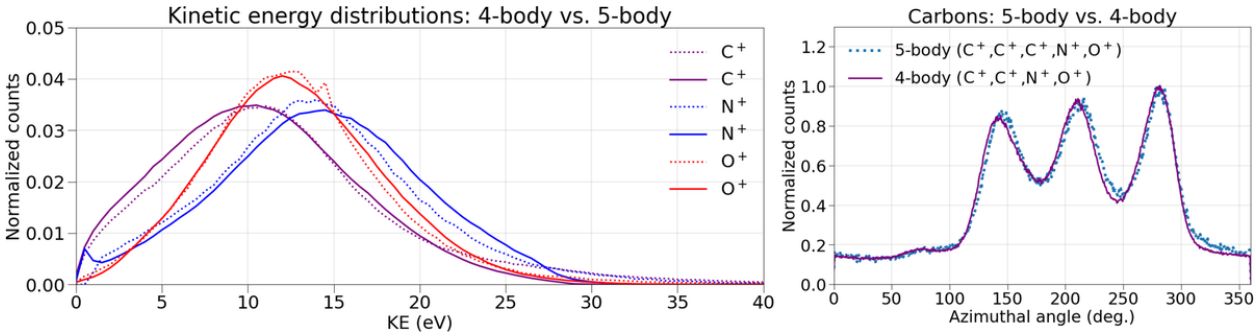

Figure 4.15: Comparison between the kinetic energy (left) and azimuthal angle (right) distributions obtained from the 4-fold (C^+, C^+, N^+, O^+) (solid) and the 5-fold $(C^+, C^+, C^+, N^+, O^+)$ (dotted) coincidence channels. The kinetic energy distribution of each fragment is normalized by its area under the curve. The distribution of azimuthal angle is normalized to its maximum value.

For all the ions the kinetic energy distributions from the 4-fold and 5-fold channels coincide after normalized by individual area under the curves. Likewise, the carbon azimuthal distributions show the same peak positions and separations. These similarities support that the 4-fold and 5-fold events originate from the same final state, with 4-fold events occurring when one carbon ion is not detected for those events. This reinforces using kinematically incomplete coincidence for structural fingerprinting, while also showcasing the benefits of complete detection discussed below.

4.6.2 Complete Coincidence

We next compare the (H^+, C^+, N^+, O^+) 4-fold channel with the complete 8-fold channel in which all atomic ions are detected in coincidence. For this comparison we adopt a different molecular reference frame that uses the sum and differences of the fragment momenta: the x axis is chosen along vector difference of the $p(O^+)$ and $p(N^+)$ momenta and the xy plane is defined by their sum.

Figure 4.16 shows the resulting Newton plots and the corresponding azimuthal-angle histograms. In the complete channel, fragment lobes are distinct and clearly separated from background. In contrast, in the 4-fold channel the eight atomic features can be identified but exhibit greater overlap and background contamination. This is emphasized greatly in azimuthal angle distributions, panel (c) in Fig. 4.16, where the C^+ peaks are very well separated for the complete channel but exhibit significant overlap in the 4-fold channel. Panel (d) compares the kinetic–energy spectra for the 4-fold and complete 8-fold channels. Peak positions and overall shapes are essentially identical for all species; the 8-fold curves are slightly narrower with reduced wings, consistent

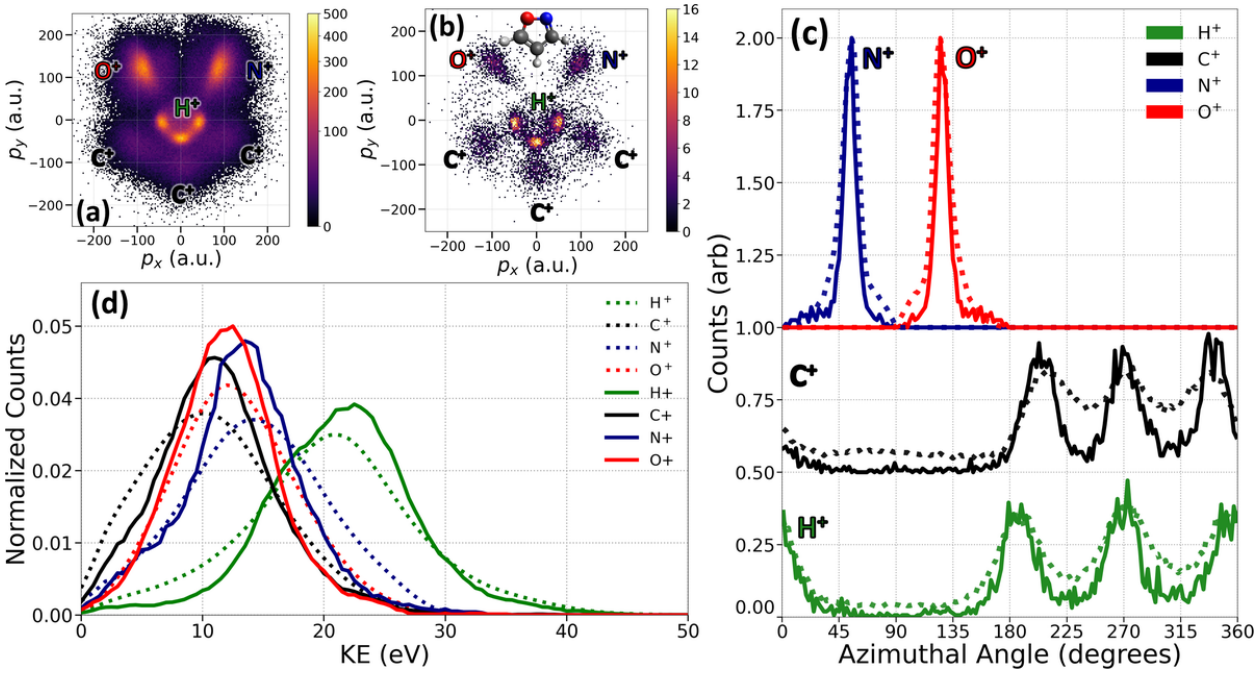

Figure 4.16: Comparison of isoxazole four-ion and eight-ion channels. Newton plot for the 4-fold (H^+, C^+, N^+, O^+) channel in panel (a) and for the complete 8-fold channel in panel (b), plotted in the reference frame defined by the difference and sum of O^+–N^+ momentum vectors. The color scales represent the number of counts per bin in linear scale. (c) Azimuthal-angle distributions for H^+, C^+, N^+, and O^+ comparing the 4-fold (dashed) and 8-fold (solid) channels; the complete channel yields narrower, better-separated peaks (notably for C^+). (d) Kinetic-energy spectra for the same species and channels (4-fold: dotted; 8-fold: solid), each curve normalized with the area under the curve. Together, the complete channel sharpens correlations and reduces ambiguities relative to the kinematically incomplete 4-fold case.

with the removal of background/false-coincidence contributions in the complete channel. Together with the angular agreement in panel (c), this supports the interpretation that the 4-, 5-, and 8-fold channels originate from dissociation of the same eight-fold charge state, with events from the lower-coincidence incomplete channels occur, when one or more fragments are not detected.

4.7 Conclusion

Single-pulse CEI with tabletop lasers yields distinct, localized three-dimensional momentum fingerprints for planar and nonplanar molecules, even when only a subset of fragments is detected in coincidence. A simple classical model captures the angular correlations that encode geometry while overestimating kinetic energies, and the combination of careful gating with supplementary

diagnostics preserves channel purity. These results establish practical, laboratory-scale structure discrimination for ring-closed, open-chain, and ring-chain molecules and provide a platform for extended analyses that benefit from complete channels and advanced analysis methods.

The 4-fold and 5-fold isoxazole channels yield consistent angular fingerprints, indicating a common final state. Complete 8-fold coincidence detection offers several practical advantages in addition to the visual appeal. First, momentum conservation can be enforced event-by-event, strongly suppressing false coincidences and background contamination. Second, the ambiguity among identical fragments can be removed, enabling unambiguous multi-ion correlations and cleaner training for data-driven analysis. These considerations motivate the use of complete channels in the next chapter, where we employ machine-learning methods that exploit higher-dimensional correlations for fast and robust structural discrimination.

Chapter 5

Structure Identification of Dichloroethylene Isomers from Multi-Coincidence Coulomb Explosion Imaging Using Machine Learning

We report complete six-body Coulomb explosion imaging (CEI) of 1,2-dichloroethylene (1,2-DCE) in the gas-phase using a strong-field ionization probe and a velocity-map imaging spectrometer. We demonstrate that the complete 6-fold coincidence channel provides background-free, event-level structural fingerprints that allow automatic differentiation of *cis* and *trans* isomers using machine learning (ML). We acquire full three-dimensional momenta for the (H^+, H^+, C^+, C^+, Cl^+, Cl^+) coincidence channel and analyze the resulting high-dimensional momentum patterns using readily available machine-learning tools for dimensionality reduction and density-based clustering. We use a random-forest classifier to show the most informative observables for identifying the signatures of different molecular configurations. Extending the analysis to simulated geometries of *cis*- and *trans*-1,2-DCE, and further including *twisted*-1,2-DCE and 1,1-DCE, we show that a supervised model trained on simulations transfers well to experimental data.

This chapter is from our Nature Communications article "Exploiting correlations in multi-coincidence

Coulomb explosion patterns for differentiating molecular structures using machine learning"[142]

5.1 Motivation and Overview

CEI is a powerful technique for tracking time-dependent molecular motions when coupled with ultrafast light sources[21;22]. When the probe radiation can break all the bonds and fully dissociate the molecule into atomic ions, all resulting ions are detected in coincidence. In such cases, for every single shot, CEI yields information potentially sufficient to determine the absolute structures of polyatomic molecules, including enantiomers[36;37], and provides molecular frame information. In the previous chapter, we have demonstrated that CEI can image detailed 3D structures of gas-phase molecules by leveraging coincidences from a subset of ions. However, this method faces challenges when signals of interest are weak or contaminated by background noise. While complete coincidence enforces strict momentum conservation to suppress false coincidences and background contamination, detecting all ionic fragments resulting from the complete breakup of the molecule in coincidence is experimentally challenging.

Another current limitation of CEI applications for polyatomic molecules stems from the inherent complexity and multidimensionality of the data. Coincident CEI—whether performed in complete or incomplete mode—relies on analyzing the 3D momentum vectors of all detected ions. As the number of detected fragments increases, especially when pump-probe time delays are included[39;109;143], the parameter space grows rapidly. Observables defined and visualized by conventional human-driven analysis typically sample only a narrow portion of this space, leaving much of the correlated structural and dynamical information unexplored.

Building on the previous chapter's demonstration of complete-coincidence CEI, Section 4.6, we now focus on intermediate-sized molecules and address the challenges in analysis, posed by the resulting higher-dimensional data. We present a new analysis framework based on machine learning (ML) to help interpret the high-dimensional data from multi-coincidence CEI. We demonstrate that ML algorithms can efficiently recognize and exploit momentum-space patterns and correlations corresponding to distinct molecular geometries. Furthermore, we introduce a quantitative approach to determine which features in the high-dimensional CEI data are the most critical for differentiating

similar structures. As molecular size increases, momentum correlations grow combinatorially more complex, making ML particularly well suited for handling such datasets. By leveraging the readily available ML toolbox, we establish an automated and scalable analysis framework to differentiate isomer structures using multi-coincidence CEI. Although isomers share the same molecular formula, their structural differences lead to distinct physical and chemical properties that affect their behavior. For example, in pharmacology, small structural changes can result in dramatically different biological effects, as exemplified by the enantiomers of thalidomide, where one form is therapeutic and the other harmful[144]. Differentiating isomers is a critical subject of investigation across multiple fields, including chemistry, pharmacology, biochemistry, and materials science[42;144–146]. CEI has previously been used to image chiral[36;37;147–149], geometric isomers[33;35;59;150;151], and conformer[34] configurations of molecules.

In this chapter, we investigate the isomers of dichloroethylene (DCE). First, we present CEI of 1,2-DCE, where the molecule fully dissociates into six atomic ions, and the full 3D momenta of all fragments are detected in coincidence. Second, using unsupervised learning, we demonstrate that coincident CEI data can be automatically separated into distinct clusters corresponding to different isomers on an event-by-event basis. Third, we employ supervised learning to determine which projections in high-dimensional CEI data are most important for distinguishing isomeric structures and similar configurations that can arise during photochemical reactions. The methods developed here pave the way for time-resolved investigations of larger molecular systems with all-atom imaging and automated data interpretation.

5.2 Complete Six-Ion CEI of *cis*- and *trans*-1,2-DCE

For *cis*- and *trans*-1,2-DCE irradiated by a strong near-infrared laser field, the detector-plane ion images and ion yield as a function of time-of-flight and vertical position on the detector (Y-TOF maps) are shown in Fig. 5.1. The spectra exhibit prominent fragment signals from H^+, C^+, and Cl^+, with vertical dashed lines drawn to indicate these ion species, along with other major fragments produced by the ultrafast laser pulses. Multiple chlorine isotopologues ($^{35}Cl/^{37}Cl$) contribute to nearby features in the TOF axis. Exemplary "complete" CEI channels of *cis*-1,2-DCE spanning

total final-state charges from 6 to 14 are illustrated by time-of-flight coincidence maps in Fig. 5.2. Sharp lines indicate the different kinematically-complete, momentum-conserved specific fragmentation channels, and the multiple tracks within each panel arise from different chlorine isotopes. Taken together, these coincidence selections highlight the range of accessible high–charge-state channels and the improved background suppression achieved by enforcing momentum conservation.

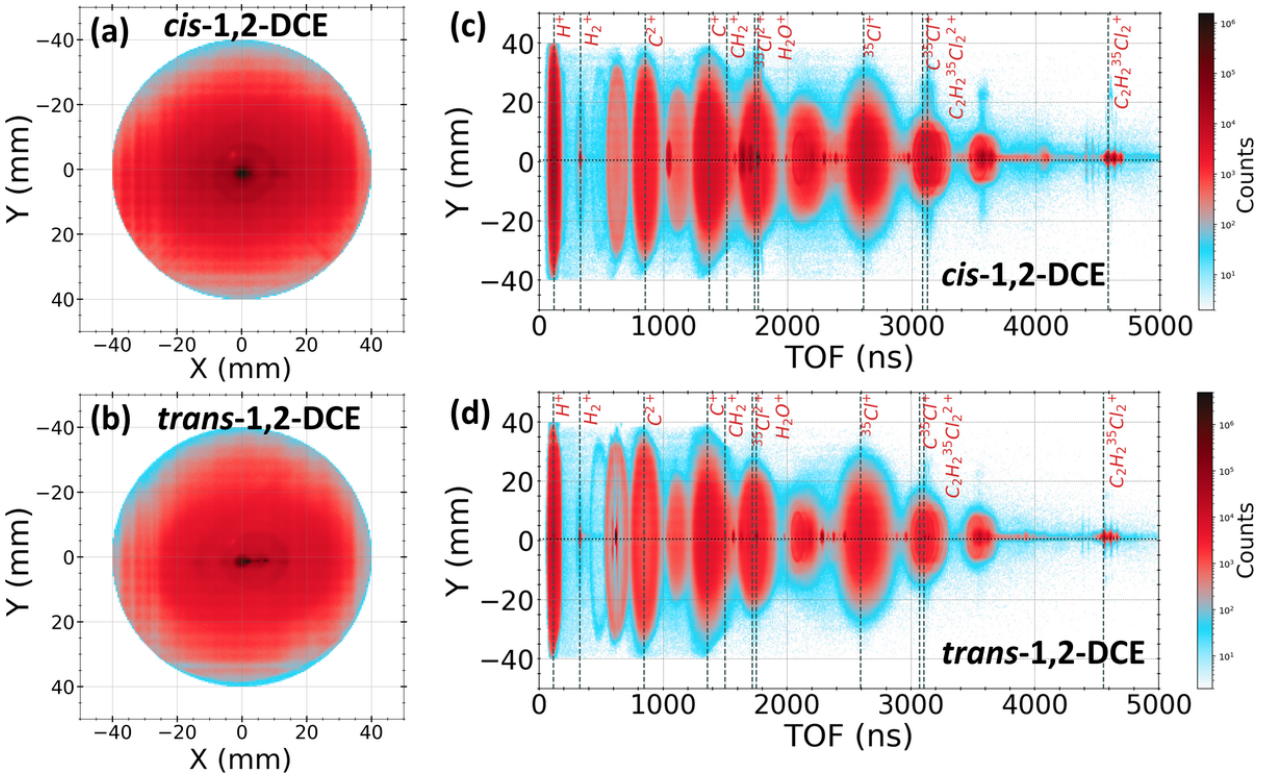

Figure 5.1: Comparison of experimental ion imaging data for *cis*- and *trans*-1,2-dichloroethylene (1,2-DCE). Panels (a) and (b) show the detector-plane XY ion images integrated over all time-of-flight (TOF) values for the *cis*- and *trans*-1,2-DCE isomers, respectively. Panels (c) and (d) display the corresponding Y-TOF maps, i.e., ion yield as a function of TOF and vertical position on the detector, for *cis*- (c) and *trans*-1,2-DCE (d). Vertical dashed lines mark the major fragment ion species, and color represents intensity on a logarithmic scale.

In the remainder of this section, we focus on the all-singly-charged six-body channel (H^+, H^+, C^+, C^+, Cl^+, Cl^+) used for our machine-learning analysis throughout. We next examine Newton maps and corresponding angular observables for this channel before turning to the ML-based dimensionality-reduction and classification results.

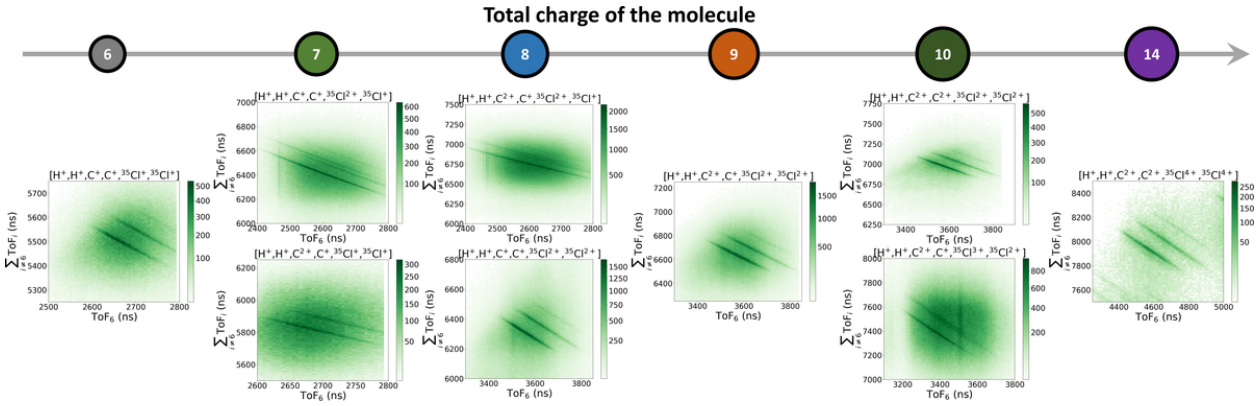

Figure 5.2: Time-of-flight coincidence maps of exemplary "complete" CEI channels. The numbers on the top indicate the total charge of the final state. The color bars report the bin counts using a power-norm color scale. Multiple lines in each panel correspond to channels with different isotopes of Cl ions.

5.2.1 Newton Maps and Classical CE Simulations

Figures 5.3 and 5.4 show Newton plots for the complete ($H^+, H^+, C^+, C^+, Cl^+, Cl^+$) channel for *cis* and *trans* isomers, respectively, together with classical CE simulations. For the *cis*-DCE, the reference frame is defined by the momenta of the two Cl^+ ions: vector difference between the two Cl^+ momenta unit vectors points along the p_x axis and the bisector between them lies in the upper p_xp_y plane. The C^+ and H^+ ions plotted in this frame. In this *trans*-DCE case, the momentum vectors of the two Cl^+ ions are nearly back-to-back, making their vector sum and consequently the p_xp_y plane less well-defined, leading to an obscured ion momentum image as shown in Fig. 5.5. To mitigate this, we define the p_xp_y plane for *trans*-DCE using the vector difference between the momenta of the two C^+ ions. The resulting momentum image reveals distinct, well-separated features corresponding to each atomic fragment. This is a clear example demonstrating that one frame of reference is not necessarily suitable for all different molecular structures. One needs to combine different representations to elucidate different reaction dynamics.

The maxima in the momentum distributions of the chlorine, carbon, and hydrogen ions are well-localized, encoding the structure information of the underlying molecular geometry. Figures 5.3(b) and 5.4(b) present the results of classical Coulomb explosion simulations, assuming point charges, purely Coulombic potential, and instantaneous ionization[43;60]. The simulations begin with the neutral molecule in its equilibrium geometry. The equilibrium geometries used in the simulation

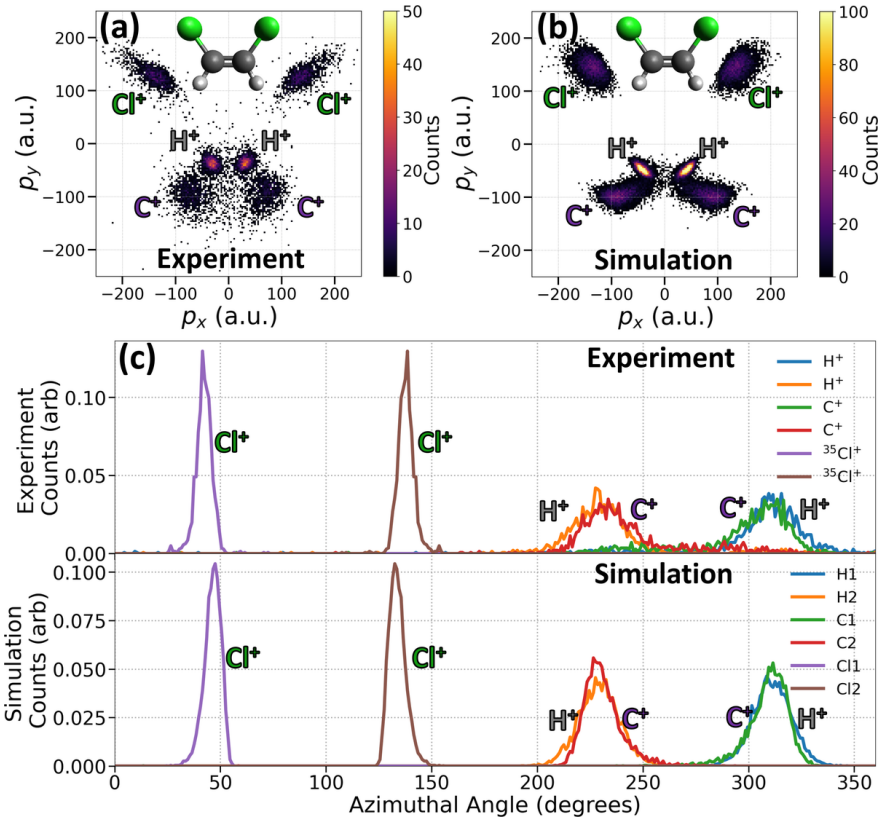

Figure 5.3: (a) Measured and (b) simulated CEI patterns (Newton plots) of *cis*-DCE from the $(H^+, H^+, C^+, C^+, {}^{35}Cl^+, {}^{35}Cl^+)$ 6-fold coincidence channel. The insets show ball-and-stick model views in the molecular plane. For each event plotted here, the coordinate frame is rotated such that the vector difference between the two Cl^+ momenta unit vectors points along the p_x axis and the bisector between them lies in the upper p_xp_y plane. The momenta of C^+ and H^+ are plotted in this coordinate frame. Panel (c) shows the experimental (top) and simulated (bottom) distributions of azimuthal angle for each ion (integrated over momentum magnitude). The azimuthal angle is measured counter-clockwise from the p_x axis.

Table 5.1: Equilibrium geometry of *cis*-1,2-DCE optimized at the B3LYP/aug-cc-pVDZ level.

cis-1,2-DCE				
	Atom	x (Å)	y (Å)	z (Å)
1	C	0.66699	0.96658	0.00000
2	C	-0.66700	0.96658	0.00000
3	H	1.22333	1.90229	0.00000
4	H	-1.22333	1.90229	0.00000
5	Cl	1.66770	-0.45304	0.00000
6	Cl	-1.66770	-0.45305	0.00000

are optimized at the B3LYP/aug-cc-pVDZ level and are given in Tables. 5.1 and 5.2, for *cis*- and *trans*-1,2-DCE respectively. The ensembles of initial geometries are generated with Gaussian-distributed spatial displacements and total kinetic energy (randomly partitioned among the atoms)

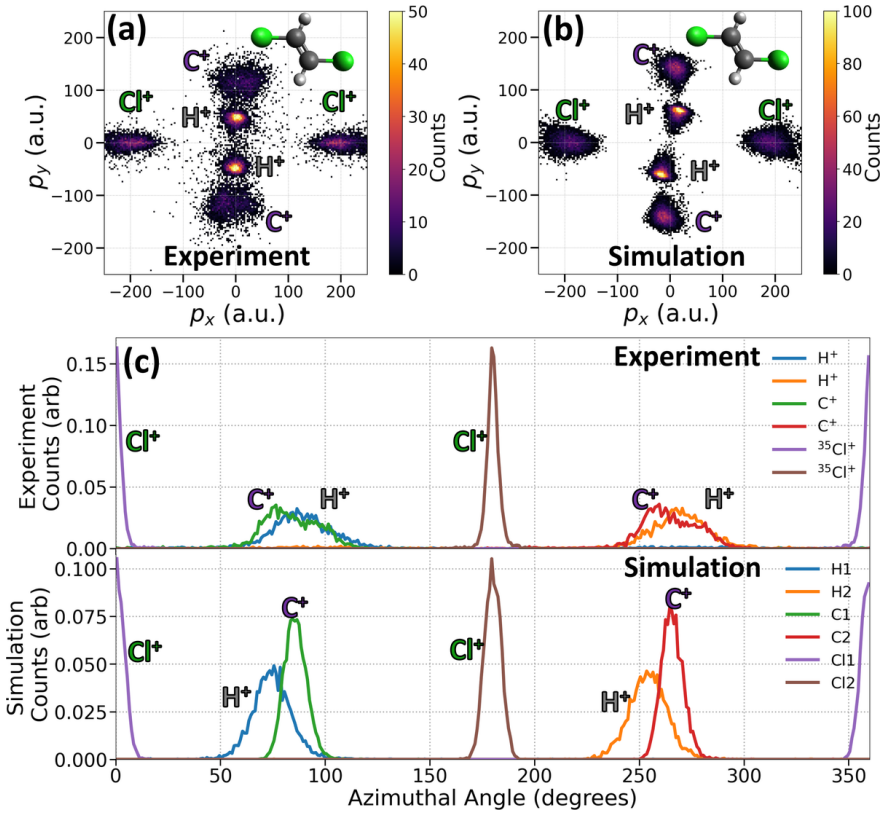

Figure 5.4: (a) Measured and (b) simulated Newton plots of *trans*-DCE from the $(H^+, H^+, C^+, C^+, {}^{35}Cl^+, {}^{35}Cl^+)$ 6-fold coincidence channel. In this case, the coordinate frame for each event is aligned such that the difference vector between the two Cl^+ momenta is parallel to the p_x axis. The $p_x p_y$ plane is established using the vector difference of the two C^+ momenta. The experimental (top) and simulated (bottom) azimuthal angular distributions for each ion (integrated over momentum magnitude) are given in panel (c).

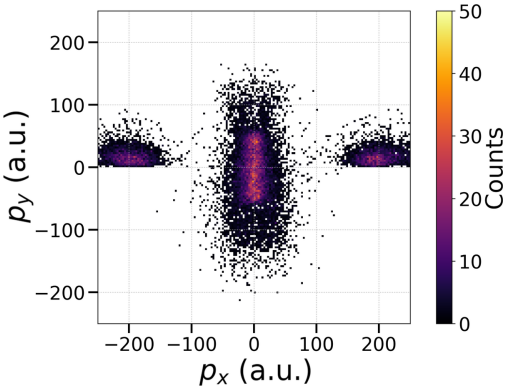

Figure 5.5: CEI patterns for *trans*-1,2-DCE in the coordinate frame defined by the vector difference of the two Cl^+ ions along the x-axis, while the xy-plane is established by their vector sum. Due to their back-to-back emission, the momentum sum of the two Cl^+ ions is near zero, leading to an inherently less well-defined xy-reference plane.

Table 5.2: Equilibrium geometry of *trans*-1,2-DCE optimized at the B3LYP/aug-cc-pVDZ level.

trans-1,2-DCE				
	Atom	x (Å)	y (Å)	z (Å)
1	C	-0.36871	0.55424	0.00000
2	C	0.36871	-0.55424	0.00000
3	H	-1.45653	0.56855	0.00000
4	H	1.45653	-0.56855	0.00000
5	Cl	0.36871	2.13823	0.00000
6	Cl	-0.36871	-2.13823	0.00000

introduced to account for the initial distribution and broadening effects due to atomic motion during the ionization process. The spatial deviation of 0.25 Å and a total kinetic energy of 500 meV are used to match the width of the experimental distributions. The simulation successfully reproduces key features of the experimental momentum distributions, capturing the separation and localization of the fragment ions with good accuracy. This agreement suggests that the measured momentum distributions faithfully reflect the molecular structure near the equilibrium of the neutral molecule.

To provide a more quantitative comparison between experiment and simulation, Figures 5.3(c) and 5.4(c) show the azimuthal angle distributions for each ion, obtained by integrating over the radial momentum coordinate. The experimental (top) and simulated (bottom) distributions exhibit excellent overall agreement, indicating that this simple Coulomb explosion model effectively captures the correlated angular relationships between fragment ions.

5.2.2 Initial Conditions and Channel Completeness

Two simulation initializations—Wigner sampling and Gaussian randomization—are benchmarked against the experimental Newton maps and azimuthal-angle distributions for the all-singly-charged six-body channel in Fig. 5.6. Both approaches reproduce the principal angular structures, while the Gaussian-randomized ensemble yields broader distributions that better reflect experimental observations and provide a closer approximation to the experimental distributions for the ML analysis framework.

Absolute momentum distributions for *cis* and *trans* further highlight the model bias: the simulation systematically overestimates fragment magnitudes across H^+, C^+, and Cl^+ (Fig. 5.7), even as angle correlations are well captured. This is consistent with our observations in earlier chapter.

As in the previous chapter, we emphasize angular observables for structural assignment and use absolute momenta only qualitatively.

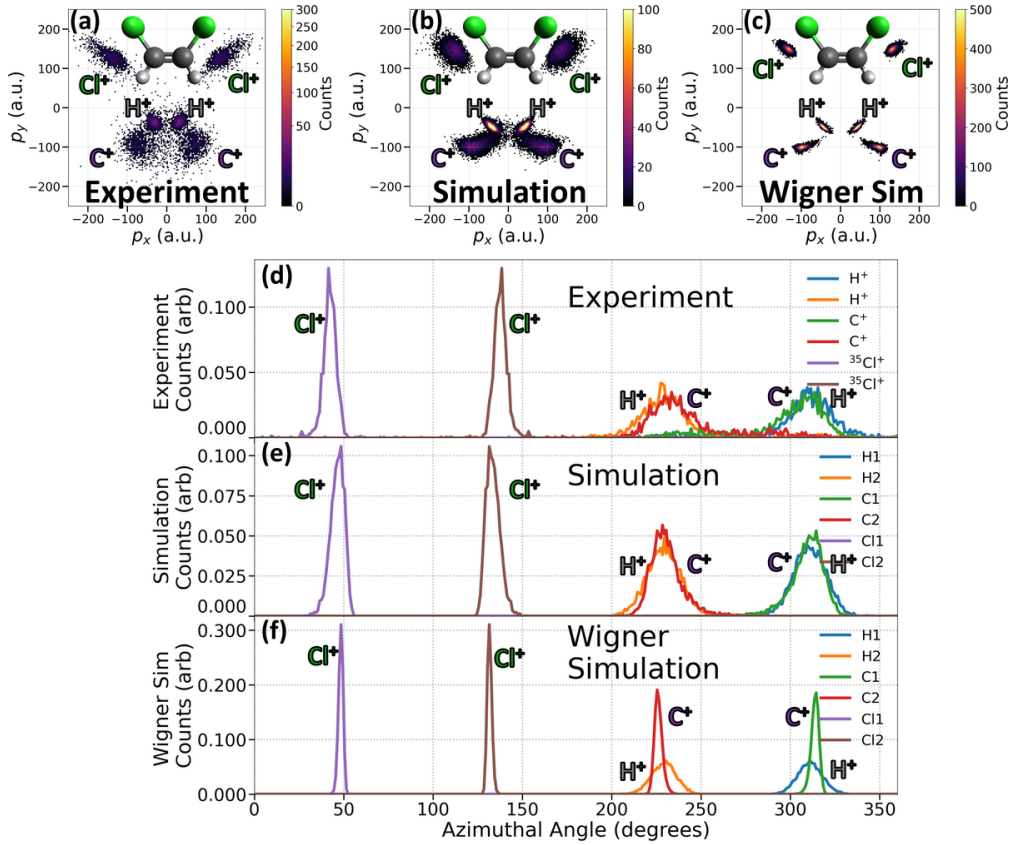

Figure 5.6: CEI patterns for *cis*-1,2-DCE: experimental, simulation from random geometries, simulation from a Wigner-sampled ensemble. Panels (a), (b) and (c) show the Newton plots of momenta projected onto the p_x–p_y plane. For each event, the coordinate frame is aligned such that the vector difference between the two Cl^+ ions defines the p_x axis, and the vector sum of the two Cl^+ lies in the upper p_xp_y plane. Panels (d), (e) and (f) show the corresponding azimuthal angle distributions, integrated over momentum magnitude, for each ion species. The azimuthal angle is measured counterclockwise from the p_x axis, and normalized to unit area.

Fig. 5.8 shows the Newton map and azimuthal-angle distributions for the four-body incomplete channel (H^+, C^+, Cl^+, Cl^+) of *cis*-1,2-DCE. While all atomic species remain identifiable in the Newton maps, the incomplete selection exhibits higher background and broader angular features—most prominently for C^+ ionic fragments. The complete six-body coincidence suppresses false coincidences via momentum-conservation filtering, yielding sharper angular peaks and highlighting the impact of kinematic completeness.

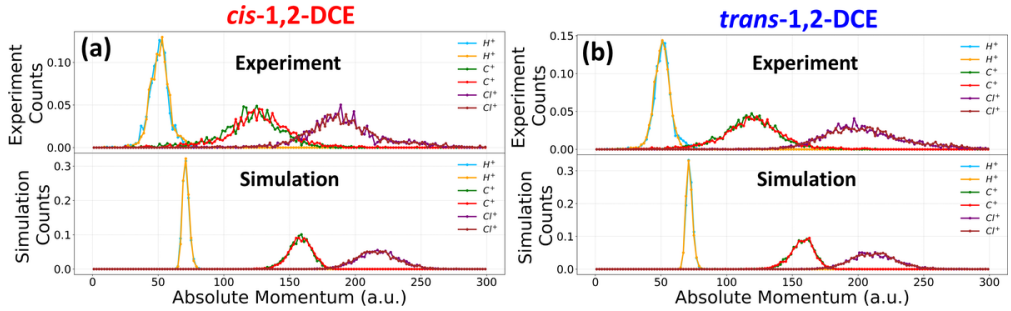

Figure 5.7: Comparison between the measured (top) and simulated (bottom) absolute momenta of coincident ions from Coulomb explosion imaging of (a) *cis*-1,2-DCE and (b) *trans*-1,2-DCE molecules. The figures show the distributions for H^+, C^+, and Cl^+ ions. The simulation systematically overestimates the magnitude of the momenta of the fragments.

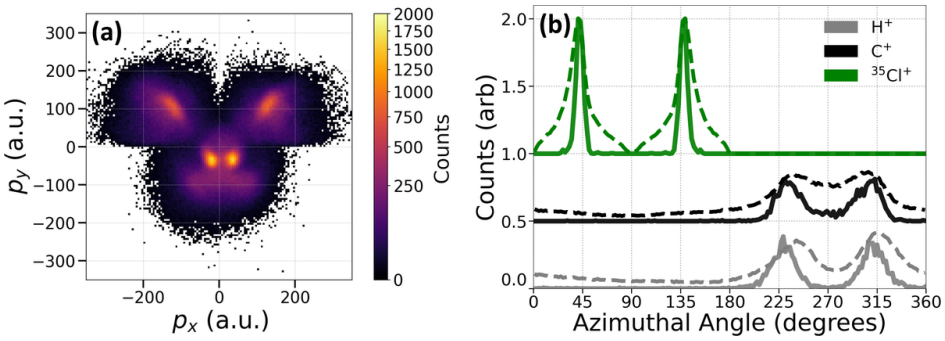

Figure 5.8: (a) Newton plot for *cis*-1,2-DCE obtained from the four-body incomplete coincidence channel (H^+, C^+, $^{35}Cl^+$, $^{35}Cl^+$). The reference frame is defined by the vector difference of the two Cl^+ ions along the x-axis, with their sum lying in the upper xy-plane. (b)Yields of H^+, C^+, and $^{35}Cl^+$ fragments as a function of the azimuthal angle in the molecular frame. Solid lines correspond to the (H^+, H^+, C^+, C^+, $^{35}Cl^+$, $^{35}Cl^+$) six-body complete coincidence fragmentation channel, while dashed lines represent the four-body incomplete coincidence channel. Distributions for C^+ and $^{35}Cl^+$ are vertically offset for clarity.

5.3 Machine-learning Separation of *cis*- and *trans*-1,2-DCE Isomers from Complete Six-body CEI

Figure 5.9: Machine learning workflow for event-level CEI data. Each event is represented by a $3 \times$ N-dimensional momentum vector. We apply dimensionality reduction to obtain a low-dimensional embedding, cluster events in that space, identify the most informative features for class separation, and visualize the corresponding observables.

We now turn to machine learning (ML) to separate *cis* and *trans* event-by-event directly from

experimental data. Each event in the six-body channel is encoded as an 18-dimensional vector composed of the three momentum components for each ion. Dimensionality reduction maps these high-dimensional vectors into a low-dimensional space where structure-related patterns are easier to visualize and analyze. Clustering in the reduced space groups events with similar momentum-space correlations and yields isomer labels without manual selection. Feature-importance analysis then identifies which observables contribute most to the separation and guides targeted visualization of angles and related internal coordinates. This workflow is summarized in Fig. 5.9 and provides a consistent backbone for the comparisons that follow.

5.3.1 Unsupervised Separation of DCE Isomers from an Experimental Mixture

We perform CEI on a sample containing a mixture of *cis* and *trans*-1,2-DCE isomers. Figure 5.10(a) shows the momentum pattern of this data after rotating each event to a frame of reference defined by the two Cl^+ momenta, as in Fig. 5.3(a,b). Compared to the data of only the *cis* isomer in Fig. 5.3(a), new features belonging to the *trans* isomer appear. Some features are well separated from the *cis*-DCE pattern, while some overlap. In order to automatically separate events corresponding to *cis* and *trans* isomers from the mixture, we first perform data reduction to map the eighteen-dimensional event vectors into two dimensions, as shown in Fig. 5.10(b). Here, we choose to use UMAP (Uniform Manifold Approximation and Projection)[47] due to its ability to handle non-linear patterns and its computational efficiency. A comparison with other common data-reduction techniques (PCA and t-SNE) is provided later in this chapter. After the dimensionality reduction, the data are clearly separated into two groups. Events from these two groups are clustered using HDBSCAN (Hierarchical Density-Based Spatial Clustering of Applications with Noise)[48], which extracts the most stable clusters and automatically labels low-density regions as noise. The events are then colored according to their cluster labels, red for *cis*, and blue for *trans* isomers in Fig. 5.10(b).

We next plot the momentum images of these events separately in Fig. 5.10(c) and Fig. 5.10(d) for events from clusters labeled red and blue, respectively. The momentum image in Fig. 5.10(c) closely resembles that in Fig. 5.3(a), indicating that these events correspond to the *cis* isomer. Meanwhile, the momentum image in Fig. 5.10(d) exhibits a distinct pattern that aligns well with

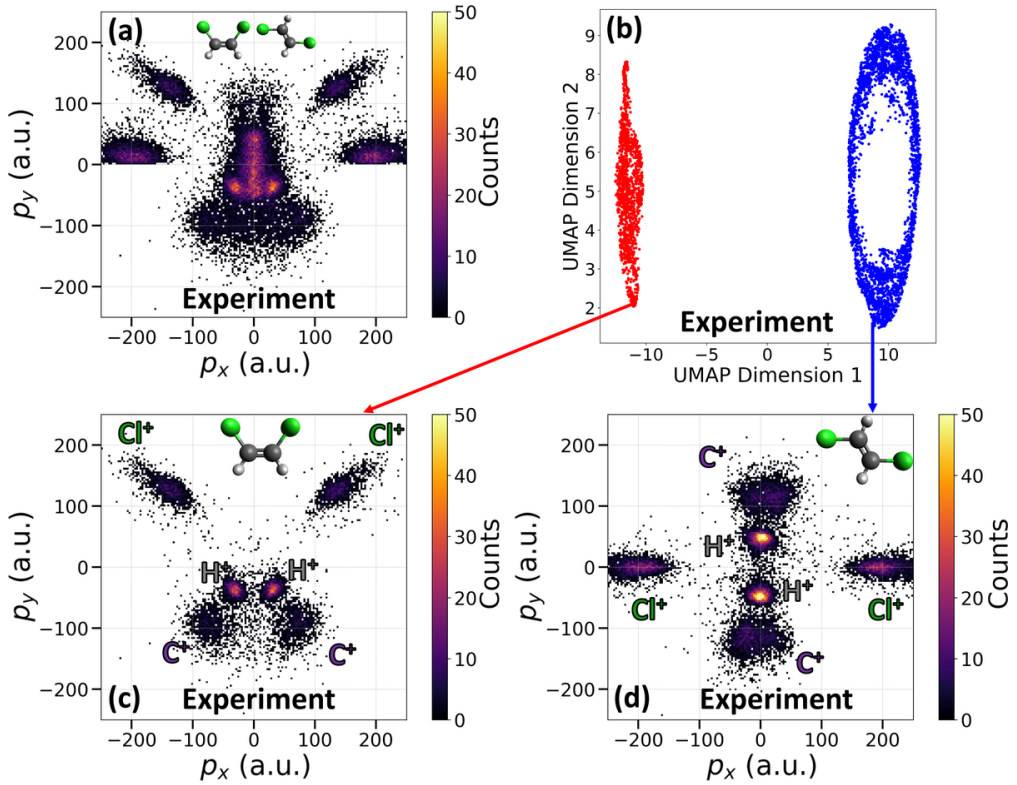

Figure 5.10: Automatic separation of *cis* and *trans* isomer events from experimental mixture data. (a) Newton plot of a mixture of isomers in the Cl-referenced frame. (b) UMAP embedding colored by HDBSCAN cluster labels. (c) and (d) Newton plots for events from the red and blue clusters, matching *cis* and *trans*, respectively. The *cis* reference follows Fig. 5.3; the *trans* reference follows Fig. 5.4.

events from the *trans* molecules, as seen in Fig. 5.4(a). The agreement between momentum images of events from these two clusters and data collected with individual isomers confirms that the data reduction and clustering algorithms have accurately separated *cis* and *trans* isomers on an event-by-event basis, automatically.

5.3.2 Supervised Feature Ranking: Discriminative Power Analysis

Now that the two isomers have been accurately clustered and labeled, we turn to a supervised ML approach to quantitatively assess which features contribute most to the differences between *cis* and *trans*. The key motivation for this analysis arises from the limitations of experimental observables, especially when used individually, in capturing the structural differences between isomers. While our current data shows a clean separation between the two isomers, it is not always guaranteed. If many closely similar configurations coexist, isomers might appear as different parts of one big

cluster, making differentiating them difficult, especially when the reduced dimension is not always readily interpretable. Our following analysis provides insights into how to construct meaningful observables to effectively differentiate similar structures.

In particular, we employ the Random Forest Classifier[152] to evaluate the discriminative power of different features. Random Forest is an ensemble learning method that builds multiple decision trees using bootstrap samples and random feature subsets, then aggregates their votes to produce a more accurate and robust classification. Features with high discriminative power can easily tell the two isomers apart, while ones with low discriminative power cannot cleanly separate the two. We perform this analysis for components of the momentum vectors in Cartesian coordinates [Fig. 5.11] and also internal momentum coordinates [Fig. 5.12] such as the angle between two momentum vectors and the magnitude of the vector differences. The bar heights in Figs. 5.11(a) and 5.12(a) represent Random Forest feature-importance scores, with larger values indicating greater discriminative power for classifying *cis* versus *trans* structures. To account for the algorithm's stochasticity, we retrain the Random Forest multiple times with different random seeds; the plotted bar is the mean value from all the different runs and the error bar shows the standard error. Panels (b)–(c) then illustrate exemplar observables ranked highly by the Random Forest classifier.

Figure 5.11(a) presents the discriminative power analysis from a Random Forest classifier trained to distinguish *cis* and *trans* using the measured Coulomb explosion momenta in Cartesian coordinates; see Fig. 5.10(a). The analysis shows that the p_x and p_y components are more informative than p_z, consistent with the planar symmetry of 1,2-DCE isomers. In particular, the chlorine p_y and proton p_x components are the most discriminative for separating the two isomers. The corresponding one-dimensional distributions for p_{5y}/p_{6y} and for p_{1x}/p_{2x} are shown in Fig. 5.11(b) and (c), respectively. The same trends are visible in the Newton plots for the isolated isomers (Figs. 5.10(c) and 5.10(d)). For chlorine, the p_y distributions exhibit two distinct peaks: a narrow peak near zero for the *trans* isomer (blue) and a peak between 100 and 200 a.u. for the *cis* isomer (red). For protons, the *trans* isomer has $p_x \approx 0$ (blue), whereas the *cis* isomer shows two peaks, symmetrically on either side of zero (red).

While the analysis in Cartesian coordinates provides insight into how momentum-space observables correlate with molecular structure, a more intuitive description that involves the momentum

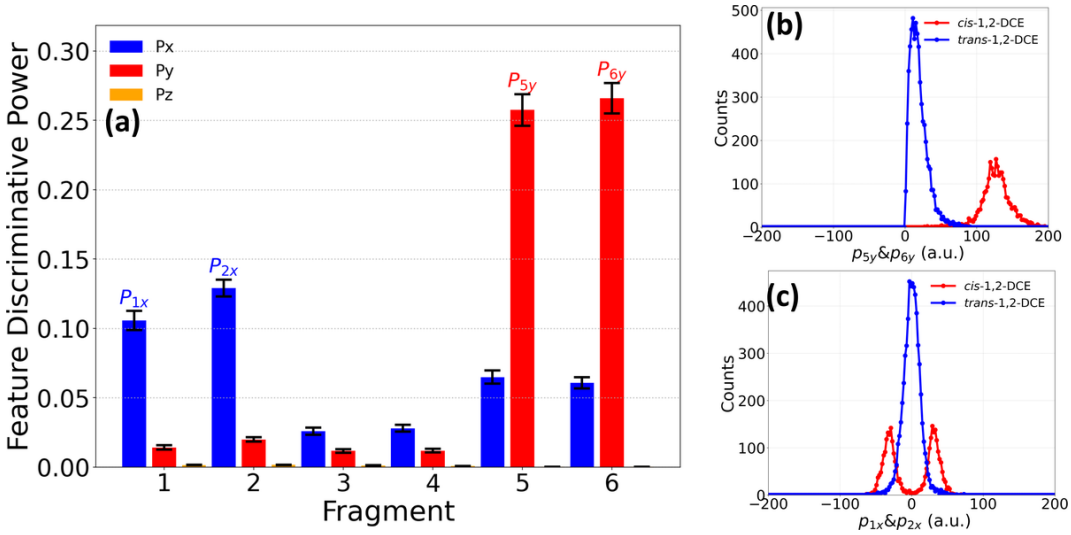

Figure 5.11: Random-forest analysis in Cartesian coordinates and exemplar 1D observables. (a) Discriminative power analysis obtained from a Random Forest classifier trained to distinguish between the *cis* and *trans* isomers based on their measured Coulomb explosion momenta in the Cartesian representation. Bars in (a) report the mean Random Forest feature-importance scores across repeated runs, and the error bars denote the standard error over iterations with different random seeds. (b) and (c) Momentum distributions illustrating two of the most informative components: p_{5y} and p_{6y} (chlorines) and p_{1x} and p_{2x} (protons). The separation of the distributions for *cis* and *trans* reflects the structural differences between the isomers and demonstrates that these momentum components are good discriminators, as quantified by our analysis using the Random Forest classifier model.

internal coordinates, such as d_{ij} and θ_{ij}, can be used. Here, $d_{ij} = |\vec{p}_j - \vec{p}_i|$ is the modulus of the difference between two momentum vectors and $\theta_{ij} = \angle(\vec{p}_i, \vec{p}_j)$ denotes the angle between them. These features are invariant to translation and rotation, offering a robust description of the structural information independent of spatial orientation. These features have been successfully used to track changes in bond lengths[22;29;153] and bond angles[109;147] in the nuclear wave packet dynamics of molecules.

The result, shown in Fig. 5.12(a), reveals that the angles (θ_{ij}) exhibit much stronger discriminative power compared to the magnitudes (d_{ij}). This is because isomers have similar bond lengths, which are the main factor in determining the momentum magnitude (through the Coulomb interactions). d_{ij} is more important when significant bond-length differences arise, such as during dissociation. Here, the angle correlations between fragment momenta — notably those involving pairs of H^+, C^+, and Cl^+ ions — serve as strong distinguishing factors between the isomers. While the role of Cl^+ and H^+ ions was evident in Cartesian coordinates, this representation highlights the

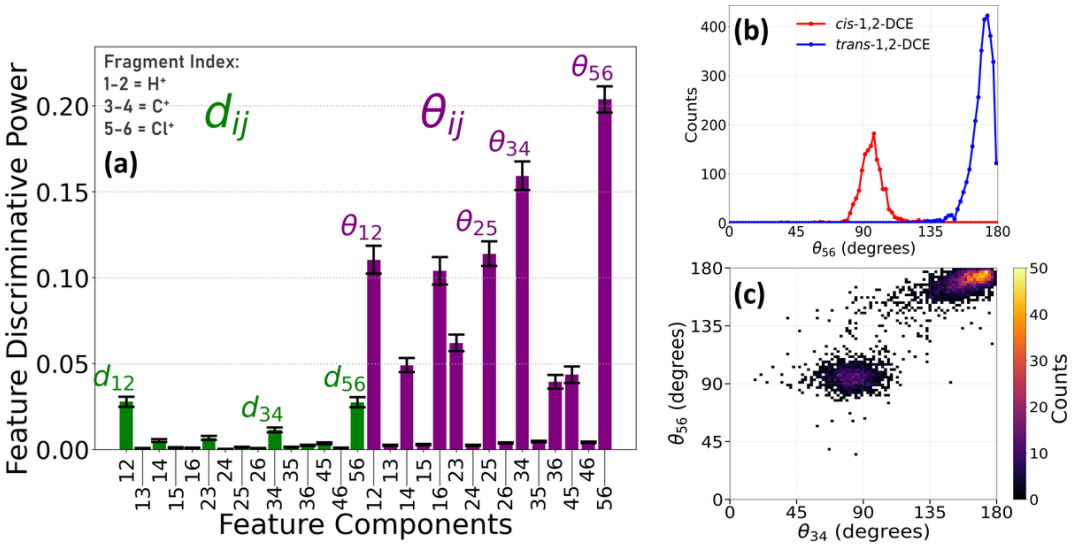

Figure 5.12: (a) Discriminative power of internal coordinates shows that angles θ_{ij} exhibit much stronger discriminative power than magnitudes d_{ij}. Bars in (a) report the mean Random Forest feature-importance scores across repeated runs, and the standard error over iterations with different random seeds are represented with the error bars. (b) Distribution of the angle between the two Cl^+ fragments, θ_{56}, previously identified as the defining structural characteristic of *cis* and *trans* configurations in similar cases[35;59;150]. (c) Two-dimensional angle correlation using $\theta_{34} = \angle(C^+, C^+)$ and θ_{56} reveals two distinct islands corresponding to the *cis* and *trans* isomers, reinforcing the effectiveness of these angles in differentiating structural isomers.

significant contribution of the angle between C^+ fragments, providing additional structural cues for isomer differentiation.

Figure 5.12(b) shows the distribution of the angle between two Cl^+ fragments (θ_{56}). This quantity was previously identified as the defining structural characteristic of *cis* and *trans* configurations in similar cases[35;59;150], which we confirm and quantify as the strongest single discriminator for the two isomers in our analysis. In our current data, this feature by itself can separate the two isomers without any overlap, unlike the partial overlap reported in three-body coincidence studies[35;59;150]. In Fig. 5.12(c), we further incorporate the angle between two C^+ ions $\theta_{34} = \angle(C^+, C^+)$ — the second-strongest discriminator — to make a two-dimensional angle correlation plot. This plot reveals two distinct islands corresponding to the *cis* and *trans* isomers. These well separated regions demonstrate that relative fragment orientations encode key molecular characteristics and reinforce the effectiveness of these angles in differentiating structural isomers.

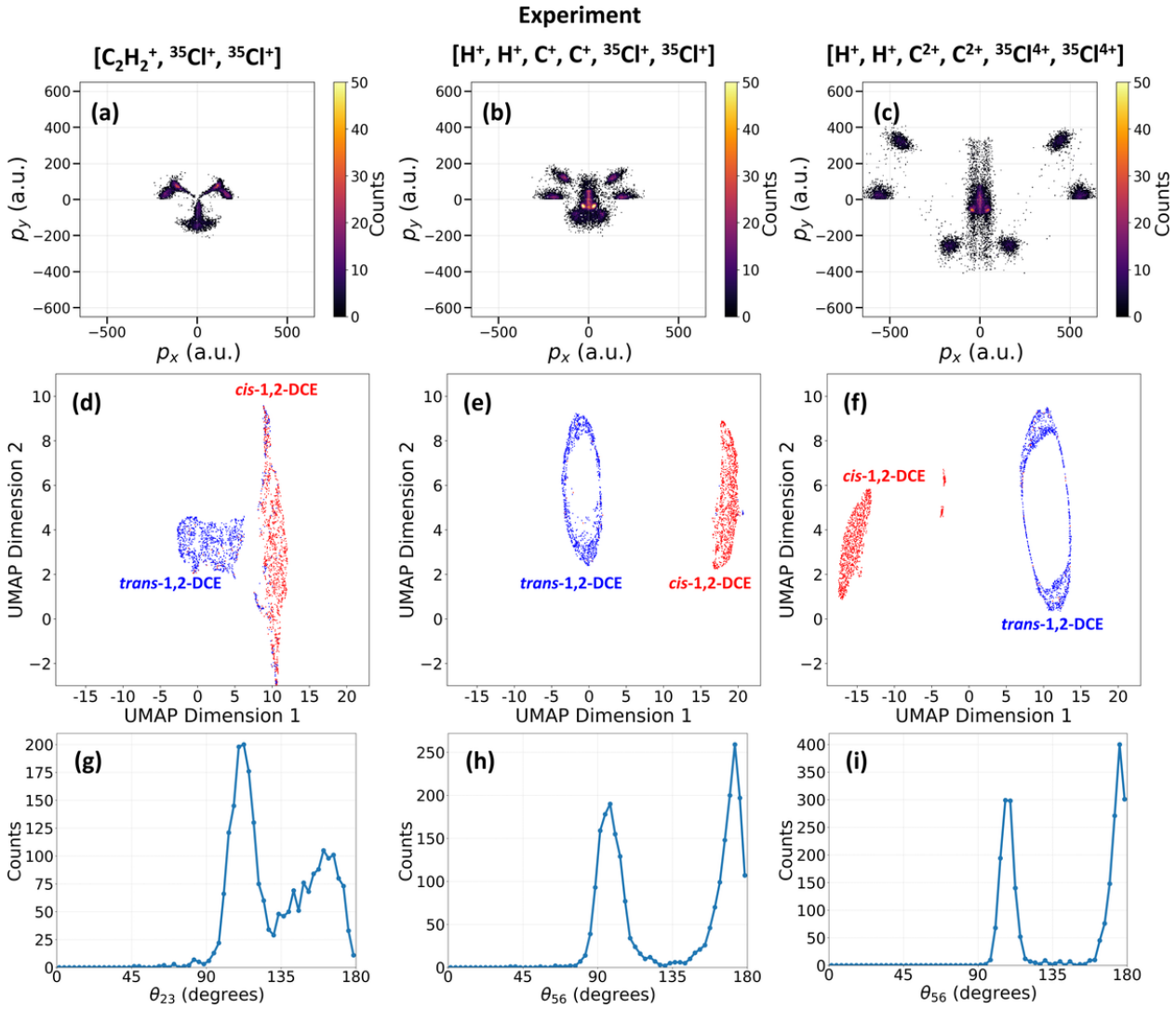

Figure 5.13: Data reduction for three fragmentation channels. (a–c) Newton plots for (a) three-body, total charge 3+ ($C_2H_2^+$, $^{35}Cl^+$, $^{35}Cl^+$), (b) six-body, total charge 6+ (H^+, H^+, C^+, C^+, $^{35}Cl^+$, $^{35}Cl^+$), and (c) six-body, total charge 14+ (H^+, H^+, C^{2+}, C^{2+}, $^{35}Cl^{4+}$, $^{35}Cl^{4+}$). (d–f) Corresponding UMAP embeddings with points colored by true geometry labels. (g–i) Distributions of the angle between the two chlorine ions, θ_{56}, for the same channels. The number of events is fixed across channels, and axis limits are matched for all Newton and UMAP panels to enable direct comparison. Higher total charge states yield clearer separation between *cis* and *trans* isomers

5.3.3 Charge-state Dependence of Isomer Separability

Building on the coincidence maps of Fig. 5.2, we compare three representative fragmentation channels to assess how the final charge state affects data reduction and isomer separation. The channels are: a three-body breakup with total charge 3+ ($C_2H_2^+$, $^{35}Cl^+$, $^{35}Cl^+$), the six-body all-singly-

charged channel with total charge 6+ (H^+, H^+, C^+, C^+, $^{35}Cl^+$, $^{35}Cl^+$), and a six-body channel with total charge 14+ (H^+, H^+, C^{2+}, C^{2+}, $^{35}Cl^{4+}$, $^{35}Cl^{4+}$). This ($C_2H_2^+$, $^{35}Cl^+$, $^{35}Cl^+$), three-body breakup channel has been widely used to distinguish geometric isomers (e.g., *cis*/*trans*) and even conformers[34;35;59;150]. For each channel we show the Newton plot in the molecular plane, the two-dimensional UMAP embedding, and the distribution of the angle between the two chlorine momenta, $\theta_{\text{Cl-Cl}}$. Across these different channels, higher total charge states yield clearer separation between *cis* and *trans* in the embedded space and in the angular distribution. Two factors contribute for the improvement: the ratio of distribution width to momentum magnitude decreases with charge, sharpening features, and higher-fold coincidence encodes richer structural correlations. For consistency, the number of events is fixed across channels, and axis limits are matched for all Newton and UMAP panels. These comparisons reinforce $\theta_{\text{Cl-Cl}}$ as a robust discriminator of the different isomer structures and illustrate how completeness and charge state improve separability.

5.4 Extending to Four Geometries: *cis*, *trans*, *twisted* 1,2-DCE, and 1,1-DCE

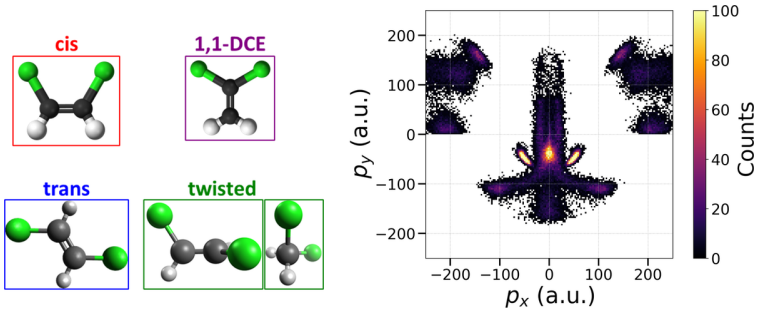

Figure 5.14: Ball-and-stick models of *cis*-, *trans*-, *twisted*-1,2-DCE, and 1,1-DCE, and the simulated Newton plot for the all-singly-charged six-body channel. The nonplanar *twisted* geometry introduces out-of-plane correlations not present in *cis*/*trans*, and 1,1-DCE reorders substituents relative to 1,2-DCE.

We now extend the analysis to four distinct geometries: *cis*-1,2-DCE, *trans*-1,2-DCE, the nonplanar *twisted* 1,2-DCE intermediate, and 1,1-DCE. The twisted geometry represents a midpoint in the torsional transition between *cis* and *trans* configurations, while 1,1-DCE represents a structure where hydrogen and chlorine migrations are involved (similar to acetylene-vinylidene isomeriza-

tion). Together, these geometries offer a broader perspective on conformational changes that may occur in photoinduced reaction dynamics that would be desirable to identify in a time-dependent pump-probe experiment. These configurations serve as a test case of whether CEI+ML can resolve nonplanar intermediates from planar *cis*/*trans*. It is important to note that the following analysis is based on simulated data, as experimental results are not available for the transient *twisted*-1,2-DCE and 1,1-DCE. Given that our simulations closely reproduce the experimental data presented earlier, we believe that this analysis is well justified and provides meaningful insights into the structural dynamics under investigation. Figure 5.14 shows ball-and-stick models alongside the combined simulated Newton plot for the (H^+, H^+, C^+, C^+, $^{35}Cl^+$, $^{35}Cl^+$) six-body channel. Compared to the simpler two-geometry case, the four-geometry simulation exhibits increased overlap, motivating a multidimensional treatment of momentum correlations.

Table 5.3: Equilibrium geometry of 1,1-DCE optimized at the B3LYP/aug-cc-pVDZ level.

1,1-DCE				
	Atom	x (Å)	y (Å)	z (Å)
1	H	0.93847	2.30932	0.00000
2	H	-0.93847	2.30932	0.00000
3	C	0.00000	1.75934	0.00000
4	C	0.00000	0.42806	0.00000
5	Cl	1.46564	-0.52185	0.00000
6	Cl	-1.46564	-0.52185	0.00000

Table 5.4: *Twisted*-1,2-DCE transient-state geometry between *cis*- and *trans*-1,2-DCE, where the C=C bond rotates 90° from the *cis*-1,2-DCE equilibrium, optimized at the B3LYP/aug-cc-pVDZ level.

twisted-1,2-DCE				
	Atom	x (Å)	y (Å)	z (Å)
1	C	-0.53475	1.19362	-0.31733
2	C	0.26899	0.32851	0.48543
3	H	-1.08439	1.95034	0.26295
4	H	0.15112	-0.00884	1.52174
5	Cl	-1.66406	-0.43127	-0.05612
6	Cl	1.81276	-0.22016	-0.10819

Optimized equilibrium coordinates for the simulated structures are used in the CE model. For completeness, the Tables 5.3 and 5.4 list the B3LYP/aug-cc-pVDZ geometries for 1,1-DCE and *twisted*-1,2-DCE; the *cis*/*trans* tables appear earlier in Tables 5.1 and 5.2.

5.4.1 Multidimensional ML Analysis of Simulated Four-geometry Data

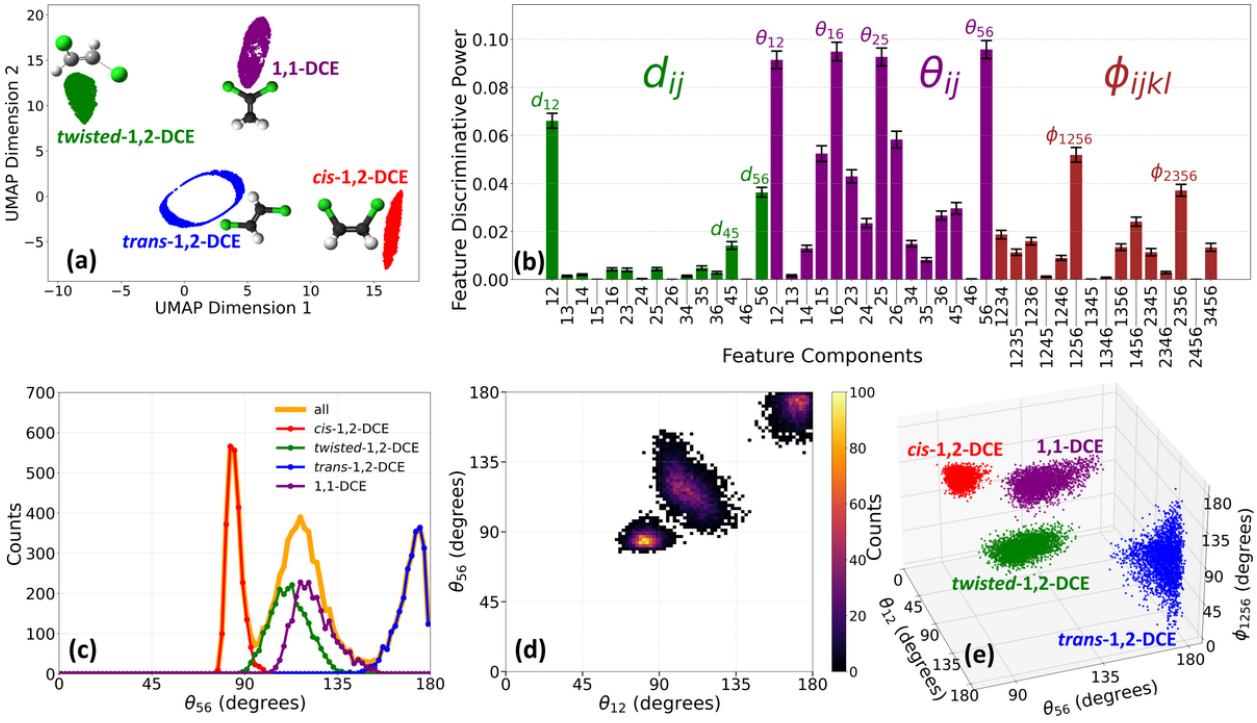

Figure 5.15: Multidimensional analysis for structure differentiation. (a) Dimensional reduction and clustering analysis of a mixture of four isomers — *cis*-, *trans*-, *twisted*-1,2-DCE, and 1,1-DCE — where ball-and-stick models of these isomers are also illustrated. (b) Discriminative power analysis of features constructed using higher-order correlations between momentum vectors, categorized into modulus difference (green) and angle (purple) between two momentum vectors, and angle between two planes (brown) formed by four momentum vectors. (c-e) demonstrate the effectiveness of high-dimensional data in differentiating isomers, where the separation between these structures is improved sequentially from one- to two- and three-dimensions.

We will apply both unsupervised learning (i.e., clustering) and supervised learning (i.e., classification) techniques to systematically analyze the momentum-space signatures of the isomers. Figure 5.15(a) presents the clustering results obtained through dimensionality reduction using UMAP, where all molecular configurations clearly separate into distinct clusters. These clusters can be accurately identified by HDBSCAN. This result shows that far more detailed structural differences from CEI data can be encoded in a reduced representation.

Since the *twisted* geometry is nonplanar, the dihedral angle needs to be included to distinguish these structures in real space. We mimic the effect of this quantity in the fragment momentum space by introducing a higher-order correlation — angles between planes: ϕ_{ijkl} — as a structural

descriptor. ϕ_{ijkl} is calculated from four momentum vectors where each pair — $(\vec{p}_i, \vec{p}_j)$ and $(\vec{p}_k, \vec{p}_l)$ — defines a plane. The discriminative power analysis shown in Fig. 5.15(b) shows that $\theta_{56} = \angle(\mathrm{Cl}^+, \mathrm{Cl}^+)$ and $\theta_{12} = \angle(\mathrm{H}^+, \mathrm{H}^+)$ are still among the most important discriminators. Fig. 5.15(c) shows that the 1D distribution of θ_{56} can reveal partial separation between isomers but cannot be used as a single feature to distinguish all the isomer structures. Significant overlap persists, particularly among the *twisted* and 1,1-DCE structures, demonstrating that this observable alone does not efficiently capture the difference between *cis-trans* isomerization and other processes. The two-dimensional correlation between θ_{56} and θ_{12}, as shown in Fig. 5.15(d), slightly enhances the separation, eliminating minor overlap and cleanly resolving *cis* and *trans* from the other two (i.e., *twisted* and 1,1-DCE). However, complete differentiation of all structures requires additional dimensions.

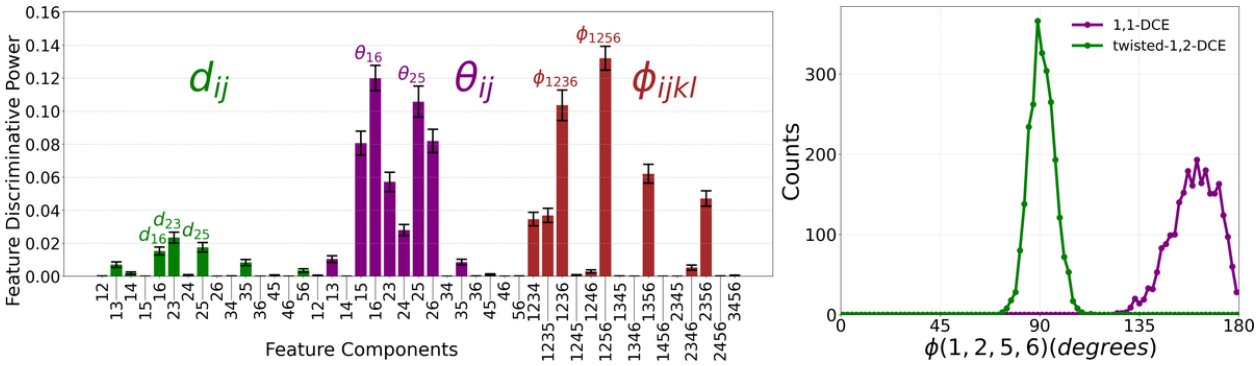

Figure 5.16: Random Forest feature-importance ranking for the *twisted*-1,2-DCE vs 1,1-DCE comparison (left), and the corresponding one-dimensional distribution of ϕ_{1256} (right). Bars report mean feature-importance scores across repeated runs, and error bars denote the standard error over iterations with different random seeds. The ϕ_{1256} dihedral-like angle serves as the most effective single discriminator for this pair.

To quantify the most informative observable for distinguishing *twisted*-1,2-DCE from 1,1-DCE, we repeat the Random Forest analysis restricted to these two structures. As expected, ϕ_{1256} — the angle between two planes formed by protons and chlorine ions — is the most critical discriminator, which can clearly separate the two, evident from Fig. 5.16(a). Figure 5.16(b) shows that the one-dimensional distribution of ϕ_{1256} cleanly separates the two molecular structures very well. Fig. 5.15(e) shows a 3D representation incorporating ϕ_{1256} in addition to θ_{56} and θ_{12}. This visualization reveals four distinct clusters and underscores the necessity of leveraging multiple observables

to achieve a clear separation of similar molecular structures.

5.5 Comparing Dimensionality-reduction Methods and Assessing Stochasticity

We compare three commonly used dimensionality-reduction techniques—Principal Component Analysis (PCA), t-distributed Stochastic Neighbor Embedding (t-SNE), and Uniform Manifold Approximation and Projection (UMAP)—on our CEI dataset. PCA is a linear technique that projects data onto orthogonal axes of maximal variance, preserving global structure but missing nonlinear relationships. t-SNE is a nonlinear, probabilistic method that excels at preserving local neighborhoods but can distort global distances and scales poorly to large datasets[46]. UMAP is a nonlinear method designed to preserve both local and some global structures of high-dimensional data while remaining computationally efficient, built upon concepts from fuzzy topology and Riemannian geometry[47]. UMAP outputs often resemble those of t-SNE because both rely on graph-based layouts in a low-dimensional space, but UMAP typically performs better in the aspects mentioned above.

Figure 5.17 shows a side-by-side comparison on experimental data containing a mixture of *cis*- and *trans*-1,2-DCE events. Figure 5.18 presents the analogous comparison on simulated data containing four geometries (*cis*-, *trans*-, *twisted*-1,2-DCE, and 1,1-DCE). In the two-isomer experiment, all three methods visibly separate the classes in two dimensions, with UMAP providing the cleanest split of all three, and t-SNE, in turn, looks better than PCA. In the four-geometry simulation, PCA degrades significantly, while t-SNE and UMAP retain clear separation, with UMAP again providing the most compact, well-separated clusters.

To quantify cluster quality across methods, we compute the Silhouette Score[154] and the Davies–Bouldin (DB) Index[155]. The Silhouette Score measures how well a point matches its assigned cluster relative to other clusters, giving values in $[-1, 1]$ with higher values indicating tighter and clearer grouping. The DB Index compares the similarity of each cluster to its most similar other cluster, taking values in $[0, \infty)$ with lower values indicating more compact, well-separated clusters. Table 5.5 lists the metrics for the two-isomer experiment and the four-geometry simulation, and Fig. 5.19 visualizes the same results. On the experimental mixture, PCA and t-SNE show similar

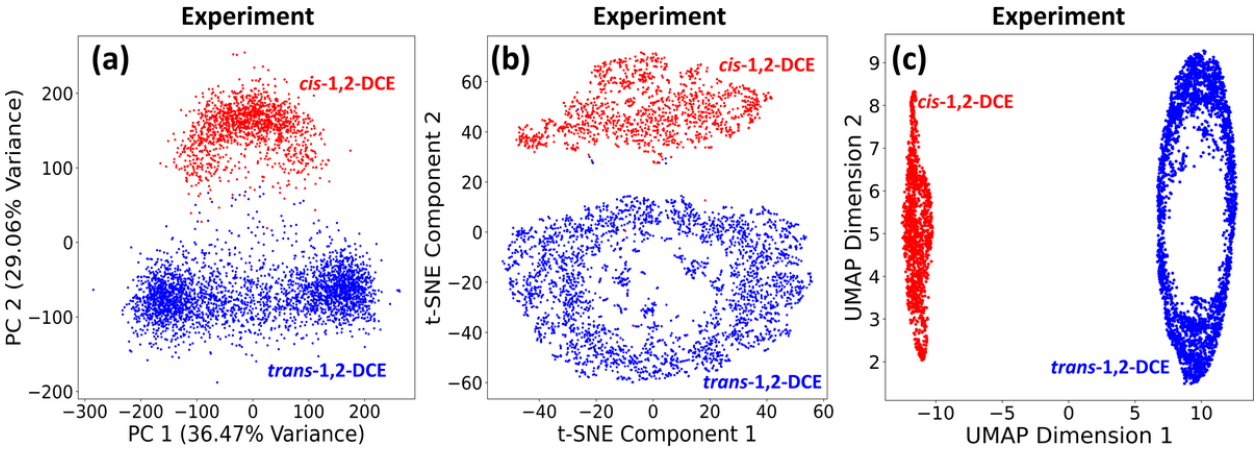

Figure 5.17: Dimensionality reduction on experimental data containing a mixture of *cis* and *trans* 1,2-DCE. (a) PCA, (b) t-SNE, and (c) UMAP applied to the same dataset. Events are colored by their known labels. In this case the dataset is robust enough that all three methods separate the two isomers in two dimensions, with UMAP providing the cleanest split.

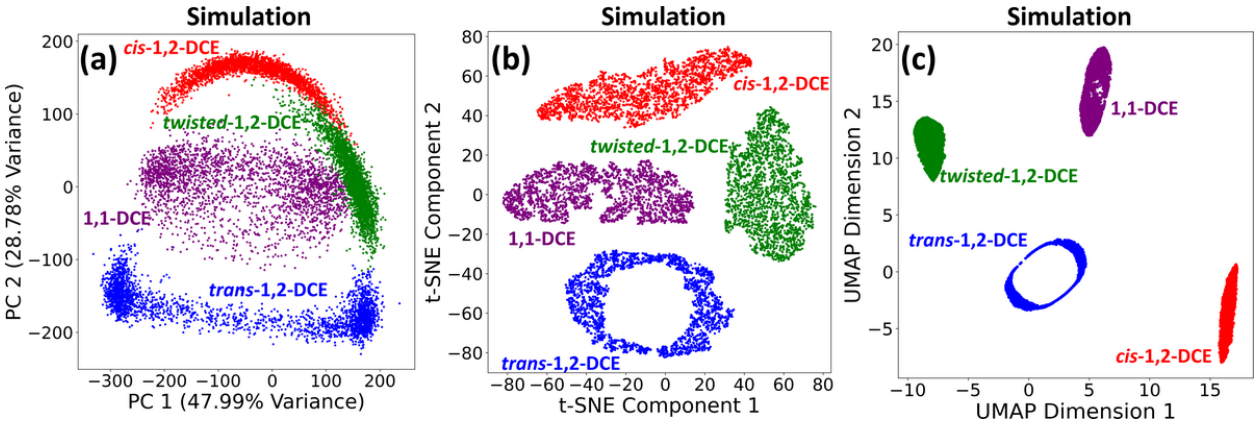

Figure 5.18: Dimensionality reduction on simulated data for *cis*-, *trans*-, *twisted*-1,2-DCE, and 1,1-DCE. (a) PCA, (b) t-SNE, and (c) UMAP applied to the same four-geometry dataset. Events are colored by their true labels. UMAP and t-SNE remain robust, whereas PCA shows markedly reduced separability.

performance while UMAP is distinctly better. On the four-geometry simulation, PCA performance drops, t-SNE is roughly unchanged, and UMAP again yields the best separation scores.

Table 5.5: Cluster-quality metrics for dimensionality-reduction methods on experimental two-isomer data and simulated four-geometry data.

	Experimental data (two isomers)			Simulated data (four geometries)		
Method	PCA	t-SNE	UMAP	PCA	t-SNE	UMAP
Silhouette Score	0.466	0.454	0.834	0.295	0.465	0.806
Davies–Bouldin Index	0.881	0.824	0.226	1.457	0.845	0.319

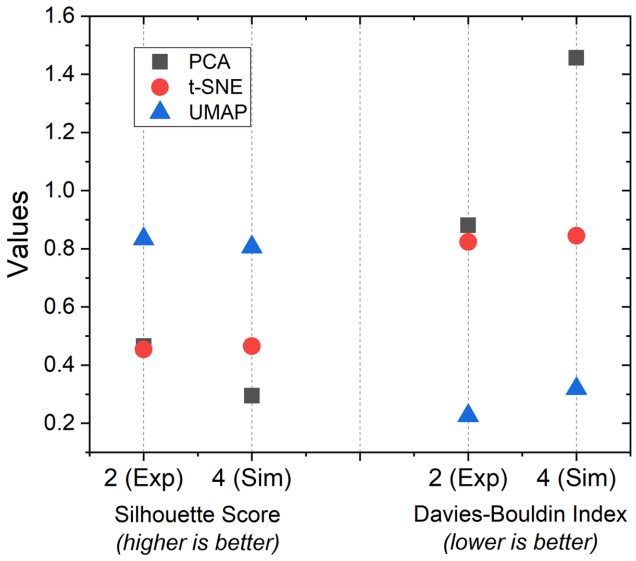

Figure 5.19: Cluster metrics across methods. Silhouette Score (higher is better) and Davies–Bouldin Index (lower is better) for PCA, t-SNE, and UMAP on the experimental two-isomer data and the simulated four-geometry data.

In general, UMAP performs well for CEI clustering because its manifold approximation can capture curved, nonlinear structures and recover both local neighborhoods and broader global trends rather than only maximizing linear variance. That said, performance is data dependent. When the separation is largely linear, PCA remains attractive for its speed, simplicity, and interpretability.

Table 5.6: Stability of UMAP analysis under stochastic initialization. Metrics are averaged over 100 runs with different random seeds and reported as mean ± standard deviation.

Metric (UMAP, 100 runs)	Value
Silhouette Score	0.84 ± 0.04
Davies–Bouldin Index	0.22 ± 0.05

We also assessed the stochastic components of the workflow. UMAP includes a "random_state" hyperparameter that seeds the data reduction algorithm, so repeated runs can yield slightly different results. To evaluate stability, we repeated the UMAP procedure 100 times with different random seeds and computed the Silhouette and DB metrics each time. The resulting averages and standard deviations shown in Table 5.6 indicate robust and stable behavior from the UMAP analysis.

5.6 Dimensionality Reduction Under Broadened Momentum Spreads

Building on the unsupervised separation and supervised feature ranking established above, we now test how strongly broadened momentum distributions impact structure separability and how simulation-trained embeddings can guide experimental analysis. Photoexcitation can deposit substantial energy into the molecule, broadening both its initial spatial distribution and its kinetic energy, which widens the final fragment-momentum spread relative to ground-state isomers. In this section, we show that moving to higher total charge states in the coincidence channel further improves separability under severe broadening even with the four geometries. Further, we consider four simulation cases with progressively larger spreads, then demonstrate that a supervised UMAP embedding trained on simulations yields a latent space in which experimental events can still be accurately assigned.

5.6.1 Employing High-charge Channels Under Broadened Momentum Spreads

Motivated by the experimental comparison of fragmentation channels in Fig. 5.13, we examine whether moving to higher total charge states offers better separability amont the four geometries when momentum spreads become large. Higher total charge sharpens momentum-space features, which improves separability in two-dimensional embeddings under increasing feature broadening. Figures 5.20 and 5.21 compare unsupervised UMAP dimensionality reduction for two six-body channels, (+6 and +14 total charge) across progressively broadened simulation conditions. In all panels, points are colored by their true geometry labels (*cis*- in red, *trans*- in blue, *twisted*-1,2-DCE in green, and 1,1-DCE in purple).

Figure 5.20 varies the spatial deviation for *twisted*-1,2-DCE and 1,1-DCE from 0.25 Å to 0.50 Å at a fixed 0.5 eV kinetic energy, while keeping *cis* and *trans* at 0.50 Å and 0.5 eV. The +6 channel (top row) shows increasing overlap—most notably the *cis* and 1,1-DCE clusters encroach upon each other as the spread grows—whereas the +14 channel (bottom row) maintains four compact, well-separated clusters over the same parameter sweep.

In Fig. 5.21, the kinetic energy is varied from 3 to 6 eV at a fixed 0.50 Å spatial deviation for

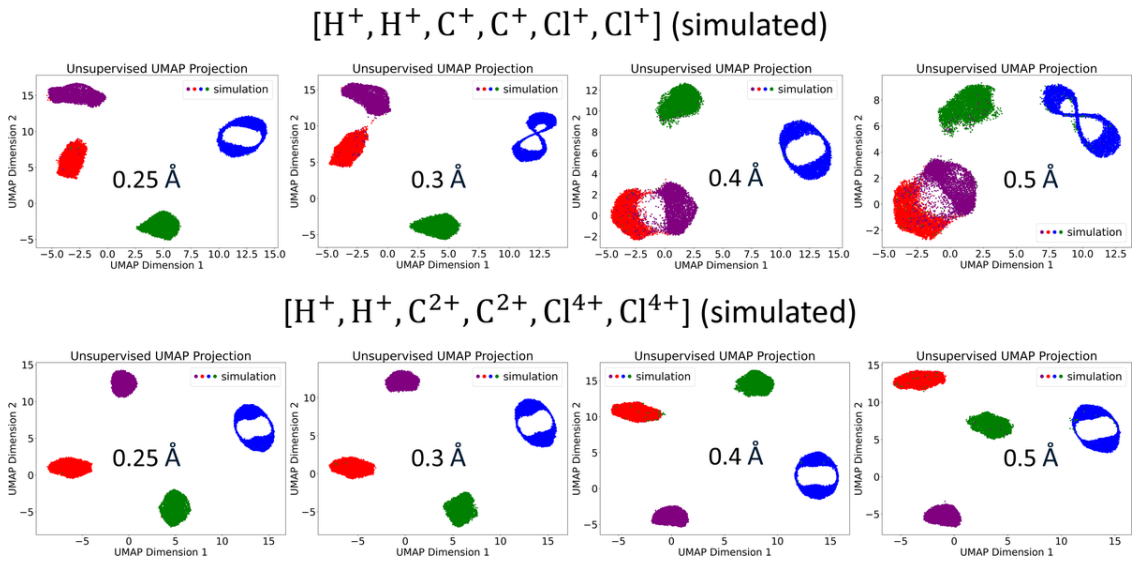

Figure 5.20: Comparison of +6 and +14 total final charge channels with increasing spatial deviation at fixed 0.5 eV kinetic energy for *twisted* and 1,1-DCE. For *cis* and *trans*, parameters are fixed at 0.25 Å and 0.5 eV. The top row shows the +6 channel, which begins to overlap as the spatial deviation grows. The bottom row shows the +14 channel, which preserves clear separation across the same conditions. The scatter plots are colored by their true geometry labels.

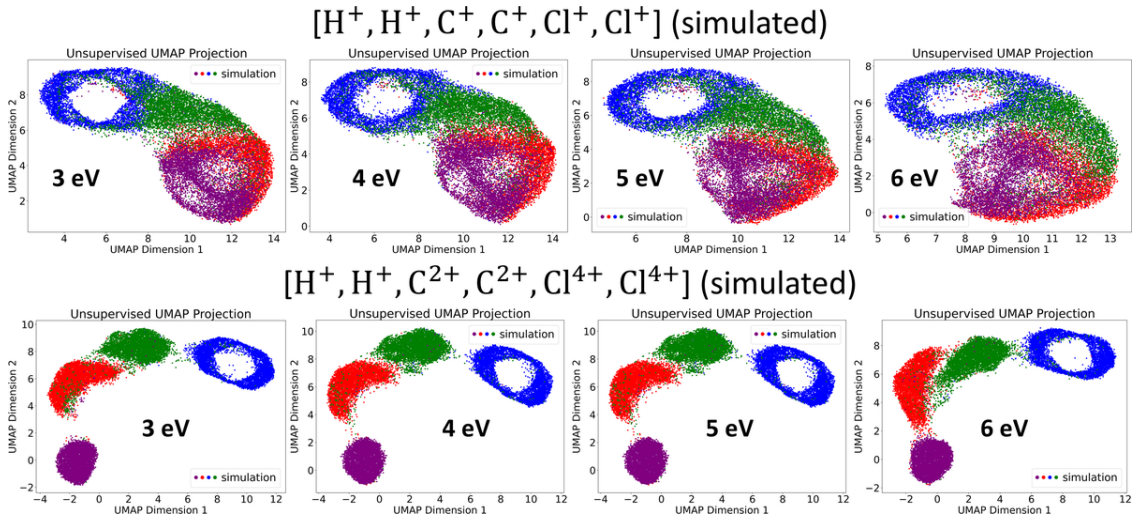

Figure 5.21: Comparison of +6 and +14 fragmentation channels while increasing kinetic energy from 3 to 6 eV at fixed 0.5 Å spatial deviation. The +6 channel (top) exhibits substantial overlap between geometries as the energy increases. The +14 channel (bottom) maintains cluster separations over the same range. Points are colored by their true geometry labels.

all geometries. With a relatively high initial kinetic energy (3 eV), both channels already exhibit substantial overlap in the UMAP dimension-reduced maps. The +6 channel (top row) progressively washes out the separation—clusters elongate and merge—whereas the +14 channel (bottom row) remains distinctly partitioned, with only slight elongation of the manifolds at higher ener-

gies. Across spatial and kinetic energetic broadening, the +14 channel maintains distinct clusters, whereas the +6 channel progressively overlaps. Together with Fig. 5.13, these simulations indicate that, under severe broadening, selecting higher total charge states in complete-coincidence CEI can markedly improve the robustness of dimensionality reduction for distinguishing the different molecular structures.

5.6.2 Supervised UMAP for Broadened Regimes: Simulation to Experiment

Proceeding with testing the ML analysis for increased feature broadening, we simulate the six-body channel ($H^+, H^+, C^+, C^+, Cl^+, Cl^+$) for a mixture of *cis*-, *trans*-, *twisted*-1,2-DCE, and 1,1-DCE with spatial and kinetic-energy spreads for four cases, listed in Table 5.7. Case I corresponds to narrow spreads representative of ground-state isomers (addressed in Sec. 5.4), whereas Cases II–IV introduce progressively larger broadening intended to emulate pump–probe conditions at later delay times. We first reduce the simulated events with unsupervised UMAP to assess intrinsic separability. We then train a supervised UMAP embedding on labeled simulations and, without using any experimental labels, project the experimental events into the learned latent space to evaluate simulation-to-experiment transfer.

Table 5.7: Simulation parameters for four broadening scenarios used to test dimensionality reduction and supervised transfer. Entries list spatial deviation (in Å) and total kinetic energy (in eV) applied to the neutral geometries before Coulomb explosion.

Simulation parameters				
Geometry	Case I	Case II	Case III	Case IV
cis-1,2-DCE	0.25 Å, 0.50 eV	0.25 Å, 0.50 eV	0.25 Å, 0.50 eV	0.50 Å, 6.00 eV
trans-1,2-DCE	0.25 Å, 0.50 eV	0.25 Å, 0.50 eV	0.25 Å, 0.50 eV	0.50 Å, 6.00 eV
twisted-1,2-DCE	0.25 Å, 0.50 eV	0.50 Å, 3.00 eV	0.50 Å, 6.00 eV	0.50 Å, 6.00 eV
1,1-DCE	0.25 Å, 0.50 eV	0.50 Å, 3.00 eV	0.50 Å, 6.00 eV	0.50 Å, 6.00 eV

Figure 5.22 summarizes Case II, where *twisted*-1,2-DCE and 1,1-DCE are substantially broadened relative to *cis*/*trans*. In this simulation, the spatial deviation and kinetic energy are 0.25 Å and 0.5 eV for *cis*- and *trans*-1,2-DCE (as before), and 0.5 Å and 3 eV for *twisted*-1,2-DCE and 1,1-DCE, yielding broad momentum distributions with no visually distinctive geometry-specific features. Panel (a) shows the simulated Newton map for the six-body channel, where broad, mixed lobes obscure any simpler visual assignment. Panel (b) shows an unsupervised UMAP projec-

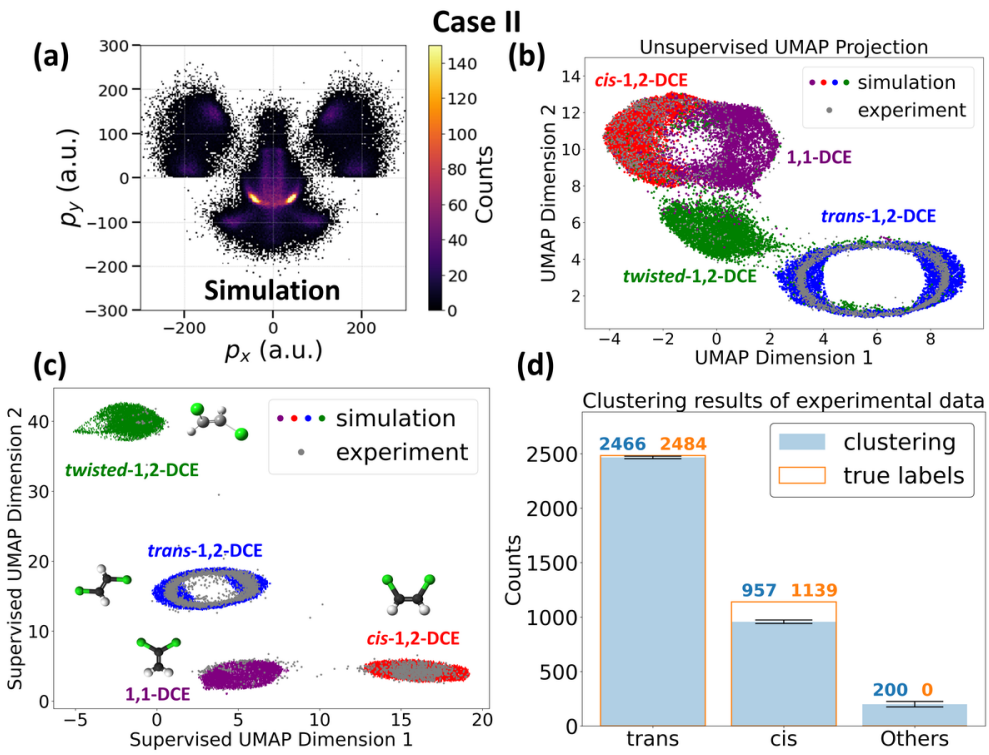

Figure 5.22: Supervised UMAP classification of experimental CEI data under broadened spreads (Case II). (a) Simulated Newton map for the six-body channel ($H^+, H^+, C^+, C^+, Cl^+, Cl^+$) combining *cis*, *trans*, *twisted*-1,2-DCE, and 1,1-DCE with parameters from Table 5.7. (b) Unsupervised UMAP of simulated events (colored by geometry) and experimental events (gray) shows partial overlap between geometries. (c) Supervised UMAP trained on simulated labels yields well-separated clusters; experimental events (gray) align with the corresponding simulation clusters. (d) Recovery of molecular identity from experimental data in the supervised space via density-based clustering. Error bars reflect the stochastic variation from repeating UMAP with different random seeds. Outlined bars: ground-truth labels derived independently. Numbers above the bars denote assigned (left) and true (right) counts.

tion: colored points are simulated events from all four geometries and gray points are experimental events from the *cis*/*trans* mixture, with partially overlapping clusters, especially between *cis* and 1,1-DCE. Because the unsupervised separation is not sufficiently distinct, automatic clustering is difficult; to address this, we train a supervised UMAP embedding on labeled simulations to improve cluster separation. Panel (c) displays the supervised embedding, in which the algorithm learns two nonlinear combinations of the original momentum components that maximize separation, producing a two-dimensional latent space with four well-separated simulation clusters. The experimental *cis*/*trans* events (gray) are projected onto the corresponding clusters with near-perfect overlap. Panel (d) reports HDBSCAN tallies for the experimental events in the supervised space, recovering

≈ 99% of *trans* and ≈ 84% of *cis* with an overall misclassifications rate of 5.5%. Error bars in panel (d) reflect stochastic variability from repeating UMAP with different random seeds. This excellent agreement validates the feasibility of this approach, showing that supervised machine learning on pure simulation can serve as an appropriate guide for experimental data analysis.

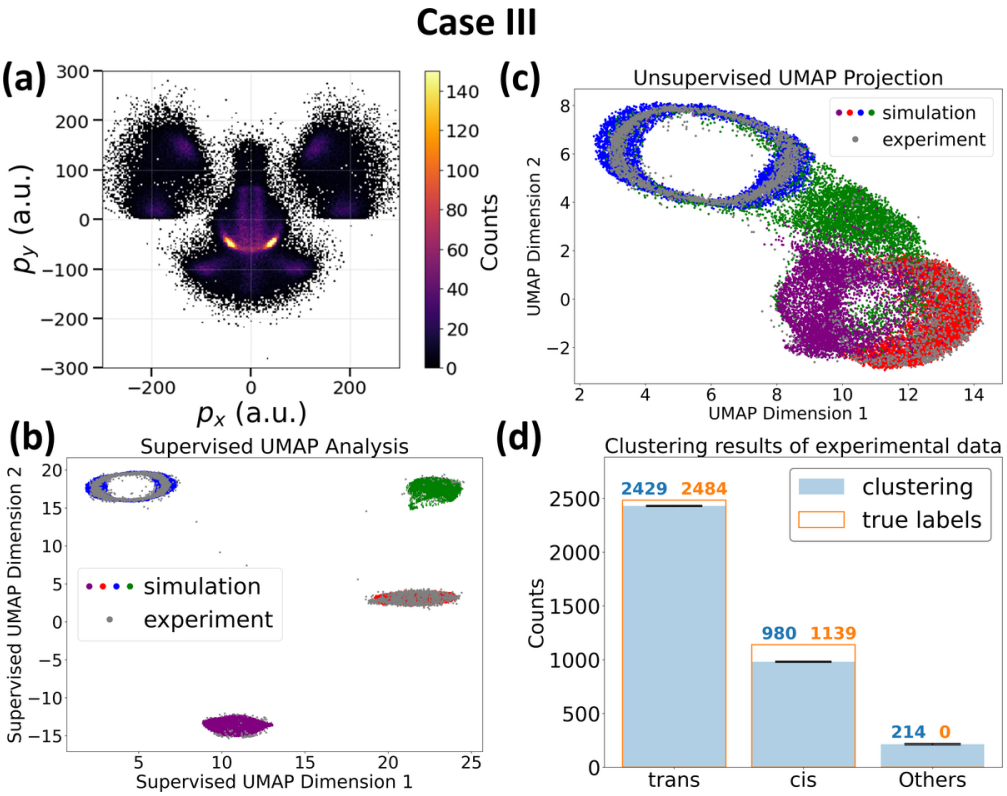

Figure 5.23: Case III: complete relaxation to ground-state kinetic energies (6 eV for *twisted* and 1,1-DCE). (a) Simulated Newton map for the six-body channel. (b) Supervised UMAP trained on simulations with experimental events projected in gray. (c) Unsupervised UMAP of simulations and experiment for reference. (d) Experimental clustering tallies in the supervised space with true-label counts for comparison.

We next apply the same workflow to Cases III and IV, which further increase kinetic energy and spatial spread. In Case III, *cis*/*trans* remain at 0.25 Å and 0.5 eV, whereas *twisted*-1,2-DCE and 1,1-DCE are broadened to 0.5 Å and 6 eV (Table 5.7). This parameter set corresponds to complete relaxation back to ground-state kinetic energies for the latter pair (6 eV, approximately a 200 nm pump), and, as expected from the kinetic-energy–driven broadening trends noted earlier in Fig. 5.21, the unsupervised UMAP projection, panel c, shows increased cluster elongation and larger overlap. Even so, the supervised UMAP embedding (Fig. 5.23(b)) cleanly separates all

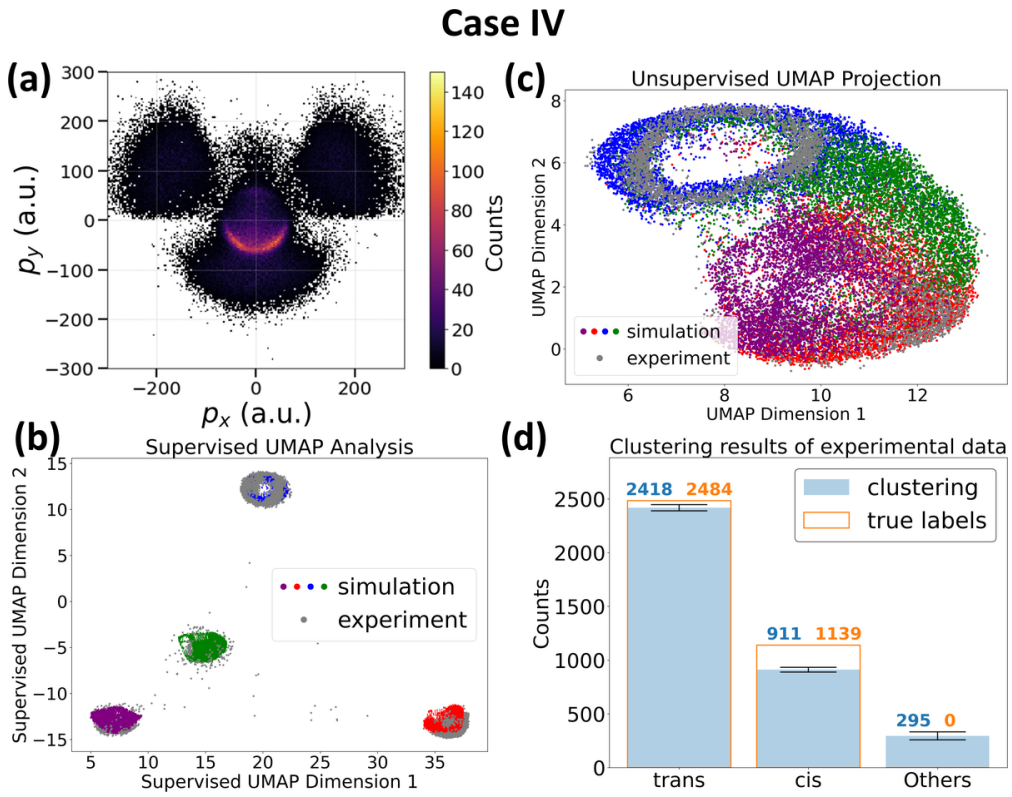

Figure 5.24: Case IV: extreme broadening scenario for all geometries. (a) Simulated Newton map for the six-body channel. (b) Supervised UMAP trained on simulations with experimental events projected in gray. (c) Unsupervised UMAP of simulations and experiment for reference. (d) Experimental clustering tallies in the supervised space with true-label counts for comparison.

four simulated geometries, and experimental *cis*/*trans* events (gray) align with their respective simulation clusters.

Case IV represents an extreme broadening scenario in which *all* four geometries are set to 0.5 Å and 6 eV. Under these conditions, the unsupervised UMAP projection (Fig. 5.24(c)) exhibits substantial overlap among clusters—consistent with the systematic increase in overlap at higher kinetic energies highlighted in Fig. 5.21. Nevertheless, the simulation-trained supervised UMAP (Fig. 5.24(b)) preserves four well separated clusters in the latent space and transfers reliably to experiment: the majority of *cis* and *trans* events are still identified correctly, and experimental *cis*/*trans* data (gray) continue to overlap well with the corresponding simulation clusters. Of the four isomers, *trans* remains the most distinct and thus is classified with the highest accuracy, whereas *cis*—whose geometry is more similar to 1,1-DCE (e.g., $\angle(C^+, C^+)$, $\angle(H^+, H^+)$)—is more challenging. Overall, even as the unsupervised projections show pronounced overlap at large

spreads, the supervised embedding trained on simulations maintains clean separation and robust simulation-to-experiment transfer. Classification tallies, shown in panels 5.23(d) and 5.24(d), remain accurate for *trans* and remain strong for *cis* despite the more severe broadening, with confusion primarily arising between *cis* and 1,1-DCE as expected from their similar angle signatures.

5.7 Summary and Outlook

We have demonstrated that complete six-ion CEI of 1,2-DCE encodes sufficient event-level information to differentiate *cis* and *trans* isomers using machine learning. Angles between fragment momenta emerge as the most robust observables for structural assignment, while absolute kinetic energies from classical CE simulations tend to be overestimated and are used qualitatively. Unsupervised learning on experimental events yields clean isomer separation in reduced dimensions, and supervised models trained on simulations transfer reliably to experiment even when momentum distributions broaden. Feature ranking with Random Forest[152] quantifies which projections carry the strongest discriminative power, guiding the construction of physically interpretable observables. Among dimensionality-reduction methods, UMAP[47] provides stable, well-separated embeddings for these datasets and outperforms PCA and t-SNE in preserving both local and global structure, with repeated runs showing consistent cluster metrics.

When momentum spreads increase—as expected under pump–probe conditions—two practical strategies improve separability. First, selecting coincidence channels with higher total final charge sharpens momentum-space features, further enhances separability under severe broadening. Second, a supervised UMAP trained on simulated labels produces a low-dimensional latent space that cleanly resolves multiple geometries and aligns well with experimental projections, enabling robust clustering. Together, these strategies provide a general recipe for molecular structure classification in multi-coincidence CEI.

Looking ahead, extending CEI + ML to larger molecular systems should benefit from ongoing advances in sources, detectors, and analysis. Higher repetition-rate and higher-intensity light sources will boost coincidence statistics and access higher charge states. Improved position-sensitive detectors and better vacuum will increase multi-hit detection efficiency and reduce background. On

the analysis side, the present framework can be extended to incomplete breakup with complete detection, where sufficient information remains to distinguish the different dynamical pathways. The ML analysis framework presented in this chapter can handle these scenarios without modification, though specific details of atoms that do not breakup are absent. In cases of complete ionization but incomplete detection (e.g., five detected fragments in DCE, ($H^+, C^+, C^+, {}^{35}Cl^+, {}^{35}Cl^+$)), the missing fragment introduces label ambiguity and tends to split each structure into two apparent clusters because the detected H^+ randomly samples one of two equivalent sites, potentially necessitating tailored multivariate reconstruction strategies[136] with explicit assumptions about geometry and/or ionization dynamics. By uniting kinematically complete coincidence imaging with data-driven inference, this framework paves the way for automated, event-level imaging of channel-specific, time-resolved dynamics in future pump–probe experiments.

Chapter 6

Channel-resolved Auger-Meitner Electron Spectroscopy of CH_3I

In this chapter, we extend the coincidence studies from ions only to a combined analysis of ions and electrons. We use multi-ion–electron coincidence spectroscopy to resolve Auger-Meitner and shake-up/shake-off electrons for specific fragmentation channels of CH_3I following I $4d$ inner-shell ionization. Soft X-ray photons at 107 eV are used to ionize the iodine $4d$ shell, and the subsequent electronic decay is recorded in a double-sided velocity map imaging spectrometer that detects electrons and multiple ionic fragments in coincidence. In contrast to the previous chapters, where the focus was on ion–ion correlations and nuclear dynamics alone, here the electron spectra provide a more direct probe of the local core hole, the electronic decay pathways, and exploit the multi-ion coincidences to disentangle and assign these electron spectra to different final charge states of the molecular cation. By exploiting ion–ion coincidence and the associated kinetic energy release (KER), we separate dication and trication fragmentation channels, extract channel-specific Auger-Meitner spectra for $CH_x^+ + I^+$ and $CH_x^+ + I^{2+}$ channels, and identify the contributions from secondary emission processes. In addition, from the electron spectra associated with incomplete two-body channels involving H^+ and CH_2^+, we show that contributions from different cationic states can be isolated using the ion KER. The results provide channel-resolved reference electron spectra for CH_3I that complement the ion-only measurements in the rest of this thesis and are relevant for interpreting time-resolved inner-shell experiments at XFEL facilities.

6.1 Introduction and Motivation

Inner-shell photoionization of CH_3I has been studied extensively near the iodine $4d$ edge using synchrotron radiation and electron spectroscopy. High-resolution electron spectroscopy near the iodine $4d$ edge has mapped out the main $4d^{-1}$ hole states, their subsequent Auger–Meitner decay, and the associated shake-up and shake-off satellites[50–53]. These studies show that following creation of a $4d$ core hole, Auger–Meitner decay and shake processes populate a manifold of highly excited dicationic and higher-charge states, many of which are repulsive and lead to fragmentation into multiple competing ionic channels[50–53]. In molecules, the Auger–Meitner decay pathways are more complex than in atoms because of the dense manifold of valence states and the coupling to nuclear motion. As a result, the conventional Auger–Meitner electron spectrum often consists of broad, overlapping features arising from many final states and, in some cases, from cascaded or double-Auger processes. Even when high energy resolution is achieved, it can be difficult to unambiguously assign individual peaks to specific electronic states or to link them to particular fragmentation outcomes[52].

Channel-resolved Auger–Meitner spectroscopy addresses this challenge by correlating electron spectra in coincidence with well-defined ionic breakup channels. Recently, Liu *et al.* showed that analyzing the photoelectron kinetic energy with the kinetic energy release of $O^+ + O^+$ ion pairs allows different intermediate core-hole states to be disentangled[56]. Related work on CH_3I and CH_2I_2 has demonstrated that selecting particular photoelectron or ion channels can isolate subsets of the $4d^{-1}$ manifold and their dissociative double-ionization pathways[55;156].

In this chapter, we apply a similar strategy to CH_3I using multi-ion–electron coincidence spectroscopy. Soft X-ray photons from synchrotron radiation at the Advanced Light Source, ionize the I $4d$ shell leaving a $4d^{-1}$ core hole that relaxes via Auger–Meitner decay. By recording the kinetic energy of the emitted electrons together with the momenta of multiple coincident fragment ions, we obtain channel-resolved electron spectra for different final charge states and molecular fragmentation channels of CH_3I^{n+}. Comparing these spectra with previous high-resolution photoionization and Auger–Meitner measurements[50–55] allows us to associate distinct electron-energy features with specific groups of dicationic and tricationic states and with their preferred fragmentation pathways.

The main goal of this chapter is to obtain channel-resolved Auger–Meitner electron spectra for CH_3I at a fixed photon energy and to interpret them in terms of the underlying electronic decay and fragmentation dynamics. By combining multi-ion and electron coincidence detection, we provide a more complete picture of the $4d$-hole relaxation pathways than is accessible from electron or ion spectroscopy alone. An additional motivation is to establish channel-resolved reference electron spectra that can support future time-resolved inner-shell experiments at X-ray free-electron lasers, where similar ionic channels may be used to probe ultrafast charge and nuclear dynamics in more complex systems.

6.2 Experimental Overview

The measurements were carried out at the Advanced Light Source (ALS) synchrotron radiation facility at Lawrence Berkeley National Laboratory. The experiment used the double-sided velocity map imaging (VMI) spectrometer on beamline 10 in the multi-bunch operation mode of the synchrotron. The general layout of the apparatus and the ion and electron imaging procedures are described in Sec. 2.1.3 and 2.2.2, and further details on this endstation can be found in earlier PhD theses[72;157] and several publications describing earlier coincidence experiments.[34;35;59]

For the measurements in this study, the photon energy was fixed at $h\nu = 107$ eV, roughly 50 eV above the $4d$ thresholds at 56.6 eV and 58.4 eV for the $4d_{5/2}$ and $4d_{3/2}$ spin–orbit components, respectively[50;55;158]. Figure 6.1 shows the calculated photoabsorption cross sections for the iodine $4s$, $4p$, $4d$, $5s$, and $5p$ subshells as a function of photon energy[159–161], with the experimental photon energy indicated by a vertical line. At 107 eV, the $4d$ cross section dominates and is approximately a factor of 25 larger than the valence ($5s$ and $5p$) cross section. This choice of photon energy provides a high probability for creating an I $4d$ hole and leaves a large kinetic energy separation between the $4d$ photoelectrons, with a kinetic energy of 50.4 and 48.6 eV for $4d_{5/2}$ and $4d_{3/2}$ photoelectrons, respectively, and the secondary electrons, which have kinetic energies below 40 eV[50;52] . Typical data sets contained single-electron events with up to three detected ions, which allowed us to construct ion–ion and ion–electron coincidence maps for all major fragmentation channels.

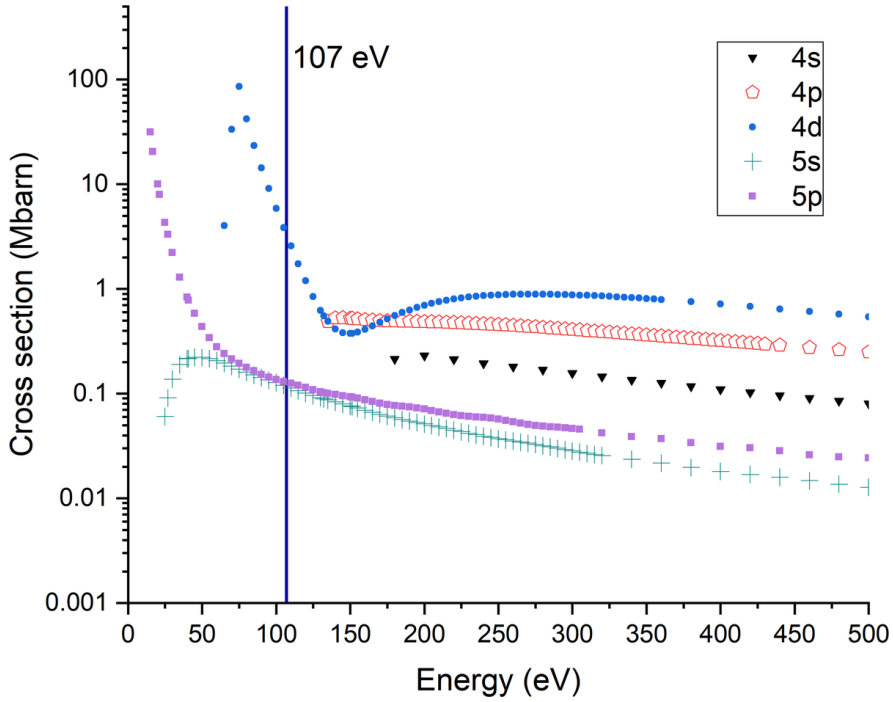

Figure 6.1: Calculated photoabsorption cross sections for the iodine $4s$, $4p$, $4d$, $5s$, and $5p$ subshells as a function of photon energy.[159–161] The experimental photon energy of 107 eV is indicated by the vertical line. The ionization thresholds are 56.6 eV and 58.4 eV for the $4d_{5/2}$ and $4d_{3/2}$ spin–orbit components of the $4d$ subshell[158], and 129 eV for the $4p$ subshell[53].

6.3 Ion and Electron Signals

Figure 6.2 shows the ion time-of-flight (TOF) spectrum and the electron VMI image, where the radius of the rings corresponds to the transverse electron momentum. The ion TOF spectrum displays clear peaks corresponding to H^+, H_2^+, a cluster of CH_x^+ fragments (x = 0–3), the iodine fragments I^+ and I^{2+}, and a weak CH_3I^+ peak; the ion yield to the right of the H^+ peak is scaled by a factor of 5, as indicated. Very low intensity of the parent ion peak indicates that the X-ray pulse predominantly ionizes the $4d$ shell of the iodine atom, followed by dissociation into dicationic and tricationic channels, in agreement with earlier studies.[50;52;53]

The electron VMI image shows a bright outer ring corresponding to the I $4d$ photoelectrons with a kinetic energy of roughly 50 eV. Closer to the center of the image, we observe a broad distribution of secondary electrons extending from a few electronvolts up to the vicinity of the photoelectron ring. These electrons arise from Auger-Meitner decay of the $4d$ hole and any shake processes accompanying the primary photoionization and the subsequent decay. From the electron

image, it is evident that the secondary electron yield is comparable to, or even larger than the photoelectron yield.

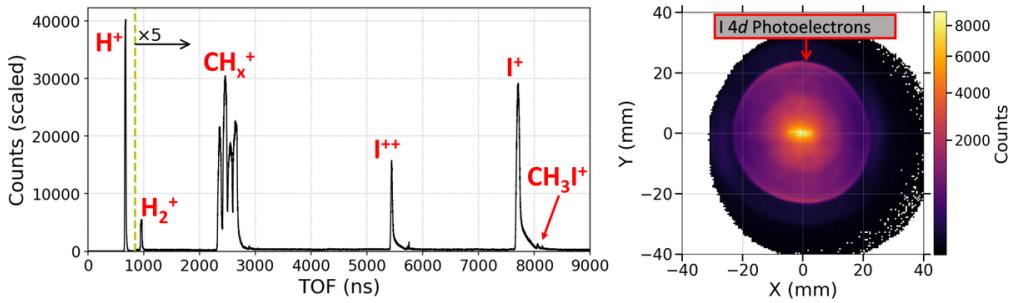

Figure 6.2: Ion time-of-flight spectrum and electron VMI image recorded for CH_3I at 107 eV photon energy. Left: ion TOF spectrum showing peaks assigned to H^+, the CH_x^+ group (x = 0–3), I^{2+}, and I^+. The ion yield to the right of the H^+ peak is scaled by a factor of 5, as indicated. Right: Accumulated electron image on the detector. The outer ring, marked by the arrow, corresponds to the I 4*d* photoelectrons, while the inner region is populated by Auger-Meitner and other secondary electrons.

6.3.1 Ion–ion Coincidence Maps

To disentangle the different fragmentation channels, we construct ion–ion time-of-flight coincidence maps from events with two or more detected ions. Figure 6.3 displays the photoion–photoion coincidence (PIPICO) map, which correlates the TOF of ion 1 with the TOF of ion 2 for all events with at least two detected ions. The PIPICO map displays several well-defined diagonal lines. The strongest group of lines corresponds to the two-body dicationic channels $CH_x^+ + I^+$ with x = 0–3. These lines are separated by the small mass differences of the hydrocarbon fragments; channels with fewer hydrogens (missing protons) appear to the left. Tricationic channels corresponding to $CH_x^+ + I^{2+}$ appear with different slopes and offsets. In both these coincidence channel groups, the lines are sharpest for the complete breakup channel $CH_3^+ + I^+$ (or $CH_3^+ + I^{2+}$), where both fragments are detected. For the channels where one or more protons are missing from the CH_x^+ ionic fragment, the coincidence lines become more diffuse because of the momentum carried away by the missing fragment(s). We also observe island-like features where a proton is the first detected ion and the partner fragment is either a CH_x^+ ion or a singly or doubly charged iodine ion. In these proton + partner-ion channels, the undetected fragment carries a considerable share of the momentum, which leads to more diffuse structures in the coincidence map.

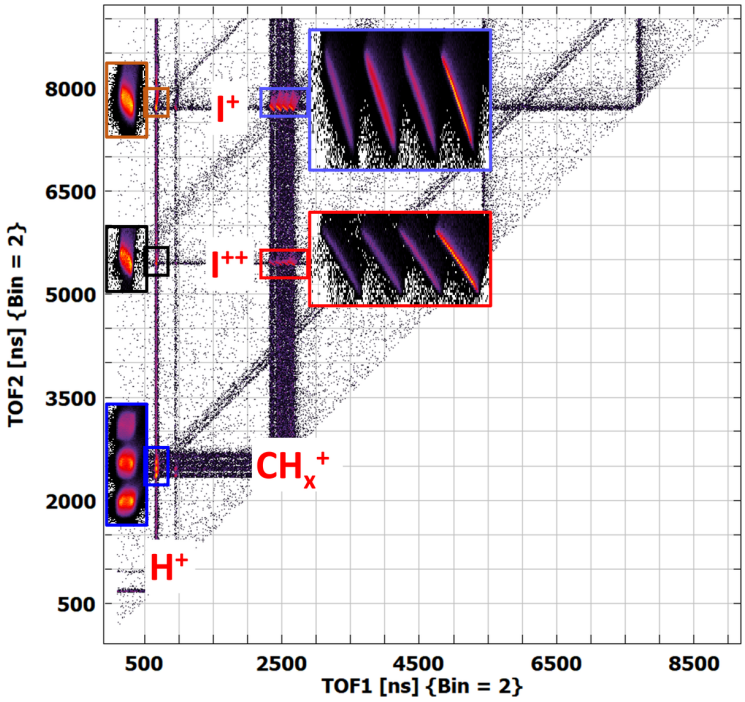

Figure 6.3: Two-ion photoion–photoion coincidence (PIPICO) map for CH_3I at 107 eV. The TOF of ion 1 is plotted against the TOF of ion 2. The insets show enlarged views of the coincidence lines marked by the rectangles of the corresponding colors. Prominent diagonal lines correspond to the two-body channels $CH_x^+ + I^+$ (x = 0–3), as well as to channels involving I^{2+}. Additional lines at shorter TOF show incomplete coincidence channels in which H^+ is the first detected ion and a second ion is recorded, while another fragment from the dissociation channel is not detected.

Figure 6.4 shows the triple-ion coincidence (TRIPICO) map, which correlates the TOF of ion 3 with the sum of TOF_1 and TOF_2 for three-ion events. In this representation, three-body channels such as $H^+ + CH_2^+ + I^+$ and $H^+ + CH_2^+ + I^{2+}$ appear as characteristic lines. Comparison of the PIPICO [Fig. 6.3] and TRIPICO [Figure 6.4] maps reveals that many of the strong two-body lines in the PIPICO map actually contain contributions from both true two-body fragmentation and three-body channels, where the third fragment that is missing in the PIPICO map may be either charged or neutral.

In the following sections, I focus on three groups of fragmentation channels: (i) two-body channels with a singly charged iodine fragment ($CH_x^+ + I^+$ with x = 0–3), (ii) two-body channels with a doubly charged iodine fragment ($CH_x^+ + I^{2+}$ with x = 0–3), and (iii) channels recorded without an iodine fragment, for example the two-body $H^+ + CH_2^+$ channel, which allow us to isolate the contribution from breakups involving neutral iodine.

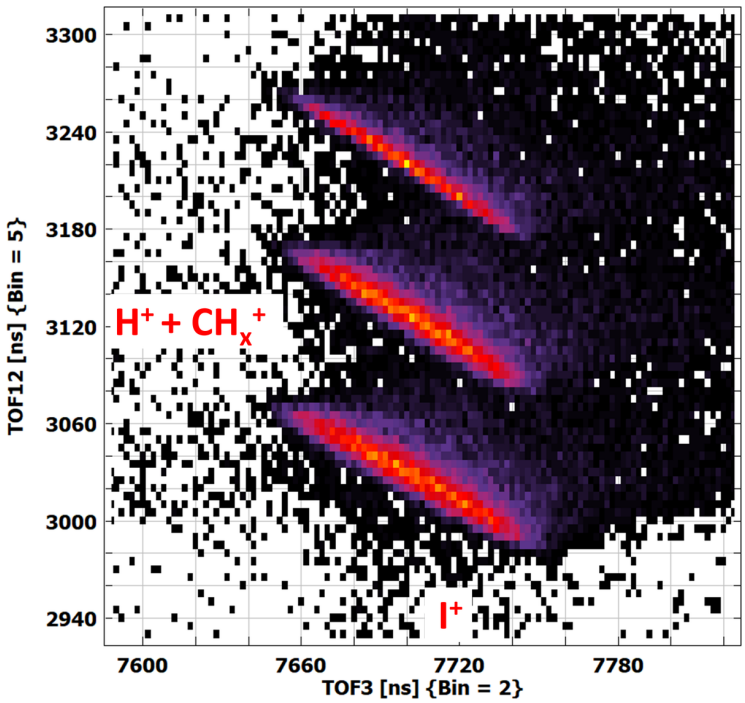

Figure 6.4: Three-ion coincidence map (TRIPICO) for CH_3I at 107 eV. The TOF of the third ion is plotted versus the sum of TOF_1 and TOF_2. Distinct lines indicate three-body breakup channels $H^+ + CH_x^+ + I^+$, with x = 0,1,2.

6.4 Two-body Channels with Singly Charged Iodine: $CH_x^+ + I^+$

We first consider the two-body fragmentation channels $CH_x^+ + I^+$ with x = 0–3. Figure 6.5 shows representative ion and electron detector images for these channels. The CH_x^+ and I^+ distributions are obtained by selecting the corresponding lines in the PIPICO map. The electron image is the sum over all events in which a given $CH_x^+ + I^+$ pair is detected.

The CH_x^+ and iodine fragments show ring-like distributions, with CH_x^+ forming larger-radius patterns that reflect their lighter masses and a more diffuse inner region that indicates more complex fragmentation dynamics. The corresponding electron images already indicate that the distribution of secondary electrons depends on the selected fragmentation channel.

To isolate the electrons belonging to a specific fragmentation channel, we gate on narrow regions around each $CH_x^+ + I^+$ line in the PIPICO map and reconstruct the corresponding electron images. Figure 6.6 summarizes this procedure: the middle panel shows the PIPICO map with colored boxes marking the gates for the four $CH_x^+ + I^+$ channels. The panels on both sides display the electron images for each gate, marked with the same colors as the corresponding PIPICO regions. The $4d$

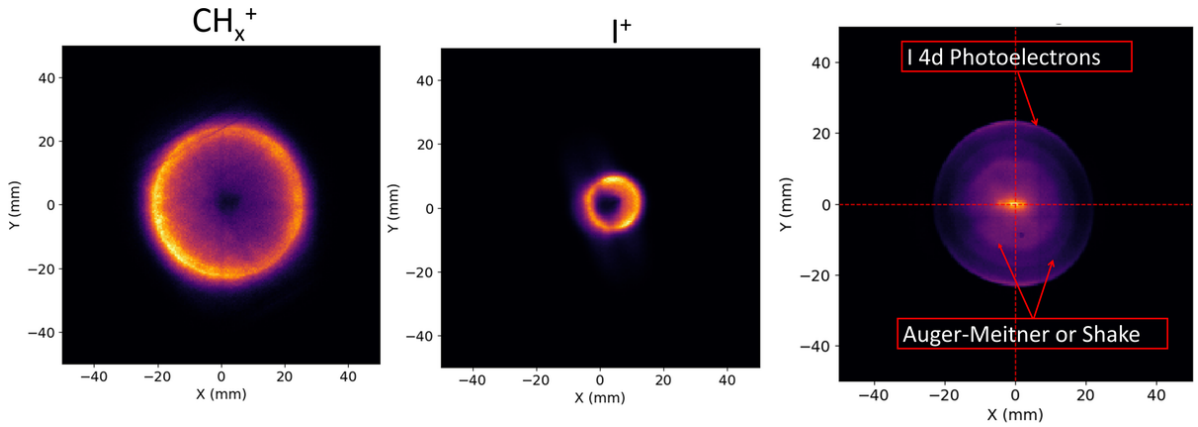

Figure 6.5: Ion and electron images associated with the two-body channels $CH_x^+ + I^+$ (x = 0–3). The left and middle panels show the CH_x^+ and I^+ ion images, while the right panel displays the corresponding accumulated electron image.

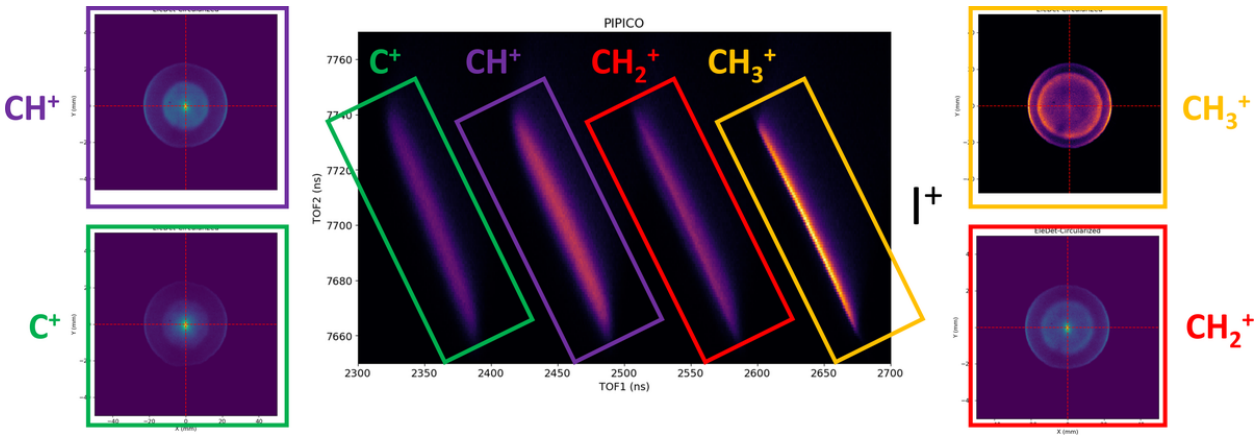

Figure 6.6: Channel selection for electrons associated with the $CH_x^+ + I^+$ channels. PIPICO map with colored boxes that define the gates for $C^+ + I^+$, $CH^+ + I^+$, $CH_2^+ + I^+$, and $CH_3^+ + I^+$. On both sides are the electron images corresponding to each gate. The $4d$ photoline appears at the same radius in all channels, while the Auger-Meitner dominated region shifts to smaller radius (lower kinetic energy) with increasing hydrogen loss.

photoelectron ring is unchanged between channels, as expected for the photolines, but the intensity and radius of the secondary-electron contribution vary strongly with the fragmentation channel. As H or H^+ are removed from the methyl group, the radius of the dominant Auger-Meitner contribution shifts inward, indicating a lower secondary electron energy.

6.4.1 Channel-resolved Electron Spectra

To quantify these changes, we perform an Abel inversion of the channel-selected electron images using the BASEX method implemented in PyAbel[85;86], as described in Sec. 2.5, and integrate

over all angles to obtain one-dimensional electron kinetic-energy distributions. Figure 6.7 shows the normalized spectra for the four $CH_x^+ + I^+$ channels. All spectra exhibit a narrow peak near 50 eV, which we assign to the I $4d$ photoline. At lower kinetic energies, around 30 eV, the $CH_3^+ + I^+$ channel shows a broad maximum that corresponds to the main Auger-Meitner decay into the dominant dicationic states, consistent with measurements at similar photon energies.[50]

As hydrogen is removed from the methyl group (as H or H^+), the maximum of the Auger-Meitner band shifts to lower kinetic energy and broadens. The $CH_2^+ + I^+$ and $CH^+ + I^+$ channels display peaks that are clearly separated from the $CH_3^+ + I^+$ band, while the $C^+ + I^+$ spectrum appears as a further broadened and slightly lower-energy distribution. Between the photoelectron peak and the main Auger-Meitner band we observe a shoulder that grows with hydrogen loss. This intermediate-energy region is attributed to shake-up and shake-off processes and possibly to additional Auger-Meitner transitions into higher-lying dicationic states.

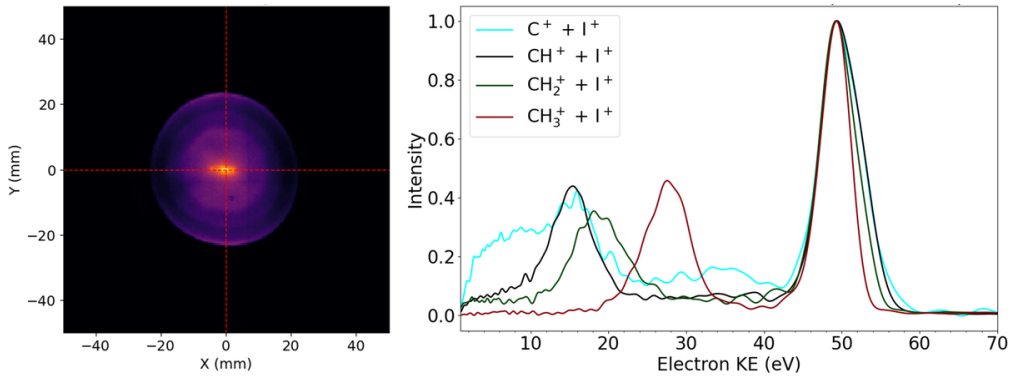

Figure 6.7: Abel-inverted, angle-integrated electron kinetic-energy distributions for the $CH_x^+ + I^+$ (x = 0–3) channels. The spectra are normalized to the maximum of the photoline. The narrow peak near 50 eV corresponds to the I $4d$ photoelectron. The broad structures around and below 30 eV arise from Auger-Meitner decay and the accompanying shake processes. The maximum of the secondary-electron band shifts to lower kinetic energy and broadens as more hydrogen (as H or H^+) are removed from the methyl group.

6.4.2 Electron Energy and Ion Kinetic Energy

The energy released in the fragmentation process is encoded both in the ion kinetic energy release (KER) and in the kinetic energy of the secondary electrons. To reveal correlations between these quantities, we plot the electron radial coordinate (as a proxy for kinetic energy) against the ion KER for each channel. Figure 6.8 shows such maps for the four $CH_x^+ + I^+$ channels. In all channels,

the horizontal band at high electron radius (energy) corresponds to the $4d$ photoline and is largely independent of the ion KER. The Auger-Meitner-dominated region appears at smaller radius and shows a systematic dependence on the ion KER.

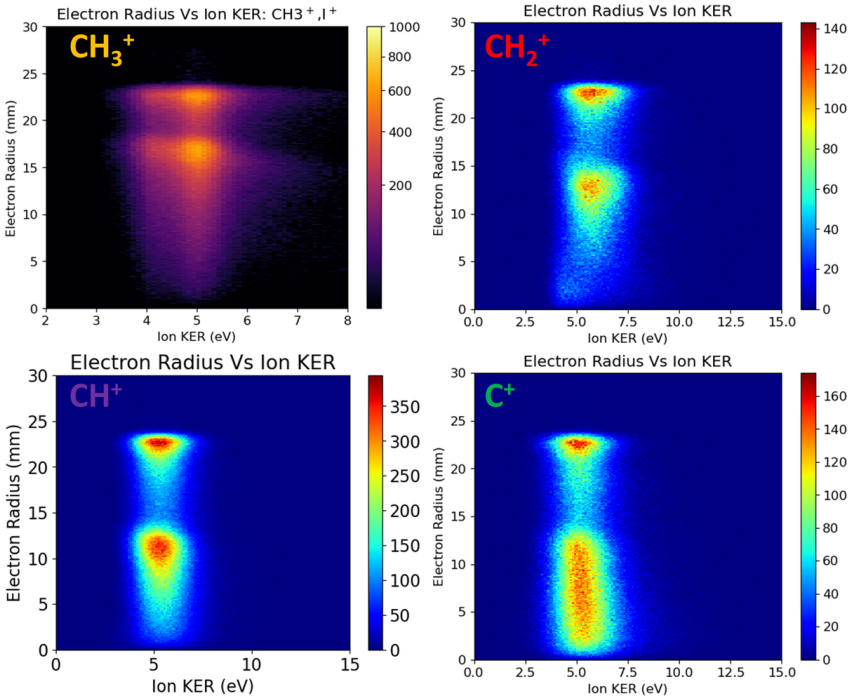

Figure 6.8: Electron radial coordinate versus ion kinetic-energy release (KER) for the $CH_x^+ + I^+$ channels. Each panel corresponds to one value of x. The color bars give the intensity in counts per bin on a linear scale. The bands at large radius reflect the $4d$ photoline, whereas the broader bands at smaller radius arise from Auger-Meitner and shake electrons. In the $CH_3^+ + I^+$ channel, two distinct KER bands are visible, and the Auger-Meitner intensity in the higher-KER band exhibits an oblique feature towards lower electron energy.

In the $CH_3^+ + I^+$ channel, the ion KER distribution exhibits two well-separated bands, which are characteristic of the competing dicationic potential energy surfaces known from previous work.[50;52] For the other dissociation channels, with one or more hydrogen lost, only a single ion KER band is observed, and the Auger-Meitner electrons, as seen in Fig. 6.7, shift to progressively lower energy with increasing hydrogen loss.

Focusing on the $CH_3^+ + I^+$ channel (top left panel), within the higher-KER band, we observe an oblique streak of electron intensity that starts near the main Auger-Meitner energy and bends towards lower electron energy as the KER increases. This indicates that part of the available energy is traded between the secondary electron and the nuclear motion, most likely through a distribution

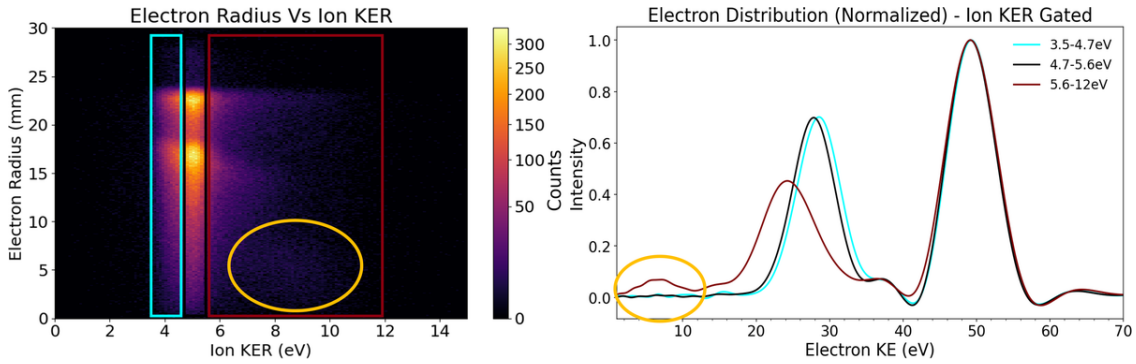

Figure 6.9: KER-gated analysis of the $CH_3^+ + I^+$ channel. (a) Electron-radius versus ion-KER map with regions marked that select the low-KER band, the central part of the high-KER band, and the highest-KER tail. (b) Abel-inverted electron kinetic-energy distributions for the three KER regions. The spectra for the low-KER and central high-KER regions are very similar and dominated by the main Auger-Meitner peak. The highest-KER region shows a reduced main peak and a pronounced low-energy contribution, indicating a decay pathway that feeds highly repulsive dicationic states.

of final dicationic states with different repulsive slopes. To analyze this correlation further, we select different KER regions that isolate the two bands, with the corresponding electron spectra shown in Fig. 6.9. The electrons associated with the lower-KER band (blue rectangular region) and with the central part of the KER band (black rectangle) have very similar distributions, dominated by the main Auger-Meitner peak. In contrast, the electrons in the highest-KER region (red rectangle) show an enhanced low-energy tail and a slight reduction of the main peak. In addition, we also observe an island of events at very low electron energy in the high KER region (marked in yellow ellipses). These features confirm the presence of additional decay pathways that lead to both higher ion KER and lower secondary-electron energies.

6.5 Two-body Channels with Doubly Charged Iodine: $CH_x^+ + I^{2+}$

We now turn to the two-body fragmentation channels in which the iodine fragment is doubly charged. These channels correspond to $4d$ photoionization followed by Auger-Meitner decay into tricationic or higher-charge final states, often accompanied by shake-up or shake-off processes. Figure 6.10 shows the electron-radius versus ion-KER maps for the $CH_x^+ + I^{2+}$ channels. Compared to the $CH_x^+ + I^+$ breakup case, the photoline is much weaker and in some channels it is hardly visible. This suggests that these final states are produced by a shake-up or shake-off (direct photo-double

ionization) processes in the first step, i.e., either by emission of a photoelectron with less kinetic energy than the usual $h\nu$-E_{thres}, or two photoelectrons that share the excess photon energy. The dominant contribution comes from broad bands of low-energy electrons below about 30 eV, which we attribute to Auger-Meitner decay and to shake processes accompanying the photoionization. For the $CH_3^+ + I^{2+}$ channel, we still observe a discernible photoline and a structured AM band. In the more strongly fragmented channels, the photoline almost disappears and the electron yield is concentrated at low energies. For these hydrogen loss channels, the KER distribution shifts towards larger values, consistent with fragmentation into three ionic fragments.

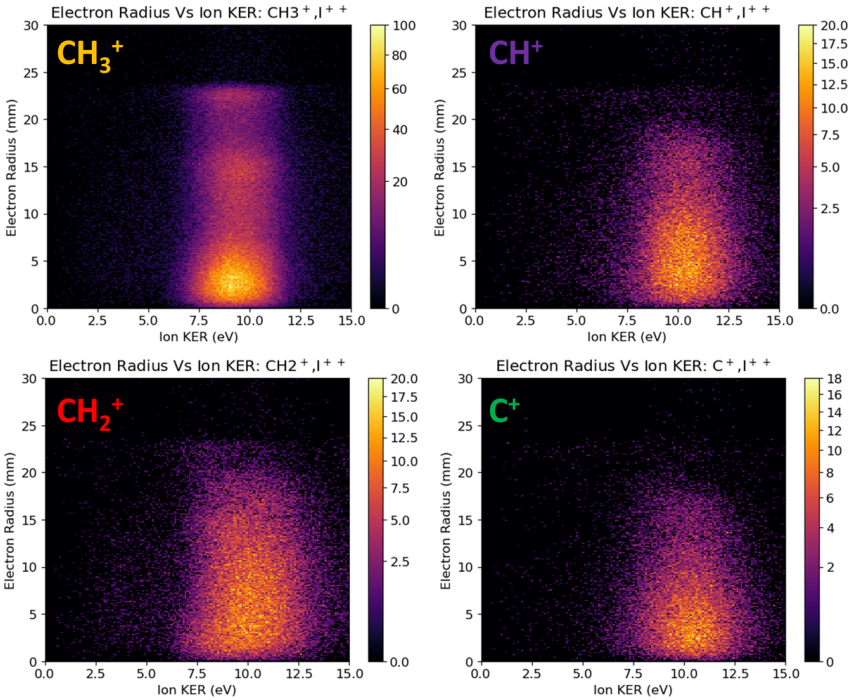

Figure 6.10: Electron-radius versus ion-KER maps for the $CH_x^+ + I^{2+}$ channels (x = 0–3). The color bars give the intensity in counts per bin on a linear scale. The photoelectron band is much weaker than in the dicationic case, and the distributions are dominated by low-energy secondary electrons. The average secondary-electron energy decreases and the low-energy tail increases as more hydrogen are removed from the methyl group.

The corresponding Abel-inverted electron spectra are shown in Fig. 6.11. The $CH_3^+ + I^{2+}$ channel exhibits a broad distribution that overlaps with, but is shifted to slightly lower energies than, the $CH_3^+ + I^+$ Auger-Meitner band. The $CH_2^+ + I^{2+}$ and $CH^+ + I^{2+}$ channels show even lower average electron energies and a stronger low-energy tail. The $C^+ + I^{2+}$ spectrum is dominated by electrons below 20 eV. The electron yield in the region marked by the black rectangle in Fig. 6.11

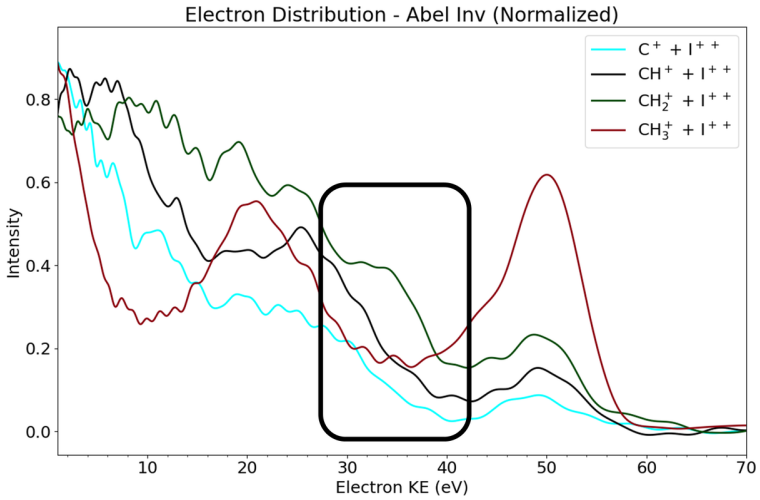

Figure 6.11: Abel-inverted, angle-integrated electron kinetic-energy distributions for the $CH_x^+ + I^{2+}$ channels (x = 0–3). All spectra are normalized to their maximum. The $CH_3^+ + I^{2+}$ channel still shows a noticeable photoline and a broad Auger-Meitner band, whereas the more fragmented channels are dominated by low-energy electrons below about 20–30 eV.

shows the same trend as in the $CH_x^+ + I^+$ two-body fragmentation channels: as more hydrogens are removed from the methyl group (as H or H^+), the intermediate-energy shoulder grows, consistent with an increasing contribution from shake processes. These observations suggest that formation of the tricationic and higher-charge state channels proceeds through highly excited intermediate states that release a large fraction of the available energy into nuclear motion and into additional low-energy electrons.

6.6 Channels Without Detected Iodine: Isolating Neutral-Iodine Breakup Contribution

In the previous sections, we analyzed two-body $CH_x^+ + (I^+ \text{ or } I^{2+})$ channels in which the iodine fragment is explicitly detected. However, a significant fraction of events contain light fragments such as H^+ and CH_x^+ in coincidence without an iodine ion. These "missing-iodine" events may arise either from breakup channels with neutral iodine ($H^+ + CH_2^+ + I$) or from events in which the iodine ion was simply not detected.

In this section, we focus on the dissociation channels that contain both H^+ and CH_2^+ fragments, as a representative case. These channels are of particular interest because they connect $H^+ + CH_2^+$

+ I (neutral) breakup with the complete three-ion breakup channels $H^+ + CH_2^+ + I^+$ and $H^+ + CH_2^+ + I^{2+}$. By comparing their ion KER distributions and electron spectra, we can isolate the electron emission associated with the neutral-iodine channel.

Figure 6.12 shows electron-radius versus ion-KER maps for three gating conditions: (a) two-body events assigned to $H^+ + CH_2^+$, (b) three-body events $H^+ + CH_2^+ + I^+$, and (c) three-body events $H^+ + CH_2^+ + I^{2+}$. All three maps exhibit a strong horizontal band at the photoelectron radius and a lower-energy band associated with the secondary electrons. The ion KER distributions differ between the channels. The $H^+ + CH_2^+$ channel spans a broad KER range that overlaps with both three-body channels, indicating that the two-body selection includes events where a charged iodine fragment was not detected.

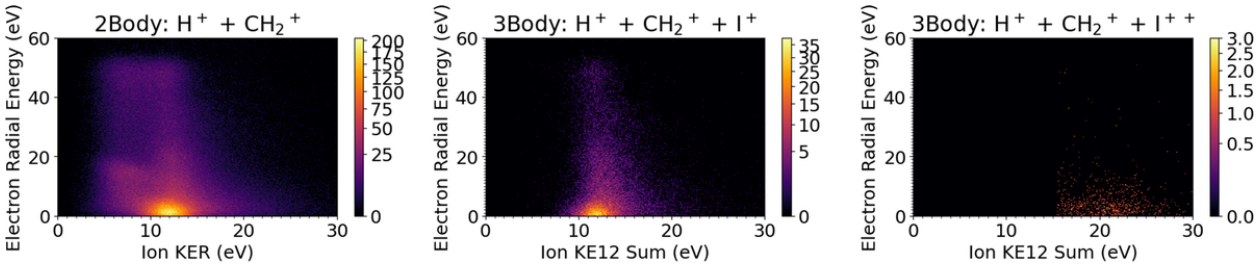

Figure 6.12: Electron energy versus ion-KER maps for hydrogen-loss channels. The color bars indicate the counts per bin on a linear scale. The three panels (left to right) show the nominal two-body channel $H^+ + CH_2^+$, the three-body channel $H^+ + CH_2^+ + I^+$, and the three-body channel $H^+ + CH_2^+ + I^{2+}$. The two-body selection contains contributions from both complete three-body channels, as seen from the overlapping KER ranges.

To extract the $H^+ + CH_2^+ + I$ (neutral) contribution, we compare the KER distributions of the two-body and three-body channels. By scaling the three-body KER spectra to match the corresponding regions in the two-body spectrum and subtracting them, we obtain a residual distribution that is dominated by events where the iodine fragment is neutral. Figure 6.13 illustrates this procedure using color-coded KER regions together with the resulting KER-gated electron spectra. The spectra for the regions dominated by the three-body channels closely resemble the electron spectra already discussed for $CH_2^+ + I^+$ and $CH_2^+ + I^{2+}$. In contrast, the residual spectrum assigned to $H^+ + CH_2^+ + I$ (neutral) shows an enhanced low-energy tail and a somewhat reduced main Auger-Meitner peak. This suggests that the neutral-iodine channel is fed by different intermediate states and may involve additional energy-sharing mechanisms among the electrons.

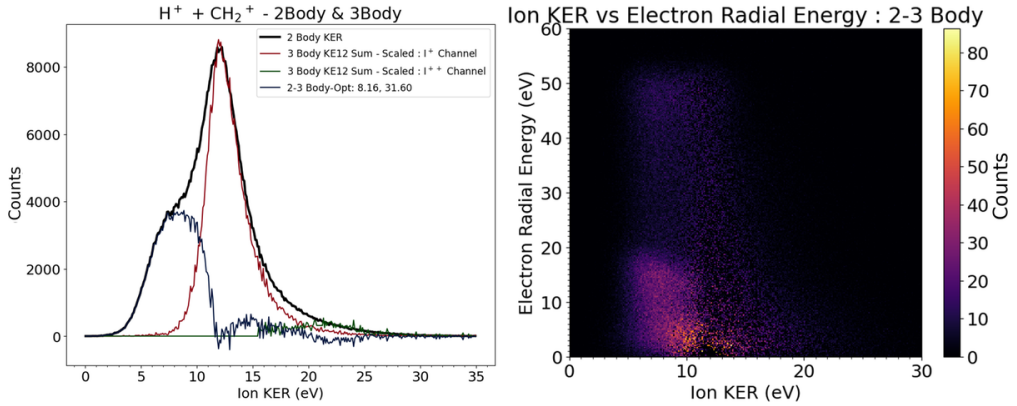

Figure 6.13: Isolation of the $H^+ + CH_2^+ + I$ (neutral) contribution. (a) Electron-radius versus ion-KER map for the $H^+ + CH_2^+$ channel with colored KER regions used to quantify the overlap with the three-body channels. (b) KER-gated electron kinetic-energy distributions. Spectra associated with the KER ranges dominated by $H^+ + CH_2^+ + I^+$ and $H^+ + CH_2^+ + I^{2+}$ resemble the corresponding $CH_2^+ + I^+$ and $CH_2^+ + I^{2+}$ electron spectra. The residual spectrum, attributed to $H^+ + CH_2^+ + I$ (neutral), shows a stronger low-energy contribution and a weaker main Auger-Meitner peak.

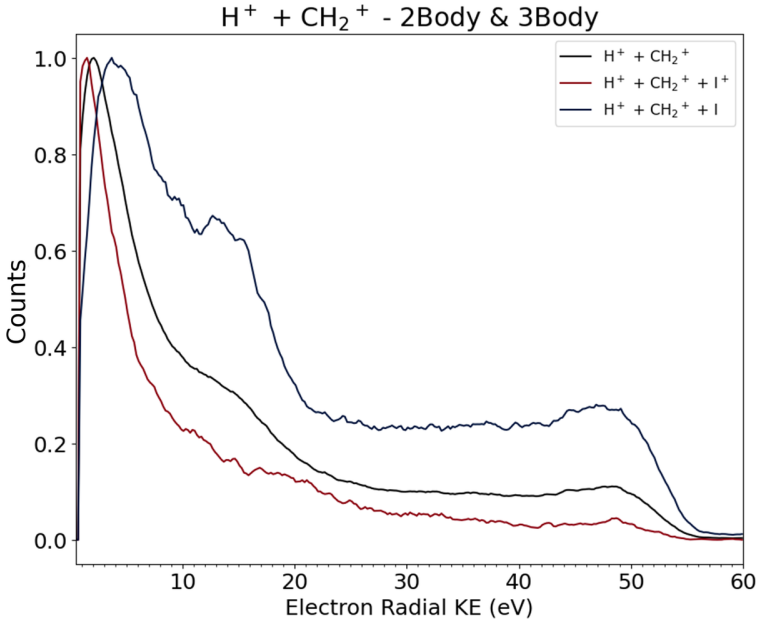

Figure 6.14: Abel-inverted electron kinetic-energy distributions for the hydrogen-loss channels. Shown are spectra associated with $H^+ + CH_2^+ + I^+$, $H^+ + CH_2^+ + I^{2+}$, and the residual $H^+ + CH_2^+ + I$ (neutral) contribution obtained after subtracting scaled three-body spectra from the nominal two-body channel. The neutral-iodine channel shows a stronger low-energy contribution and a smoother high-energy side compared to the channels with charged iodine.

The channel-resolved electron spectra for the hydrogen-loss channels are summarized in Figure 6.14. The $H^+ + CH_2^+ + I^+$ and $H^+ + CH_2^+ + I^{2+}$ spectra are qualitatively similar to the

$CH_2^+ + I^+$ and $CH_2^+ + I^{2+}$ spectra discussed earlier. The neutral-iodine channel, however, exhibits a distinct low-energy shoulder. These features highlight the sensitivity of the secondary-electron spectrum to the final charge states and fragmentation channels involved, and underline the value of the multi-ion–electron coincidence approach.

6.7 Summary and Outlook

In this chapter, we have presented a channel-resolved study of Auger-Meitner and shake electrons from CH_3I following iodine $4d$ ionization at 107 eV. Using the double-sided VMI spectrometer together with multi-particle coincidence techniques, we recorded electrons in coincidence with multiple ionic fragments and constructed ion–ion and ion–electron correlation maps. From these data, we identified the major fragmentation channels and determined their associated electron spectra.

The coincidence measurements provide a detailed view of how the secondary-electron spectrum depends on the final charge state and on the number of hydrogen, as H or H^+, removed from the methyl group. For the two-body fragmentation channels $CH_x^+ + I^+$, the main Auger-Meitner band shifts to lower kinetic energy and broadens as hydrogen are removed, while the I $4d$ photoelectron peak remains almost unchanged. For the channels $CH_x^+ + I^{2+}$, the photoelectron contribution becomes weak and the spectra are dominated by low-energy electrons, indicating that a larger fraction of the available energy is transferred into nuclear motion and additional low-energy electron emission. By comparing two-body and three-body KER distributions in the H^+ and CH_2^+ channels, we isolated the contribution of the $H^+ + CH_2^+ + I$ (neutral) channel, which exhibits a distinct low-energy shoulder compared with the channels that contain charged iodine. These findings highlight the sensitivity of the secondary-electron spectrum to the details of the fragmentation pathway and demonstrate the power of multi-ion–electron coincidence spectroscopy for disentangling complex relaxation processes in molecules.

The results obtained here complement and extend previous studies of CH_3I inner-shell photoionization. High-resolution electron spectroscopy has mapped out the multiplet structure of the photoelectron and Auger-Meitner lines,[50;52;53] and recent theoretical work has emphasized how bond dissociation modifies the core-level spectra.[54] The present measurements add an explicit con-

nection between electron spectra and specific ionic fragmentation channels, in a spirit similar to channel-resolved Auger spectroscopy of O_2,[56] but applied here to a heavier and more complex system with multiple competing pathways.

Beyond the intrinsic interest in the relaxation dynamics of CH_3I, these channel-resolved electron spectra are relevant for interpreting time-resolved experiments at X-ray free-electron laser (XFEL) facilities. The spectra reported here provide a reference for linking characteristic electron-energy ranges to particular cationic charge states and fragmentation channels. Combining such static coincidence measurements at synchrotrons with time-resolved studies at XFELs could help disentangle the roles of different electronic decay pathways in ultrafast molecular dynamics, and support the interpretation of experiments on larger, more complex systems.

Chapter 7

Summary and Outlook

In this thesis, coincidence momentum imaging of charged particles is used to probe the structure and dynamics of gas-phase molecules. The work employs different methods such as time-resolved pump–probe Coulomb explosion imaging (CEI), static strong-field CEI for structural fingerprinting, high-dimensional multi-ion coincidence combined with machine learning, and ion–electron coincidence spectroscopy. The central goal is to understand how molecular geometry and electronic structure evolve following interaction with light and how this evolution is encoded in fragment-ion momenta and electron energy distributions.

In the time-resolved study, we focused on ultraviolet (UV) pump–infrared (IR) probe CEI of diiodomethane (CH_2I_2), where 290 nm and 330 nm UV pulses initiate the photochemical process and a delayed strong-field IR pulse drives Coulomb explosion. By measuring coincident fragment-ion momenta as a function of pump–probe delay, several competing pathways are identified, including dominant C–I bond fission, three-body breakup channels, and molecular iodine formation. Analysis of delay-dependent kinetic energy release, angular distributions, and fragment energy sharing reveals signatures of a short-lived molecular configuration that resembles iso-CH_2I_2 geometries forming and decaying on a sub-100 fs timescale. The relative yield and lifetime of these transient products appear similar for both excitation wavelengths, suggesting that their formation is not strongly dependent on the excitation wavelengths used in this study. These results demonstrate that time-resolved CEI can isolate weak transient geometries in the presence of more dominant channels and provide detailed insight into ultrafast bond rearrangement and halogen elimination

dynamics in a prototypical dihalomethane.

Next, we extended the laser-induced CEI to static structural imaging of polyatomic molecules that are representative of ring-opening photoproducts. Here, an intense near-infrared pulse is used to Coulomb explode molecules such as isoxazole, 3-chloro-1-propanol, and epichlorohydrin. Three-dimensional fragment-ion momentum maps (Newton maps) are constructed from multi-ion coincidence events and used as structural fingerprints. Distinct momentum patterns associated with planar five-membered rings, open-chain, and ring–chain structures are observed. Classical Coulomb explosion simulations qualitatively reproduce the features encoding the underlying geometry. These measurements show that robust structural discrimination for medium-sized organic molecules is achievable with tabletop strong-field CEI and motivate the pursuit of complete coincidence detection and more quantitative structural retrieval.

In the next part, we explored high-dimensional CEI with complete six- and eight-ion coincidence and combined it with data-driven analysis to differentiate molecular structures. Using 1,2-dichloroethylene (1,2-DCE), we analyze events in which all six atomic fragments are detected are analyzed with dimensionality reduction and clustering algorithms. Unsupervised methods separate *cis*- and *trans*-1,2-DCE isomers directly from experimental momentum data and reveal clear differences in their multi-ion momentum correlations. Supervised models are trained on simulated momentum patterns for multiple geometries, including 1,1-DCE and twisted intermediate configurations, and then used to classify events simulated after a photoexcitation process. Together, these results establish that multi-coincidence CEI combined with machine learning can automatically cluster events by molecular structure and can possibly identify reaction channels in high-dimensional momentum space.

Finally, we turned to ion–electron coincidence measurements on core-ionized iodomethane (CH_3I) at the ALS synchrotron facility. Using 107 eV soft X-ray photons to ionize the iodine $4d$ shell, we measured Auger–Meitner electrons in coincidence with fragment-ion momenta, yielding channel-resolved electron spectra for different fragmentation patterns. The coincidence analysis reveals systematic shifts and broadenings in the Auger–Meitner electron spectra with hydrogen loss, and comparison of two-body and three-body kinetic energy release distributions allows us to identify channels that involve neutral fragments. These results provide benchmark channel-resolved refer-

ence spectra for inner-shell relaxation in a prototypical halomethane and complement the ion-only CEI studies by connecting core-level decay pathways to specific nuclear fragmentation patterns.

Looking forward, several developments in light sources and endstations promise to greatly extend the capabilities demonstrated in this work. On the tabletop side, the new high-repetition-rate strong-field laser system Konza in JRML, operating at 100 kHz, will enable CEI measurements with significantly improved statistics, making it possible to obtain high-quality momentum maps and coincidence datasets in shorter acquisition times and to resolve low-yield channels more reliably. At large-scale facilities, upgrades such as the superconducting linac of LCLS-II, which delivers up to $\sim 10^6$ X-ray pulses per second, will similarly increase the volume of coincidence data that can be collected in a single experiment. In parallel, next-generation reaction microscopes and multi-particle imaging endstations, including DREAM-type instruments[162], provide multi-hit detection of several ions and electrons from each X-ray shot. Together, these advances will make it realistic to obtain channel-resolved CEI and Auger–Meitner spectra for more complex molecules, to access weak fragmentation pathways that are currently statistics-limited, and to perform time-resolved pump–probe experiments that track how inner-shell decay and charge redistribution compete with nuclear motion in chemically relevant systems.

On the analysis side, the integration of coincidence momentum imaging with machine learning and other data-driven techniques is likely to become increasingly important. The studies on dichloroethylene show that unsupervised clustering and supervised classification can successfully disentangle overlapping channels and assign complete multi-ion events to specific structural groups. For larger molecules, where complete detection of all atomic fragments is often unrealistic, similar approaches can be explored for incomplete or partial channels, using a subset of ions to infer underlying structures and dynamical pathways. In the longer term, coincidence momentum imaging, augmented by these experimental and computational advances, may enable structural differentiation of complex molecular configurations and provide time-resolved mapping of transient geometries to track ultrafast light-driven chemistry in the gas phase.

Bibliography

[1] Prashant V. Kamat, George S. Schatz, Gregory Scholes, and Timothy Zwier. Photons, physical chemistry, and the year of light - a virtual issue. *Journal of Physical Chemistry Letters*, 6(8):1420–1422, 4 2015. ISSN 19487185. doi: 10.1021/ACS.JPCLETT.5B00607. URL https://pubs.acs.org/doi/full/10.1021/acs.jpclett.5b00607.

[2] Ksenija Glusac. What has light ever done for chemistry? *Nature Chemistry*, 8(8):734–735, 2016. doi: 10.1038/nchem.2582.

[3] Govindjee and Rajni Govindjee. The absorption of light in photosynthesis. *Scientific American*, 231(6):68–82, 1974. doi: 10.1038/scientificamerican1274-68. URL https://www.jstor.org/stable/24950240.

[4] Gernot Renger. The light reactions of photosynthesis. *Current Science*, 98(10):1305–1319, 2010. URL http://www.jstor.org/stable/24107509.

[5] Monika Zubik, Rafal Luchowski, Michal Puzio, Ewa Janik, Joanna Bednarska, Wojciech Grudzinski, and Wieslaw I Gruszecki. The negative feedback molecular mechanism which regulates excitation level in the plant photosynthetic complex LHCII: Towards identification of the energy dissipative state. *Biochimica et Biophysica Acta (BBA)-Bioenergetics*, 1827(3): 355–364, 2013. doi: 10.1016/j.bbabio.2012.11.013. URL http://dx.doi.org/10.1016/j.bbabio.2012.11.013.

[6] R. W. Schoenlein, L. A. Peteanu, R. A. Mathies, and C. V. Shank. The first step in vision: Femtosecond isomerization of rhodopsin. *Science*, 254(5030):412–415, 1991. ISSN 00368075. doi: 10.1126/SCIENCE.1925597.

[7] Linda A. Peteanu, Robert W. Schoenlein, Qing Wang, Richard A. Mathies, and Charles V. Shank. The first step in vision occurs in femtoseconds: complete blue and red spectral

studies. *Proceedings of the National Academy of Sciences*, 90(24):11762–11766, 12 1993. ISSN 00278424. doi: 10.1073/PNAS.90.24.11762. URL https://www.pnas.org/doi/abs/10.1073/pnas.90.24.11762.

[8] Qing Wang, Robert W. Schoenlein, Linda A. Peteanu, Richard A. Mathies, and Charles V. Shank. Vibrationally coherent photochemistry in the femtosecond primary event of vision. *Science*, 266(5184):422–424, 10 1994. ISSN 00368075. doi: 10.1126/SCIENCE.7939680. URL https://www.science.org/doi/10.1126/science.7939680.

[9] Dario Polli, Piero Altoè, Oliver Weingart, Katelyn M. Spillane, Cristian Manzoni, Daniele Brida, Gaia Tomasello, Giorgio Orlandi, Philipp Kukura, Richard A. Mathies, Marco Garavelli, and Giulio Cerullo. Conical intersection dynamics of the primary photoisomerization event in vision. *Nature*, 467(7314):440–443, 2010. doi: 10.1038/nature09346. URL https://www.nature.com/articles/nature09346.

[10] M. F. Holick, J. A. Maclaughlin, M. B. Clark, S. A. Holick, J. T. Potts, R. R. Anderson, I. H. Blank, J. A. Parrish, and P. Elias. Photosynthesis of previtamin D_3 in human skin and the physiologic consequences. *Science*, 210(4466):203–205, 1980. ISSN 00368075. doi: 10.1126/SCIENCE.6251551.

[11] J. A. Maclaughlin, R. R. Anderson, and M. F. Holick. Spectral character of sunlight modulates photosynthesis of previtamin D_3 and its photoisomers in human skin. *Science*, 216(4549): 1001–1003, 1982. ISSN 0036-8075. doi: 10.1126/science.6281884.

[12] Rajeshwar P Sinha and Donat-P Häder. UV-induced DNA damage and repair: a review. *Photochemical & Photobiological Sciences*, 1(4):225–236, 2002. doi: 10.1039/b201230h.

[13] L. O. Essen and T. Klar. Light-driven DNA repair by photolyases. *Cellular and Molecular Life Sciences*, 63(11):1266–1277, 6 2006. ISSN 1420682X. doi: 10.1007/S00018-005-5447-Y. URL https://link.springer.com/article/10.1007/s00018-005-5447-y.

[14] Thomas Gustavsson, Roberto Improta, and Dimitra Markovitsi. DNA/RNA: Building blocks

of life under UV irradiation. *The Journal of Physical Chemistry Letters*, 1(12):2025–2030, 2010. doi: 10.1021/jz1004973. URL https://doi.org/10.1021/jz1004973.

[15] H. Keller-Rudek, G. K. Moortgat, R. Sander, and R. Sörensen. The mpi-mainz UV/VIS spectral atlas of gaseous molecules of atmospheric interest. *Earth System Science Data*, 5 (2):365–373, 12 2013. ISSN 1866-3516. doi: 10.5194/essd-5-365-2013. URL https://essd.copernicus.org/articles/5/365/2013/.

[16] Shashank Pathak, Lea M. Ibele, Rebecca Boll, Carlo Callegari, Alexander Demidovich, Benjamin Erk, Raimund Feifel, Ruaridh Forbes, Michele Di Fraia, Luca Giannessi, Christopher S. Hansen, David M. P. Holland, Rebecca A. Ingle, Robert Mason, Oksana Plekan, Kevin C. Prince, Arnaud Rouzée, Richard J. Squibb, Jan Tross, Michael N. R. Ashfold, Basile F. E. Curchod, and Daniel Rolles. Tracking the ultraviolet-induced photochemistry of thiophenone during and after ultrafast ring opening. *Nature Chemistry*, 12(9):795–800, sep 2020. ISSN 1755-4330. doi: 10.1038/s41557-020-0507-3.

[17] Yusong Liu, Spencer L. Horton, Jie Yang, J. Pedro F. Nunes, Xiaozhe Shen, Thomas J. A. Wolf, Ruaridh Forbes, Chuan Cheng, Bryan Moore, Martin Centurion, Kareem Hegazy, Renkai Li, Ming Fu Lin, Albert Stolow, Paul Hockett, Tamás Rozgonyi, Philipp Marquetand, Xijie Wang, and Thomas Weinacht. Spectroscopic and structural probing of excited-state molecular dynamics with time-resolved photoelectron spectroscopy and ultrafast electron diffraction. *Physical Review X*, 10(2):021016, 2020. ISSN 2160-3308. doi: 10.1103/PhysRevX.10.021016. URL https://doi.org/10.1103/PhysRevX.10.021016.

[18] Joao Pedro Figueira Nunes, Lea Maria Ibele, Shashank Pathak, Andrew R. Attar, Surjendu Bhattacharyya, Rebecca Boll, Kurtis Borne, Martin Centurion, Benjamin Erk, Ming-Fu Lin, Ruaridh J. G. Forbes, Nathan Goff, Christopher S. Hansen, Matthias Hoffmann, David M. P. Holland, Rebecca A. Ingle, Duan Luo, Sri Bhavya Muvva, Alexander H. Reid, Arnaud Rouzée, Artem Rudenko, Sajib Kumar Saha, Xiaozhe Shen, Anbu Selvam Venkatachalam, Xijie Wang, Matt R. Ware, Stephen P. Weathersby, Kyle J. Wilkin, Thomas J. A. Wolf, Yanwei Xiong, Jie Yang, Michael N. R. Ashfold, Daniel Rolles, and Basile F. E. Curchod. Monitoring the evolu-

tion of relative product populations at early times during a photochemical reaction. *Journal of the American Chemical Society*, 146(6):4134–4143, 2024. doi: 10.1021/jacs.3c13046. URL https://doi.org/10.1021/jacs.3c13046.

[19] Stuart W. Crane, Jason W. L. Lee, Michael N. R. Ashfold, and Daniel Rolles. Molecular photodissociation dynamics revealed by Coulomb explosion imaging. *Physical Chemistry Chemical Physics*, 25(25):16672–16698, 2023. doi: 10.1039/D3CP01360A.

[20] Matthijs R. Panman, Elisa Biasin, Oskar Berntsson, Markus Hermann, Stephan Niebling, Ashley J. Hughes, Joachim Kübel, Kalina Atkovska, Emil Gustavsson, Amke Nimmrich, Asmus O. Dohn, Mads Laursen, Diana B. Zederkof, Alireza Honarfar, Kensuke Tono, Tetsuo Katayama, Shigeki Owada, Tim B. Van Driel, Kasper Kjaer, Martin M. Nielsen, Jan Davidsson, Jens Uhlig, Kristoffer Haldrup, Jochen S. Hub, and Sebastian Westenhoff. Observing the structural evolution in the photodissociation of diiodomethane with femtosecond solution X-ray scattering. *Physical Review Letters*, 125(22):226001, 2020. doi: 10.1103/PhysRevLett.125.226001.

[21] Zeev Vager, Ron Naaman, and Edward P. Kanter. Coulomb explosion imaging of small molecules. *Science*, 244(4903):426–431, 1989. doi: 10.1126/science.244.4903.426.

[22] Henrik Stapelfeldt, Eric Constant, Hirofumi Sakai, and Paul B. Corkum. Time-resolved Coulomb explosion imaging: A method to measure structure and dynamics of molecular nuclear wave packets. *Physical Review A*, 58(1):426–429, 1998. doi: 10.1103/PhysRevA.58.426.

[23] Christian Cornaggia. Ultrafast Coulomb explosion imaging of molecules. *Laser Physics*, 19:1660–1668, 2009. doi: 10.1134/S1054660X09130012.

[24] François Légaré, Kevin F. Lee, Igor V. Litvinyuk, Paul W. Dooley, Stanley S. Wesolowski, Philip R. Bunker, Peter Dombi, Ferenc Krausz, André D. Bandrauk, David M. Villeneuve, and Paul B. Corkum. Laser Coulomb-explosion imaging of small molecules. *Physical Review A*, 71(1):013415, 2005. doi: 10.1103/PhysRevA.71.013415.

[25] Tomoyuki Yatsuhashi and Nobuaki Nakashima. Multiple ionization and Coulomb explosion of molecules, molecular complexes, clusters and solid surfaces. *Journal of Photochemistry and Photobiology C: Photochemistry Reviews*, 34:52–84, 3 2018. ISSN 13895567. doi: 10.1016/j.jphotochemrev.2017.12.001.

[26] Akiyoshi Hishikawa, Akitaka Matsuda, and Mizuho Fushitani. Ultrafast reaction imaging and control by ultrashort intense laser pulses. *Bulletin of the Chemical Society of Japan*, 93:1293–1304, 11 2020. ISSN 0009-2673. doi: 10.1246/bcsj.20200158.

[27] Xiaokai Li, Xitao Yu, Pan Ma, Xinning Zhao, Chuncheng Wang, Sizuo Luo, and Dajun Ding. Ultrafast Coulomb explosion imaging of molecules and molecular clusters. *Chinese Physics B*, 31:103304, 10 2022. ISSN 1674-1056. doi: 10.1088/1674-1056/ac89df.

[28] Constant A. Schouder, Adam S. Chatterley, James D. Pickering, and Henrik Stapelfeldt. Laser-induced Coulomb explosion imaging of aligned molecules and molecular dimers. *Annual Review of Physical Chemistry*, 73:323–347, 2022. doi: 10.1146/annurev-physchem-090419-053627.

[29] Th. Ergler, A. Rudenko, B. Feuerstein, K. Zrost, C. D. Schröter, R. Moshammer, and J. Ullrich. Spatiotemporal imaging of ultrafast molecular motion: Collapse and revival of the D_2^+ nuclear wave packet. *Physical Review Letters*, 97:193001, 11 2006. ISSN 0031-9007. doi: 10.1103/PhysRevLett.97.193001.

[30] I. A. Bocharova, A. S. Alnaser, U. Thumm, T. Niederhausen, D. Ray, C. L. Cocke, and I. V. Litvinyuk. Time-resolved Coulomb-explosion imaging of nuclear wave-packet dynamics induced in diatomic molecules by intense few-cycle laser pulses. *Physical Review A*, 83(1):013417, 1 2011. ISSN 1050-2947. doi: 10.1103/PhysRevA.83.013417. URL https://link.aps.org/doi/10.1103/PhysRevA.83.013417.

[31] María E. Corrales, Jesús González-Vázquez, Rebeca de Nalda, and Luis Bañares. Coulomb explosion imaging for the visualization of a conical intersection. *The Journal of Physical Chemistry Letters*, 10(2):138–143, 2019. doi: 10.1021/acs.jpclett.8b03422.

[32] Tomoyuki Endo, Simon P. Neville, Vincent Wanie, Samuel Beaulieu, Chen Qu, Jude Deschamps, Philippe Lassonde, Bruno E. Schmidt, Hikaru Fujise, Mizuho Fushitani, Akiyoshi Hishikawa, Paul L. Houston, Joel M. Bowman, Michael S. Schuurman, François Légaré, and Heide Ibrahim. Capturing roaming molecular fragments in real time. *Science*, 370(6520): 1072–1077, 2020. doi: 10.1126/science.abc2960.

[33] Michael Burt, Kasra Amini, Jason W. L. Lee, Lars Christiansen, Rasmus R. Johansen, Yuki Kobayashi, James D. Pickering, Claire Vallance, Mark Brouard, and Henrik Stapelfeldt. Gas-phase structural isomer identification by Coulomb explosion of aligned molecules. *Journal of Chemical Physics*, 148(9):091102, 2018. doi: 10.1063/1.5023441.

[34] Shashank Pathak, Razib Obaid, Surjendu Bhattacharyya, Johannes Bürger, Xiang Li, Jan Tross, Travis Severt, Brandin Davis, René C. Bilodeau, Carlos A. Trallero-Herrero, Niranjan Shivaram, Daniel Rolles, Matthias F. Kling, Itzik Ben-Itzhak, C. Lewis Cocke, and Artem Rudenko. Differentiating and quantifying gas-phase conformational isomers using Coulomb explosion imaging. *The Journal of Physical Chemistry Letters*, 11(23):10205–10211, 2020. doi: 10.1021/acs.jpclett.0c02959.

[35] Utuq Ablikim, Cédric Bomme, Hui Xiong, Evgeny Savelyev, Razib Obaid, Balram Kaderiya, Sven Augustin, Kirsten Schnorr, Ileana Dumitriu, Timur Osipov, René Bilodeau, David Kilcoyne, Vinod Kumarappan, Artem Rudenko, Nora Berrah, and Daniel Rolles. Identification of absolute geometries of cis and trans molecular isomers by Coulomb Explosion Imaging. *Sci Rep*, 6(1):38202, dec 2016. ISSN 2045-2322. doi: 10.1038/srep38202.

[36] Philipp Herwig, Kerstin Zawatzky, Manfred Grieser, Oded Heber, Brandon Jordon-Thaden, Claude Krantz, Oldřich Novotný, Roland Repnow, Volker Schurig, Dirk Schwalm, Zeev Vager, Andreas Wolf, Oliver Trapp, and Holger Kreckel. Imaging the absolute configuration of a chiral epoxide in the gas phase. *Science*, 342(6163):1084–1086, 2013. doi: 10.1126/science.1246549.

[37] Martin Pitzer, Maksim Kunitski, Allan S. Johnson, Till Jahnke, Hendrik Sann, Felix Sturm, Lothar Ph. H. Schmidt, Horst Schmidt-Böcking, Reinhard Dörner, Jürgen Stohner, Julia

Kiedrowski, Michael Reggelin, Sebastian Marquardt, Alexander Schießer, Rainer Berger, and Markus S. Schöffler. Direct determination of absolute molecular stereochemistry in gas phase by Coulomb explosion imaging. *Science*, 341(6150):1096–1100, 2013. doi: 10.1126/science.1240362.

[38] Rebecca Boll, Julia M. Schäfer, Benoît Richard, Kilian Fehre, Gregor Kastirke, Zoltan Jurek, Markus S. Schöffler, Malik M. Abdullah, Nils Anders, Thomas M. Baumann, Sebastian Eckart, Benjamin Erk, Alberto De Fanis, Reinhard Dörner, Sven Grundmann, Patrik Grychtol, Alexander Hartung, Max Hofmann, Markus Ilchen, Ludger Inhester, Christian Janke, Rui Jin, Max Kircher, Katharina Kubicek, Maksim Kunitski, Xiang Li, Tommaso Mazza, Severin Meister, Niklas Melzer, Jacobo Montano, Valerija Music, Giammarco Nalin, Yevheniy Ovcharenko, Christopher Passow, Andreas Pier, Nils Rennhack, Jonas Rist, Daniel E. Rivas, Daniel Rolles, Ilme Schlichting, Lothar Ph. H. Schmidt, Philipp Schmidt, Juliane Siebert, Nico Strenger, Daniel Trabert, Florian Trinter, Isabel Vela-Perez, Rene Wagner, Peter Walter, Miriam Weller, Pawel Ziolkowski, Sang-Kil Son, Artem Rudenko, Michael Meyer, Robin Santra, and Till Jahnke. X-ray multiphoton-induced Coulomb explosion images complex single molecules. *Nature Physics*, 18:423–428, 2022. doi: 10.1038/s41567-022-01507-0.

[39] Till Jahnke, Sebastian Mai, Surjendu Bhattacharyya, Keyu Chen, Rebecca Boll, Maria Elena Castellani, Simon Dold, Ulrike Frühling, Alice E. Green, Markus Ilchen, Rebecca Ingle, Gregor Kastirke, Huynh Van Sa Lam, Fabiano Lever, Dennis Mayer, Tommaso Mazza, Terence Mullins, Yevheniy Ovcharenko, Björn Senfftleben, Florian Trinter, Atia-Tul-Noor, Sergey Usenko, Anbu Selvam Venkatachalam, Artem Rudenko, Daniel Rolles, Michael Meyer, Heide Ibrahim, and Markus Gühr. Direct observation of ultrafast symmetry reduction during internal conversion of 2-thiouracil using Coulomb explosion imaging. *Nature Communications*, 16(1):2074, Feb 2025. ISSN 2041-1723. doi: 10.1038/s41467-025-57083-3.

[40] Alice E. Green, Keyu Chen, Surjendu Bhattacharyya, Felix Allum, Sergey Usenko, Michael N. R. Ashfold, Thomas M. Baumann, Kurtis D. Borne, Mark Brouard, Michael Burt, Basile F. E. Curchod, Benjamin Erk, Ruaridh J. G. Forbes, Lea M. Ibele, Rebecca A. Ingle, Huynh Van Sa Lam, Xiang Li, Kang Lin, Tommaso Mazza, Joseph W. McManus, Michael Meyer,

Terence Mullins, Joao Pedro Figueira Nunes, Daniel E. Rivas, Aljoscha Roerig, Arnaud Rouzée, Philipp Schmidt, John Searles, Björn Senfftleben, Henrik Stapelfeldt, Rico Mayro P. Tanyag, Florian Trinter, Anbu Selvam Venkatachalam, Enliang Wang, Emily M. Warne, Peter M. Weber, Thomas J. A. Wolf, Till Jahnke, Artem Rudenko, Rebecca Boll, and Daniel Rolles. Visualizing the three-dimensional arrangement of hydrogen atoms in organic molecules by Coulomb explosion imaging. *Journal of the American Chemical Society*, 147(41):37133–37143, 2025. doi: 10.1021/jacs.5c08730. URL https://doi.org/10.1021/jacs.5c08730.

[41] Naveen Chhabra, Madan L. Aseri, and Deepak Padmanabhan. A review of drug isomerism and its significance. *International Journal of Applied and Basic Medical Research*, 3(1):16–18, 2013. doi: 10.4103/2229-516X.112233.

[42] Solomon Habtemariam. *Isomerism in organic compounds and drug molecules: chemistry and significance in biology*, pages 149–194. The Royal Society of Chemistry, 5 2023. doi: 10.1039/9781839168086-00149. URL https://books.rsc.org/books/book/2094/chapter/7578049/Isomerism-in-Organic-Compounds-and-Drug-Molecules.

[43] Huynh Van Sa Lam, Anbu S. Venkatachalam, Surjendu Bhattacharyya, Enliang Wang, Kurtis Borne, Keyu Chen, Artem Rudenko, and Daniel Rolles. Coulomb explosion imaging: a robust method for distinguishing molecular structures and tracking structural changes in photochemical reactions. In Zhiwen Liu, Demetri Psaltis, and Kebin Shi, editors, *Ultrafast Nonlinear Imaging and Spectroscopy XI*, pages 12758–29, San Diego, United States, October 2023. SPIE. ISBN 978-1-5106-6576-7. doi: 10.1117/12.2677218. URL https://doi.org/10.1117/12.2677218.

[44] Yifei Zhu, Jiawei Peng, Chao Xu, and Zhenggang Lan. Unsupervised machine learning in the analysis of nonadiabatic molecular dynamics simulation. *J. Phys. Chem. Lett.*, pages 9601–9619, sep 2024. doi: 10.1021/acs.jpclett.4c01751.

[45] Kyle Acheson and Adam Kirrander. Automatic clustering of excited-state trajectories: Application to photoexcited dynamics. *J. Chem. Theory Comput.*, page acs.jctc.3c00776, September 2023. doi: 10.1021/acs.jctc.3c00776.

[46] L.J.P. van der Maaten and G.E. Hinton. Visualizing high-dimensional data using t-SNE. *Journal of Machine Learning Research*, 9(nov):2579–2605, 2008. ISSN 1532-4435.

[47] Leland McInnes, John Healy, and James Melville. UMAP: Uniform manifold approximation and projection for dimension reduction, sep 2018. arXiv:1802.03426.

[48] Ricardo J. G. B. Campello, Davoud Moulavi, and Joerg Sander. Density-based clustering based on hierarchical density estimates. In Jian Pei, Vincent S. Tseng, Longbing Cao, Hiroshi Motoda, and Guandong Xu, editors, *Advances in Knowledge Discovery and Data Mining*, pages 160–172, Berlin, Heidelberg, 2013. Springer. ISBN 978-3-642-37456-2. doi: 10.1007/978-3-642-37456-2_14.

[49] Demetrios Matsakis, Anthea Coster, Brenda Laster, and Ruth Sime. A renaming proposal: "The Auger–Meitner effect". *Physics Today*, 72(9):10, September 2019. doi: 10.1063/PT.3.4281. URL https://physicstoday.aip.org/letters/a-renaming-proposal-the-auger-meitner-effect.

[50] Ruaridh Forbes, Alberto De Fanis, Daniel Rolles, Stephen T. Pratt, Ivan Powis, Nicholas A. Besley, Aleksandar R. Milosavljević, Christophe Nicolas, John D. Bozek, and David M. P. Holland. Photoionization of the I 4*d* and valence orbitals of methyl iodide. *Journal of Physics B: Atomic, Molecular and Optical Physics*, 53(15), 2020. doi: 10.1088/1361-6455/ab8c5a.

[51] Ruaridh Forbes, Alberto De Fanis, Cédric Bomme, Daniel Rolles, Stephen T. Pratt, Ivan Powis, Nicholas A. Besley, Marc Simon, Saikat Nandi, Aleksandar R. Milosavljević, Christophe Nicolas, John D. Bozek, Jonathan G. Underwood, and David M. P. Holland. Photoionization of the iodine 3d, 4s, and 4p orbitals in methyl iodide. *The Journal of Chemical Physics*, 149(14):144302, 2018. doi: 10.1063/1.5035496. URL https://pubs.aip.org/aip/jcp/article/149/14/144302/196822.

[52] D. M. P. Holland, I. Powis, G. Öhrwall, L. Karlsson, and W. von Niessen. A study of the photoionisation dynamics of chloromethane and iodomethane. *Chemical Physics*, 326(2–3):535–550, 2006. doi: 10.1016/j.chemphys.2006.03.017.

[53] D. W. Lindle, P. H. Kobrin, C. M. Truesdale, T. A. Ferrett, P. A. Heimann, H. G. Kerkhoff, U. Becker, and D. A. Shirley. Inner-shell photoemission from the iodine atom in CH_3I. *Physical Review A*, 30(1):239, 1984. doi: 10.1103/PhysRevA.30.239.

[54] Ludger Inhester, Zheng Li, Xiaolei Zhu, Nikita Medvedev, and Thomas J. A. Wolf. Spectroscopic signature of chemical bond dissociation revealed by calculated core-electron spectra. *The Journal of Physical Chemistry Letters*, 10(21):6536–6544, 2019. doi: 10.1021/acs.jpclett.9b02370.

[55] Mizuho Fushitani, Yasumasa Hikosaka, Motomichi Tashiro, and Akiyoshi Hishikawa. State-selective dissociative double ionization of CH_3I and CH_2I_2 via I $4d$ core-hole states studied by multi-electron-ion coincidence spectroscopy. *The Journal of Chemical Physics*, 160(17):174307, 2024. doi: 10.1063/5.0204769.

[56] Xiao-Jing Liu, Christophe Nicolas, Minna Patanen, and Catalin Miron. Disentangling auger decays in O_2 by photoelectron-ion coincidences. *Scientific Reports*, 7:2898, 2017. doi: 10.1038/s41598-017-02875-x.

[57] D. W. Chandler and P. L. Houston. Two-dimensional imaging of state-selected photodissociation products. *The Journal of Chemical Physics*, 87(2):1445–1447, 1987. doi: 10.1063/1.453276. URL https://doi.org/10.1063/1.453276.

[58] A. T. J. B. Eppink and D. H. Parker. Velocity map imaging of ions and electrons using electrostatic lenses: Application in photoelectron and photofragment ion imaging. *Review of Scientific Instruments*, 68(9):3477–3484, 1997. doi: 10.1063/1.1148310. URL https://doi.org/10.1063/1.1148310.

[59] Utuq Ablikim, Cédric Bomme, Timur Osipov, Hui Xiong, Razib Obaid, René C. Bilodeau, Nora G. Kling, Ileana Dumitriu, Sven Augustin, Shashank Pathak, Kirsten Schnorr, David Kilcoyne, Nora Berrah, and Daniel Rolles. A coincidence velocity map imaging spectrometer for ions and high-energy electrons to study inner-shell photoionization of gas-phase molecules. *Review of Scientific Instruments*, 90(5):055103, 05 2019. ISSN 0034-6748. doi: 10.1063/1.5093420.

[60] Huynh Van Sa Lam, Anbu Selvam Venkatachalam, Surjendu Bhattacharyya, Keyu Chen, Kurtis Borne, Enliang Wang, Rebecca Boll, Till Jahnke, Vinod Kumarappan, Artem Rudenko, and Daniel Rolles. Differentiating three-dimensional molecular structures using laser-induced Coulomb explosion imaging. *Physical Review Letters*, 132(12):123201, 2024. doi: 10.1103/PhysRevLett.132.123201.

[61] Donna Strickland and Gérard Mourou. Compression of amplified chirped optical pulses. *Optics Communications*, 56(3):219–221, 1985. doi: 10.1016/0030-4018(85)90120-8. URL https://www.sciencedirect.com/science/article/pii/0030401885901208.

[62] P. Maine, D. Strickland, P. Bado, M. Pessot, and G. Mourou. Generation of ultrahigh peak power pulses by chirped pulse amplification. *IEEE Journal of Quantum Electronics*, 24(2): 398–403, 1988. doi: 10.1109/3.137. URL https://ieeexplore.ieee.org/document/12545.

[63] Rick Trebino. *Frequency-Resolved Optical Gating: The Measurement of Ultrashort Laser Pulses*. Springer US, New York, NY, 2000. doi: 10.1007/978-1-4615-1181-6.

[64] D. J. Kane and R. Trebino. Characterization of arbitrary femtosecond pulses using frequency-resolved optical gating. *IEEE Journal of Quantum Electronics*, 29(2):571–579, 1993. doi: 10.1109/3.199311.

[65] K. W. DeLong, B. Kohler, K. Wilson, D. N. Fittinghoff, and R. Trebino. Pulse retrieval in frequency-resolved optical gating based on the method of generalized projections. *Optics Letters*, 19(24):2152–2154, 1994. doi: 10.1364/OL.19.002152.

[66] Rick Trebino and Daniel J. Kane. Using phase retrieval to measure the intensity and phase of ultrashort pulses: frequency-resolved optical gating. *Journal of the Optical Society of America A*, 10(5):1101–1111, 1993. doi: 10.1364/JOSAA.10.001101.

[67] Advanced Light Source, Lawrence Berkeley National Laboratory. Beamlines at the Advanced Light Source, 2025. URL https://als.lbl.gov/beamlines/. Accessed 2025-11-10.

[68] Advanced Light Source, Lawrence Berkeley National Laboratory. Beamline 10.0.1: Angle- and

spin-resolved photoelectron spectroscopy, 2025. URL https://als.lbl.gov/beamlines/10-0-1/. Accessed 2025-11-10.

[69] LBNL/ALS Beamline 10 team. ALS beamline 10.0.1 overview (energy range and sgm), 2025. URL https://sites.google.com/lbl.gov/bl12-arpes-als/beamline-10. Accessed 2025-11-10.

[70] John Byrd et al. Creating a pseudo single bunch at the als. In *Proceedings of PAC 2007*, 2007. URL https://accelconf.web.cern.ch/p07/PAPERS/TUPMN115.PDF. States 2 ns bucket spacing and typical multibunch fill.

[71] Seyyed Javad Robatjazi. *Ion-electron coincidence studies of femtosecond dynamics triggered by extreme ultraviolet photoionization of atoms and molecules*. PhD thesis, Kansas State University, Manhattan, KS, 2021. URL https://krex.k-state.edu/items/833e5c4b-50db-4211-b930-aaa6dbf0ee78. Doctoral dissertation.

[72] Shashank Pathak. *Isomerization and fragmentation of polyatomic molecules induced by ultraviolet and extreme UV light*. PhD thesis, Kansas State University, Manhattan, KS, 2021. URL https://krex.k-state.edu/items/58d5d954-be0f-4f54-9dc3-201dff75a4b7. Doctoral dissertation.

[73] Balram Kaderiya. *Imaging Photo-Induced Dynamics in Halomethane Molecules with Coincident Ion Momentum Spectroscopy*. Ph.d. dissertation, Kansas State University, Manhattan, Kansas, USA, 2021. URL https://hdl.handle.net/2097/41294. Advisor: Dr. Artem Rudenko.

[74] D. Rolles, Z. D. Pešić, M. Perri, R. C. Bilodeau, G. D. Ackerman, B. S. Rude, A. L. D. Kilcoyne, J. D. Bozek, and N. Berrah. A velocity map imaging spectrometer for electron–ion and ion–ion coincidence experiments with synchrotron radiation. *Nuclear Instruments and Methods in Physics Research Section B: Beam Interactions with Materials and Atoms*, 261(1):170–174, 2007. ISSN 0168-583X. doi: 10.1016/j.nimb.2007.04.186. URL https://www.sciencedirect.com/science/article/pii/S0168583X07009949.

[75] Arno Vredenborg, Wim G. Roeterdink, and Maurice H. M. Janssen. A photoelectron–photoion coincidence imaging apparatus for femtosecond time-resolved molecular dynamics with electron time-of-flight resolution of 18 ps and energy resolution $\delta e/e = 3.5\%$. *Review of Scientific Instruments*, 79(6):063108, 2008. doi: 10.1063/1.2949142. URL https://doi.org/10.1063/1.2949142.

[76] L. Strüder, S. Epp, et al. Large-format, high-speed, X-ray pnccds combined with electron and ion imaging spectrometers in a multipurpose chamber for experiments at 4th-generation light sources. *Nuclear Instruments and Methods in Physics Research Section A: Accelerators, Spectrometers, Detectors and Associated Equipment*, 614:483–496, 2010.

[77] Benjamin Erk, Jan P. Müller, Cédric Bomme, Rebecca Boll, Günter Brenner, Henry N. Chapman, Jonathan Correa, Stefan Düsterer, Siarhei Dziarzhytski, Stefan Eisebitt, Heinz Graafsma, Sören Grunewald, Lars Gumprecht, Robert Hartmann, Günter Hauser, Barbara Keitel, Clemens von Korff Schmising, Marion Kuhlmann, Bastian Manschwetus, Laurent Mercadier, Erland Müller, Christopher Passow, Elke Plönjes, Daniel Ramm, Dimitrios Rompotis, Artem Rudenko, Daniela Rupp, Mario Sauppe, Frank Siewert, Dieter Schlosser, Lothar Strüder, Angad Swiderski, Simone Techert, Kai Tiedtke, Thomas Tilp, Rolf Treusch, Ilme Schlichting, Joachim Ullrich, Robert Moshammer, Thomas Möller, and Daniel Rolles. CAMP@FLASH: an end-station for imaging, electron- and ion-spectroscopy, and pump–probe experiments at the FLASH free-electron laser. *Journal of Synchrotron Radiation*, 25(5):1529–1540, 9 2018. ISSN 16005775. doi: 10.1107/S1600577518008585.

[78] T. Osipov, C. Bostedt, et al. The lamp instrument at the linac coherent light source free-electron laser. *Review of Scientific Instruments*, 89:035112, 2018.

[79] K. Fehre, D. Trojanowskaja, J. Gatzke, M. Kunitski, F. Trinter, S. Zeller, L. Ph. H. Schmidt, J. Stohner, R. Berger, A. Czasch, O. Jagutzki, T. Jahnke, R. Dörner, and M. S. Schöffler. Absolute ion detection efficiencies of microchannel plates and funnel microchannel plates for multi-coincidence detection. *Review of Scientific Instruments*, 89:045112, 2018. ISSN 0034-6748. doi: 10.1063/1.5022564.

[80] Photonis/Exosens. High collection efficiency (Hi-CE) microchannel plates. https://www.photonis.com/products/microchannel-plates, 2025. Technical brochure describing funneled pore entrances and increased open-area ratio; accessed 2025.

[81] H. Okano, T. Oka, T. Mori, M. Mitsuhashi, and S. Kuma. Multi-electron–ion coincidence spectrometer with a high-efficiency microchannel plate. *International Journal of Mass Spectrometry*, 469:116753, 2022. doi: 10.1016/j.ijms.2022.116753.

[82] Facility for Rare Isotope Beams (FRIB). *SpecTcl and NSCLDAQ Documentation*. Michigan State University, 2024. URL https://docs.frib.msu.edu/daq/spectcl/. User documentation for SpecTcl/NSCLDAQ.

[83] NSCL/FRIB DAQ Group. NSCLDAQ / SpecTcl. https://sourceforge.net/projects/nscldaq/, 2024. Project page and source distribution.

[84] Scientific Instrument Services, Inc. *SIMION 8.1: The Field and Particle Trajectory Simulator*. Scientific Instrument Services, Inc., Ringoes, NJ, 2013. URL https://simion.com/. Version 8.1.

[85] Daniel D. Hickstein, Roman Yurchak, Stephen T. Gibson, et al. PyAbel: A Python package for Abel transform methods. *Computer Physics Communications*, 207:341–355, 2016. doi: 10.1016/j.cpc.2016.05.005.

[86] V. Dribinski, A. Ossadtchi, V. A. Mandelshtam, and H. Reisler. Reconstruction of Abel-transformable images: The BASEX method. *Review of Scientific Instruments*, 73(7):2634–2642, 2002. doi: 10.1063/1.1482156.

[87] Surjendu Bhattacharyya, Kurtis Borne, Farzaneh Ziaee, Shashank Pathak, Enliang Wang, Anbu Selvam Venkatachalam, Xiang Li, Nathan Marshall, Kevin D. Carnes, Charles W. Fehrenbach, Travis Severt, Itzik Ben-Itzhak, Artem Rudenko, and Daniel Rolles. Strong-field-induced Coulomb explosion imaging of tribromomethane. *The Journal of Physical Chemistry Letters*, 13(25):5845–5853, 2022. doi: 10.1021/acs.jpclett.2c01007. PMID: 35727076.

[88] Anbu Selvam Venkatachalam, Huynh Van Sa Lam, Surjendu Bhattacharyya, Balram Kaderiya, Enliang Wang, Yijue Ding, Loren Greenman, Artem Rudenko, and Daniel Rolles. Imaging transient molecular configurations in UV-excited diiodomethane. *The Journal of Chemical Physics*, 163(16):164308, 2025. doi: 10.1063/5.0284410.

[89] Eugene Wigner. On the quantum correction for thermodynamic equilibrium. *Physical Review*, 40(5):749–759, 1932. doi: 10.1103/PhysRev.40.749.

[90] Mario Barbatti, Giovanni Granucci, Matthias Ruckenbauer, Felix Plasser, Rachel Crespo-Otero, Jiří Pittner, Maurizio Persico, and Hans Lischka. NEWTON-X: a package for newtonian dynamics close to the crossing seam (v. 2.2), 2018. Available at https://www.newtonx.org.

[91] Mario Barbatti, Matthias Ruckenbauer, Felix Plasser, Jiří Pittner, Giovanni Granucci, Maurizio Persico, and Hans Lischka. NEWTON-X: a surface-hopping program for nonadiabatic molecular dynamics. *WIREs Computational Molecular Science*, 4(1):26–33, 2014. doi: 10.1002/wcms.1158.

[92] Charles R. Harris, K. Jarrod Millman, Stéfan J. van der Walt, Ralf Gommers, Pauli Virtanen, David Cournapeau, Eric Wieser, Julian Taylor, Sebastian Berg, Nathaniel J. Smith, Robert Kern, Matti Picus, Stephan Hoyer, Marten H. van Kerkwijk, Matthew Brett, Allan Haldane, Jaime Fernández del Río, Mark Wiebe, Pearu Peterson, Pierre Gérard-Marchant, Kevin Sheppard, Tyler Reddy, Warren Weckesser, Hameer Abbasi, Christoph Gohlke, and Travis E. Oliphant. Array programming with NumPy. *Nature*, 585(7825):357–362, 2020. doi: 10.1038/s41586-020-2649-2.

[93] Pauli Virtanen, Ralf Gommers, Travis E. Oliphant, Matt Haberland, Tyler Reddy, David Cournapeau, Evgeni Burovski, Pearu Peterson, Warren Weckesser, Jonathan Bright, and et al. SciPy 1.0: fundamental algorithms for scientific computing in python. *Nature Methods*, 17(3):261–272, 2020. doi: 10.1038/s41592-019-0686-2.

[94] Lutz Schomburg and Josef Köhrle. On the importance of selenium and iodine metabolism for

thyroid hormone biosynthesis and human health. *Mol. Nutr. Food Res*, 52:1235–1246, 2008. doi: 10.1002/mnfr.200700465. URL www.mnf-journal.com.

[95] Theodore K. Koenig, Rainer Volkamer, Eric C. Apel, James F. Bresch, Carlos A. Cuevas, Barbara Dix, Edwin W. Eloranta, Rafael P. Fernandez, Samuel R. Hall, Rebecca S. Hornbrook, R. Bradley Pierce, J. Michael Reeves, Alfonso Saiz-Lopez, and Kirk Ullmann. Ozone depletion due to dust release of iodine in the free troposphere. *Science Advances*, 7(52): eabj6544, 2021. doi: 10.1126/sciadv.abj6544.

[96] Lucy J. Carpenter. Iodine in the marine boundary layer. *Chemical Reviews*, 103(12):4953–4962, 12 2003. ISSN 0009-2665. doi: 10.1021/cr0206465.

[97] M. Kawasaki, S. J. Lee, and R. Bersohn. Photodissociation of molecular beams of methylene iodide and iodoform. *The Journal of Chemical Physics*, 63(2):809–814, 7 1975. ISSN 0021-9606. doi: 10.1063/1.431361. URL /aip/jcp/article/63/2/809/215756/Photodissociation-of-molecular-beams-of-methylene.

[98] Peter M. Kroger, Peter C. Demou, and Stephen J. Riley. Polyhalide photofragment spectra. I. two-photon two-step photodissociation of methylene iodide. *The Journal of Chemical Physics*, 65(5):1823–1834, 9 1976. ISSN 0021-9606. doi: 10.1063/1.433274. URL /aip/jcp/article/65/5/1823/765423/Polyhalide-photofragment-spectra-I-Two-photon-two.

[99] Steven L. Baughcum and Stephen R. Leone. Photofragmentation infrared emission studies of vibrationally excited free radicals CH_3 and CH_2I. *The Journal of Chemical Physics*, 72(12): 6531–6545, 6 1980. ISSN 0021-9606. doi: 10.1063/1.439111. URL /aip/jcp/article/72/12/6531/86717/Photofragmentation-infrared-emission-studies-of.

[100] Haifeng Xu, Ying Guo, Shilin Liu, Xingxiao Ma, Dongxu Dai, and Guohe Sha. Photodissociation dynamics of CH_2I_2 molecules in the ultraviolet range studied by ion imaging. *The Journal of Chemical Physics*, 117(12):5722–5729, September 2002. doi: 10.1063/1.1503316. URL https://doi.org/10.1063/1.1503316.

[101] Aimable Kalume, Lisa George, and Scott A. Reid. Isomerization as a key path to molecular

products in the gas-phase decomposition of halons. *Journal of Physical Chemistry Letters*, 1 (20):3090–3095, 10 2010. ISSN 19487185. doi: 10.1021/JZ101250S.

[102] Scott A. Reid. When isomerisation is electron transfer: the intriguing story of the isohalocarbons. *International Reviews in Physical Chemistry*, 33(3):341–370, 2014. ISSN 1366591X. doi: 10.1080/0144235X.2014.942548. URL https://www.tandfonline.com/doi/abs/10.1080/0144235X.2014.942548.

[103] Alexander N. Tarnovsky, Villy Sundström, Eva Åkesson, and Torbjörn Pascher. Photochemistry of diiodomethane in solution studied by femtosecond and nanosecond laser photolysis. formation and dark reactions of the CH_2I–I isomer photoproduct and its role in cyclopropanation of olefins. *Journal of Physical Chemistry A*, 108(2):237–249, 2004. doi: 10.1021/jp035406n.

[104] Taehoon Kim, Hyun Sun Kim, Yoonsoo Lee, Kyung Hyun Kim, Hyotcherl Kim, and Hyotcherl Ihee. Fate of transient isomer of CH_2I_2: Mechanism and origin of ionic photoproducts formation unveiled by time-resolved X-ray liquidography. *The Journal of Chemical Physics*, 150(22):224201, 2019. doi: 10.1063/1.5097179. URL https://doi.org/10.1063/1.5097179.

[105] Veniamin A. Borin, Sergey M. Matveev, Darya S. Budkina, Patrick Z. El-Khoury, and Alexander N. Tarnovsky. Direct photoisomerization of CH_2I_2 vs $CHBr_3$ in the gas phase: a joint 50 fs experimental and multireference resonance-theoretical study. *Physical Chemistry Chemical Physics*, 18(41):28883–28892, 2016. ISSN 1463-9076. doi: 10.1039/C6CP05129D. URL http://xlink.rsc.org/?DOI=C6CP05129D.

[106] X. Li, A. Rudenko, M. S. Schöffler, N. Anders, Th M. Baumann, S. Eckart, B. Erk, A. De Fanis, K. Fehre, R. Dörner, L. Foucar, S. Grundmann, P. Grychtol, A. Hartung, M. Hofmann, M. Ilchen, Ch Janke, G. Kastirke, M. Kircher, K. Kubicek, M. Kunitski, T. Mazza, S. Meister, N. Melzer, J. Montano, V. Music, G. Nalin, Y. Ovcharenko, Ch Passow, A. Pier, N. Rennhack, J. Rist, D. E. Rivas, I. Schlichting, L. Ph H. Schmidt, Ph Schmidt, J. Siebert, N. Strenger, D. Trabert, F. Trinter, I. Vela-Perez, R. Wagner, P. Walter, M. Weller, P. Ziolkowski, A. Czasch, D. Rolles, M. Meyer, T. Jahnke, and R. Boll. Coulomb explosion

imaging of small polyatomic molecules with ultrashort X-ray pulses. *Physical Review Research*, 4(1):013029, 2022. ISSN 2643-1564. doi: 10.1103/PhysRevResearch.4.013029. URL https://doi.org/10.1103/PhysRevResearch.4.013029.

[107] H. Stapelfeldt, E. Constant, and P. B. Corkum. Wave packet structure and dynamics measured by Coulomb explosion. *Physical Review Letters*, 74(19):3780–3783, 5 1995. ISSN 0031-9007. doi: 10.1103/PhysRevLett.74.3780. URL https://link.aps.org/doi/10.1103/PhysRevLett.74.3780.

[108] Th Ergler, A Rudenko, B Feuerstein, K Zrost, C D Schröter, R Moshammer, and J Ullrich. Ultrafast mapping of $H_2^+(D_2^+)$ nuclear wave packets using time-resolved coulomb explosion imaging. *Journal of Physics B: Atomic, Molecular and Optical Physics*, 39(13):S493–S501, 7 2006. ISSN 0953-4075. doi: 10.1088/0953-4075/39/13/S22. URL https://iopscience.iop.org/article/10.1088/0953-4075/39/13/S22.

[109] Huynh Van Sa Lam, Van-Hung Hoang, Anbu Selvam Venkatachalam, Surjendu Bhattacharyya, Keyu Chen, Sina Jacob, Sanduni Kudagama, Tu Thanh Nguyen, Daniel Rolles, Uwe Thumm, Artem Rudenko, and Vinod Kumarappan. Simultaneous imaging of vibrational, rotational, and electronic wave-packet dynamics in a triatomic molecule. *Physical Review A*, 111(6):L061101, 2025. doi: 10.1103/PhysRevA.111.L061101. URL https://link.aps.org/doi/10.1103/PhysRevA.111.L061101.

[110] Kasra Amini, Evgeny Savelyev, Felix Brauße, Nora Berrah, Cédric Bomme, Mark Brouard, Michael Burt, Lauge Christensen, Stefan Düsterer, Benjamin Erk, Hauke Höppner, Thomas Kierspel, Faruk Krecinic, Alexandra Lauer, Jason W. L. Lee, Maria Müller, Erland Müller, Terence Mullins, Harald Redlin, Nora Schirmel, Jan Thøgersen, Simone Techert, Sven Toleikis, Rolf Treusch, Sebastian Trippel, Anatoli Ulmer, Claire Vallance, Joss Wiese, Per Johnsson, Jochen Küpper, Artem Rudenko, Arnaud Rouzée, Henrik Stapelfeldt, Daniel Rolles, and Rebecca Boll. Photodissociation of aligned CH_3i and $C_6H_3F_2I$ molecules probed with time-resolved Coulomb explosion imaging by site-selective extreme ultraviolet ionization. *Structural Dynamics*, 5(1):14301, 1 2018. ISSN 2329-7778.

doi: 10.1063/1.4998648. URL https://pubs.aip.org/sdy/article/5/1/014301/365407/Photodissociation-of-aligned-CH3I-and-C6H3F2I.

[111] Farzaneh Ziaee, Kurtis Borne, Ruaridh Forbes, Kanaka Raju, Yubaraj Malakar, Balram Kaderiya, Travis Severt, Itzik Ben-Itzhak, Artem Rudenko, and Daniel Rolles. Single- and multiphoton-induced ultraviolet excitation and photodissociation of CH_3I probed by coincident ion momentum imaging. *Physical Chemistry Chemical Physics*, 25:9999, 2023. doi: 10.1039/d3cp00498h.

[112] Surjendu Bhattacharyya, Enliang Wang, Kurtis Borne, Keyu Chen, Anbu Selvam Venkatachalam, Huynh Van Sa Lam, Farzaneh Ziaee, Shashank Pathak, Anton Khmelnitskiy, Kevin D. Carnes, Charles W. Fehrenbach, Itzik Ben-Itzhak, Artem Rudenko, and Daniel Rolles. Delayed dissociation and transient isomerization during the ultrafast photodissociation of the tribromomethane cation. *The Journal of Physical Chemistry Letters*, 15(49): 12188–12196, 2024. doi: 10.1021/acs.jpclett.4c02838. URL https://doi.org/10.1021/acs.jpclett.4c02838. PMID: 39622006.

[113] F. Légaré, Kevin F. Lee, I. V. Litvinyuk, P. W. Dooley, A. D. Bandrauk, D. M. Villeneuve, and P. B. Corkum. Imaging the time-dependent structure of a molecule as it undergoes dynamics. *Physical Review A*, 72(5):052717, 11 2005. ISSN 1050-2947. doi: 10.1103/PhysRevA.72.052717. URL https://link.aps.org/doi/10.1103/PhysRevA.72.052717.

[114] Benjamin W. Toulson, Jonathan P. Alaniz, J. Grant Hill, and Craig Murray. Near-UV photodissociation dynamics of CH_2I_2. *Physical Chemistry Chemical Physics*, 18(16):11091–11103, 4 2016. ISSN 14639076. doi: 10.1039/C6CP01063F.

[115] Marta L. Murillo-Sánchez, Sonia Marggi Poullain, Juan J. Bajo, María E. Corrales, Jesús González-Vázquez, Ignacio R. Solá, and Luis Bañares. Halogen-atom effect on the ultrafast photodissociation dynamics of the dihalomethanes CH_2ICl and CH_2BrI. *Physical Chemistry Chemical Physics*, 20(32):20766–20778, 2018. ISSN 1463-9076. doi: 10.1039/C8CP03600D. URL https://xlink.rsc.org/?DOI=C8CP03600D.

[116] Felix Allum, Michael Burt, Kasra Amini, Rebecca Boll, Hansjochen Köckert, Pavel K. Olshin, Sadia Bari, Cédric Bomme, Felix Brauße, Barbara Cunha de Miranda, Stefan Düsterer, Benjamin Erk, Marie Géléoc, Romain Geneaux, Alexander S. Gentleman, Gildas Goldsztejn, Renaud Guillemin, David M. P. Holland, Iyas Ismail, Per Johnsson, Loïc Journel, Jochen Küpper, Jan Lahl, Jason W. L. Lee, Sylvain Maclot, Stuart R. Mackenzie, Bastian Manschwetus, Andrey S. Mereshchenko, Robert Mason, Jérôme Palaudoux, Maria Novella Piancastelli, Francis Penent, Dimitrios Rompotis, Arnaud Rouzée, Thierry Ruchon, Artem Rudenko, Evgeny Savelyev, Marc Simon, Nora Schirmel, Henrik Stapelfeldt, Simone Techert, Oksana Travnikova, Sebastian Trippel, Jonathan G. Underwood, Claire Vallance, Joss Wiese, Farzaneh Ziaee, Mark Brouard, Tatiana Marchenko, and Daniel Rolles. Coulomb explosion imaging of CH_3I and CH_2ClI photodissociation dynamics. *The Journal of Chemical Physics*, 149(20):204313, 2018. doi: 10.1063/1.5041381. URL https://doi.org/10.1063/1.5041381.

[117] Sonia Marggi Poullain, David V. Chicharro, Eduardo Navarro, Luis Rubio-Lago, Jesús González-Vázquez, and Luis Bañares. Photodissociation dynamics of bromoiodomethane from the first and second absorption bands: A combined velocity map and slice imaging study. *Physical Chemistry Chemical Physics*, 20:3490, 2018. doi: 10.1039/c7cp07077b.

[118] Hansjochen Köckert, Jason W.L. Lee, Felix Allum, Kasra Amini, Sadia Bari, Cédric Bomme, Felix Brauße, Mark Brouard, Michael Burt, Barbara Cunha De Miranda, Stefan Düsterer, Per Eng-Johnsson, Benjamin Erk, Marie Géléoc, Romain Geneaux, Alexander S. Gentleman, Renaud Guillemin, Gildas Goldsztejn, David M.P. Holland, Iyas Ismail, Loïc Journel, Thomas Kierspel, Jochen Küpper, Jan Lahl, Stuart R. Mackenzie, Sylvain Maclot, Bastian Manschwetus, Andrey S. Mereshchenko, Terence Mullins, Pavel K. Olshin, Jérôme Palaudoux, Francis Penent, Maria Novella Piancastelli, Dimitrios Rompotis, Arnaud Rouzée, Thierry Ruchon, Artem Rudenko, Nora Schirmel, Marc Simon, Simone Techert, Oksana Travnikova, Sebastian Trippel, Claire Vallance, Enliang Wang, Joss Wiese, Farzaneh Ziaee, Tatiana Marchenko, Daniel Rolles, and Rebecca Boll. UV-induced dissociation of CH_2BrI probed by intense femtosecond XUV pulses. *Journal of Physics B: Atomic, Molecular and Optical Physics*, 55(1), 1 2022. ISSN 13616455. doi: 10.1088/1361-6455/AC489D.

[119] Pedro Recio, Javier Cachón, Luis Rubio-Lago, David V. Chicharro, Alexandre Zanchet, Paulo Limão-Vieira, Nelson De Oliveira, Peter C. Samartzis, Sonia Marggi Poullain, and Luis Bañares. Imaging the photodissociation dynamics and fragment alignment of CH_2BrI at 193 nm. *Journal of Physical Chemistry A*, 126(45):8404–8422, 11 2022. ISSN 15205215. doi: 10.1021/ACS.JPCA.2C05897. URL https://pubs.acs.org/doi/full/10.1021/acs.jpca.2c05897.

[120] T. Walmsley, J. Unwin, F. Allum, S. Bari, R. Boll, K. Borne, M. Brouard, P. Bucksbaum, N. Ekanayake, B. Erk, R. Forbes, A. J. Howard, P. Eng-Johnsson, J. W.L. Lee, Z. Liu, B. Manschwetus, R. Mason, C. Passow, J. Peschel, D. Rivas, D. Rolles, A. Rörig, A. Rouzée, C. Vallance, F. Ziaee, and M. Burt. Characterizing the multi-dimensional reaction dynamics of dihalomethanes using XUV-induced Coulomb explosion imaging. *Journal of Chemical Physics*, 159(14):144302, 10 2023. ISSN 10897690. doi: 10.1063/5.0172749. URL https://doi.org/10.1063/5.0172749.

[121] Shun Yi Chen, Po Yu Tsai, Hsiang Chin Lin, Chia Ching Wu, King Chuen Lin, B. J. Sun, and A. H.H. Chang. I_2 molecular elimination in single-photon dissociation of CH_2I_2 at 248 nm by using cavity ring-down absorption spectroscopy. *Journal of Chemical Physics*, 134(3), 1 2011. ISSN 00219606. doi: 10.1063/1.3523571.

[122] A. M. Sayler, E. Eckner, J. McKenna, B. D. Esry, K. D. Carnes, I. Ben-Itzhak, and G. G. Paulus. Nonunique and nonuniform mapping in few-body Coulomb-explosion imaging. *Physical Review A*, 97:033412, 3 2018. ISSN 2469-9926. doi: 10.1103/PhysRevA.97.033412.

[123] Benjamin J. Whitaker. *Imaging in Molecular Dynamics: Technology and Applications*. Cambridge University Press, 2003.

[124] Reza Karimi, Wing-Ki Liu, and Joseph Sanderson. Femtosecond laser-induced Coulomb explosion imaging. In *Advances in Multi-Photon Processes and Spectroscopy*, pages 97–153. World Scientific, 2016. doi: 10.1142/9789814749763_0003.

[125] Horst Schmidt-Böcking, Joachim Ullrich, Reinhard Dörner, and Charles Lewis Cocke. The COLTRIMS reaction microscope—the spyhole into the ultrafast entangled dynamics of atomic

and molecular systems. *Annalen der Physik*, 533(7):2100134, 2021. doi: 10.1002/andp.202100134.

[126] T. Jahnke, V. Mergel, O. Jagutzki, A. Czasch, K. Ullmann, R. Ali, V. Frohne, T. Weber, L. P. Schmidt, S. Eckart, M. Schöffler, S. Schößler, S. Voss, A. Landers, D. Fischer, M. Schulz, A. Dorn, L. Spielberger, R. Moshammer, R. Olson, M. Prior, R. Dörner, J. Ullrich, C. L. Cocke, and H. Schmidt-Böcking. High-resolution momentum imaging—from stern's molecular beam method to the COLTRIMS reaction microscope. In Bretislav Friedrich and Horst Schmidt-Böcking, editors, *Molecular Beams in Physics and Chemistry*, chapter 18, pages 375–441. Springer International Publishing, 2021. doi: 10.1007/978-3-030-63963-1_18.

[127] Ammar S. Alnaser, Xiao-Min Tong, Timur Osipov, Stefan Voss, Chandra M. Maharjan, Petar Ranitovic, Brian Ulrich, Bing Shan, Zenghu Chang, C. D. Lin, and C. L. Cocke. Routes to control of H_2 Coulomb explosion in few-cycle laser pulses. *Physical Review Letters*, 93(18): 183202, 2004. doi: 10.1103/PhysRevLett.93.183202.

[128] Tsukasa Takanashi, Kosuke Nakamura, Edwin Kukk, Koji Motomura, Hironobu Fukuzawa, Kiyonobu Nagaya, Shin ichi Wada, Yoshiaki Kumagai, Denys Iablonskyi, Yuta Ito, Yuta Sakakibara, Daehyun You, Toshiyuki Nishiyama, Kazuki Asa, Yuhiro Sato, Takayuki Umemoto, Kango Kariyazono, Kohei Ochiai, Manabu Kanno, Kaoru Yamazaki, Kuno Kooser, Christophe Nicolas, Catalin Miron, Theodor Asavei, Liviu Neagu, Markus Schöffler, Gregor Kastirke, Xiao-Jing Liu, Artem Rudenko, Shigeki Owada, Tetsuo Katayama, Tadashi Togashi, Kensuke Tono, Makina Yabashi, Hirohiko Kono, and Kiyoshi Ueda. Ultrafast Coulomb explosion of a diiodomethane molecule induced by an X-ray free-electron laser pulse. *Physical Chemistry Chemical Physics*, 19:19707–19721, 2017. ISSN 1463-9076. doi: 10.1039/C7CP01669G.

[129] Travis Severt, Zachary L. Streeter, Wael Iskandar, Kirk A. Larsen, Averell Gatton, Daniel Trabert, Bethany Jochim, Brandon Griffin, Elio G. Champenois, Matthew M. Brister, Dylan Reedy, Demitri Call, Richard Strom, Allen L. Landers, Reinhard Dörner, Joshua B. Williams, Daniel S. Slaughter, Robert R. Lucchese, Thorsten Weber, C. William McCurdy, and Itzik

Ben-Itzhak. Step-by-step state-selective tracking of fragmentation dynamics of water dications by momentum imaging. *Nature Communications*, 13:5146, 9 2022. ISSN 2041-1723. doi: 10.1038/s41467-022-32836-6.

[130] Andrew J. Howard, Mathew Britton, Zachary L. Streeter, Chuan Cheng, Ruaridh Forbes, Joshua L. Reynolds, Felix Allum, Gregory A. McCracken, Ian Gabalski, Robert R. Lucchese, C. William McCurdy, Thomas Weinacht, and Philip H. Bucksbaum. Filming enhanced ionization in an ultrafast triatomic slingshot. *Communications Chemistry*, 6:81, 4 2023. ISSN 2399-3669. doi: 10.1038/s42004-023-00882-w.

[131] Takao Fuji, Yoshi-Ichi Suzuki, Takuya Horio, Toshinori Suzuki, Roland Mitrić, Ute Werner, and Vlasta Bonačić-Koutecký. Ultrafast photodynamics of furan. *The Journal of Chemical Physics*, 133(23):234303, dec 2010. ISSN 0021-9606. doi: 10.1063/1.3518441.

[132] Weijie Hua, Sven Oesterling, Jason D. Biggs, Yu Zhang, Hideo Ando, Regina de Vivie-Riedle, Benjamin P. Fingerhut, and Shaul Mukamel. Monitoring conical intersections in the ring opening of furan by attosecond stimulated X-ray raman spectroscopy. *Structural Dynamics*, 3(2):023601, mar 2016. ISSN 2329-7778. doi: 10.1063/1.4933007.

[133] Jun Cao. Photoinduced reactions of both 2-formyl-2H-azirine and isoxazole: a theoretical study based on electronic structure calculations and nonadiabatic dynamics simulations. *The Journal of Chemical Physics*, 142(24):244302, jun 2015. ISSN 0021-9606. doi: 10.1063/1.4922742.

[134] Jun Cao, Zhi-Zhong Xie, and Xiaodong Yu. Excited-state dynamics of oxazole: a combined electronic structure calculations and dynamic simulations study. *Chemical Physics*, 474:25–35, aug 2016. ISSN 0301-0104. doi: 10.1016/j.chemphys.2016.05.003.

[135] M. J. Frisch, G. W. Trucks, H. B. Schlegel, G. E. Scuseria, M. A. Robb, J. R. Cheeseman, G. Scalmani, V. Barone, G. A. Petersson, H. Nakatsuji, X. Li, M. Caricato, A. Marenich, J. Bloino, B. G. Janesko, R. Gomperts, B. Mennucci, H. P. Hratchian, J. V. Ortiz, A. F. Izmaylov, J. L. Sonnenberg, D. Williams-Young, F. Ding, F. Lipparini, F. Egidi, J. Goings, B. Peng, A. Petrone, T. Henderson, D. Ranasinghe, V. G. Zakrzewski, J. Gao, N. Rega,

G. Zheng, W. Liang, M. Hada, M. Ehara, K. Toyota, R. Fukuda, J. Hasegawa, M. Ishida, T. Nakajima, Y. Honda, O. Kitao, H. Nakai, T. Vreven, K. Throssell, J. A. Montgomery Jr., J. E. Peralta, F. Ogliaro, M. Bearpark, J. J. Heyd, E. Brothers, K. N. Kudin, V. N. Staroverov, T. Keith, R. Kobayashi, J. Normand, K. Raghavachari, A. Rendell, J. C. Burant, S. S. Iyengar, J. Tomasi, M. Cossi, J. M. Millam, M. Klene, C. Adamo, R. Cammi, J. W. Ochterski, R. L. Martin, K. Morokuma, O. Farkas, J. B. Foresman, and D. J. Fox. Gaussian 09, revision e.01, 2016. Gaussian, Inc., Wallingford, CT.

[136] Benoît Richard, Rebecca Boll, Sourav Banerjee, Julia M. Schäfer, Zoltan Jurek, Gregor Kastirke, Kilian Fehre, Markus S. Schöffler, Nils Anders, Thomas M. Baumann, Sebastian Eckart, Benjamin Erk, Alberto De Fanis, Reinhard Dörner, Sven Grundmann, Patrik Grychtol, Max Hofmann, Markus Ilchen, Max Kircher, Katharina Kubicek, Maksim Kunitski, Xiang Li, Tommaso Mazza, Severin Meister, Niklas Melzer, Jacobo Montano, Valerija Music, Yevheniy Ovcharenko, Christopher Passow, Andreas Pier, Nils Rennhack, Jonas Rist, Daniel E. Rivas, Daniel Rolles, Ilme Schlichting, Lothar Ph H Schmidt, Philipp Schmidt, Daniel Trabert, Florian Trinter, Rene Wagner, Peter Walter, Pawel Ziolkowski, Artem Rudenko, Michael Meyer, Robin Santra, Ludger Inhester, and Till Jahnke. Imaging collective quantum fluctuations of the structure of a complex molecule. *Science*, 389(6760): 650–654, 2025. doi: 10.1126/science.adu2637. URL https://www.science.org/doi/10.1126/science.adu2637.

[137] Michael J. Fuller, E.Bright Wilson, and Walther Caminati. Rotational isomerism in 3-chloro-1-propanol from the microwave spectrum. *Journal of Molecular Spectroscopy*, 96:131–145, 11 1982. ISSN 00222852. doi: 10.1016/0022-2852(82)90219-3.

[138] Alan D. Richardson and Kenneth Hedberg. Conformational analysis 20. a gas-phase electron-diffraction and ab initio molecular orbital investigation of 3-chloro-propan-1-ol. *Journal of Molecular Structure*, 413-414:61–71, 9 1997. ISSN 00222860. doi: 10.1016/S0022-2860(97)00150-6.

[139] Hassan M. Badawi and Wolfgang Förner. Analysis of vibrational spectra of 3-halo-1-propanols

$CH_2XCH_2CH_2OH$ (X is Cl and Br). *Spectrochimica Acta Part A: Molecular and Biomolecular Spectroscopy*, 71:1095–1101, 12 2008. ISSN 13861425. doi: 10.1016/j.saa.2008.03.002.

[140] Feng Wang and Prasad L. Polavarapu. Conformational stability of (+)-epichlorohydrin. *The Journal of Physical Chemistry A*, 104:6189–6196, 7 2000. ISSN 1089-5639. doi: 10.1021/jp000757c.

[141] Yasuki Endo and Takamasa Momose. Ftmw spectroscopy of epichlorohydrin: Detection of three conformers. *Journal of Molecular Spectroscopy*, 372:111348, 7 2020. ISSN 00222852. doi: 10.1016/j.jms.2020.111348.

[142] Anbu Selvam Venkatachalam, Loren Greenman, Joshua Stallbaumer, Artem Rudenko, Daniel Rolles, and Huynh Van Sa Lam. Exploiting correlations in multi-coincidence Coulomb explosion patterns for differentiating molecular structures using machine learning. *Nature Communications*, 16:11366, December 2025. doi: 10.1038/s41467-025-66369-5. URL https://www.nature.com/articles/s41467-025-66369-5.

[143] Enliang Wang, Surjendu Bhattacharyya, Keyu Chen, Kurtis Borne, Farzaneh Ziaee, Shashank Pathak, Huynh Van Sa Lam, Anbu Selvam Venkatachalam, Xiangjun Chen, Rebecca Boll, Till Jahnke, Artem Rudenko, and Daniel Rolles. Time-resolved Coulomb explosion imaging unveils ultrafast ring opening of furan, 2023.

[144] Tommy Eriksson, Sven Björkman, and Peter Höglund. Clinical pharmacology of thalidomide. *European Journal of Clinical Pharmacology*, 57(5):365–376, Aug 2001. ISSN 1432-1041. doi: 10.1007/s002280100320.

[145] David Patterson, Melanie Schnell, and John M. Doyle. Enantiomer-specific detection of chiral molecules via microwave spectroscopy. *Nature*, 497(7450):475–477, May 2013. ISSN 1476-4687. doi: 10.1038/nature12150.

[146] Xiaoyu Zhou, Zhuofan Wang, Shuai Li, Xianle Rong, Jiexun Bu, Qiang Liu, and Zheng Ouyang. Differentiating enantiomers by directional rotation of ions in a mass spectrometer. *Science*, 383(6683):612–618, 2024. doi: 10.1126/science.adj8342.

[147] Jonas L. Hansen, Jens H. Nielsen, Christian Bruun Madsen, Anders Thyboe Lindhardt, Mikael P. Johansson, Troels Skrydstrup, Lars Bojer Madsen, and Henrik Stapelfeldt. Control and femtosecond time-resolved imaging of torsion in a chiral molecule. *The Journal of Chemical Physics*, 136(20):204310, 05 2012. ISSN 0021-9606. doi: 10.1063/1.4719816.

[148] K. Fehre, S. Eckart, M. Kunitski, M. Pitzer, S. Zeller, C. Janke, D. Trabert, J. Rist, M. Weller, A. Hartung, L. Ph. H. Schmidt, T. Jahnke, R. Berger, R. Dörner, and M. S. Schöffler. Enantioselective fragmentation of an achiral molecule in a strong laser field. *Science Advances*, 5(3):eaau7923, mar 2019. doi: 10.1126/sciadv.aau7923.

[149] D. Tsitsonis, F. Trinter, J. B. Williams, K. Fehre, Ph. V. Demekhin, T. Jahnke, R. Dörner, and M. S. Schöffler. Enantioselective one-photon excitation of formic acid. *Phys. Rev. Lett.*, 133:093002, Aug 2024. doi: 10.1103/PhysRevLett.133.093002. URL https://link.aps.org/doi/10.1103/PhysRevLett.133.093002.

[150] Joseph W. McManus, Felix Allum, Josh Featherstone, Chow-Shing Lam, and Mark Brouard. Two-dimensional projected-momentum covariance mapping for Coulomb explosion imaging. *J. Phys. Chem. A*, 128(16):3220–3229, April 2024. ISSN 1089-5639. doi: 10.1021/acs.jpca.4c01084.

[151] Hang Yuan, Yue Gao, Bo Yang, Shaofei Gu, Hong Lin, Dalong Guo, Junliang Liu, Shaofeng Zhang, Xinwen Ma, and Shenyue Xu. Coulomb explosion imaging of complex molecules using highly charged ions. *Phys. Rev. Lett.*, 133(19):193002, nov 2024. doi: 10.1103/PhysRevLett.133.193002.

[152] Leo Breiman. Random forests. *Machine Learning*, 45:5–32, 10 2001. ISSN 08856125. doi: 10.1023/A:1010933404324.

[153] A. Rudenko, Th. Ergler, B. Feuerstein, K. Zrost, C. D. Schröter, R. Moshammer, and J. Ullrich. Real-time observation of vibrational revival in the fastest molecular system. *Chemical Physics*, 329(1):193–202, October 2006. ISSN 0301-0104. doi: 10.1016/j.chemphys.2006.06.038.

[154] Peter J. Rousseeuw. Silhouettes: A graphical aid to the interpretation and validation of cluster analysis. *Journal of Computational and Applied Mathematics*, 20:53–65, 1987. ISSN 0377-0427. doi: 10.1016/0377-0427(87)90125-7.

[155] David L. Davies and Donald W. Bouldin. A cluster separation measure. *IEEE Transactions on Pattern Analysis and Machine Intelligence*, PAMI-1(2):224–227, apr 1979. ISSN 1939-3539. doi: 10.1109/TPAMI.1979.4766909.

[156] Koji Motomura, Edwin Kukk, Hironobu Fukuzawa, Shin-ichi Wada, Kiyonobu Nagaya, Satoshi Ohmura, Subhendu Mondal, Tetsuya Tachibana, Yuta Ito, Ryosuke Koga, Tsukasa Sakai, Kenji Matsunami, Artem Rudenko, Christophe Nicolas, Xiao-Jing Liu, Catalin Miron, Yizhu Zhang, Yuhai Jiang, Jianhui Chen, Mailam Anand, Dong Eon Kim, Kensuke Tono, Makina Yabashi, Makoto Yao, and Kiyoshi Ueda. Charge and nuclear dynamics induced by deep inner-shell multiphoton ionization of CH_3I molecules by intense X-ray free-electron laser pulses. *The Journal of Physical Chemistry Letters*, 6(15):2944–2949, 2015. doi: 10.1021/acs.jpclett.5b01205. URL https://doi.org/10.1021/acs.jpclett.5b01205.

[157] Utuq Ablikim. *Coulomb Explosion Imaging of Polyatomic Molecules after Photoionization with X-Rays and Strong Laser Fields*. PhD thesis, Kansas State University, Manhattan, KS, Aug 2017. URL http://hdl.handle.net/2097/36252. Doctoral dissertation.

[158] J. N. Cutler, G. M. Bancroft, and K. H. Tan. Ligand-field splittings and core-level linewidths in I 4*d* photoelectron spectra of iodine molecules. *The Journal of Chemical Physics*, 97(11): 7932–7943, 1992. doi: 10.1063/1.463468. URL https://doi.org/10.1063/1.463468.

[159] Atomic calculation of photoionization cross-sections and asymmetry parameters: Iodine (I). https://vuo.elettra.eu/services/elements/mnu_elem.cgi?ELEMENT=I. Virtual User Office, Elettra-Sincrotrone Trieste. Accessed 19 November 2025.

[160] J. J. Yeh and I. Lindau. Atomic subshell photoionization cross sections and asymmetry parameters: $1 \leq z \leq 103$. *Atomic Data and Nuclear Data Tables*, 32:1–155, 1985.

[161] J.-J. Yeh. *Atomic Calculation of Photoionization Cross-Sections and Asymmetry Parameters*. Gordon and Breach, Langhorne, PA, 1993. ISBN 2-88124-585-4.

[162] Peter Walter, Micheal Holmes, Razib Obaid, Lope Amores, Xianchao Cheng, James P. Cryan, James M. Glownia, Xiang Li, Ming-Fu Lin, May Ling Ng, Joseph Robinson, Niranjan Shivaram, Jing Yin, David Fritz, Justin James, Jean-Charles Castagna, and Timur Osipov. The DREAM Endstation at the Linac Coherent Light Source. *Applied Sciences*, 12(20):10534, 2022. doi: 10.3390/app122010534. URL https://doi.org/10.3390/app122010534.

Appendix A

UV–IR Cross-Correlation and UV Pulse Intensity

A.1 UV–IR Cross-Correlation and Instrument Response

To determine the effective instrument response function (IRF), which we subsequently use as an approximate measure of the UV pulse duration, we measured the Ar^+ yield as a function of the delay between the UV pulse (either 290 nm or 330 nm) and the 800 nm near-infrared (NIR) pulse. The resulting delay scans and fits are shown in Figs. A.1 and A.2.

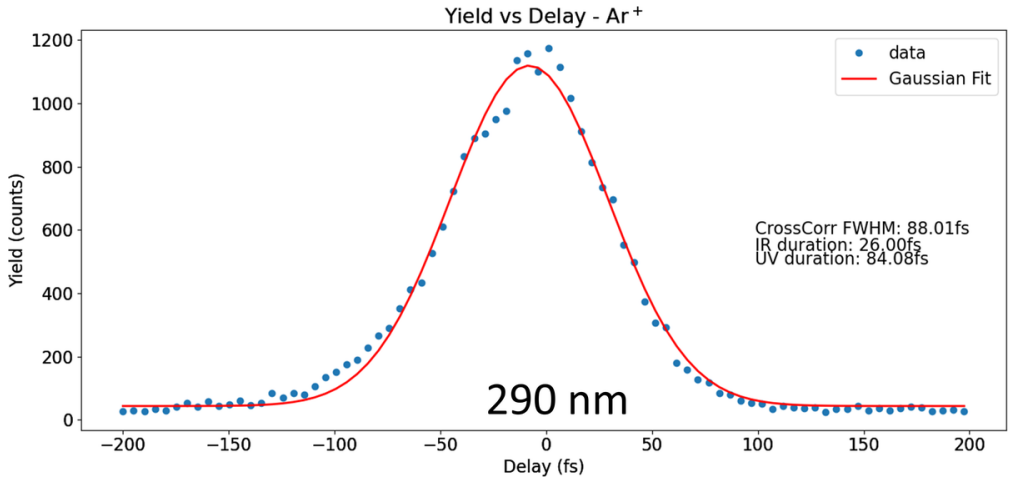

Figure A.1: UV–NIR cross-correlation trace used to determine the UV pulse duration at 290 nm. The Ar^+ yield is plotted as a function of delay between the 290 nm UV pulse and the 800 nm NIR pulse, together with a Gaussian fit yielding a cross-correlation FWHM of $\sim$ 88 fs and a UV pulse duration of $\sim$ 84 fs, assuming a 26 fs NIR pulse.

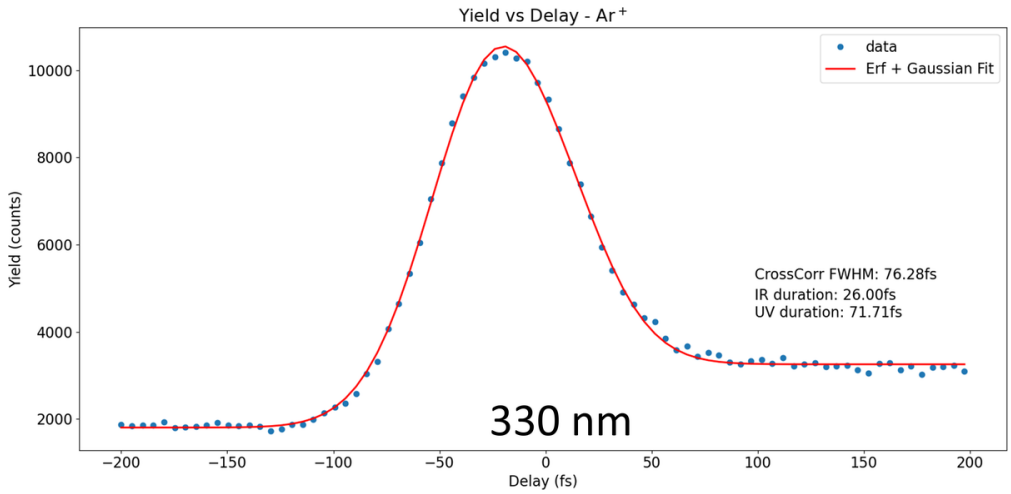

Figure A.2: UV–NIR cross-correlation trace used to determine the UV pulse duration at 330 nm. Beyond the yield increase at temporal overlap, the 330 nm data exhibit a step-like offset, so they are fitted with the sum of an error-function step and a Gaussian peak, giving a cross-correlation FWHM of ~ 76 fs and a UV pulse duration of ~ 72 fs, again assuming a 26 fs NIR pulse.

For the 290 nm data, the cross-correlation trace is well described by a Gaussian

$$Y(\tau) = y_0 + A \exp\left[-\frac{(\tau - \tau_0)^2}{2\sigma^2}\right], \tag{A.1}$$

with a full width at half maximum (FWHM) of $\Delta\tau_{\mathrm{xcorr}} = 2\sqrt{2\ln 2}\,\sigma \simeq 88$ fs.

In addition to the yield increase at temporal overlap, the 330 nm data exhibit a step-like offset after the overlap and are therefore fitted with the sum of an error-function step and a Gaussian peak,

$$Y(\tau) = y_{0,\mathrm{e}} + \frac{A_{\mathrm{e}}}{2}\left[1 + \mathrm{erf}\left(\frac{\tau - \tau_{\mathrm{e}}}{\sqrt{2}\,f_{\mathrm{e}}}\right)\right] + y_{0,\mathrm{g}} + A_{\mathrm{g}} \exp\left[-\frac{(\tau - \tau_{\mathrm{g}})^2}{2\sigma^2}\right], \tag{A.2}$$

which yields a cross-correlation FWHM of $\Delta\tau_{\mathrm{xcorr}} \simeq 76$ fs.

Assuming Gaussian temporal profiles for both pulses, the cross-correlation FWHM is related to the individual pulse durations by $\Delta\tau^2_{\mathrm{xcorr}} = \Delta\tau^2_{\mathrm{NIR}} + \Delta\tau^2_{\mathrm{UV}}$. Using a NIR pulse duration of $\Delta\tau_{\mathrm{NIR}} \approx 26$ fs (from SHG-FROG measurements), we obtain $\Delta\tau_{\mathrm{UV}}(290\ \mathrm{nm}) \approx 84$ fs and $\Delta\tau_{\mathrm{UV}}(330\ \mathrm{nm}) \approx 72$ fs.

In the following, we treat these values as the effective UV pulse durations and as a measure of the instrument response function for the time-resolved measurements.

A.2 Estimate of the UV Peak Intensity

To estimate the UV peak intensity at the interaction region, we assume a Gaussian beam with a $1/e^2$ diameter of ~ 3 mm before focusing and a spherical focusing mirror with a focal length of 75 mm. Using standard Gaussian optics, this corresponds to a beam diameter at focus of order

$$w_0 \sim (9\text{–}17)\ \mu\text{m} \tag{A.3}$$

for M^2 values between 1 and 1.6 at 290 nm and 330 nm. The average UV power in the experiments was in the range of 0.4–1.5 mW at 330 nm ($\sim$ 72 fs) and 0.3–0.6 mW at 290 nm ($\sim$ 84 fs) at a repetition rate of 3 kHz, corresponding to pulse energies of a few 10^{-7} J. The peak intensity of a Gaussian pulse is then approximated by

$$I_0 \approx \frac{2E_\mathrm{p}}{\pi w_0^2\, \Delta\tau_\mathrm{UV}}, \tag{A.4}$$

where E_p is the pulse energy, w_0 the $1/e^2$ radius at focus, and $\Delta\tau_\mathrm{UV}$ the UV pulse duration (FWHM).

Table A.1: Estimated UV peak intensities for typical powers and focal spot sizes. The intensities are obtained from Gaussian-beam optics assuming a $1/e^2$ input diameter of ~ 3 mm, a 75 mm focusing optic, and UV pulse durations of ~ 72 fs (330 nm) and ~ 84 fs (290 nm).

Wavelength (fs)	Power (mW)	I_0 for $w_0 = 0.01$ mm	I_0 for $w_0 = 0.017$ mm
330 nm (72 fs)	0.4	4.3×10^{12} W/cm^2	1.5×10^{12} W/cm^2
	1.5	1.66×10^{13} W/cm^2	5.75×10^{12} W/cm^2
290 nm (84 fs)	0.3	3.5×10^{12} W/cm^2	1.26×10^{12} W/cm^2
	0.6	7.0×10^{12} W/cm^2	2.5×10^{12} W/cm^2

Inserting the values above yields peak intensities on the order of $I_0 \sim$ a few $\times\, 10^{12}$ W/cm^2, as summarized in Table A.1. These numbers should be regarded as approximate, but they indicate that the UV excitation in the present experiments operates in the mid-10^{12} to low-10^{13} W/cm^2 range.